Finanziato dall'Unione europea NextGenerationEU | Ministero dell'Università e della Ricerca | Italiadomani PIANO NAZIONALE DI RIPRESA E RESILIENZA | Università degli Studi di Palermo

multi-Risk sciEnce for resilienT commUnities undeR a changiNg climate

PhD COURSE

Advances In Modelling, Health-Monitoring, Infrastructures, Geomatics, Geotechnics, Hazards, Engineering Structures, Transportation (AIM HIGHEST)

Curriculum: Structural and Geotechnical Engineering

SSD – CEAR-07/A

Structural Performance of FRCM/CRM-Strengthened Calcarenite Masonry: Experimental and Numerical Investigation on Shear Behaviour of Panels and Asymmetrically Loaded Barrel Vaults

Ph.D. CANDIDATE

Marielisa Di Leto

COORDINATOR

Prof. Piero Colajanni

SUPERVISORS

Prof. Lidia La Mendola

Prof. Piero Colajanni

CO-SUPERVISORS

Prof. Paulo Lourenço

Prof. Daniel Oliveira

PhD Cycle XXXVIII – PNRR

Academic Year 2024/2025

Abstract

The conservation and strengthening of existing masonry buildings represent one of the main challenges in structural engineering, particularly in the context of the preservation of the built heritage, due to the vulnerability of these structures to seismic actions and the need to ensure an adequate level of safety while preserving their historical and architectural value. This need drives research into the mechanical behaviour of common structural elements, such as walls, arches and vaults, with a view to understanding their load-bearing mechanisms under severe conditions and identifying effective and compatible reinforcement strategies.

In recent years, inorganic matrix composites, including Fabric Reinforced Cementitious Matrix (FRCM) and Composite Reinforced Mortar (CRM) systems, have emerged as innovative solutions for reinforcing masonry structures. Despite extensive research in this area, several aspects still require further investigation. While technical documents are available to support the design of FRCM systems, recent experimental results have highlighted the need to investigate the numerous variables involved in their application in greater depth, with a view to updating and improving current calculation methods. Existing formulations for the shear reinforcement of masonry panels focus primarily on the mechanical properties of the fabric, while neglecting the contributions of the matrix, connectors, and complementary geometric parameters. Further studies are also required to assess the compatibility of the reinforcement system with the masonry substrate in terms of both the materials used and the mechanics involved.

The formulations developed for FRCM systems are not directly applicable to CRM systems due to differences in geometry, mechanics and behaviour. Furthermore, the available experimental evidence, particularly on full-scale structural elements, remains limited. Another growing area of interest is the potential use of CRMs as integrated systems for improving the structural performance and energy efficiency of buildings.

The aim of this research is to expand the experimental database available in the literature and contribute to a better understanding of the effectiveness of these technologies. To this end, an extensive experimental programme is carried out on structural elements made of calcarenite masonry, a material widely used in historic city centres in Mediterranean regions. The study focuses on two critical vulnerabilities commonly observed in historic masonry

buildings subjected to seismic actions: the in-plane shear strength of walls and the structural behaviour of barrel vaults. The effectiveness of FRCM and CRM systems for shear reinforcement was evaluated using diagonal compression tests on masonry panels. In parallel, the behaviour of barrel vaults reinforced with CRM systems featuring both traditional and geopolymer matrices was analysed through mechanical tests under asymmetric loading conditions. This helped to expand the limited knowledge available in the literature. Thermal tests were also conducted on the same vaults to evaluate the potential application of CRM as a dual structural and energy retrofitting solution.

The entire experimental campaign was supported by the 2 Dimensional Digital Image Correlation (2D-DIC) technique, which was used to monitor strain field evolution, cracking phenomena, and delamination processes. The experimental work was complemented by simplified and detailed numerical modelling, which was employed as a predictive tool and to aid interpretation of the results. The results of the diagonal compression tests were incorporated into a database of experimental data from the literature. This was done with a view to analysing the main influencing parameters, as well as contributing to the validation and updating of existing formulations. On the other hand, the results relating to vaults and the use of CRM systems as an integrated solution provide an original contribution to the development of intervention strategies aimed at jointly optimising the structural and energy performance of existing masonry buildings. These findings highlighted the importance of the interaction between masonry, matrix and reinforcement in determining the effectiveness of FRCM and CRM systems, with the properties of the matrix contributing to the observed improvement in shear response. For the vaulted elements, the experimental and numerical analyses confirmed the relevance of the interaction between the strengthening system, the masonry and the boundary conditions, while the thermal tests indicated the potential of CRM with geopolymer matrix as a combined solution for structural and energy retrofitting.

CONTENTS

Chapter 1 Introduction 9
1.1 Background and motivation 9
1.2 Objectives and scope of the research 11
1.3 Structure of the thesis 13
Chapter 2 Literature Review 17
2.1 Concept of seismic retrofitting 18
2.2 Inorganic matrix composite materials 20
2.2.1 Fabric Reinforced Cementitious Matrix (FRCM) Systems 21
2.2.2 Composite Reinforced Mortar (CRM) Systems 24
2.3 Applications on structural elements 27
2.3.1 Shear strengthening of masonry walls 29
2.3.2 Strengthening of arches and vaults 34
2.3.3 Thermal aspects 38
2.4 Technical guidelines 41
2.5 Numerical modelling of masonry composite strengthening 44
Chapter 3 Materials and Experimental Methodology 49
3.1 Experimental plan and materials overview 50
3.2 Masonry characterization 54
3.2.1 Properties of Marsala and Sabucina calcarenite 55
3.2.2 Properties of joints mortar 62
3.2.3 Masonry uniaxial compressive tests 63
3.3 Description of composite strengthening materials 68
3.3.1 Matrices and meshes used in FRCM systems 68
3.3.2 Matrices and meshes used in CRM systems 71
Chapter 4 Experimental Campaign on Calcarenite Masonry Panels 75
4.1 Experimental plan 77
4.2 Specimen geometry and preparation 78
4.2.1 FRCM system configuration 80
4.2.2 CRM system configuration 85
4.3 Setup and acquisition systems of diagonal compressive tests 86

4.4 Experimental results 90
4.4.1 Failure modes 91
4.4.2 Analysis of the main experimental results 99
4.4.3 Digital Image Correlation Analysis (DIC) 101
4.5 Comparisons with analytical outcomes 112
4.6 Comparisons with the literature database 117
Chapter 5 Numerical Modelling of Diagonal Compressive Tests 127
5.1 Overview of STKO and OpenSees 128
5.2 Model development 130
5.2.1 Geometry, mesh, and boundary conditions 132
5.2.2 Constitutive models and material parameters 135
5.3 Model calibration based on experimental data 138
5.4 Numerical vs experimental results 143
5.5 Additional numerical investigations 152
Chapter 6 Experimental Campaign on Calcarenite masonry vaults 161
6.1 Experimental plan 163
6.2 Preliminary studies 165
6.3 Geometry and construction of masonry vault specimens 170
6.3.1 Unreinforced Vault sample (Specimen 1, UR/V) 170
6.3.2 CRM Repaired vault sample (Specimen 1, REP/V and REP/V+T) 172
6.3.3 CRM Reinforced vault samples (Specimen 2, R/V+T and Specimen 3 R/V_G+T) 174
6.4 Load test and monitoring setup 177
6.5 Experimental results on unreinforced vault 179
6.6 Numerical modelling of load tests on unreinforced vault 186
6.6.1 Numerical vs Experimental comparisons 188
6.6.2 Calibration and model updating 189
6.7 Experimental results on strengthened vault samples 192
6.7.1 CRM Repaired vault sample (REP/V and REP/V+T) 193
6.7.2 Traditional CRM reinforced vault sample (R/V+T) 199

6.7.3 Geopolymer CRM reinforced vault sample (R/V+T) 203
6.8 Comparisons and discussion of the results 206
6.9 Thermal test on CRM reinforced vault samples 208
Chapter 7 General Discussion and Conclusions 213
7.1 Summary of the main findings.....213
7.2 Recommendations and future research directions 219
Appendix A 223
Research fundings 249
References 251
***Acknowledgments* 269**
***Ringraziamenti*.....273**

Chapter 1
Introduction

1.1 Background and motivation

The Mediterranean region is characterised typically by a moderate to high level of seismic hazard. Such hazard, combined with the widespread presence of existing masonry buildings constructed before modern seismic standards were introduced, results in a significant level of risk. These buildings are particularly prevalent in historic town centres and were primarily designed to withstand vertical loads, meaning they have limited capacity to resist seismic forces. In this context, developing effective solutions to improve structural and seismic safety and ensure the preservation of historic and cultural built heritage is essential.

The structural and material complexity of these buildings, together with the assessment of the effectiveness of the various available strengthening solutions, represent one of the main challenges in structural engineering. For this reason, research in literature focuses on the mechanical behaviour of common structural elements, such as walls, arches and vaults. The aim is to understand their load-bearing mechanisms and identify the parameters that enable effective, compatible solutions. Among the available strengthening techniques, particular attention has therefore been devoted to solutions that combine structural effectiveness with compatibility with the existing masonry.

In recent years, inorganic matrix composites, including Fabric Reinforced Cementitious Matrix (FRCM) and Composite-Reinforced Mortar (CRM) systems, have emerged as innovative solutions for strengthening masonry structures. The two systems differ mainly in terms of the thicknesses to which they are applied, the type of reinforcement used, the mesh size of the fabric, the type of connectors, and their mechanical behaviour. The advantages they share, which make these systems preferable when compared to other techniques, include better compatibility with masonry substrates than solutions using resin matrices, breathability, reversibility of the intervention, minimal increase in mass and stiffness added to the structure, limited invasiveness, and the ability to create numerous material combinations according to the required performance. However, their effectiveness depends on the interaction between the reinforcement, matrix and masonry substrate, and their application to complex masonry elements such as vaults remains less extensively investigated. Furthermore, CRM system's greater thickness enables the selection of suitable materials to create a structural reinforcement system that incorporates energy retrofitting. This feature also makes CRM systems particularly promising as multifunctional solutions, although their potential for simultaneously improving structural and energy performance requires further investigation.

Despite extensive research in this field, several aspects still require further investigation, particularly regarding the application of these approaches to structural elements. This issue is particularly relevant in the Italian and Mediterranean context, where a large part of the existing building stock consists of historic masonry structures characterised by a wide variety of materials, construction techniques and mechanical properties. While technical documents are available in Italy to support the design of interventions using FRCM systems, recent experimental results have emphasised the importance

of investigating the numerous variables involved in their application in more depth, with a view to updating and improving the current calculation methods. In particular, existing formulas for the shear reinforcement of masonry panels primarily consider the mechanical properties of the fabric, while neglecting the contribution of the matrix, connectors, and complementary geometric parameters. Further studies are also required to assess the compatibility of the reinforcement system with the masonry substrate. The aim is to guide the choice towards the most effective solution that achieves the best possible performance of the system.

Regarding CRM systems, the formulations developed for FRCMs cannot be applied directly due to geometric and mechanical differences in installation between the two systems. Studies focusing on the mechanical characterisation of these materials are relatively recent, and the available experimental evidence, particularly concerning full-scale structural elements, remains limited. Another growing area of interest is the potential use of CRM systems as integrated solutions to improve the structural and energy performance of buildings simultaneously. Further investigation is required to identify the most effective combinations of mesh and matrices that guarantee good mechanical and thermal performance.

1.2 Objectives and scope of the research

This research aims to expand the available experimental database and contribute to a better understanding of the effectiveness of FRCM and CRM reinforcement technologies. The study focuses first on assessing the effectiveness of these systems in improving the shear response of masonry panels and on identifying the main parameters governing their performance, with particular attention to the interaction between the reinforcement, matrix and masonry substrate. The experimental results are then used to assess the

applicability and predictive capability of existing analytical formulations and to investigate their possible improvement through the analysis of an extended experimental database. The research further examines the structural behaviour of CRM-reinforced masonry barrel vaults under asymmetric loading, considering the influence of matrix type, pre-existing damage and connection conditions, and explores the ability of numerical models to reproduce and interpret the observed response. Finally, the potential of CRM systems as integrated solutions for improving both the structural and energy performance of masonry vaults is investigated. To address these objectives, an extensive experimental programme was conducted on structural elements made of *calcarenite* stone masonry, a sedimentary stone commonly found in historic centres across the Mediterranean region. *Calcarenite* is a sedimentary stone characterised by a high variability in its mechanical properties. A more detailed description of the material and its properties is provided in Chapter 3. In the present study, two types of *calcarenite* were selected to represent different construction contexts and to investigate two significant applications of these materials in the seismic strengthening of historic masonry buildings: enhancing the in-plane shear capacity of masonry walls and improving the structural behaviour of barrel vaults. The lower-strength *calcarenite*, commonly found in modest residential buildings and historically associated with less valuable construction, was used for the investigation of the in-plane shear response of masonry walls. A higher-quality *calcarenite*, characterised by better mechanical properties and typically employed in more prestigious historic buildings, was instead adopted for the experimental campaign on barrel vaults, where higher-quality and more expensive materials were generally used.

The effectiveness of FRCM and CRM systems for shear reinforcement was assessed via diagonal compression tests on masonry panels. Consideration was given to several aspects that have not yet been fully clarified within the

scientific community, including the role of mortar, the mortar-fibre combination and the role of connectors. In parallel, the behaviour of barrel vaults reinforced with CRM systems featuring traditional and geopolymer matrices was analysed through mechanical tests under asymmetric loading conditions. This helped to expand the limited knowledge currently available in the literature on this topic. Various configurations were studied, with a focus on aspects such as constraint conditions, the presence of pre-existing vault damage, and the role and distribution of connectors on the vault's surface. Thermal tests were also conducted on the same vaults to evaluate the potential application of CRM systems as an integrated solution for improving both structural performance and energy efficiency simultaneously.

The entire experimental campaign was supported by the Two-Dimensional Digital Image Correlation (2D-DIC) technique, which was adopted to monitor strain field evolution, cracking phenomena, and delamination processes. Traditional measuring instruments were used in addition to validate the effectiveness and accuracy of the DIC-based measurements. The experimental work was also complemented by both simplified and detailed numerical modelling, which was employed as a predictive tool and to aid the interpretation of the obtained results.

The experimental results obtained from the diagonal compression tests were further analysed to investigate the main parameters influencing the effectiveness of the strengthening systems and to assess the applicability of existing calculation formulations. The experimental and numerical investigations on masonry vaults also provided insights into the potential of CRM systems for integrated structural and energy retrofitting.

1.3 Structure of the thesis

This thesis presents and discusses the experimental, analytical and numerical

results obtained during the various stages of the research. After selecting and mechanically characterising the materials employed, research proceeded through two experimental campaigns involving structural elements: wall panels subjected to diagonal compression tests, and vaults subjected to thermal tests and load tests with the load applied at one-quarter of the span, simulating an antisymmetric loading configuration designed to maximise bending effects. These results are critically analysed and compared with those in the literature, and where possible with existing analytical formulations. The experimental work was carried out in parallel with numerical modelling, which was also employed as a predictive tool. For clarity and consistency, the numerical analyses are presented differently for the two experimental campaigns. A dedicated chapter is devoted to the numerical investigation of the wall panels subjected to diagonal compression tests, whereas the numerical modelling of the barrel vaults is integrated within the chapter describing the corresponding experimental campaign.

The structure of the thesis is outlined below, providing an overview of the main content and results presented in each chapter.

- *Chapter 1* introduces the research context, motivations, main objectives, and key aspects addressed throughout the thesis;
- *Chapter 2* provides a critical review of the state of the art relating to the topics covered. It analyses the main findings from the literature concerning FRCM and CRM reinforcement systems and their applications. Both experimental and numerical aspects are examined in relation to the currently available regulatory framework. The chapter concludes by identifying the main knowledge gaps that motivated the research activities carried out in this thesis;
- *Chapter 3* describes the entire experimental campaign conducted as part of the research, including tests on both masonry panels and barrel

vaults. It presents the materials used and the results of the mechanical characterisation tests carried out on individual components and the mechanical parameters of the reinforcement systems;

- *Chapter 4* provides a detailed account of the experimental campaign relating to the diagonal compression tests. It describes the experimental setup, the data acquisition equipment, and the test procedures adopted. It also presents and discusses the results obtained for both unreinforced and reinforced panels, paying particular attention to the contribution made by the different reinforcement configurations. While the tests on unreinforced panels are part of the masonry characterisation, they are included in this chapter to ensure direct comparability with the results for the reinforced elements. A specific section is also provided for comparing the results with those available in the literature and existing analytical formulations;
- *Chapter 5* is focused on the numerical micro-modelling of diagonal compression tests. After defining and calibrating constitutive models based on material characterisation tests, it presents the numerical models developed to interpret the observed experimental behaviour and analyse the influence of specific parameters. The chapter concludes with a critical comparison of experimental, analytical, and numerical results;
- *Chapter 6* presents the experimental programme relating to the load and thermal tests carried out on both reinforced and unreinforced barrel vaults. It describes the experimental setup, the instrumentation used, and the various test configurations adopted. The results are discussed, with a focus on the key structural and thermal properties that emerged from the analysis. The chapter also presents a simplified numerical

model of the vaults that is used as both a predictive tool and to support the interpretation of the experimental results;

- *Chapter 7* summarises the main results obtained and discusses their contribution concerning the research objectives. Finally, recommendations are provided for the practical application of the studied systems, and potential future research directions are outlined.

Chapter 2

Literature Review

Italy and, more generally, the Mediterranean region are characterised by a wide range of buildings, consisting mainly of masonry structures in terms of existing buildings. This building typology is particularly widespread in historic town centres, where there are complex and heterogeneous types of construction that are often not designed to withstand seismic forces adequately. The recent earthquakes that have affected the country have, in fact, highlighted the significant vulnerability of these structures [1].

During seismic events, masonry structures may exhibit various collapse mechanisms. Among the most frequent are in-plane failures [2], generally associated with the limited shear strength of the materials and the presence of openings in the walls [3][4][5], out-of-plane failure mechanisms, caused by a lack of effective connections between orthogonal walls [6] and the collapse of vaulted elements, due to the action of horizontal forces and the absence of adequate connection systems [7]. These critical issues highlight the need to adopt intervention strategies aimed at reducing seismic vulnerability and improving the structural capacity of existing Italian and Mediterranean buildings.

In this context, it is particularly important to develop and adopt strengthening techniques that improve the structural performance of masonry buildings,

while ensuring that the interventions are compatible with the buildings' historical and architectural value and have minimal economic and visual impact.

2.1 Concept of seismic retrofitting

Over the years, several structural strengthening techniques have been developed and adapted to improve the seismic performance of existing buildings and ensure they meet the required safety standards.

There are two main approaches to seismic improvement: reducing the seismic load acting on the structure or increasing its resistance capacity [8]. In the first approach, the aim is to modify the building's dynamic behaviour by implementing solutions such as base isolation, installing energy-dissipating devices, or redistributing structural masses. In the second case, however, interventions are carried out directly on the structural elements to increase their strength and/or deformation capacity. Among the numerous strengthening techniques available, some of the most commonly adopted for masonry structures include the confinement and encasement of structural elements, application of surface coatings, insertion of metal or composites bars, strengthening of joints, introduction of internal reinforcement, use of tie rods, the installation of reinforced concrete ring beams, and injection of mortar or filling of openings. These techniques are well-established and widely used methods for seismic improvement and retrofitting in the case of masonry structures.

However, using these traditional techniques presents challenges relating to the materials and methods involved. In particular, adding steel or reinforced concrete elements to historic masonry structures creates hybrid structural systems with different mechanical and deformation properties. This can lead to problems of material and structural compatibility, as well as increasing the

mass of the building and consequently the seismic forces acting on it.

Greater understanding of these issues has led to a new approach to earthquake-related consolidation and rehabilitation, with a focus on lightweight, effective solutions that are compatible with existing heritage sites. Attention has gradually shifted towards minimally invasive, reversible and durable interventions that preserve the historical and architectural authenticity of buildings over time.

In this context, innovative materials and unconventional methods have become widespread, including Fibre-Reinforced Polymer (FRP) reinforcement systems. These systems consist of high-strength fabrics embedded in an organic matrix, typically an epoxy resin, to ensure stress transfer to the fibres and bonding to the structural substrate. They are becoming increasingly popular due to their high mechanical performance, light weight, corrosion resistance, good durability against chemical and environmental agents, and limited thickness that allows strengthening interventions to be carried out without significantly affecting the overall structural stiffness [9][10].

Despite their multiple advantages, FRP systems have certain limitations relating to durability, reversibility and compatibility with historic masonry substrates. It is mainly the compatibility issue that has prompted the replacement of organic matrices with inorganic ones, as the latter are capable of ensuring better physical, chemical and mechanical compatibility with the masonry [11].

Recent research has therefore focused on Textile Reinforced Mortar (TRM) systems, consisting of fabrics and inorganic matrices. This category includes various types of composites, including Fabric Reinforced Cementitious Matrix (FRCM) and Composite Reinforced Mortar (CRM) systems [12][13][14][15]. A key difference issue between FRCM and CRM is the amount and configuration of the composite reinforcement within the mortar matrix. FRCM

systems are characterised by thin render layers into which continuous fabrics are embedded. In the other hand, CRM systems involve the use of preformed FRP meshes embedded within a thicker layer of structural render, typically between 30 and 50 mm thick, with higher overall amount of composite material. These differences in geometry and reinforcement configuration also lead to differences in their mechanical response and in the way, stresses are transferred between the strengthening system and the masonry substrate. The main aspects distinguishing the two technologies include their mechanical behaviour, failure mechanisms, interface behaviour, and connection systems, which are discussed in the following sections.

Both technologies offer significant advantages for the strengthening of existing structures. As well as ensuring high mechanical performance, they are resistant to atmospheric agents and preserve their properties even when exposed to prolonged periods of solar radiation, humidity, rain and freeze-thaw cycles. Furthermore, they demonstrate satisfactory behaviour in the case of a fire and have a high long-term durability. Thanks to these characteristics, CRM and FRCM systems, are now among the most promising solutions for the seismic retrofitting and reinforcement of masonry structures. They combine structural effectiveness with compatibility with historic materials and minimal impact on existing building fabric.

2.2 Inorganic matrix composite materials

The use of inorganic matrix composite materials as strengthening systems for existing masonry structures has been the subject of increasing investigation. These composites consist of a reinforcing phase embedded within an inorganic matrix that transfers stresses between the reinforcement and the existing substrate. Different systems can be distinguished depending on the type of reinforcement and matrix adopted. Some of the most widely investigated

solutions are TRM, FRCM and CRM.

The following sections outline the main characteristics of both technologies, paying particular attention to the constituent materials and the most common methods of mechanical characterisation.

2.2.1 Fabric Reinforced Cementitious Matrix (FRCM) Systems

FRCM systems (Fig. 2.1) are suitable for reinforcing concrete structures that are subject to flexural and shear loads, such as floor slabs, beams and columns. They can also be used for strengthening masonry buildings to provide protection against collapse, structural reinforcement and seismic retrofitting.



Figure 2.1 Example of FRCM system's configuration and application (Source: [16])

The type of fabric used in the system can vary; the most common include glass, basalt, carbon, aramid and PBO fibres, which can be combined with different types of matrices.

The resulting composite exhibits a characteristic tensile response that can be investigated through tensile testing using different gripping configurations, such as clamping and clevis systems (Fig.2.2) [17][18]. In the clamping configuration (Fig.2.2a), the specimen is gripped directly at its ends by mechanical clamps, enabling the tensile load to be transferred from the testing

machine to the composite. In the clevis configuration (Fig.2.2b), the specimen is connected to the testing machine via end tabs and pinned clevis joints. This provides a hinged connection, which helps to reduce the effects of bending and eccentricity during loading. When subjected to tensile loading, the material typically exhibits an initial phase in which the matrix plays a predominant role until the first crack forms. As the tensile load increases, cracking progressively develops within the matrix, leading to a second phase characterised by the transfer of tensile stresses from the cracked matrix to the reinforcement. A third phase is finally reached, in which the matrix is extensively cracked, and the tensile response is predominantly governed by the reinforcement (dashed blue line in Fig.2.2c), providing the composite's residual load-carrying capacity. This trilinear behaviour (red curve in Fig.2.2c) is more clearly observed when the tensile tests are performed using the clamping method [18]. Conversely, when the clevis method is adopted, the second and third phases are not always clearly distinguishable (green curve in Fig.2.2c), resulting in an overall bilinear tensile response[17].

Organic components may also be present, with a maximum total weight percentage of 10% of the inorganic binder. Examples include fibre-matrix adhesion promoters, additives to improve the matrix's rheological properties, and components added in situ to promote adhesion to the substrate. These composites are applied with a thickness lower than 30 mm. Therefore, an FRCM reinforcement system can be defined as either a single mesh embedded in a specified thickness of mortar or multiple meshes embedded in a single layer of mortar, which may be up to 30 mm thick in this case.

The interface between the two components of the FRCM system is crucial in establishing the composite's overall behaviour, as the effectiveness of stress transfer between the matrix and the mesh depends on it. The main function of the interface is to ensure the system operates correctly by promoting a uniform

distribution of stresses. In some cases, this effectiveness can be enhanced further through the use of connectors and anchoring devices designed to prevent the composite from detaching prematurely from the substrate.

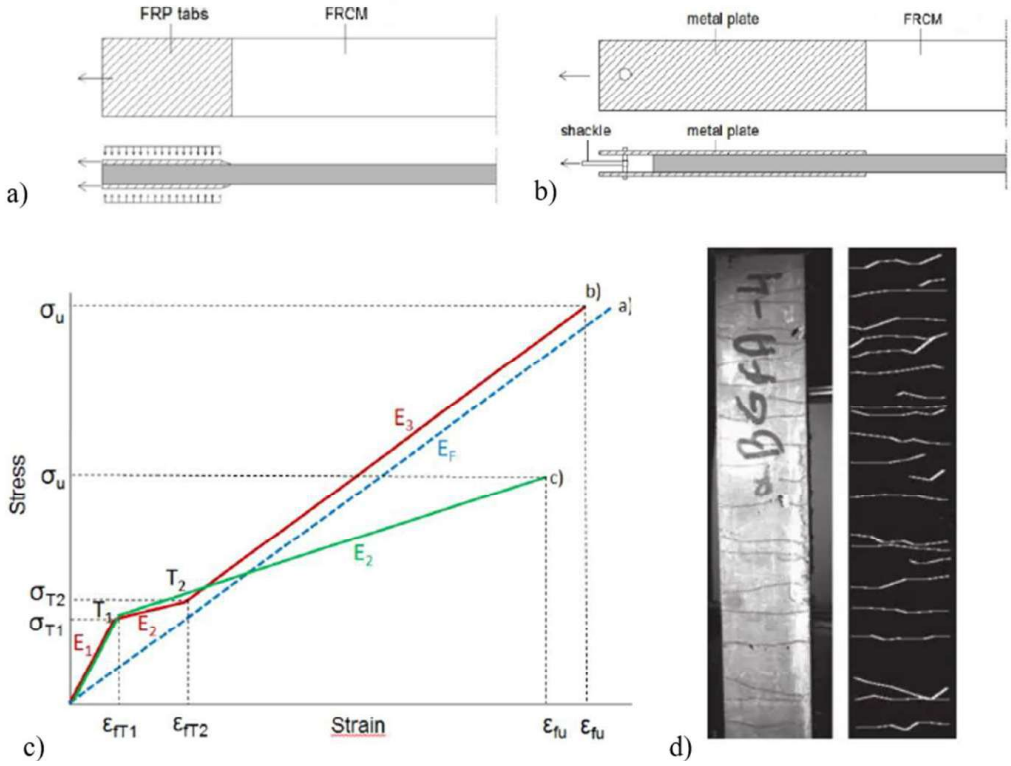


Figure 2.2 Tensile tests on FRCM systems (Figure adapted and elaborated by the author based on [17][18]): a) Clamping method setup; b) Clevis method setup; c) tensile tests results; d) example of failure mode and cracking on matrix

From a structural point of view, it is well known that the effectiveness of this reinforcement technique primarily depends on the material's capacity to withstand tensile loads, thereby improving the structural performance of the reinforced element. To this aim, technical standards recommend two main types of tests to determine the mechanical properties and load-bearing behaviour of FRCM composites: the direct tensile test and the shear bond test. These tests make it possible to determine key properties of FRCM composites

such as stiffness and tensile strength, as well as analysing their crack behaviour and failure modes [17][18].

According to shear bond test results, six different failure modes may occur in general when no mechanical connectors are used (Fig. 2.3)[19]:

- detachment with cohesive failure of the reinforcement substrate;
- detachment at the matrix-reinforcement interface;
- detachment at the matrix-fabric interface;
- slippage of the fabric within the matrix;
- slippage of the fabric accompanied by cracking of the external mortar layer;
- tensile failure of the fabric.

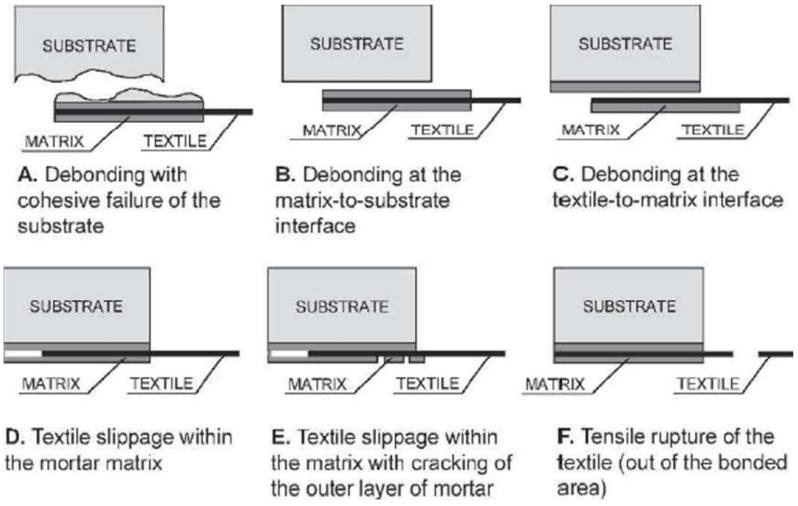


Figure 2.3 Failure modes after shear bond tests on FRCM (Figure adapted by the author based on [18]):

2.2.2 Composite Reinforced Mortar (CRM) Systems

CRM systems (Fig. 2.4) are a strengthening solution created following the reinforced render methodology, which involves the use of a pre-formed FRP mesh embedded in an inorganic matrix. The mesh absorbs tensile stresses,

while the matrix withstands mostly compressive stresses. Furthermore, stresses are transferred from the masonry to the mesh not only through the bond between the materials, but also through the presence of connectors. In terms of the composition of the reinforcement system, CRMs can be considered comparable to the FRCM systems described above. The key difference between the two technologies is that CRM systems use a fibre mesh with larger spacing that is pre-impregnated with resin and always requires mechanical connectors, whereas FRCM systems use a dry mesh with smaller openings and connectors are optional. Due to similarities between FRCM and CRM systems, particularly with regard to their inorganic cementitious matrix, the available experimental evidence for FRCM systems may also be useful for CRM systems. This is particularly relevant for aspects such as substrate compatibility, resistance to atmospheric agents, including prolonged exposure to sunlight, low temperatures, rain and humidity, and fire behaviour.



Figure 2.4 Example of CRM system's configuration and application (Source: [20])

The CRM systems also ensure a high level of effectiveness in increasing the

load-bearing capacity of reinforced structural elements, providing significant benefits in terms of strength and deformability [21].

However, there are further differences between the two types of material relating mainly to the application methods and their impact on the load-bearing capacity of the structural element. FRCM systems generally require a more complex installation process, involving the application of an initial thin layer of mortar, positioning of the fibre fabric, impregnation with an adhesion promoter and subsequent application of a second layer of mortar. However, this technology results in a smaller increase in mass of the reinforced element than CRM systems, which require thicker application layers.

In the latter system the FRP mesh is the component that carries the tensile load and determines its main mechanical properties. Consisting of a preformed mesh, the size of which varies depending on the manufacturer, it is made from long, continuous fibres that are interwoven and impregnated with a thermosetting polymeric material.

Tensile tests on CRM composites are generally carried out according to procedures similar to those adopted for FRCM systems [22]. The experimental results show that an initial elastic region can be identified, during which it can be assumed that the mortar and reinforcement are working under conditions of perfect adhesion. Subsequently, the occurrence of the first cracks, oriented orthogonally to the direction of loading, is observed. This leads to a reduction in load-bearing capacity. As tensile stress increases, load rises again until further cracks appear. This process repeats progressively until the specimen fails, with cracks forming along the transverse wires of the mesh.

The lack of specific guidelines and regulations that clearly define the experimental setup for such tests, coupled with the limited availability of experimental results in the literature, makes it difficult to make general and definitive assessments of the mechanical behaviour of CRM composites.

Further studies and experimental programmes are therefore needed to establish agreed testing procedures and deepen our understanding of the characteristics and potential of this type of composite material.

2.3 Applications on structural elements

Both FRCM and CRM systems are employed for strengthening structural elements. Thanks to their mechanical properties, they are particularly suitable for applications involving limited deformation, which is typically required in the reinforcement of masonry structures [24].

An analysis of the available scientific literature shows that FRCM systems are generally used for the following applications on masonry:

- strengthening of walls subjected to in-plane shear and axial forces (Fig. 2.5a);
- strengthening of walls subjected to out-of-plane mechanisms (Fig. 2.5b);
- constructing top beams (Fig. 2.6);
- confinement of masonry columns (Fig. 2.7);
- strengthening of structures characterised by single or double curvature (Fig. 2.8).

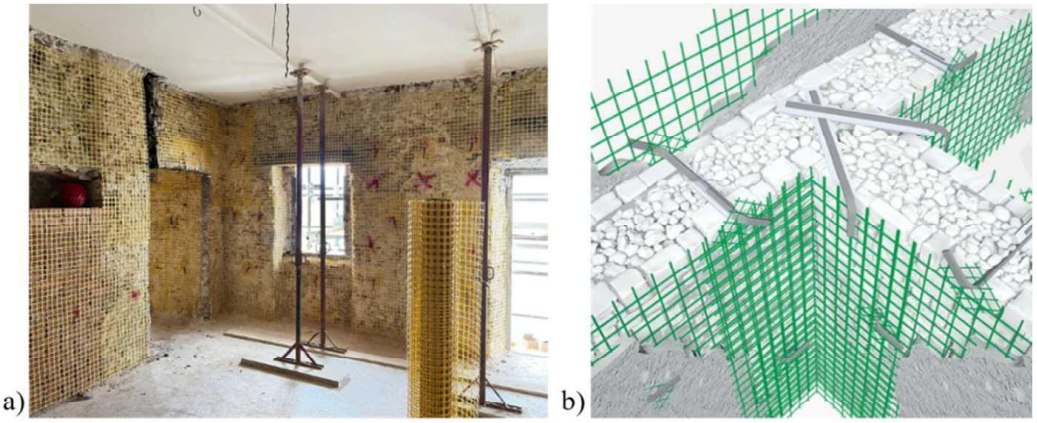


Figure 2.5 Example of strengthening applications: a) for in-plane actions (Souce: [23]); b) for out-of-plane mechanisms (Adapted from [24]).



Figure 2.6 Example of strengthening applications: construction of top beams and strengthening of floor-to-wall connections (Source: [25])



Figure 2.7 Example of strengthening applications: confinement of masonry columns (Sources: [24] [25])



Figure 2.8 Example of strengthening applications: strengthening of vaults and arches (Sources: [24] [25])

2.3.1 Shear strengthening of masonry walls

The increase in in-plane shear strength is particularly significant, especially in the context of seismic retrofitting. This behaviour can be analysed using direct shear compression tests, whether static or cyclic, or diagonal compression tests. Direct compression-shear tests provide a more direct approach to assessing masonry's response to shear forces, providing an analysis of the interaction between normal and shear stresses. These tests can be performed by applying a monotonic load or by using loading and unloading cycles. The latter method also provides information on the hysteretic response, stiffness degradation, strength reduction and dissipative capacity of the system. However, the test setup may be more complex, particularly with regard to defining and controlling loading conditions and constraints. Diagonal compression tests, on the other hand, are a widely adopted experimental method for assessing the shear strength of masonry. This test involves applying a diagonal load, which generally leads to the formation of a diagonal crack. This crack may develop along horizontal and vertical mortar joints, or through the stone or brick elements. Therefore, the test provides a direct assessment of the shear strength and deformability of masonry using parameters derived from the panel's overall response. The relative simplicity of the experimental setup, coupled with the capability to compare results from various masonry configurations and reinforcement systems, has led to its extensive use in experimental research. Diagonal compression tests are particularly useful for assessing the effectiveness of FRCM and CRM systems in modifying the shear response of masonry panels and allow for a direct comparison of the behaviour of reinforced and unreinforced specimens. However, the results obtained depend on the test configuration, panel dimensions, masonry properties and the interaction between the reinforcement and substrate. Therefore, the results must be interpreted in considering the specific experimental conditions.

A review of the literature shows that such tests have been applied to various types of masonry panels using different reinforcement configurations characterised by variations in fabric composition, matrix type, and overall geometric characteristics [24].

Diagonal compression tests are generally carried out on masonry panels measuring approximately 1 m × 1 m, with the specimens subjected to compressive loads applied along a diagonal. This causes diagonal tensile failure, resulting in separation of the panel in a direction perpendicular to the applied load. The experimental procedure and test setup comply with the requirements of ASTM standard E519-22 [27].

During the test, specific instruments measure the shortening of the loaded diagonal, usually the vertical one, and the elongation of the other diagonal, usually the horizontal one. Based on the recorded displacements and applied loads, it is possible to determine key mechanical parameters such as maximum shear strength, shear strain and shear modulus in the central area of the panel.

The effectiveness of FRCM and CRM systems in enhancing the in-plane shear behaviour of masonry panels depends on several factors, including the mechanical and geometric properties of the matrix and reinforcement mesh, the use of mechanical anchors and the characteristics of the masonry substrate [24][28]. Available studies highlight the significant influence of the matrix's mechanical properties on the panels' maximum load-bearing capacity [30]. Similarly, the axial stiffness of the reinforcement mesh affects the system’s performance: greater stiffness in the fabric allows for a higher increase in capacity than less rigid fabrics [24].

Regardless of the extent of the increase in strength, the reinforcement fabric plays a fundamental role in post-peak inelastic behaviour by helping to increase the structure’s capacity for deformation, even when the gain in strength is limited [31].

Experimental evidence confirms that FRCM and CRM systems effectively improve the structural behaviour of masonry walls, particularly with regard to in-plane shear strength, ductility, and energy dissipation capacity in the post-peak phase [24][32][33][29][34]. These results are consistent across different types and configurations of masonry, demonstrating the remarkable versatility of these techniques. While glass and carbon fibre meshes are the most commonly used materials, alternative options, such as hemp fibres, have demonstrated promising results, particularly in the context of sustainable consolidation projects [35][36].

The performance of strengthening systems depends on various parameters, including the type and geometry of the mesh, the mortar composition, how the reinforcement is configured, whether it is applied to one or both faces of the wall, and whether mechanical connectors are present.

Regarding the progression of damage, experimental studies have shown that it is governed by a sequence of interacting mechanisms reflecting both the behaviour of the masonry and the contribution of the strengthening system. The first cracks typically emerge within the masonry, often at mortar joints or in areas of pre-existing weakness, due to shear deformations caused by increased load. An increase in stresses causes cracks to propagate and progressively activate the embedded reinforcement grid, which begins to absorb tensile forces and redistribute stresses across a larger area of the panel than in unreinforced masonry. As the load increases further, the behaviour of the system becomes more complex, and the interaction between the masonry and the strengthening system does not always occur under conditions of perfect compatibility. In the absence of mechanical connectors, localised detachment or slippage may occur at the interface between the matrix and the masonry substrate, particularly near cracks or along the edges of the panel [28]. This reduces the effectiveness of tensile force transfer. Under such conditions, the

mesh may be subject to localised deformation concentrations, which, although rarely observed in experimental tests, can lead to the progressive failure of individual fibres or fibre bundles. Typically, the final failure is the result of the combined action of these mechanisms rather than a single sudden event. The cracking pattern typically becomes multidirectional along the compressed diagonal and continues to develop until the strengthening system can no longer withstand the imposed tensile stresses (Fig.2.9).

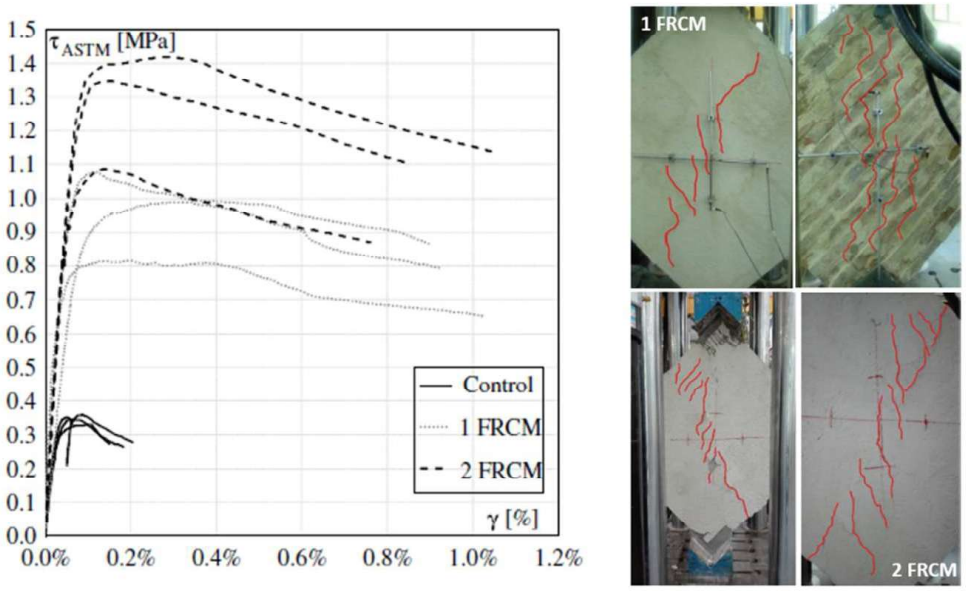


Figure 2.9 Example of Diagonal compressive test results: stress-strain curves and failure modes (Sources: [29])

The experimental results depend on specimen geometry due to scale effects, the mechanical properties of the masonry, the strengthening system configuration, boundary conditions, and the presence of an axial compressive load. Significant differences in structural behaviour are revealed by a comparison between diagonal compression tests, shear-compression tests on masonry blocks and shear-bending tests on floor slabs.

Diagonal compression tests are relatively simple and cost-effective to carry out. The panels initially exhibit a very rigid response until the maximum load is reached, which is generally associated with cracking and damage to the

mortar matrix. Subsequently, a gradual reduction in strength is observed. This behaviour is confirmed by the fact that panels reinforced solely by a layer of mortar can achieve maximum load values comparable to those obtained with complete reinforcement but lose load-bearing capacity much more rapidly in the post-peak phase.

Strengthening system leads not only to an increase in maximum shear strength, but also to a significant increase in deformation capacity and the ability to withstand high levels of drift during repeated loading cycles.

Finally, tests on masonry panels indicate that, while ensuring qualitatively similar behaviour in both load directions, applying the system to only one face of the wall results in lower values for both maximum shear strength and ultimate drift compared to symmetrical configurations applied to both faces [32]. Nevertheless, the improvement in performance compared to unreinforced masonry still remains significant.

Overall, the available experimental evidence confirms the effectiveness of FRCM and CRM systems in improving the in-plane shear behaviour of masonry panels, with benefits in terms of shear strength, deformation capacity and post-peak response. However, the results also highlight a dependence of the strengthening effectiveness on the characteristics of the masonry substrate and on the configuration of the strengthening system. In particular, the type and mechanical properties of the matrix and reinforcement, the reinforcement stiffness and geometry, the application on one or both faces of the panel, and the presence and configuration of mechanical connectors can significantly affect the resulting response. Despite the considerable amount of experimental research, some aspects remain insufficiently investigated and do not yet allow fully generalised conclusions to be drawn. In particular, the influence of the matrix properties on the overall shear response is still not completely clarified, especially when different matrix types are combined with the same

reinforcement. Similarly, the role of mechanical connectors and their interaction with the reinforcement and masonry substrate require further investigation, particularly in relation to crack development, interface behaviour and post-peak response. The effects of strengthening configuration, including one-sided and two-sided applications, also warrant further systematic assessment. Moreover, the available experimental evidence is largely based on relatively small-scale panels and standardised test configurations, while the influence of specimen geometry, axial load level and boundary conditions on the transferability of the results to full-scale structural elements remains less extensively investigated. These aspects indicate the need for further experimental and analytical studies aimed at identifying the parameters governing the effectiveness of FRCM and CRM systems and at developing more reliable and generalisable approaches for the assessment and design of strengthened masonry panels.

2.3.2 Strengthening of arches and vaults

As it is well known, the collapse mechanism of unreinforced arches and vaults is influenced by the reduced tensile strength of the masonry, being mostly governed by geometry. This leads to the formation of four or five alternating plastic hinges, depending on whether the load is applied asymmetrically or symmetrically, including piers.

The development of cracks indicates sections of the arch that are connected by hinges, enabling the elements to rotate relative to one another. Opposite to the crack, compressive stresses develop, which can lead to crushing of the material. Meanwhile, in the cracked part, tensile stresses had developed to open the crack and detach the affected parts.

In light of this experimental evidence, when the load-bearing capacity of such structural elements needs to be increased, strengthening system aims to

compensate for the masonry's limited tensile strength in areas subject to the greatest stress. This aspect is particularly crucial for arches and vaults, which are frequently found in buildings of historical and architectural significance. In such cases, composite strengthening systems typically involve intervention on one of the two surfaces of the structural element. Therefore, the choice between the intrados and the extrados is a critical aspect of the strengthening design. Access to the intrados may be limited by the presence of frescoes, decorative elements or other valuable finishes. Conversely, interventions at the extrados may be constrained by the presence of historically significant or valuable flooring. Recent research has therefore focused on composite materials and solutions that ensure optimal performance in terms of structural integrity, cost-effectiveness, material compatibility and improved thermal insulation of the structural elements.

The fundamental theory behind the behaviour of arches is that the structure remains in equilibrium as long as the line of pressure remains within its thickness. However, when a composite material is applied to the surface of an arch, its structural behaviour changes, as it becomes a strengthened element. This leads to a different collapse mechanism. In this case, the tensile strength of the composite is used to stop certain hinges from opening, which increases the arch’s load-bearing capacity [37].

Generally, the load-bearing capacity and ductility of arches and vaults depend on the position of the strengthening system, which can be applied to either the intrados or the extrados, or both. Strengthening system on the intrados prevents hinges from opening inwards, while strengthening system on the extrados prevents hinges from opening outwards. In both cases, the reinforced element can withstand greater loads than the unreinforced configuration. Reinforcing both the intrados and the extrados, however, prevents the formation of all hinges although it is often difficult to implement due to potential constraints

related to the preservation of frescoes, decorative elements, or valuable finishes. However, localised strengthening system positioned in areas of high tensile stress does not prevent hinge formation, merely altering their position [38][39].

In the case of arches reinforced with FRCM systems, more ductile structural behaviour has been observed. In these configurations, the strengthening system inhibits hinge opening and induces diffuse cracking of the matrix prior to failure. This demonstrates that the type of strengthening system influences not only the load-bearing capacity, but also the nature of the collapse mechanism itself. Failure modes in reinforced arches and vaults may affect the masonry, the composite material, or both. Experimental evidence allows us to distinguish four main failure modes:

- Crushing of masonry due to an increase in compressive stresses within the curved surface resulting from the presence of the strengthening system;
- Failure of the composite material when its tensile strength is reached;
- Detachment of the composite material caused by the normal forces generated by the curvature of the arch or vault which can cause it to separate from the masonry support;
- Shear failure along a mortar joint due to the local shear strength being reached in a specific section.

Combined failure modes may also occur, characterised by a combination of masonry failure and detachment of the composite material [40] or shear slippage along a mortar joint and detachment of the strengthening system [37]. However, a comparison of the available experimental results requires careful consideration of the different geometric and loading conditions adopted in the various studies. The effectiveness of the reinforcement system is influenced not only by its position on the intrados or extrados, but also by the geometry

of the arch or vault, the type and distribution of the applied load, the configuration of the reinforcement and the presence of mechanical connectors. These parameters influence the position and opening of the hinges, the interaction between the composite and the masonry support and, ultimately, the collapse mechanism governing the structural response. Therefore, the generally observed greater effectiveness of reinforcement applied to the extrados should not be considered in isolation from the specific experimental conditions adopted in the various studies. Differences in a geometry, load configuration and the arrangement of the reinforcement may contribute to the observed variability in terms of load-bearing capacity, deformation capacity and collapse mechanism. Furthermore, the available evidence relating to masonry vaults remains relatively limited. This aspect is particularly relevant as vaults exhibit a complex three-dimensional structural behaviour, in which geometry, load distribution, boundary conditions and the interaction between the various structural components can significantly influence the response of the reinforced element. Consequently, the results obtained from tests on arches cannot necessarily be directly extrapolated to vaults. In particular, the limited experimental evidence available on vaults reinforced with CRM systems highlights the need for further studies aimed at investigating the effectiveness of different reinforcement configurations and the mechanisms governing their collapse. This gap in the literature is one of the reasons behind the experimental and numerical investigations into CRM-reinforced masonry vaults presented in this thesis.

Within this limited body of research, the available literature has primarily focused on FRCM systems, with numerous studies investigating their behaviour and the mechanisms governing their performance. In contrast, despite their growing use, experimental and theoretical research on CRM systems remains limited [41][42][43]. Available results indicate that

strengthening system on the upper surface generally results in greater strength increases than strengthening system on the lower surface, although the former is associated with lower displacement capacity. Overall, the experimental evidence suggests that applying the CRM system to the extrados is more effective than applying it to the intrados [43] both for technological reasons and because the resulting force component acting at the interface tends to promote detachment of the composite from the masonry surface. However, using stronger or more connectors could significantly improve the effectiveness of interventions carried out on the intrados (Fig.2.10).



Figure 2.9 Example of cyclic test on masonry vaults: test setup (Sources: [43])and results in terms of ultimate load and ultimate displacement (Sources: [15])

2.3.3 Thermal aspects

Recent advances in building materials, particularly in composite materials technology, combined with a growing focus on the environmental sustainability of buildings, have directed research towards solutions that integrate seismic retrofitting with energy efficiency improvements. In this context, CRM systems are a particularly promising solution compared to FRCMs as they are applied as a structural render that generally covers a large portion of the building envelope and is characterised by significant thicknesses (≥30 mm). This feature enables improved energy performance while providing

a strengthening layer capable of contributing to the structural response of the masonry. The possibility of combining these two functions within a single intervention is particularly relevant for existing and historic buildings, where minimising the number and invasiveness of interventions is often a key requirement. However, the improvement of thermal performance cannot be considered independently of the mechanical properties of the matrix, since the materials adopted for the insulating function must also provide adequate strength, stiffness and compatibility with the masonry substrate.

An analysis of the main seismic retrofitting and energy efficiency techniques based on fibre-reinforced composite materials reveals increasing interest in integrated solutions that combine structural strengthening and thermal insulation, as with CRM systems. This trend is reflected in both the growing amount of scientific literature and the increasing number of European research projects and funding initiatives that address the combined improvement of the structural and energy performance of existing and historic buildings. Notable examples include the SPEctRUM project (2018–2020), which was funded under the Horizon 2020 programme and focused specifically on simultaneously retrofitting masonry buildings for seismic and energy efficiency, and the FuturHist project (2024–2027), which is funded under Horizon Europe and focuses on developing solutions specifically designed to improve the energy performance of historic buildings while preserving their architectural and cultural value.

The thermal performance of these systems primarily depends on the thermal conductivity and thickness of the mortar matrix, while the contribution of the reinforcement mesh is negligible from an energy standpoint. Consequently, the use of mortars with low thermal conductivity and adequate mechanical properties is an effective solution for integrated interventions. From a structural perspective, the selection of the matrix is particularly important

because its mechanical properties, together with those of the reinforcement and the masonry substrate, influence the load-transfer mechanisms and the overall response of the strengthened element. Therefore, the development of CRM systems for integrated retrofitting requires a balance between thermal insulation performance and mechanical effectiveness.

The integrated approach to masonry structures was initially developed by Longo et al. [44][45][46] who designed and tested an innovative CRM system based on geopolymer mortars. Experimental tests have shown that these systems can deliver mechanical performance that is comparable to, and in some cases superior to, that of traditional lime-based CRMs. They also exhibit lower thermal conductivity and consequently better insulating performance. These results are particularly relevant because they demonstrate the possibility of improving the thermal performance of the strengthening layer without compromising its structural function. Despite the promising results obtained so far, most of the available research still focuses on material characterisation or tests conducted on small-scale masonry panels. Studies at structural scale remain limited, as does the development of theoretical models and design procedures capable of describing the mechanical and energy performance of these interventions jointly. In particular, further investigation is required to clarify whether the thermal improvements observed at material and small-scale levels can be effectively achieved at structural scale while maintaining the required strengthening performance. This aspect is particularly relevant for masonry vaults, where the strengthening system contributes directly to the load-bearing response and where its thickness, position and material properties may affect both the structural behaviour and the thermal performance of the element. Consequently, this is a particularly promising area of research in which further experimental studies, reliable computational models and a multidisciplinary approach to facilitate the transfer of scientific knowledge to

professional practice and retrofitting of existing buildings are necessary.

2.4 Technical guidelines

Since their introduction to the commercial scene, inorganic matrix composites, initially FRCM systems and later CRM systems, have attracted considerable interest from professionals in the industry, resulting in their increasing use in the strengthening of masonry structures. The growing range of applications has led to the development of standardised guidelines and acceptance criteria to ensure proper material qualification and reliable strengthening project design.

In the United States, as an initiative from the International Code Council Evaluation Service (ICC-ES), the AC434 [47] acceptance criteria were developed to regulate the use of FRCM composites. These criteria provide a framework for evaluating this innovative reinforcement technique, particularly in cases where existing codes do not specify requirements for verifying structural capacity, reliability and in-service performance. The document defines FRCM as a composite material consisting of one or more layers of a cementitious matrix reinforced with fibrous grids or meshes. When applied to concrete or masonry structures, these materials constitute an FRCM system.

AC434 [47] specifies the mechanical tests required to characterise TRM systems. These include tests on individual components, such as mortar and mesh, as well as tensile tests on TRM panels manufactured using procedures similar to those employed in actual applications. It also provides an overview of the tests needed to evaluate the structural performance of TRM-reinforced elements, including shear and diagonal compression tests on walls and axial and flexural tests on columns.

The American Concrete Institute (ACI) has also contributed to the regulatory development of the sector through document ACI 549.4R-20 [17], which is dedicated to the design and construction of externally applied FRCM systems

for the repair and reinforcement of concrete and masonry structures. The guidelines provide a comprehensive theoretical framework and illustrate numerous practical applications of TRM systems, describing their main properties and presenting structural design procedures.

While this guide does not introduce significant changes to the qualification and durability requirements set out in AC434 [47], the ACI 549.4R-20 [17] document offers valuable resources for designing repair and maintenance projects. Notably, it offers formulas to evaluate the in-plane and out-of-plane load-bearing capacity of masonry elements reinforced with TRM. This analysis is based on the following assumptions: compatibility of deformations between the masonry and the TRM; maintenance of flat cross-sections; and bilinear behaviour of the TRM up to failure. It neglects the contribution of the reinforcement prior to cracking.

The design approach involves summing the resistance contributions of the unreinforced masonry and the TRM system, with maximum deformations assumed to be 1.2% for out-of-plane strains and 0.4% for in-plane strains. To facilitate practical application, the guidelines include calculation examples for TRM-reinforced structural elements subjected to different loading conditions.

In Italy, the Italian Technical Standards for Constructions [48] requires that all materials and products intended for structural use must be correctly identified, qualified and inspected. In line with this principle, specific guidelines have been developed for identifying, qualifying and accepting FRCM systems intended for reinforcing existing structures [49][50][51][52]. This document outlines the potential applications of FRCM systems, the key principles for planning interventions and the design approaches to be adopted. The specified qualification process includes tensile tests on textile meshes and FRCM specimens.

These guidelines provide a systematic approach to ensure the reliability and

performance of FRCM systems in reinforcement design. They emphasise the importance of proper material characterisation and adherence to standardised testing procedures. The Italian National Research Council (CNR) has developed specific guidelines for the use of FRCM systems in the strengthening of existing structures [18]. By defining the main mechanical parameters and their role in design verifications, these guidelines facilitate the effective and informed application of FRCM systems.

Currently, there are no guidelines specifically geared towards the design of CRM systems; only documents dedicated to the identification and qualification of these systems are available [53]. Calculation models for in-plane shear reinforcement using CRM are usually based on formulations for reinforced plaster or FRCM systems. These formulations are then adapted using empirical coefficients calibrated against available experimental results. However, models designed for FRCMs cannot be directly applied to CRM due to significant differences in composition, interaction mechanisms, and failure modes between the two systems.

In FRCM systems characterised by thicknesses lower than 30 mm the strength contribution primarily depends on the bond between the fabric, the matrix and the substrate, as well as the fibres' ability to transfer stresses after the matrix cracks. In CRM systems, however, the structural mortar layer is significantly thicker (30–40 mm) and contributes directly to compressive and shear strength. Furthermore, the use of mechanical connectors limits detachment and promotes more effective interaction between the mesh and the matrix.

Consequently, FRCM-based models typically underestimate the continuous stress transfer characteristic of CRM systems, particularly in shear reinforcement applications. While the contribution of the mortar after cracking is generally neglected in FRCM formulations, in CRMs the matrix significantly contributes to the strength capacity and interacts with the mesh to

generate synergistic effects that increase stiffness, strength and energy dissipation capacity.

Introducing empirical coefficients to adapt FRCM formulations to CRM systems also makes the reliability of the models heavily dependent on the experimental database used for calibration. As the available CRM data is still relatively limited and covers a wide range of materials and configurations, such as lime or cement-based mortars, glass or carbon fibre meshes, and various masonry types, the validity of the formulations is often confined to the specific conditions considered during the calibration phase. This limits their applicability to different contexts, highlighting the need for further research to contribute to the development of comprehensive guidelines and technical documents to support the design of strengthening interventions.

2.5 Numerical modelling of masonry composite strengthening

Guidelines and analytical formulations aside, numerical modelling is one of the most widely used tools today for predicting structural behaviour, analysing performance and designing interventions. The elements that make up a masonry structure can be studied using various well-established methods in the literature: macro-modelling, simplified micro-modelling and detailed micro-modelling. These approaches have proven particularly effective in describing and simulating the behaviour of masonry structures. The choice of approach depends primarily on the objectives of the analysis and the desired trade-off between the accuracy of the results and the computational cost [54][55].

Micro-modelling is based on the explicit representation of the individual components of the masonry, namely units, mortar and the interface, while macro-modelling treats the masonry as a homogenised composite material. More specifically:

- in detailed micro-modelling, the units and mortar are represented by

continuous elements, while the unit-mortar interface is modelled using discontinuous elements representing potential fracture or slip surfaces. This approach enables extremely accurate analysis of the interactions between the units, mortar and interface;

- in simplified micro-modelling, the units are modelled as continuous elements and expanded to include the thickness of the mortar joints. The interface between adjacent units is represented by discontinuous elements. In this way, the masonry is schematised as a set of blocks connected by potential fracture or slip surfaces. However, this simplification results in the loss of the Poisson effect of the mortar and consequently a slight reduction in the accuracy of the analysis;
- finally, in macro-modelling, the units, mortar and unit-mortar interface are considered a homogeneous continuum.

Although micro-modelling allows for a more accurate description of masonry behaviour, it generally requires significant computational effort in terms of both computation time and the number of parameters and materials to be calibrated. For this reason, homogenisation-based approaches often represent a good compromise between numerical efficiency and accuracy of results [56][57]. While numerical simulation based on macro-modelling simplifies the analysis process, more detailed models obtained through micro-modelling techniques are necessary when specific local mechanisms, such as the behaviour of interfaces between masonry units and mortar joints, need to be studied.

In the field of numerical modelling of masonry arches, many researchers prefer homogenisation-based approaches, particularly for complex geometries such as cross vaults. In contrast, detailed micro-modelling generally yields more accurate results, albeit at significantly higher computational cost [57].

Although composite materials are considered an effective solution for reinforcing masonry structures, the mechanical interactions that govern the response of reinforced structures are complex, particularly in the case of curved elements. The development of reliable numerical models therefore presents many challenges, partly because many of the parameters required for simulation cannot easily be determined through simple experimental tests.

Various numerical strategies have been proposed in the literature for modelling the behaviour of reinforcement systems in curved structures. These approaches generally share a common feature: modelling the interaction between the reinforcement and the masonry using nonlinear interface elements. For instance, Monaco et al. [58] conducted a study on three-dimensional finite-element models of *calcarenite* masonry walls reinforced with C-FRP composites and subjected to out-of-plane loads. This study demonstrated the effectiveness of using shell elements to represent the reinforcement bands, which were assumed to exhibit linear elastic behaviour, combined with a cohesive law to describe the reinforcement-masonry interface.

Conversely, Ricci et al. [59] simulated the mechanical behaviour of an arch reinforced on the extrados using a PBO-FRCM system. They modelled the composite as two layers of mortar matrix connected to each other by an interface, as well as to the structural element via a second interface. This strategy enabled both the potential delamination of the fibres from the matrix and the possible detachment of the composite from the substrate to be represented. Furthermore, a smeared cracking model was adopted for the matrix capable of simulating the formation and propagation of cracks.

On the other hand, the study by Castellano et al. [60] proposes a simple yet highly effective modelling technique for FRCM and CRM systems. The authors represent the reinforcement as a continuous material corresponding to the mortar matrix, reinforced by bar elements that simulate the fibre mesh. This

approach effectively reproduces the effects of matrix cracking and the contribution of the reinforcement mesh to tensile strength.

Overall, comparing the numerical results with available experimental evidence shows that the proposed models accurately reproduce the response of reinforced vaulted structures in terms of load bearing capacity. Any discrepancies observed in the initial phase of the load-displacement curves are likely due to settlement phenomena occurring during experimental tests, which are difficult to represent in numerical models [60].

Chapter 3
Materials and Experimental Methodology

This chapter introduces the experimental campaign conducted as part of this research project. As stated in previous chapters, the experimental work assessed the effectiveness of FRCM and CRM systems applied to masonry structural elements. Particular attention was given to the shear reinforcement of masonry panels and the reinforcement of barrel vaults. Tests and results relative to the mechanical characterization of the used materials are present and discussed in the chapter, with a brief description of the entire experimental campaign. The two main topics will be explored in greater depth in subsequent chapters, which will present the results and related analyses in detail.

A preliminary phase of the research was dedicated to material characterisation, which is a fundamental activity for defining the mechanical properties of the materials used, as well as for the proper design and planning of the experimental setups. Specifically, characterisation tests were performed on the *calcarenite* masonry, bedding mortars and matrices used in the reinforcement systems. Regarding the reinforcement fabrics and meshes, however, reference was made to the mechanical properties declared by the respective manufacturers in their technical datasheets.

All experimental activities on structural element and materials were carried out at the Materials and Structures Laboratory of the Department of Engineering

at the University of Palermo (Italy). The thermal characterization tests on materials, on the other hand, were conducted at the Indoor Environments and Sustainable Technologies Laboratory, which is also part of the Department of Engineering at the University of Palermo.

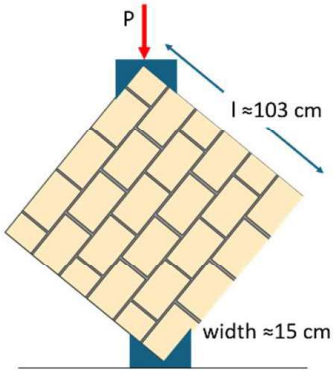
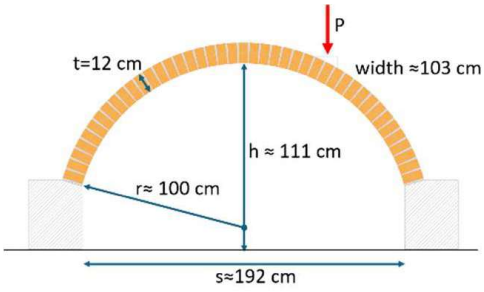
3.1 Experimental plan and materials overview

The experimental work conducted as part of this study constitutes its main content and involves various types of materials. Tests on structural elements include twelve panels built for diagonal compression tests and three barrel-vault specimens designed for load tests. Table 3.1 provides an overview of the experimental campaign conducted on the structural elements. The first column shows a description of the type of specimen tested, while the second describes the type of test to which each specimen was subjected. The third column presents a graphical representation of the test configuration, illustrating some of the key geometric features of the tested specimens. In the test configurations, P corresponds to the load applied during the test; l is the length of the panel's side; t is the thickness of the vault, r is the radius of the vault, h is the intrados height and s is the span. The last column indicates the number of tests carried out for each experimental campaign, while the table provides a brief overview of the different configurations investigated. The individual configurations and the corresponding experimental procedures are described in greater detail in Chapters 4 and 6.

The masonry used to construct the specimens consists of *calcarenite* blocks extracted from two quarries located in southern Italy, in Sicily. The two quarries are the *Marsala* quarry, located in the province of *Trapani* in western Sicily, and the *Sabucina* quarry, located in the province of *Caltanissetta* in central Sicily. Each type of *calcarenite*, which exhibit different mechanical properties, was combined with a specific bedding mortar. Regarding strengthening, three types of systems were applied to the panels, two FRCM

and one CRM, while three types of CRM systems were applied at the extrados of the vaults.

Table 3.1 Overview of the experimental campaign on structural elements carried out as part of this thesis

Specimen type	Experimental test	Geometry	no. of tests
Square masonry panel	Diagonal compressive test		- 3 unreinforced - 1 Strengthened with mortar - 6 Strengthened with FRCM syst. - 2 Strengthened with CRM syst.
Masonry barrel vault	Asymmetrically vertical load applied at one-quarter of the span		-1 unreinforced -2 repaired with CRM syst. -2 Strengthened with CRM syst.

To further clarify the different materials used and make them easier to distinguish, a summary table (Tab. 3.2) is provided below. The Table 3.2 provides an overview of the materials used in the experimental campaign. The first column shows the identification code (ID) given to each material. This ID is used throughout the text to refer to each material. The second column specifies the material type, the third indicates the structural element in which it was used and the final column specifies the type of mechanical characterisation test performed on the material. If no mechanical characterisation tests were carried out, the last column states “datasheet

properties", meaning that the material properties were obtained from the manufacturer's technical datasheet. The materials are identified by abbreviations: the letter C identifies calcarenites, the letter M identifies mortars, and Mas identifies masonry. For mortars, the letter M is followed by a number indicating their compressive strength, except for geopolymer mortar, for which the letter G is used. Bedding mortars are distinguished from those forming the matrix for the reinforcements by the addition of the letter J to indicate joints. *Calcarenites*, mortars and masonry are also labelled with the letters P and V depending on whether they were used in panel or vault testing. MasP and MasV indicate the masonry used for the Masonry Panels and Masonry Vaults, respectively. The MasP consists of *calcarenite* stone from the *Marsala* quarry, named CMP, and M5PJ mortar, while the MasV consists of *calcarenite* stone from the *Sabucina* quarry, named CSM, and M5VJ mortar. Fabrics and mesh, on the other hand, are identified by name according to their material type.

To ensure the correct identification of the various materials used, a summary of the experimental tests carried out is provided in Table 3.3, indicating the materials used for each set of samples. The first column of the table indicates the experimental campaign to which each sample belongs, while the second column indicates the identification code used in the remainder of this thesis. The third column specifies the type of masonry constituting the substrate, while the fourth column shows the number of tests carried out for each type of sample. The last three columns identify, respectively, the type of fibre, the matrix and the presence or absence of connectors. The codes used for the materials refer to Table 3.2 above. The mechanical properties of the specific materials will be described in the subsequent Sections 3.2 and 3.3. However, in the subsequent chapters, where the respective experimental campaigns are presented, the combinations of materials used for specimens will be specified.

Table 3.2 Identification of the materials used in the experimental tests

ID	Description	Application	Test
CMP	*Calcarenite* stone from *Marsala* quarry	Masonry panels	- Uniaxial compression - Thermal test
CSV	*Calcarenite* stone from *Sabucina* quarry	Masonry vaults	- Uniaxial compression - Thermal test
M5PJ	Lime-based mortar	Joints mortar for panels	- Uniaxial compression - Three-point bending test
M5VJ	Lime-cement mortar	Joints mortar for vaults	- Uniaxial compression - Three-point bending test
MasP	Masonry made of CMP and MPJ5	Masonry panels	- Uniaxial compression - Diagonal compression
MasV	Masonry made of CSV and MVJ5	Masonry vaults	Uniaxial compression
M10P	FRCM matrix	Panel strengthening	- Uniaxial compression - Three-point bending test
M15P	CRM matrix	Panel strengthening	- Uniaxial compression - Three-point bending test
M10V	Traditional CRM matrix	Vault strengthening	- Uniaxial compression - Three-point bending test
MGV	Geopolymer CRM matrix	Vault strengthening	- Uniaxial compression - Three-point bending test
Carbon	Carbon textile for FRCM	Panel strengthening	Datasheet properties
Glass	Glass textile for FRCM	Panel strengthening	Datasheet properties
GFRP1	Glass FRP for CRM	Panel and vault strengthening	Datasheet properties
GFRP2	Glass FRP for CRM	Vault strengthening	Datasheet properties

Table 3.3 Indication of the materials used for each sample

	ID	Masonry	n. of tests	Fibre layer	Matrix	Connectors
Panels	URM_*x*	MasP	3	-	-	-
	CM	MasP	1	-	M10P	-
	C_FRCM_*x*	MasP	2	Carbon	M10P	No
	G_FRCM_*x*	MasP	2	Glass	M10P	No
	C_FRCM+c	MasP	1	Carbon	M10P	Yes
	G_FRCM+c	MasP	1	Glass	M10P	Yes
	G_CRM_*x*	MasP	2	GFRP1	M15P	Yes
Vaults	UR/V	MasV	1	-	-	-
	REP/V	MasV	1	GFRP1	M10V	Yes
	REP/V+T	MasV	1	GFRP1	M10V	Yes
	R/V+T	MasV	2	GFRP2	M10V	Yes
	R/V_G+T	MasV	3	GFRP2	MVG	Yes

3.2 Masonry characterization

The masonry selected for this experimental campaign's test specimens is a fundamental aspect of the work. Since a key focus of this study is the preservation of existing buildings, the choice was made to use the *calcarenite* stone, a material widely used throughout Sicily and found in many historic and monumental buildings in the architectural heritage of southern Italy (Fig. 3.1)[61][62]. *Calcarenite* is a sedimentary rock resulting from the successive stratification and cementation of sand-sized limestone grains. These clasts are often of biological origin, meaning they are composed of shell fossils from living organisms. The compressive strength of these natural rocks varies widely depending on their origin and, consequently, their extraction site. Regarding *calcarenite* of Sicilian origin, the compressive strength of Agrigento ca*lcarenite* is approximately 4.4 MPa and that of Marsala calcarenite is

approximately 6.5 MPa [63]. However, higher values are observed for the types of *calcarenite* in the centre part of Sicily, ranging from 8 to 15 MPa for the calcarenite from Palermo [64][65].

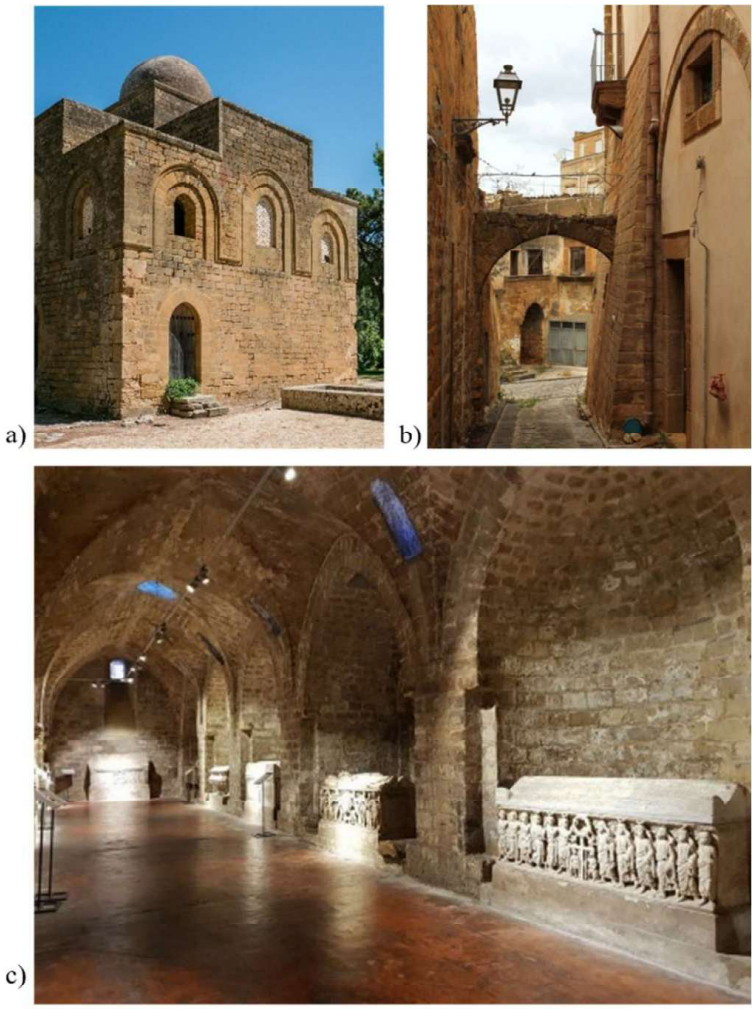


Figure 3.1 *Calcarenite* stone in Sicily (South of Italy): a) *Chiesa della Santissima Trinità di Delia* in *Castelvetrano*; b) Town centre of *Sambuca di Sicilia*; c) *Palermo* Cathedral

3.2.1 Properties of Marsala and Sabucina calcarenite

This experimental study uses two distinct types of *calcarenite*, extracted from western (*Marsala*) and central (*Sabucina*) Sicily, respectively. The two types of *calcarenite* were selected to represent different construction contexts and to investigate the behaviour of the strengthening systems on masonry substrates characterised by different mechanical properties. The lower-strength

calcarenite, representative of masonry commonly found in modest residential buildings, was used for the masonry panels investigated under in-plane shear loading. The higher-quality calcarenite, characterised by better mechanical properties and historically associated with more prestigious buildings, was instead used for the barrel vaults. Due to the variability in their mechanical properties, characterisation tests were performed on both types.

Marsala Calcarenite

The *calcarenite* used in the experimental campaign involving diagonal compression tests was sourced from a quarry in Marsala, Sicily. As previously mentioned, this type of stone is characterised by significant heterogeneity and exhibits variable chemical and mechanical properties. four different *calcarenite* blocks were supplied by the same quarry and subjected to a preliminary mechanical characterisation in order to compare their main mechanical properties and select the most suitable material for the experimental campaign. Cubic specimens with a side length of 100 mm were cut from each block and tested as part of the preliminary characterisation programme (Fig. 3.2). From a macroscopic perspective, the samples can be grouped into two pairs based on their aspect and their composition. The first two series, labelled “G” and “GS” respectively (Fig.3.2), show greater compactness and homogeneity. In contrast, the other two series, labelled “FC” and “FS” (Fig.3.2), exhibit more intense colouring and a higher concentration of fossils.



Figure 3.2 *Calcarenite* stone from Marsala quarry (photos taken during the experimental activities)

Compressive strength was determined for all four types [66]. Tests were performed using a Zwick-Roell Z600 universal testing machine (UTM) in displacement control mode with a loading rate of 0.4 mm/min. The experimental results are shown in Table 3.4. The Table 3.4 shows the number of tests performed for each series, followed by the average weight per unit volume ρ and compressive strength values σ_c. The test results showed that the FC and GS series have the best mechanical properties. However, the FC series has greater variability in compressive strength results. The G and GS series, on the other hand, have lower compressive strength values, but with less variation. For the purposes of this study, stone from the GS series was selected, considering that this type is the most used in local construction.

Table 3.4 Mechanical properties of *calcarenite* stone tested: average values

SERIE	no. of tests	ρ [kN/m^3]	σ_c [MPa]
G	6	16.2 *(CoV=2 %)*	2.97 *(CoV=17 %)*
GS	6	17.1 *(CoV=2 %)*	4.47 *(CoV=13 %)*
FC	6	17.5 *(CoV=4 %)*	4.60 *(CoV=40 %)*
FS	6	16.2 *(CoV=5%)*	2.90 *(CoV=3%)*

Due to the high variability in the material's properties, a second characterisation study was conducted on the type of stone selected for the panels, with six samples extracted from the same batch used for their construction. Six cubic samples, each with a side length of 100 mm, were tested. This type will herein be identified by the code CMP, in accordance with Table 3.2. After testing, the samples exhibited the expected hourglass-shaped

fracture pattern (Fig. 3.3a). The stress-strain curve results obtained are shown in Fig. 3.3b.

Table 3.5 shows the average values obtained from the tests and their respective coefficients of variation. The table lists the number of samples tested, the average values and the coefficients of variation for density ρ, compressive strength σ_c and porosity *n*. Porosity *n* was estimated using an analytical formula based on the material type (Eq. 3.1).

$$n = \left(1 - \frac{\gamma_d}{\gamma_s}\right) * 100 \tag{3.1}$$

Here, γ_d represents the weight per unit volume of the dry sample, calculated as the ratio of weight to total volume. Meanwhile, γ_s is the true specific weight of the solid grains, which was assumed to be 2.71 g/cm³ [65].

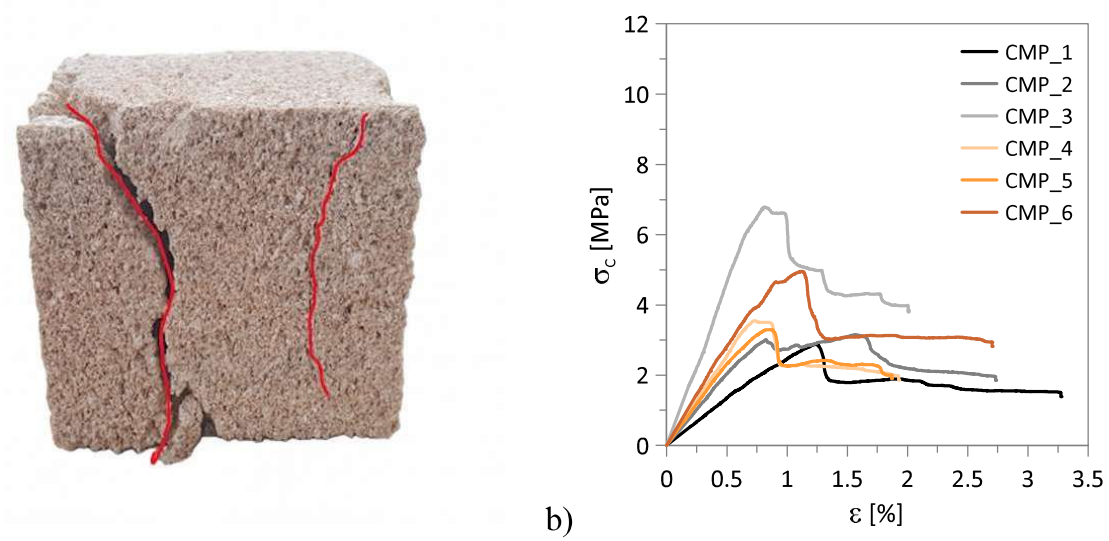


Figure 3.3 Uniaxial compressive tests on CMP *calcarenite*: a) CMP_2 sample after test (photo taken during the experimental activities); b) stress vs strain curves for all specimens

Table 3.5 Mechanical properties of CMP *calcarenite* stone tested

ID	n. of tests	ρ [kN/m³]	σ c [MPa]	n [%]
CMP	6	14.6 *(CoV=3.7 %)*	4.09 *(CoV=37 %)*	46 *(CoV=4.4 %)*

The *calcarenite* was also subjected to thermal characterisation tests in accordance with UNI EN 12664:2002 [67]. These tests involved three cylindrical samples (Fig. 3.4a), which were tested using a LaserComp FOX 50 thermal fluxmeter (Fig. 3.4b). This device can measure cylindrical samples with diameters ranging from 50 to 60 mm and a maximum height of 25 mm. It operates within a thermal conductivity range of 0.1 W/mK to 10 W/mK. The results obtained for the three specimens are reported in Table 3.6. It shows, in the first column, the sample identification number; in the second, the weight per unit volume measured prior to the test; and in the third, the measured thermal conductivity values. The last two rows, meanwhile, show the mean values and the coefficient of variation.

a) 

b) 

Figure 3.4 Thermal test on *calcarenite* cylindrical samples: a) from Sabucina quarry with "S" and from Marsala quarry with "M"; b) LaserComp thermal fluxmeter (photos taken during the experimental activities)

Table 3.6 Thermal properties of CMP *calcarenite* stone tested

ID SAMPLE	**ρ [kN/m³]**	**λ [W/mK]**
CMP_1	13.9	0.965
CMP_2	13.9	0.959
CMP_3	14.1	0.879
Average	13.9	0.934
Coefficient of Variation	0.6 %	4.2 %

The measured values were considered reliable as they fit within the range of variation shown in Table 3 of UNI EN ISO 10456:2008 [68].This table provides design values for the thermal properties of limestone at different levels of compactness (Fig. 3.5).

Sabucina Calcarenite

The vaults were constructed using *calcarenite* sourced from the *Sabucina* quarry (*Caltanissetta*, in the Central part of Sicily). This building material is widely used in historic Sicilian buildings, particularly in the *Caltanissetta* area. Yellowish-brown *Sabucina calcarenite* is a rock characterised by grains an average size of 1 mm, originating from the compaction and cementation of fine sand carbonate clasts. It contains a carbonate cementing material that does not completely fill the intergranular spaces, which may in turn include a matrix consisting of silt and/or clay particles. This type of *calcarenite* exhibits relatively low interparticle porosity due to prolonged cementation [65]. Consequently, it is more compact and resistant than Marsala *calcarenite*.

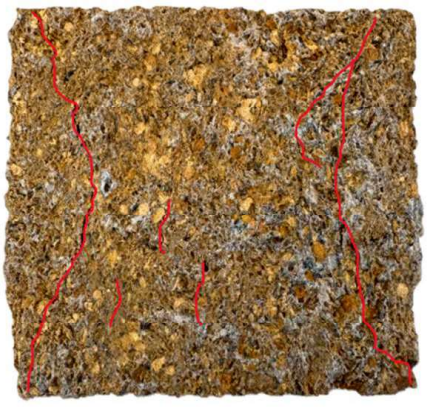
Uniaxial compression tests were also performed on this *calcarenite* [66]. Eight cubic specimens, each with a side length of 100 mm, were tested. The specimens exhibited the expected hourglass-shaped failure pattern at the end of the test (Fig. 3.6a). The resulting stress vs strain curves are shown in Figure 3.6(b), and the average compressive strength values σ_c are listed in Table 3.7. The table also provides information on the number of tests performed, weight per unit volume ρ and porosity n (Eq. 3.1).

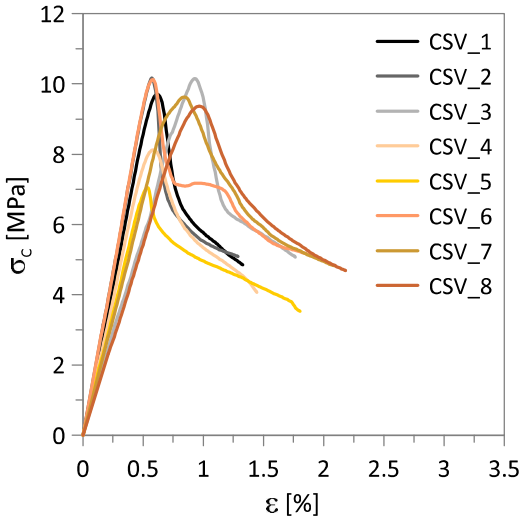
Similarly to the Marsala calcareni*te*, thermal characterisation tests were performed as described above and the results are presented in Table 3.8. The values obtained in this case were also considered reliable as they fall within the range specified in Table 3 of UNI EN ISO 10456:2008 (Fig. 3.5) [68]. Furthermore, these values are consistent with those obtained for the Marsala *calcarenite*, which, due to its higher porosity, exhibits significantly lower

thermal conductivity. The results therefore confirm the influence of the material's porous structure on its thermal properties, with lower porosity generally associated with higher thermal conductivity.

Material group or application		Density ρ kg/m³	Design thermal conduct-ivity λ W/(m·K)	Specific heat capacity c_p J/(kg·K)	Water vapour resistance factor μ	
					dry	wet
Stone	Natural, crystalline rock	2 800	3,5	1 000	10 000	10 000
	Natural, sedimentary rock	2 600	2,3	1 000	250	200
	Natural, sedimentary rock, light	1 500	0,85	1 000	30	20
	Natural, porous, e.g. lava	1 600	0,55	1 000	20	15
	Basalt	2 700 – 3 000	3,5	1 000	10 000	10 000
	Gneiss	2 400 – 2 700	3,5	1 000	10 000	10 000
	Granite	2 500 – 2 700	2,8	1 000	10 000	10 000
	Marble	2 800	3,5	1 000	10 000	10 000
	Slate	2 000 – 2 800	2,2	1 000	1000	800
	Limestone, extra soft	1 600	0,85	1 000	30	20
	Limestone, soft	1 800	1,1	1 000	40	25
	Limestone, semi-hard	2 000	1,4	1 000	50	40
	Limestone, hard	2 200	1,7	1 000	200	150
	Limestone, extra hard	2 600	2,3	1 000	250	200
	Sandstone (silica)	2 600	2,3	1 000	40	30
	Natural pumice	400	0,12	1 000	8	6
	Artificial stone	1 750	1,3	1 000	50	40

Figure 3.5 Extract from Table 3 of UNI EN ISO 10456:2008 [68]





a) b)

Figure 3.6 Uniaxial compressive tests on CSV *calcarenite*: a) CSV_4 sample after test (photo taken during the experimental activities); b) stress vs strain curves for all specimens

Table 3.7 Mechanical properties of CSV *calcarenite* stone tested

ID	n. of tests	ρ [kN/m^3]	σ_c [MPa]	n [%]
CSV	8	19.5 (CoV=1.1 %)	9.29 (CoV=23 %)	20 (CoV=3.7 %)

Table 3.8 Thermal properties of CSV *calcarenite* stone tested

ID SAMPLE	ρ [kg/m^3]	λ [W/mK]
CSV_1	17.3	1.722
CSV_2	17.5	1.725
CSV_3	17.4	1.842
Average	17.4	1.763
Coefficient of Variation	0.7 %	3.2 %

3.2.2 Properties of mortar for the joints

The bedding mortars used belong to two different product categories and were selected based on the type of *calcarenite* employed. The bedding mortar used for the panels, indicated as M5PJ, is an Natural Hydraulic Lime (NHL) 3.5 mortar of class M5. The bedding mortar used for the vaults, indicated as M5VJ, is a premixed powdered masonry mortar consisting of hydrated lime, Portland cement and natural sands, also of class M5.

The mechanical properties of the bedding mortars were evaluated in accordance with UNI EN 1015-11 [69]. Test specimens measuring 160 × 40 × 40 mm were cast using dedicated moulds during the construction of the panels and vault. The specimens were subjected to experimental tests to determine their main mechanical properties: flexural and compressive strength.

The flexural strength was determined by performing three-point bending tests using a ZwickRoell Z005 Universal Testing Machine (UTM) equipped with a 5 kN load cell. These tests were conducted in displacement control mode at a rate of 0.5 mm/min with a preload of 10 N and a support span of 100 mm.

Uniaxial compression tests were performed in the halved specimens resulting from flexural testing using an MP Strumenti Once502 UTM machine with a 50 kN load cell. The tests were conducted under displacement control at a displacement rate of 0.5 mm/min and a preload of 50 N. The Table 3.9 summarises the results obtained for the two types of mortar. Here, σ_{fl} is the flexural strength and σ_c is the compressive strength.

The variability observed in the results of the mortar characterisation tests can be attributed to several factors. A first factor relates to the intrinsic heterogeneity of the material, which is typical of composite materials consisting of a binder and aggregates, and which can lead to local differences in the properties of individual test specimens. A second factor relates to the variability between the different mixes prepared in the laboratory, despite the proportions and preparation conditions having been kept as consistent as possible. Finally, a further source of variation may be linked to the methods used to prepare the individual test specimens and, in particular, to the manual operations required for their moulding, which may introduce differences in compaction and material distribution.

Table 3.9 Mechanical properties of joints mortars tested

ID	n. of tests	σ_{fl} [MPa]	σ_c [MPa]
M5PJ	4	1.27 CoV=6.9 %	4.90 CoV=11.4 %
M5VJ	6	1.87 CoV=7.1 %	5.28 CoV=2.5 %

3.2.3 Masonry uniaxial compressive tests

To characterise the masonry material consisting of *calcarenite* and the above-described mortar, uniaxial compression tests were performed on small panels in accordance with UNI EN 772-1 [70]. The panels were constructed with almost square shapes (Fig. 3.5).

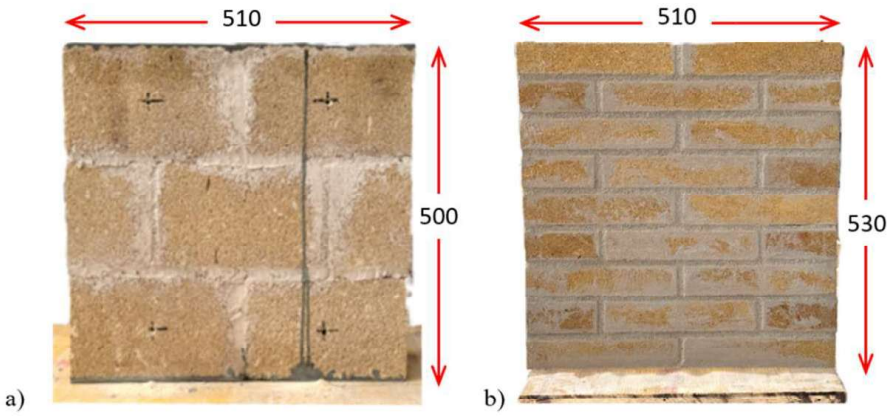


Figure 3.5 Masonry walls for uniaxial compressive tests (dimension in mm; photo taken during the experimental activities): a) MasP used for panels; b) MasV used for vaults

The MasP masonry specimens have dimensions of 510 × 500 × 150 mm, whereas the MasV specimens have dimensions of 510 × 530 × 120 mm. The differences in the dimensions of the panels tested under uniaxial compression are due to differences in the dimensions of the *calcarenite* units used.

Threaded bars were installed on each panel to allow the dial gauges to be installed subsequently (Figs. 3.6, 3.7). The dial gauges were arranged on both surfaces, with two vertical gauges on one side (Figs. 3.6a, 3.7a) and one vertical and one horizontal gauge on the other (Figs. 3.6b, 3.7b). The gauges' reading bases were also measured as these were necessary for calculating the subsequent deformations.

Before conducting the tests, the upper and lower surfaces of the specimens were flattened using a self-levelling mortar. A total of six uniaxial compression tests were performed, with three tests conducted on each type of masonry. These were conducted under displacement control at a rate of 1 mm/min and with a preload of 20 kN using a ZwickRoell 4000 machine with a maximum capacity of 4000 kN. The curves recorded by the dial gauges for each panel are reported in the graphs shown in Figures 3.8 and 3.9. The x-axis shows the vertical strain ε_v and the horizontal strain ε_v, while the y-axis shows the compressive stress σ_c. Some curves, e.g. the horizontal strain curves of

MasP_2 (Fig. 3.8) and MasV_3 (Fig. 3.9) samples, have not been included because errors were detected in the corresponding measurements.

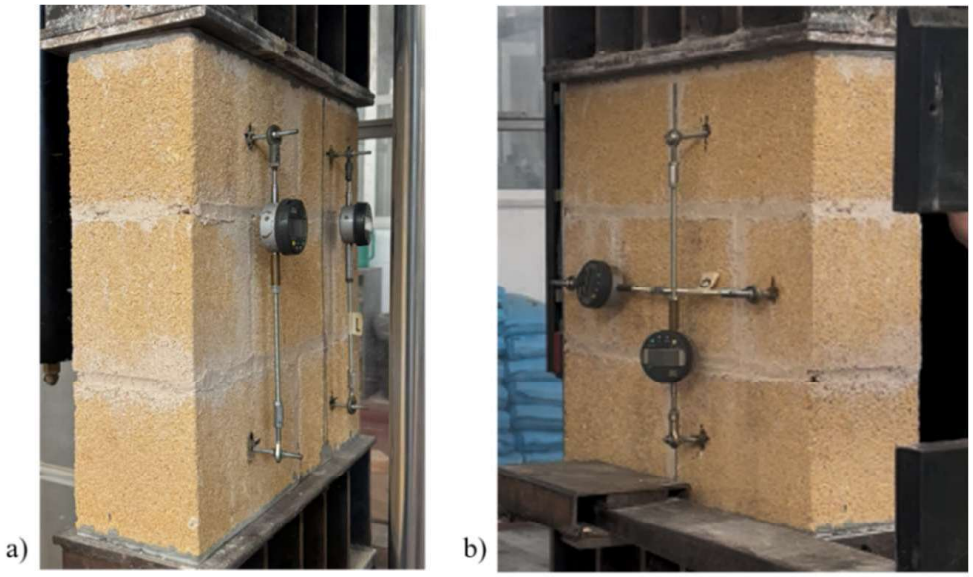


Figure 3.6 Dial gauges on MasP panels for uniaxial compressive tests (photos taken during the experimental activities): a) two verticals on front side; b) one vertical and one horizontal on back side

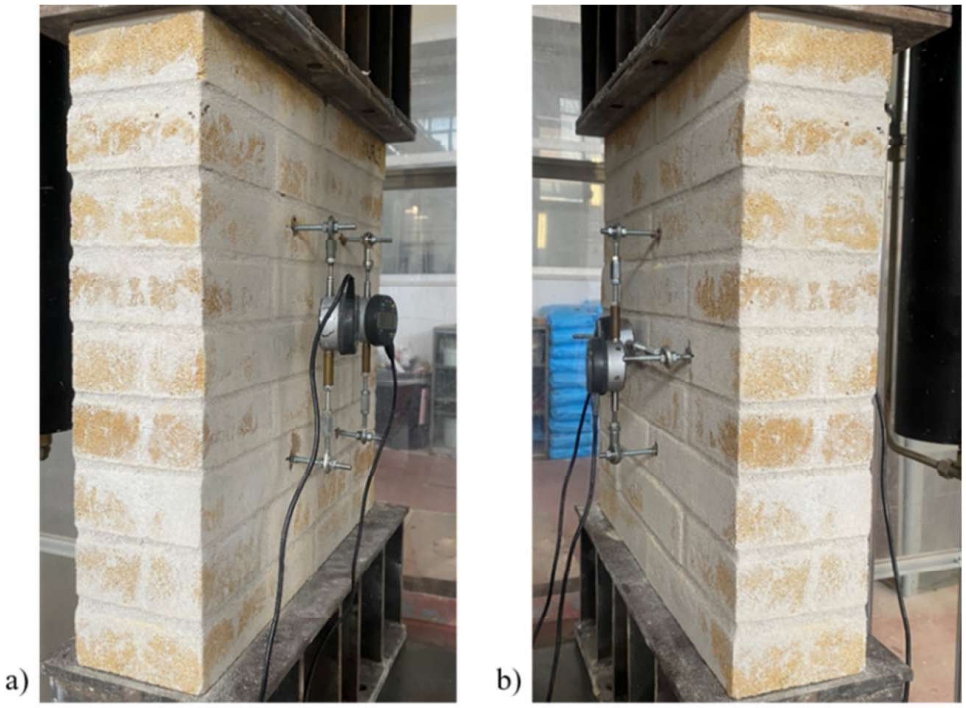


Figure 3.7 Dial gauges on MasV panels for uniaxial compressive tests (photos taken during the experimental activities): a) two verticals on front side; b) one vertical and one horizontal on back side

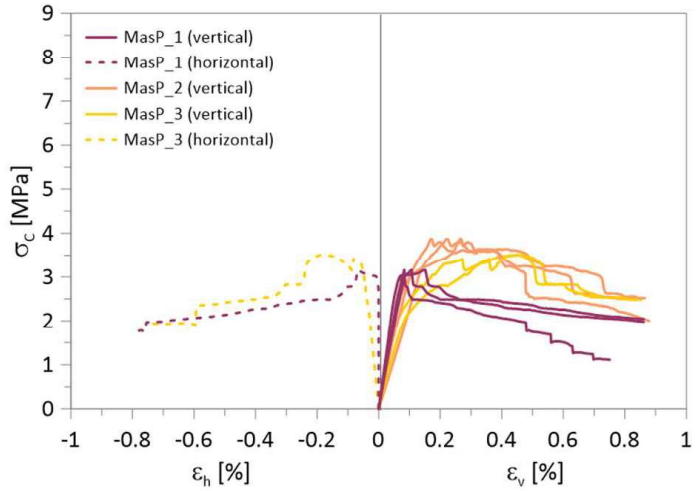


Figure 3.8 Stress vs vertical/horizontal strain of MasP masonry

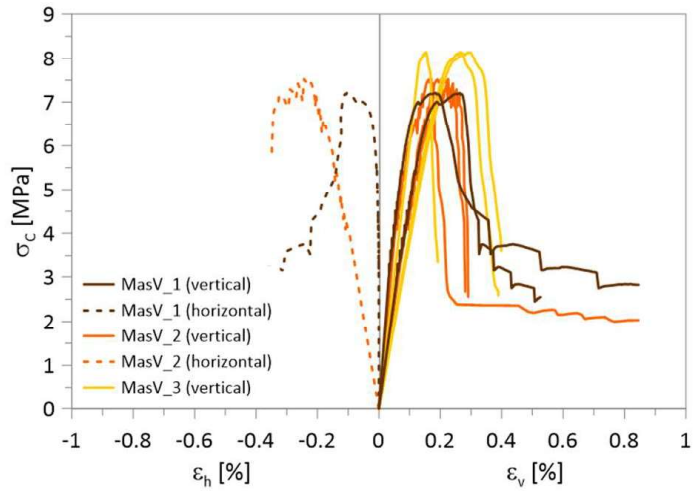


Figure 3.9 Stress vs vertical/horizontal strain of MasV masonry

The results obtained for both types of masonry are summarised in Table 3.10. The table lists the average values and coefficient of variation of compressive strength σ_c, the strain at peak stress ε_p, the modulus of elasticity E and Poisson's ratio ν. Figures 3.10 and 3.11 show the panels at the end of the tests. The MasP masonry specimens (Fig. 3.10) exhibited cracks inclined at approximately 45° near the corners that became vertical in the central part of the panel and crossed the vertical joints. The MasV masonry specimens (Fig. 3.11), on the other hand, exhibited predominantly sub-vertical cracks.

It should also be noted that three diagonal compression tests were conducted

on unreinforced masonry for the purposes of the shear mechanical characterisation of the masonry and the evaluation of the effectiveness of the reinforcement. This test is aimed at characterising the masonry, allowing for a direct comparison with the results of the reinforced specimens. For clarity, the results are included in the following Chapter (Section 4.3), which is dedicated to the experimental campaign on the panels.

Table 3.10 Mechanical properties of masonry from uniaxial compressive tests

ID	n. of tests	σ_c [MPa]	ε_p [%]	E [MPa]	υ [-]
MasP	3	3.59	0.24	4050	0.19
		CoV=16 %	CoV=27 %	CoV=10 %	CoV=14 %
MasV	3	7.62	0.25	5580	0.15
		CoV=5 %	CoV=20%	CoV=19 %	CoV=13 %



Figure 3.10 Failure mode for masonry MasP (photos taken during the experimental activities): a) Sample 1; b) Sample 2; c) Sample 3

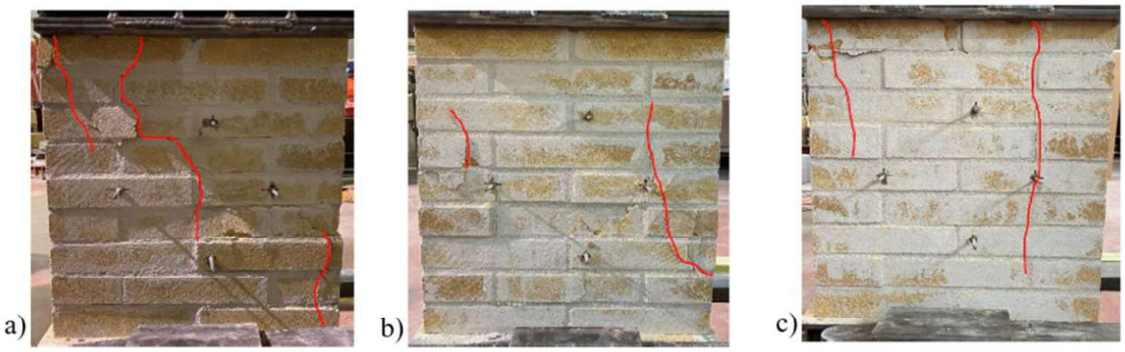


Figure 3.11 Failure mode for masonry MasV (photos taken during the experimental activities): a) Sample 1; b) Sample 2; c) Sample 3

3.3 Description of composite strengthening materials

Mortar specimens were prepared for mechanical characterisation for all strengthening systems used in the investigation. For the mesh and fabrics, the mechanical properties listed in the manufacturers' technical data sheets will be provided.

3.3.1 Matrices and fabrics used in FRCM systems

Matrix

The matrix used for the FRCM system is unique and the same for all samples. It is identified by the code M10P. This is a ready-to-use, light-coloured, fibre-reinforced, two-component mortar consisting of natural hydraulic lime (NHL), eco-pozzolana, natural sands, special additives and synthetic polymers in an aqueous dispersion. The mortar samples were prepared simultaneously with the installation of the reinforcement and tested shortly before the diagonal compression tests. Similar to the tests described in the previous section regarding bedding mortars, flexural and compression tests were performed on the samples. The results are shown in Table 3.11. Table 3.10 shows the number of specimens that were subjected to a three-point bending test. Compression tests were then performed on the two halves obtained from each of these specimens, for a total of 16 tests. The mean values and respective coefficients of variation for flexural and compressive strength are shown.

Table 3.11 Mechanical properties of matrix from bending and uniaxial compressive tests

ID	n. of tests	σ_{fl} [MPa]	σ_c [MPa]
M10P	8	4.15 CoV=7.6 %	14.27 CoV=11 %

Textiles

Two types of fabric are used in the FRCM system: a fibreglass fabric identified as *Glass*, and a carbon fibre fabric identified as *Carbon*.The fibreglass fabric

has a mesh size of 12 × 12 mm (Fig. 3.12a). It has a weight g of 220 g/m², a density ρ of 2.5 g/cm³ and an equivalent fibre thickness t_f (i.e. the thickness of the textile fibre considered to be uniformly distributed across the cross-section) equal to 0.04 mm. The technical data sheet lists the following mechanical properties for the fibreglass mesh: tensile strength f_{fu} = 56 kN/m, ultimate strain ε_{fu} = 2.0%, and elastic modulus E_f = 74 GPa.

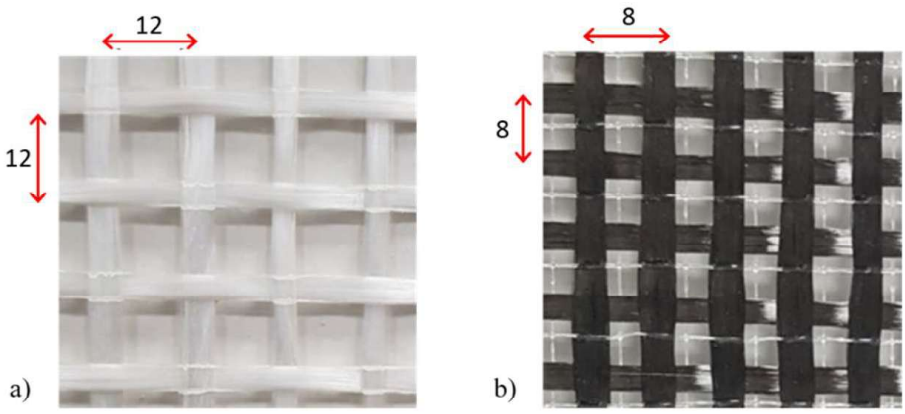


Figure 3.12 FRCM fabrics (openings expressed in mm, (photos taken during the experimental activities): a) Glass; b) Carbon

The carbon fibre fabric has a mesh size of 8 × 8 mm (Fig. 3.12b). It has a weight g of 225 g/m², a density ρ of 2.25 g/cm³ and an equivalent fibre thickness t_f equal to 0.056 mm (i.e. the thickness of the textile fibre assumed to be uniformly distributed across the cross-section). The technical data sheet lists the following mechanical properties for the carbon fibre mesh: tensile strength f_{fu} = 60 kN/m, ultimate strain ε_{fu} = 1.8%, and Young's modulus E_f = 240 GPa. The data provided by the manufacturer for both fabrics are reported in Table 3.12.

As it will be explained in the next Chapter (Section 4.2.1), the system has been installed using fan-shaped connectors in selected configurations. These were fabricated in the laboratory from high-strength, unidirectional Type E fibreglass rope with a diameter of 10 mm (Fig. 3.13a). The mechanical properties of the glass rope, as specified by the manufacturer, are listed in

Table 3.13. It lists the following properties: density ρ, equivalent cross section A_{eq}, tensile strength f_{fu}, elongation in correspondence of peak stress value ε_{fu} and elastic modulus E_f. The rope was cut to the recommended dimensions, impregnated with a superfluid, solvent-free, two-component epoxy resin (Fig. 3.13b), and then fixed in place. The resin impregnation of the fibres was carried out carefully to ensure a uniform distribution of the resin throughout the connector and to promote adequate adhesion between the fibres and the resin matrix. To keep them straight during the resin curing process, the ends of the connectors were then fixed in place (Fig. 3.13c).

Table 3.12 Mechanical properties of FRCM fabrics by datasheets

	g [g/m^2]	ρ [g/cm^3]	t_f [mm]	f_{fu} [kN/m]	ε_{fu} [%]	E_f /GPa]
Glass	220	2.50	0.020	56	2.0	74
Carbon	225	2.25	0.056	60	1.8	240

Table 3.13 Mechanical properties of Glass fibre rope for FRCM connectors by datasheets

	ρ [g/cm^3]	A_{eq} [mm^2]	f_{fu} [MPa]	ε_{fu} [%]	E_f [GPa]
Glass rope	2.62	27.58	2560	>3	80.7

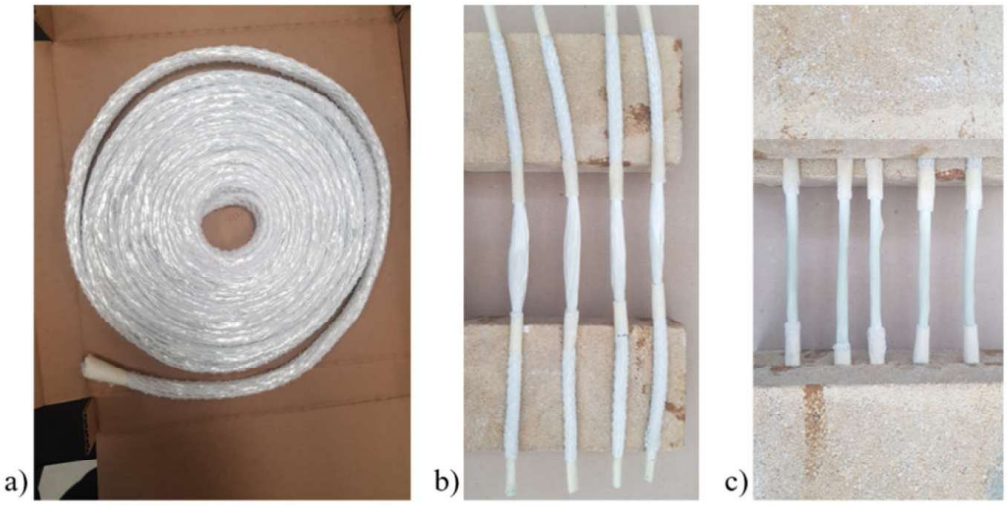


Figure 3.13 Connectors (photos taken during the experimental activities): a) fibre glass rope; b) binding with epoxy resin; c) curing in straight configuration

3.3.2 Matrices and meshes used in CRM systems

The CRM systems are designed using a combination of three types of mortar and two types of mesh.

Matrices

The M15P mortar used for the CRM system applied to the panels is a fibre-reinforced, premixed mortar based on natural hydraulic lime (NHL 3.5 and NHL 5), inorganic reactive composites, natural sands, special additives and microfibres. It is characterised by extremely low emissions of volatile organic compounds.

M10V mortar is a premixed structural mortar based on hydrated lime and hydraulic binders. It is highly breathable and suitable for the application of reinforced plasters. It is used for the CRM system applied to the vault. MGV mortar, on the other hand, is a geopolymer mortar used for the CRM system applied to the vault. Its mix design, developed at the University of Salento in collaboration with ITC-CNR [71], combines fly ash, metakaolin, expanded glass and an alkaline solution of sodium silicate and sodium hydroxide.

The mortars were tested in the same way as the other types and the results are shown in the Table 3.14.

Table 3.14 Mechanical properties of CRM matrices from bending and uniaxial compressive tests

ID	n. of tests	σ_{fl} [MPa]	σ_c [MPa]
M15P	3	5.63 CoV=3.6 %	19.42 CoV =0.091
M10V	6	5.36 CoV =8.4 %	20.20 CoV =17 %
MGV	8	2.09 CoV =11.4 %	10.81 CoV =19.8 %

Grids

Two grids are used in the CRM system. Both are made of glass-fibre-reinforced plastic (GFRP) and labelled GFRP1 (Fig. 3.14a) and GFRP2 (Fig. 3.14b).

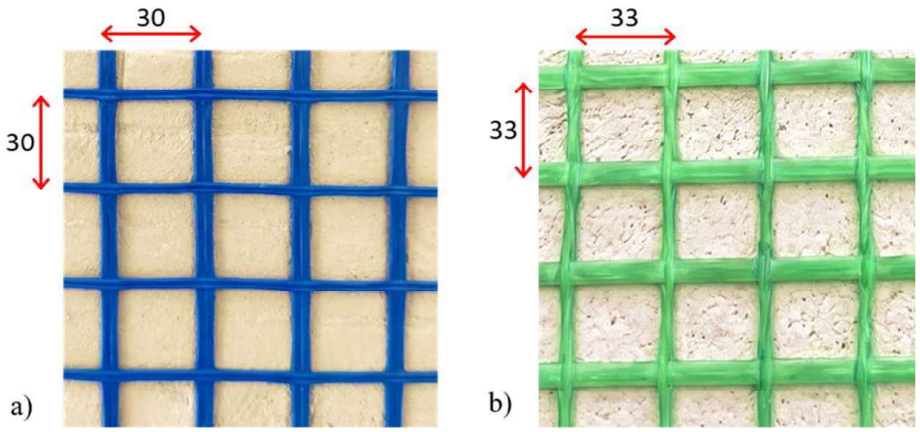


Figure 3.14 CRM meshes (Grid spacing is shown in mm; photos taken during the experimental activities): a) GFRP1; b) GFRP2.

The GFRP1 mesh, which is used in the CRM system for both the panels and the vault, has a mesh size of 30 × 30 mm, a unit weight of 460 g/m², a density of 2.68 g/cm³, an equivalent fibre thickness t_f equal to 2.46 mm and an average tensile strength f_{fu} of 567 MPa.

The GFRP2 mesh, which is used in the CRM system for the vaults, has a mesh size of 33 × 33 mm, a unit weight of 820 g/m², a density of 2.68 g/cm³, an equivalent fibre thickness t_f equal to 3.84 mm and an average tensile strength f_{fu} of 495 MPa.

A summary of the main mechanical properties is provided in Table 3.15.

Table 3.15 Mechanical properties of CRM meshes by datasheets

ID	g [g/m²]	ρ [g/cm³]	t_f [mm]	f_{fu} [kN/m]	ε_{fu} [%]	E_f [GPa]
GFRP1	460	2.68	2.46	567	2.37	25
GFRP2	820	2.60	3.84	495	1.45	25

The GFRP meshes were installed using preformed L-shaped connectors (Fig. 3.15), in accordance with the manufacturer's recommendations and the

procedures illustrated in subsequent chapters. The connectors used are identified below by the abbreviation 'LS' (for 'L-shaped') and consist of two types: LS1 (Fig. 3.15a), which is used for the GFRP1 mesh; and LS2 (Fig. 3.15b), which is used for the GFRP2 mesh. Both connectors are made of GFRP, consisting of glass fibres and a vinyl ester-epoxy thermosetting resin. However, they differ in size and mechanical properties. LS1 connectors measure 200 × 100 mm and have an equivalent bar diameter of 7 mm. LS2 connectors measure 100 × 70 mm and have a nominal cross-section of 10 × 7 mm.

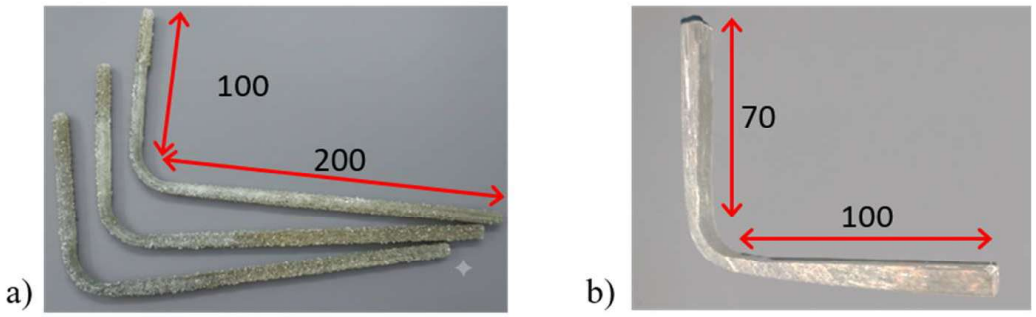


Figure 3.15 CRM connectors (dimensions in mm; photos taken during the experimental activities): a) LS1; b) LS2

The mechanical properties of the two connectors are shown in Table 3.15. In particular, in Table 3.16 the specifications provided by the manufacturer are listed, such as the lengths of the two connector sections, the nominal cross-sectional area A_n, the average tensile strength f_t, the elongation at break ε_u, and the average value of the modulus of elasticity E_f.

Table 3.16 Mechanical properties of GFRP connectors for CRM systems by datasheets

ID	Dimensions [mm]	A_n [mm^2]	f_t [MPa]	ε_u [%]	E_f [GPa]
LS1	200h x 100L	24.3	949	2.11	39.0
LS2	100h x 70L	78.9	455	1.40	26.5

Chapter 4

Experimental Campaign on Calcarenite Masonry Panels

As discussed in previous chapters, using inorganic matrix composite materials is an effective solution for the strengthening of masonry panels subjected to in-plane loads. Although this technique is now widely used, some aspects still require further investigation. The correct design of the intervention requires careful consideration of the materials to be used, based on their mechanical properties and, above all, their compatibility with the characteristics of the masonry substrate. Numerous configurations can be achieved by combining different types of mortar and fabric, as well as through the application methods, such as the thickness and number of layers, symmetrical or asymmetrical configuration, and the presence or not of connectors. All of these variables influence the design of the reinforcement system and consequently the increase in shear strength provided to the panel due to the intervention.

The current formulations proposed in the regulatory documents enable this increase to be estimated primarily based on the mechanical properties of the fibres. However, available experimental evidence in the literature suggests that the reinforcement matrix also plays a fundamental role in the system's overall behaviour. Furthermore, the currently available formulations for FRCM systems are still ineffective in accurately assessing the contribution of CRM systems.

In this context, the experimental programme proposed in this study was

developed to contribute to expanding the database relating to diagonal compression tests in the literature, by adding a further twelve experimental tests and increasing knowledge on the topic. The study was conducted on Sicilian *calcarenite* masonry characterised by low mechanical strength, whose properties are representative of those of existing historic buildings constructed using local materials. This aspect is one of the research's key features, given that studies relating to diagonal compression tests on masonry constructed from sedimentary rocks, such as *calcarenite*, account for only around 5 per cent of the total. Furthermore, the majority of available experimental programmes (around 92%) focus on materials whose mechanical properties are superior to those typically found in existing historic masonry. Therefore, it is essential to understand the effectiveness of the currently available reinforcement systems when applied to poor-quality masonry substrates, and to correctly identify the parameters governing the assessment of increased shear strength. The results of this experimental campaign are described in detail in the following sections and have been integrated into a database of 742 diagonal compression tests from the literature [28]–[36], [72]–[126]. The database was developed in an external file and includes, for each experimental campaign, information on the geometry of the specimens, the characteristics of the masonry substrate and strengthening materials, the strengthening configuration and the main experimental results available from the original studies. Due to the large amount of information collected, the complete database is not included in the thesis. Instead, Appendix A reports a selection of the most relevant parameters and results, together with the bibliographic reference for each test, allowing the data to be traced back to the corresponding source. The complete database was used to analyse the main parameters influencing the shear response of strengthened masonry panels and to assess the applicability of existing analytical formulations. Comparing the results of

the present thesis with existing data was useful for verifying their consistency with those of other experimental campaigns and for analysing the influence of the main mechanical and geometric parameters on the behaviour of the reinforcement systems. An analysis was also carried out using this database, regarding the main parameters characterising the masonry and the reinforcement system, with the aim of identifying possible correlations that could provide useful guidance for improving and updating the current analytical formulations.

4.1 Experimental plan

To improve understanding of the aspects that still require further investigation, the experimental programme was designed to analyse the influence of various variables on the behaviour of the reinforcement system. These variables included the presence and type of fabric, the use of connectors, and the type of composite system (FRCM or CRM).

To this end, various experimental configurations were selected. Firstly, the configuration in which the reinforcement consists solely of the matrix, corresponding to the mortar used in the FRCM system, was analysed to assess the matrix's contribution alone. Subsequently, two different FRCM systems characterised by two different types of fabric (glass fibre and carbon fibre) were considered. Configurations with and without connectors were also investigated to assess their effect on the reinforcement system's overall behaviour. Finally, the performance of a CRM system was compared with that of the FRCM systems, in order to assess the influence of the different system configurations on the improvement of the masonry’s mechanical response.

A summary of the configurations investigated as part of the experimental programme on masonry panels subjected to diagonal compression tests is provided in Table 4.1. The first column shows the identification code assigned

to each set of samples. The letter 'x' corresponds to the serial number of the test. The unreinforced masonry samples used as references are indicated by the abbreviation 'URM'. The panel in which the reinforcement consists exclusively of the cementitious matrix used in the FRCM system is identified by the abbreviation 'CM', which stands for 'Cementitious Matrix'.

The other configurations are identified by an abbreviation consisting of the first letter of the material that constitutes the reinforcement fabric or mesh, followed by the system designation: FRCM or CRM. In the case of FRCM systems, the presence of connectors is indicated by the suffix '+c'.

The second column shows the number of tests carried out for each configuration. The third and fourth columns show the two materials that constituted the composite reinforcement system adopted for each series of tests, as classified and characterised in the previous chapter (Table 3.1). The final column specifies whether connectors are present, as described previously.

Table 4.1 Overview of the experimental campaign carried out as part of this thesis

ID	n. of tests	Fibre layer	Matrix	Connectors
URM_*x*	3	-	-	-
CM	1	-	M10P	-
C_FRCM_*x*	2	Carbon	M10P	No
G_FRCM_*x*	2	Glass	M10P	No
C_FRCM+c	1	Carbon	M10P	Fan-shaped
G_FRCM+c	1	Glass	M10P	Fan-shaped
G_CRM_*x*	2	GFRP1	M15P	LS1

4.2 Specimen geometry and preparation

The specimens subjected to diagonal compression tests consist of twelve medium-scale panels with approximately 1030 mm side lengths and a thickness of 150 mm (Fig. 4.1).

The masonry used to build the panels is designated MasP and consists of

calcarenite blocks from the Marsala area (CMP) and a lime-based mortar (M5PJ). This mortar was chosen from various commercially available options because it is lime-based and specifically recommended for building and restoring masonry made of natural stone, tuff, and mixed masonry. The stone units used to construct the panels measure 250×160×150 mm. The mortar joints were laid to an average thickness of approximately 10 mm.

During sample preparation, the high porosity of the *calcarenite* required the stone units to be pre-saturated to prevent absorption of the mixing water necessary for the chemical reactions involved in mortar curing. This procedure was particularly important to limit premature water loss from the mortar and to promote adequate hydration of the binder. After the initial curing period, the specimens were maintained under the same laboratory conditions until testing, ensuring a consistent curing process for all samples.

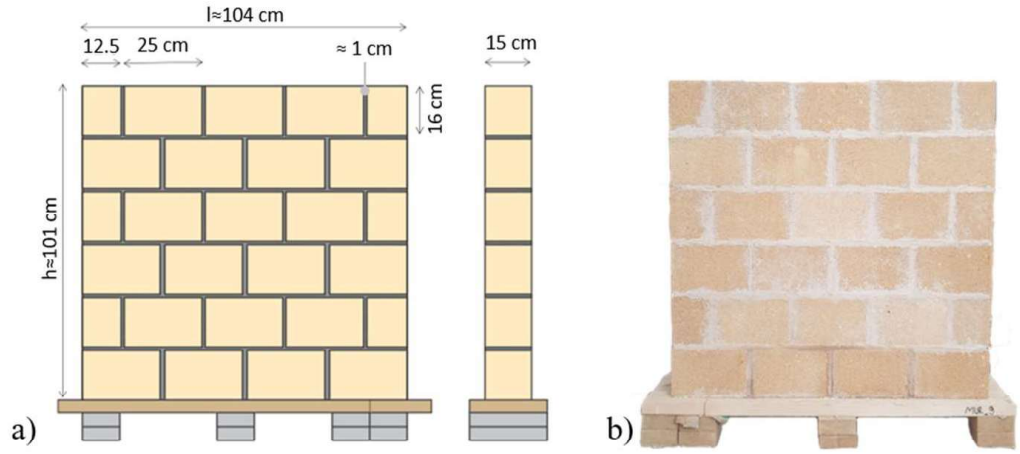


Figure 4.1 Masonry panels configuration; a) geometry common to all specimens; b) URM sample (photo taken during the experimental activities)

Prior to applying the reinforcement systems, the specimens' surfaces were treated with a water-based acrylic primer. This was used as a dustproofing and consolidating agent, which is specifically recommended for masonry substrates. The product is recommended by the manufacturer of the reinforcement systems and allows for the consolidation of the masonry surface

prior to application of the reinforcement, thereby improving the bond between the substrate and the composite system. Three of the panels manufactured according to this procedure were left unreinforced and used as control specimens. A further panel, identified by the code CM (Table 4.1), was instead reinforced by applying a single layer of mortar (M10P), corresponding to the matrix used in the FRCM system subsequently applied.

In order to ensure a uniform thickness of the mortar layer while maintaining an appropriate gap from the edges of the panel, special wooden frames were used. These elements also facilitated the application and levelling of the mortar (Figs. 4.2a, 4.2b). The matrix was applied to both surfaces of the panel, resulting in a uniform thickness of 10 mm (Fig. 4.2c).

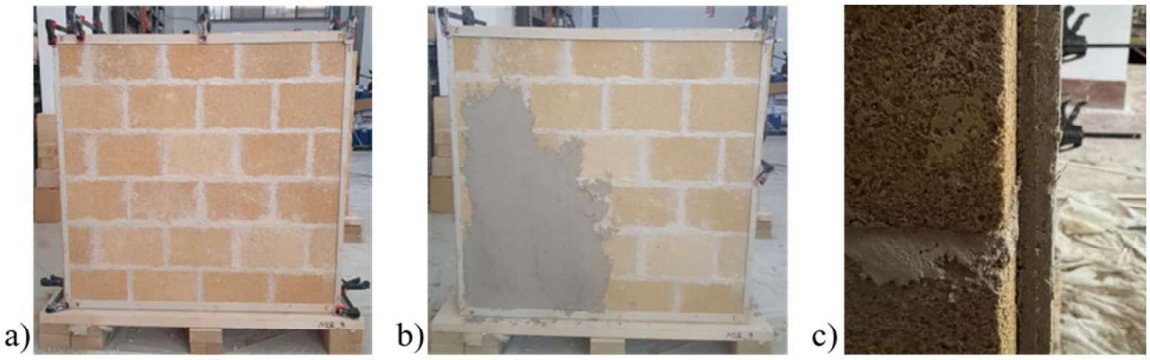


Figure 4.2 Sample CM, application of mortar layer (photos taken during the experimental activities): a) Installation of the wooden frame; b) application of the mortar; c) surface levelling

4.2.1 FRCM system configuration

The FRCM reinforcement system was applied to the panels once the bedding mortar had cured. The system was installed in a symmetrical configuration, i.e. on both surfaces of the panel. This approach aligns with previous studies that have demonstrated significant performance improvements when reinforcement is applied to both surfaces rather than just one [34].

The system was also installed 2 cm from the four edges of the panel to prevent load transfer directly to the reinforcement during the diagonal compression

test. This could lead to a localised concentration of stresses and possible premature detachment of the reinforcement layer [28][112].

Figure 4.3 illustrates the installation process for the FRCM reinforcement system. As an example, images showing the application of the carbon fibre fabric (C_FRCM_x series) are included; this procedure is also applicable to the glass fibre fabric system (G_FRCM_x series). First, a layer of mortar was applied to the previously moistened panel surfaces to a thickness of 5 mm (Fig. 4.3a). A uniform thickness was ensured by using a 5 mm thick, 20 mm wide wooden frame. After levelling the mortar layer, the surface was treated with an adhesion promoter to improve adhesion between the two materials at the fibre-matrix interface (Fig. 4.3b).

In configurations featuring connectors, the panel is pre-drilled before the reinforcement system is applied. Experimental outcomes have demonstrated that impregnating the fibres with an adhesion promoter enhances their compatibility with the matrix and improves the interaction between the fibres and the mortar [128][129]. The adhesion promoter used is a two-component, water-based product consisting of resins supported on a microcrystalline inorganic matrix. It has been specifically developed for impregnating glass and carbon fibre reinforcements.

The fabric was then applied (Fig. 4.3c) with light pressure to ensure adhesion to the underlying mortar layer. The fabric's ends were then clamped between the first frame, which had previously been installed, and a second frame to hold the fabric in place, ensuring correct alignment and tensioning of the filaments. A second layer of adhesion promoter was then applied to the fabric to promote adhesion to the outer layer of mortar (Fig. 4.3d). Finally, the second layer of mortar was applied using the second frame to ensure a uniform thickness of 5 mm (Fig. 4.3e). The outer layer of the reinforcement was levelled and smoothed until a total thickness of 10 mm was achieved (Fig. 4.3f).



Figure 4.3 Installation of the strengthening system on C_FRCM sample (photos taken during the experimental activities): a) first layer of mortar; b) adhesion promoter; c) carbon fabric; d) adhesion promoter; e) second layer of mortar; f) surface finishing up to a thickness of 10 mm

Particular care was taken during their installation to ensure proper alignment and full contact with the surrounding mortar. The same surface finishing procedure was then followed to obtain a uniform reinforcement layer suitable for the subsequent application of the DIC paint pattern.

For configurations involving connectors (G_FRCM+c and C_FRCM+c samples), the reinforcement system application process is similar to that described for other FRCM-reinforced samples. The system involves applying the primer to the masonry surface, followed by two layers of mortar, the fibre fabric, and the adhesion promoter, in these configurations too. The connectors were positioned at the locations defined by the adopted strengthening configuration and embedded within the reinforcement system to ensure adequate interaction between the strengthening layers and the masonry substrate.

Figure 4.4 shows the installation process for the connectors on the G_FRCM+c panel; the procedure is similar for the C_FRCM+c sample. Five through-type connectors were installed on the panel in accordance with the manufacturer's recommendations, which specify the use of five connectors per square metre.

The connectors were manufactured with a total length of 460 mm, of which 150 mm corresponded to the combined length of the two fans, totalling 300 mm. Of this, 150 mm were embedded within the masonry and 10 mm passed through the first layer of mortar (5 mm on each side). The connectors were fixed within the masonry using a two-component chemical anchor based on a hybrid vinyl ester resin, as recommended by the manufacturer (Fig. 4.4a). A layer of mortar mixed with an adhesion promoter was then applied onto which the fibre mesh was laid (Fig. 4.4b). Finally, the connectors were opened and secured to the fibre layer, completing the connection between the reinforcement and the masonry (Fig. 4.4c, d). The second layer of adhesion promoter was then applied to the mesh, followed by the second layer of mortar.

The external surface of the reinforcement was then levelled. The resulting panels were left to cure in the laboratory under natural environmental conditions of temperature and humidity. Prior to the tests, which were carried out 28 days after installation of the reinforcement system, the panel surfaces were prepared for application of the Digital Image Correlation (DIC) technique [131]. This technique requires a surface with high colour contrast to enable the optical acquisition and subsequent processing of deformations during testing. To this end, a speckled surface is generally created, consisting of a random black-and-white pattern that is defined according to the dimensions of the specimen, the type of test, and the acquisition system used.



Figure 4.4 Installation of the strengthening system with connectors on G_FRCM+c sample (photos taken during the experimental activities): a) fixing the connectors into the holes that were previously drilled; b) application of the first mortar, adhesion promoter and fabric; c) Opening of the fan-shaped connectors on the fabric; d) fixing on the grid.

One of the sample surfaces was painted with white matt water-based paint (Fig. 4.5a), and the speckle pattern was then applied using matt black spray paint (Fig. 4.5b). Surface preparation was carried out on only one side of the panel to allow dial gauges to be installed on the other side.

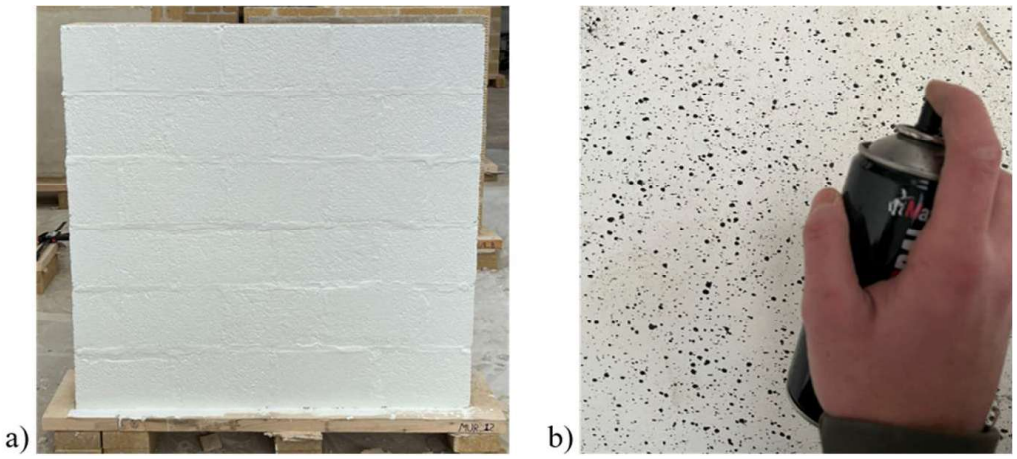


Figure 4.5 Surface preparation for DIC technique (photos taken during the experimental activities): a) application of white matte water-based paint; b) creation of the speckle pattern using matte black spray paint.

4.2.2 CRM system configuration

Once the bedding mortar in the panels had cured, the CRM reinforcement system was applied to the specimens in the G_CRM_x series. The reinforcement was installed in a symmetrical configuration on both sides of each panel. The total thickness of the reinforcement system is 30 mm on each side. Special wooden frames were also used to ensure the offset from the panel edges was maintained and to control the thickness of the reinforcement layer. As required by the application method, the CRM system was installed using connectors. Figure 4.6 shows the sequence of steps involved in applying the reinforcement system.

Before applying the CRM, holes were drilled into the panel for inserting the connectors. To allow the reinforcement system to connect to both surfaces of the panel, through-holes were drilled to ensure a minimum anchorage length

of 10 cm on each side. Five connectors were installed on each side of the panel in accordance with the manufacturer's instructions (Fig. 4.6a). The connectors were fixed using a two-component chemical anchor based on hybrid vinyl ester resin, as recommended by the manufacturer.

The connections were positioned to ensure full insertion into the first layer of 15 mm thick mortar (Fig. 4.6b). A further layer of mortar, also 15 mm thick, was then applied onto which the reinforcement mesh was subsequently laid (Fig. 4.6c). Particular care was taken during mesh installation to ensure correct connector insertion and connection within the reinforcement system (Fig. 4.6d). Finally, a second 15 mm-thick layer of mortar was applied (Fig. 4.6e), followed by smoothing and levelling until a total thickness of 30 mm was achieved (Fig. 4.6f). As in the previous case, the surface of the panels was then prepared for the Digital Image Correlation (DIC) technique, using a procedure similar to that described and shown in Figure 4.5.

4.3 Setup and acquisition systems of diagonal compressive tests

The test setup for the diagonal compression tests was determined based on the dimensions of the specimens to be tested and the estimated maximum load. The test procedure and interpretation of the results were carried out in accordance with the provisions of ASTM E519M-22 [27]. To acquire the experimental data, an MGC-PLUS data acquisition system and a computer dedicated to data management and recording were used. The MGC-PLUS device enabled the force applied by the hydraulic jack to be acquired, as measured by a load cell. Figure 4.7 shows the experimental set-up used to carry out the tests. Diagonal compression tests were carried out under load control. A load was applied at a rate of 0.01 kN/s using a hydraulic jack, and the tests proceeded through more than ten loading steps in accordance with the requirements of the standard.

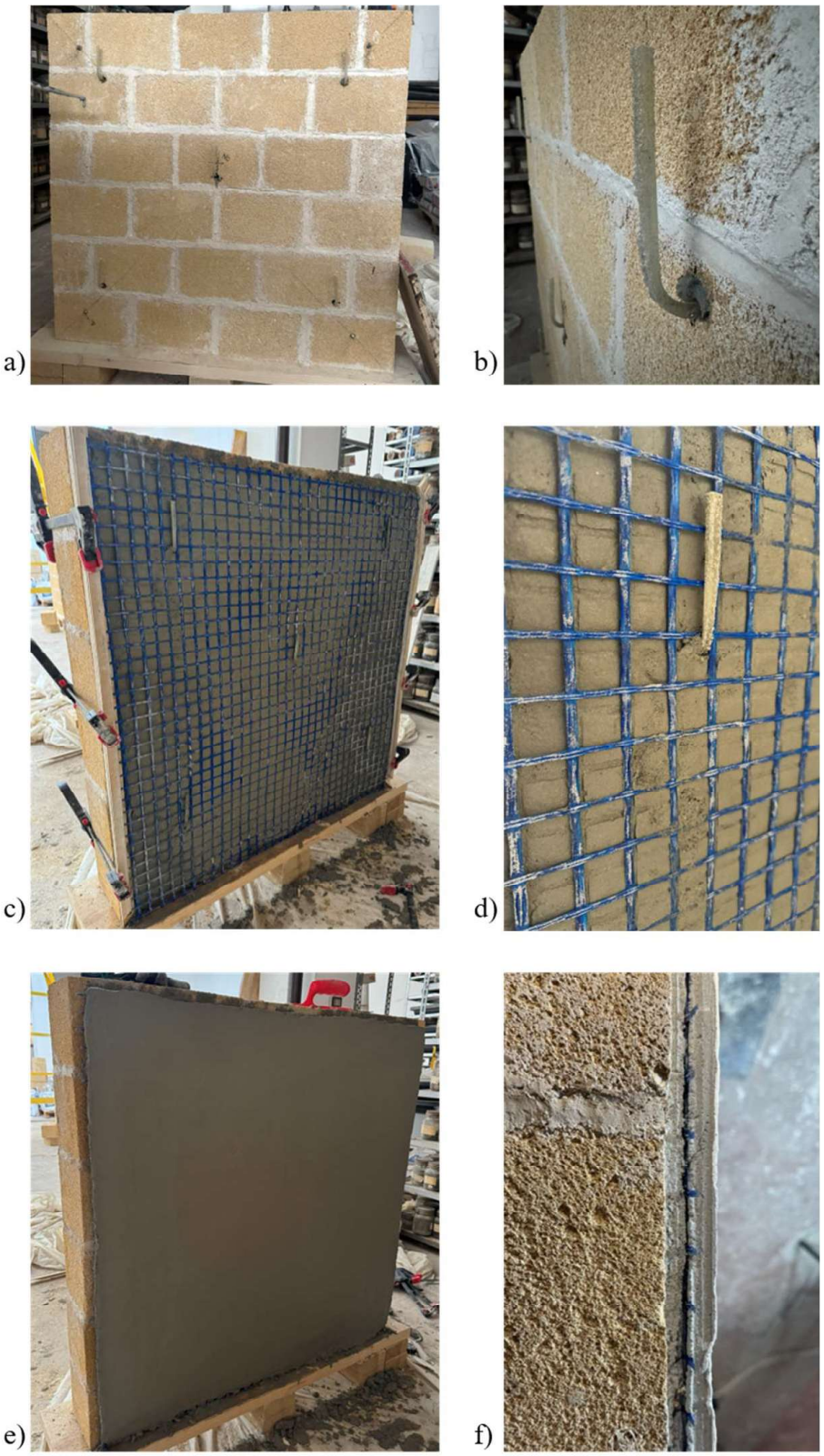


Figure 4.6 Installation of the strengthening system on G_CRM sample (photos taken during the experimental activities): a) connectors application; b) distance from the panel surface; c) first mortar layer and GFRP grid application; d) Check the connectors on the grid; e) second layer of mortar; f) surface finishing up to a thickness of 30 mm

For the test, the panels were rotated by 45°, as specified in the relevant standard, with a layer of gypsum plaster placed between the specimen and the upper and lower load shoes. This layer serves to smooth the contact surfaces, ensuring a more uniform distribution of stresses, and preventing local effects due to geometric irregularities.

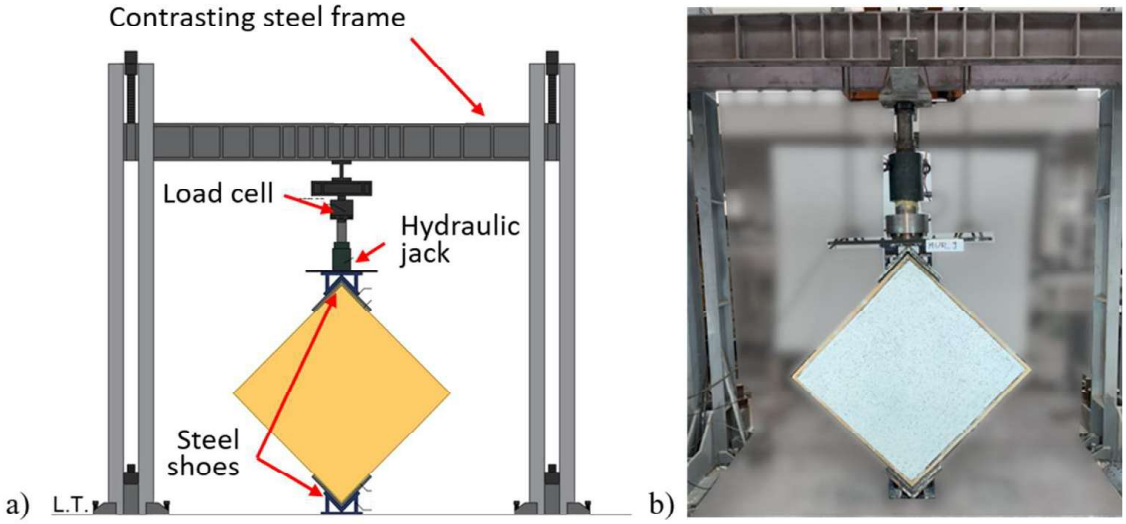


Figure 4.7 Diagonal compressive test set-up: a) Design; b) test set-up in laboratory (photo taken during the experimental activities)

The deformations required for interpreting the experimental results were recorded using appropriate measuring equipment. In particular, two dial gauges were installed on one of the specimen's surfaces: one was positioned vertically to measure shortening and the other horizontally to measure elongation (Fig. 4.8a). On the other hand, the opposite surface was prepared for the application of the DIC technique, as described previously (Fig. 4.8b). The decision to use two different measurement systems simultaneously stems from multiple considerations. Firstly, depending on how the specimen fracture occurs, which may be sudden, the devices could be damaged, resulting in the

loss of acquired data. Furthermore, the DIC technique enables contactless measurement and assessment of the full range of deformations on the observed surface. Finally, using two independent measurement techniques simultaneously allows the results to be compared, increasing the chance of successfully acquiring the experimental data. The two dial gauges were installed on the panels using threaded rods that were anchored directly into the masonry for the unreinforced specimens. In the case of the strengthened panels, to avoid interference with the reinforcement fabric, the dial gauges were installed using metal plates bonded securely to the outer surface of the reinforcement system. The positioning of the dial gauges was determined in accordance with the provisions of the ASTM E-519M-22 standard [27], with the measurement points arranged at a distance corresponding to at least 80 per cent of the diagonal length of the panels.

Regarding the application of the DIC technique, the experimental setup shown in Figure 4.8b was used for each test.

The 2D-DIC method requires a specific configuration in which the specimen must be positioned on a plane perpendicular to the direction in which the camera captures the images (Fig. 4.8b). White light sources were used for illumination to increase the contrast between the white and black areas of the surface speckle, to reduce shadows that could interfere with image processing and improve image quality.

A Nikon Z6 II digital camera with a 24-megapixel sensor was used to acquire the images, positioned approximately 2 metres from the panel, and the acquisition rate was set to one image every 3 seconds. The photographs were acquired using a constant aperture of f/4, while the ISO sensitivity and shutter speed varied within the ranges of 180–450 and 1/100–1/125 s, respectively, depending on the ambient lighting conditions during the different acquisition

sessions. Despite these variations, the resulting images maintained sufficiently consistent characteristics for the subsequent 2D-DIC analysis.

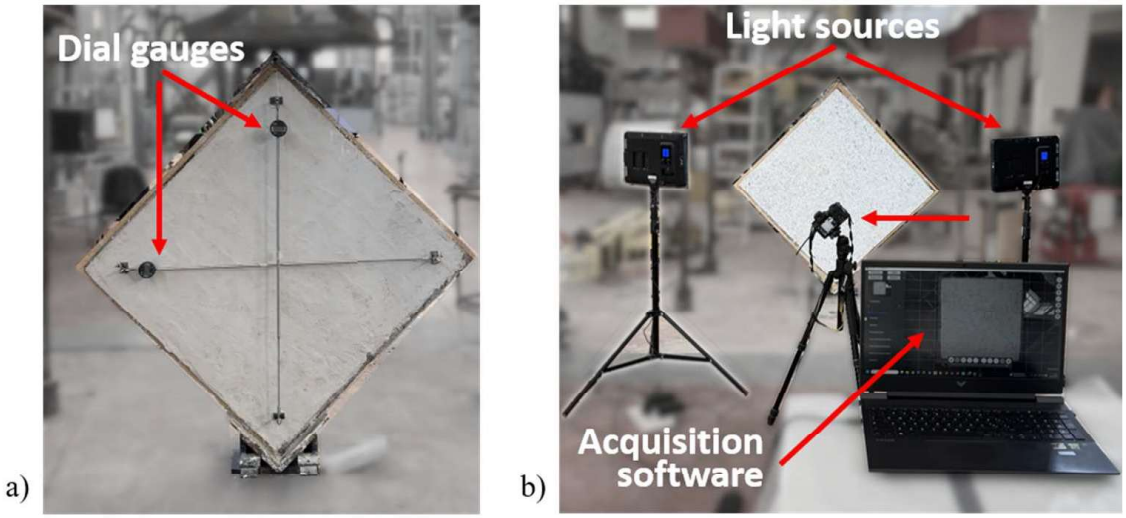


Figure 4.8 Acquisition systems (photo taken during the experimental activities): a) Dial gauges; b) Equipment for DIC technique application

4.4 Experimental results

The experimental results were assessed in line with the guidelines outlined in ASTM E519-22 [27]. According to this approach, the stress state at the centre of the panel is assumed to be characterised by pure shear.

This differs from the RILEM concept, which considers the panel to be a homogeneous, isotropic material characterised by a non-uniform stress state with simultaneous shear and normal stresses.

According to the interpretation of the stress state in ASTM E519, the maximum tangential stress corresponds to the panel's shear stress, τ_0, which is calculated using the following expression:

$$\tau_0 = \frac{P}{\sqrt{2}A_n} \tag{4.1}$$

where P represents the applied diagonal load and A_n is the net cross-sectional area of the specimen. The latter is calculated as $A_n = 0.5(w + h)t$, where w is

the width of the panel, h is its height and t is its thickness.

Shear strain γ, on the other hand, is calculated as follows:

$$\gamma = \frac{\Delta V + \Delta H}{L_g} \tag{4.2}$$

where ΔV represents vertical shortening, ΔH represents horizontal elongation, and L_g represents the measuring base of the dial gauges. A schematic representation of the test is provided in Figure 4.9, showing the specimen geometry (Fig. 4.9a), identified using the notation adopted by the ASTM standard, together with the measurements recorded during the test (Fig. 4.9b).

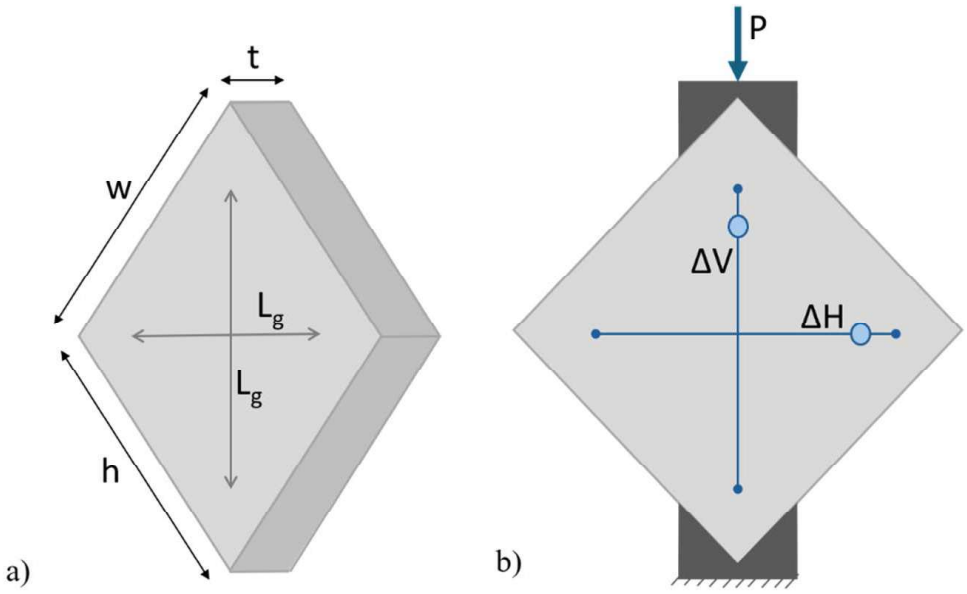


Figure 4.9 Schematic representation of the test setup (symbols according to ASTM E519-22): a) specimen geometry; b) measured quantities

The following sections present and discuss the results obtained from the experimental tests. In particular, failure modes of the specimens, stress-strain curves, and results obtained using the DIC technique will be discussed.

4.4.1 Failure modes

The failure modes exhibited by the panels when subjected to diagonal compression tests depended on the configuration analysed.

The unreinforced panels (URM_2, Fig. 4.10 and URM_3, Fig. 4.11) exhibited brittle failure, characterised by splitting into two parts along an almost vertical crack. Panel URM_2 (Fig. 4.10) exhibited a crack that primarily damaged the stone units and was associated with some slip at the horizontal mortar joints. Observation of the fracture surface revealed that the crack predominantly developed along the interface between the mortar and the block at the joints, showing a clear separation surface. In contrast, Panel URM_3 (Fig. 4.11) exhibited a mixed failure mode, primarily affecting the mortar joints and passing through the stone units only at certain points. Inspection of the fracture surfaces here too reveals a clear separation between the mortar and the block. As normally observed, the interface between the two materials is the weakest point in the system rather than the mortar itself.

A different failure mode was observed in URM_1 panel (Fig. 4.12). During the test, rotation within the plane of the panel was detected, leading to a concentration of stresses at the corner on the opposite side. Cracks originating from these areas caused the specimen to lose its equilibrium, resulting in the test being terminated prematurely.

In contrast, panels reinforced using FRCM and CRM systems exhibited different failure modes compared with unreinforced specimens.

The CM panel, which was reinforced exclusively using the matrix of the FRCM system, exhibited a failure characterised by the formation of a crack localised at the base of the panel (Fig. 4.13). Prior to the appearance of the main crack, detachment of the mortar layer was observed in the lower region, at a distance of approximately 40 cm from the panel's edge. No vertical cracks were detected in the reinforcing mortar layer.

The G_FRCM series panels exhibited cracks localised at the bottom of the panel and extending along its thickness (Fig. 4.14). These cracks are consistent with a compression failure mechanism and can be explained by the confining

effect of the reinforcement system in the in-plane direction, which limited the formation of the typical diagonal crack associated with tensile phenomena. Consequently, failure occurred in the orthogonal direction, indicating that sufficient compression had been applied to cause the masonry to fail. Inspection of the internal masonry at the end of the test revealed extensive damage, with the material in the affected areas almost completely reduced to dust, indicating that the local compressive strength had been exceeded.



Figure 4.10 Failure mode of URM_2 panel (photo taken during the experimental activities)



Figure 4.11 Failure mode of URM_3 panel (photo taken during the experimental activities)

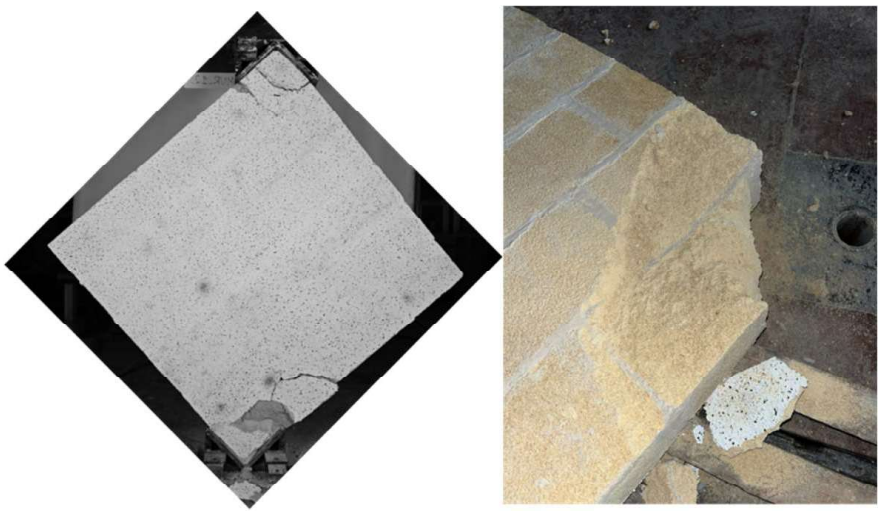


Figure 4.12 Failure mode of URM_1 panel (photo taken during the experimental activities)



Figure 4.13 Failure mode of CM panel (photo taken during the experimental activities)

The C_FRCM series panels (Fig. 4.15), on the other hand, showed premature collapse in one case (C_FRCM_1) due to failure of the lower panel corner in correspondence of steel shoe, resulting in the panel tipping over and termination of the test. In the second case (C_FRCM_2), a similar crack developed within the thickness of the panel near the upper edge. The premature failure in this case also prevented the test from being completed. An overall analysis of the results suggests that the reinforcement systems under consideration, and in particular the matrix used, exhibit mechanical properties

superior to those required by the low-quality masonry used as the substrate. This difference may lead to reduced interaction between the reinforcement system and the masonry, resulting in failure modes that do not always correspond to the expected behaviour of the reinforced element.

The C_FRCM+c panel, reinforced with carbon fibre fabric and connectors, exhibited behaviour similar to that of the C_FRCM series, with cracks developing within the panel's thickness and near the upper edge (Fig. 4.16). In this case too, the specimen failed prematurely.

By contrast, the G_FRCM+c panel, which was reinforced using a glass fibre fabric and connectors, exhibited different behaviour. The specimen showed widespread cracking of the reinforcement matrix along the diagonal of the panel, which is consistent with the behaviour expected in a diagonal compression test (Fig. 4.17). However, at the end of the test, a crack was observed that had propagated into the thickness of the masonry.

This different behaviour can be attributed to the presence of the connectors, which provide confinement to the masonry and promote better interaction between the substrate and the reinforcement system.

However, this effect appears to be less evident in the case of the C_FRCM+c system, probably due to the greater stiffness of the carbon fibre system. These results suggest that in cases where masonry substrates have low mechanical properties, less rigid systems, such as those with glass fibre fabric, may be more effective.

The panels strengthened with the CRM system showed similar failure modes, primarily characterised by the detachment of the reinforcement system (Fig. 4.18). However, in this case, the presence of connectors and the greater thickness of the matrix provided greater confinement of the masonry, resulting in a greater ability to limit transversal strains. Consequently, failure occurred primarily through the detachment of the reinforcement, with no significant

damage observed in either the thickness of the masonry or the matrix surface. Overall, the results demonstrate good adhesion between the FRCM and CRM systems and the masonry substrate. Furthermore, the presence of connectors can significantly improve the interaction between the masonry and the reinforcement system, particularly in the case of masonry characterised by low mechanical properties. The results also highlight the importance of selecting the appropriate stiffness and strength of the composite system according to the substrate's characteristics, favouring less stiff and less strong systems when applied to poor-quality masonry.



Figure 4.14 Failure mode of G_FRCM panels (photo taken during the experimental activities)

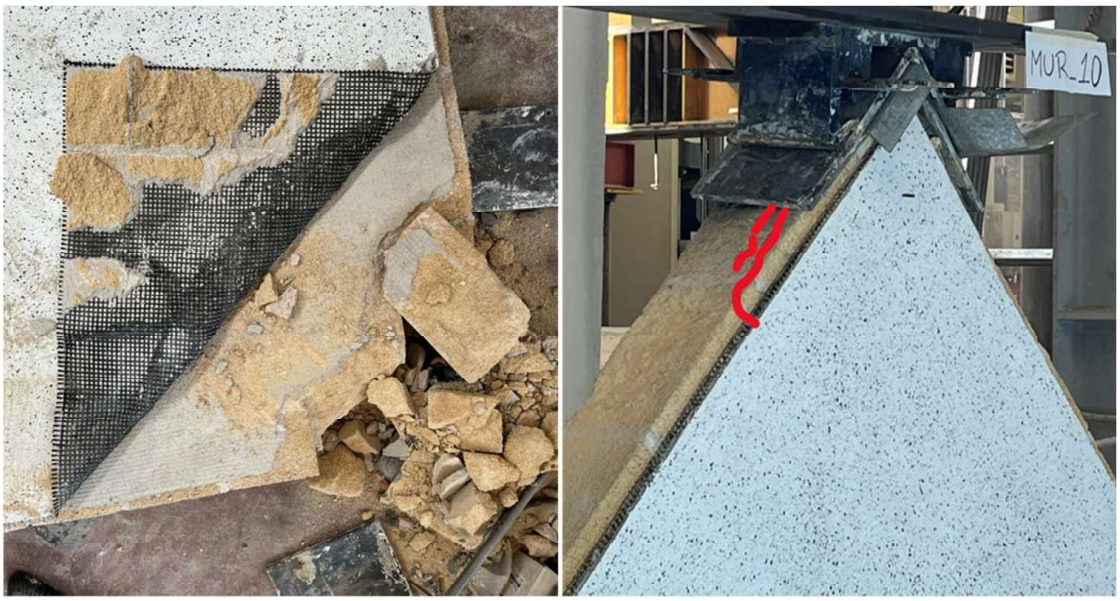


Figure 4.15 Failure mode of C_FRCM panels (photo taken during the experimental activities)



Figure 4.16 Failure mode of C_FRCM+c panel (photo taken during the experimental activities)

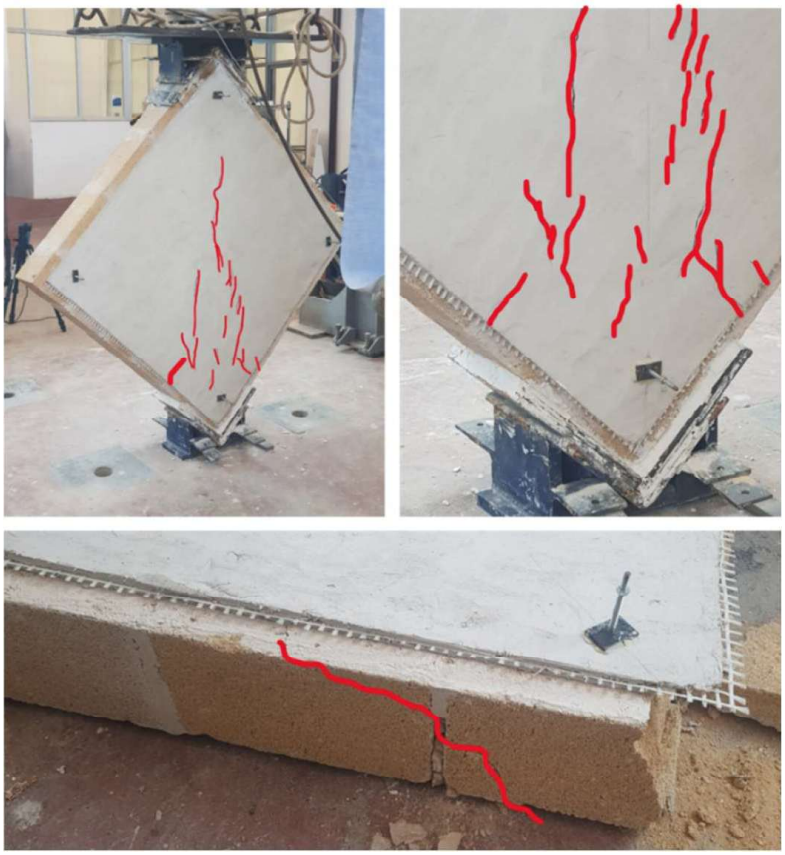


Figure 4.17 Failure mode of G_FRCM+c panel (photo taken during the experimental activities)



Figure 4.18 Failure mode of CRM panels (photo taken during the experimental activities)

4.4.2 Analysis of the main experimental results

The main results of the diagonal compression tests carried out on the unreinforced and reinforced panels are shown in Table 4.2. These results are presented in terms of maximum load P_{exp}, average load for each series of specimens, maximum shear stress τ_{max} (Eq. 4.1), shear modulus G, and the percentage increase in maximum load compared to the URM series. When the data are not available because it was not possible to calculate the corresponding value, the entry "n.d." is reported in the Table 4.2. The curves recorded during the test are reported in the following Section 4.4.3, together with the measurements obtained by DIC. Please note that for the calculation of the tangential stress, the nominal area was taken to be equal to that of the masonry, even for the reinforced panels. The shear modulus G was calculated as the slope of the secant line connecting the points on the shear stress–strain (τ–γ) curve corresponding to 5% and 30% of the maximum experimental shear stress, respectively [127]. The recorded values were obtained from measurements taken using dial gauges. The experimental curves obtained are therefore incomplete as the dial gauges were removed before the end of the test to prevent damage to the instrumentation. Consequently, analyses were performed based on the maximum load reached, the shear modulus G, which was calculated from the initial section of the curve, and the increases relative to the unreinforced configuration.

The first tests carried out were those used to characterise the unreinforced masonry. According to the procedure set out in ASTM E519, the URM_2 panel, which failed under diagonal tensile stress, reached a maximum shear stress of 0.59 MPa. In contrast, the URM_3 panel, characterised by a diagonal crack associated with slippage along the mortar joints, achieved a lower value of 0.41 MPa. The results reveal that all reinforcement systems result in an increase in maximum load compared to the unreinforced configuration. The

highest increases, which are comparable with one another, were obtained from panels reinforced with a cementitious matrix or glass fibre fabric alone. Although further experimental studies are needed to confirm these findings, the results suggest that the matrix plays a decisive role in the panel's shear response. Indeed, the maximum load achieved with the fabric present is essentially the same as that obtained with mortar alone. In contrast, the use of carbon fibre fabric, which is characterised by greater stiffness, appears to promote the premature onset of failure mechanisms, resulting in a lower maximum load than the other analysed systems.

Despite having a mortar thickness approximately three times greater than that of the FRCM system, the CRM system yielded results of the same order of magnitude. This result does not necessarily imply that an increase in matrix thickness has a negligible impact on shear response. Rather, the similar strength values may be attributed to the observed failure mode of the specimens, which was governed by the limited compressive strength of the masonry substrate. In this case, it is possible that the masonry acted as the limiting component of the system, preventing the thicker CRM matrix from contributing effectively. Overall, the results obtained suggest that stiffness of the strengthening system is probably the most significant parameter influencing the contribution of the reinforcement system. This suggests that, when assessing the shear contribution of composite systems, consideration should be given to both the fibre and the matrix contributions. The results obtained for the specimens strengthened with carbon textile (C_FRCM) show somewhat greater dispersion compared with those obtained for the glass textile (G_FRCM) and CRM systems (G_CRM). This behaviour may be partly related to the higher stiffness of the carbon textile reinforcement, which can promote a different stress transfer and, in some cases, lead to premature failure of the strengthening system. Furthermore, the connectors in FRCM system appear to

enhance the interaction between the reinforcement system and the masonry substrate, primarily affecting the mode of failure rather than significantly increasing the shear capacity. Finally, the results suggest that increasing the thickness of the matrix alone does not necessarily improve the shear behaviour of the reinforced masonry.

Table 4.2 Diagonal compressive tests results

SAMPLE ID	P_{exp} [kN]	$P_{exp,med}$ [kN]	τ_{max} [MPa]	G [MPa]	Incr. P [%]
URM_1	108.5	110.1 (CoV=18%)	0.49	1570	-
URM_2	130.7		0.59	n.d.	
URM_3	91.1		0.41	n.d.	
CM	180.4	-	0.82	1780	+38.9
G_FRCM_1	177.1	176.1 (CoV=0.7%)	0.83	n.d.	+37.9
G_FRCM_2	175.1		0.79	1690	
G_FRCM+C	182.8	-	0.83	n.d.	+39.5
C_FRCM_1	158.1	137.8 (CoV=20%)	0.72	2410	+20.1
C_FRCM_2	117.5		0.53	n.d.	
C_FRCM+c	151.5	-	0.69	n.d.	+27.3
G_CRM_1	173.7	174.1 (CoV=0.2%)	0.79	n.d.	+36.7
G_CRM_2	174.4		0.79	n.d.	

4.4.3 Digital Image Correlation Analysis (DIC)

To provide a thorough analysis of how the panels performed, the images acquired during the tests were processed using DIC with GOM Correlate software [132]. This software determines the strain field by comparing images captured at successive time points during the test. For this purpose, the

reference image is divided into a set of subsets (facets) characterised by a random distribution of light intensity resulting from the speckle pattern. The GOM Correlate algorithm is based on maximising the correlation between the reference image subsets and those of the deformed images using iterative optimisation procedures that enable displacements to be estimated with sub-pixel precision. The deformation fields are then derived from the spatial distribution of the displacements using appropriate numerical derivation procedures.

In the analysis, the entire panel surface was defined as the analysis surface (Fig. 4.19a). The images were captured at a resolution of 6048 x 4024 pixels. The camera was positioned approximately two metres from the sample, and the optical zoom was used to minimise the effects of perspective distortion. Given the sensor resolution and the actual dimensions of the panel, each pixel corresponds to approximately 0.31 mm of the sample's surface.

The measurement area was defined in the software by setting the two parameters that govern the analysis's accuracy: facet size and point distance. Facet size represents the size of the region used as a correlation unit. Smaller values allow for a higher spatial resolution, whereas larger values improve the robustness of the correlation, reducing the ability to describe local variations in the strain field. Point distance, on the other hand, represents the distance between the centres of two adjacent facets, determining the degree of overlap between correlation regions. Greater overlap ensures better continuity of the displacement field and reduces measurement noise.

Two virtual extensimeters were also defined on the same surface (Fig. 4.19b): one was oriented vertically and the other horizontally. They were positioned in a configuration similar to that of the dial gauges used during the experimental tests to allow direct comparison of the measurements obtained using the two acquisition techniques.

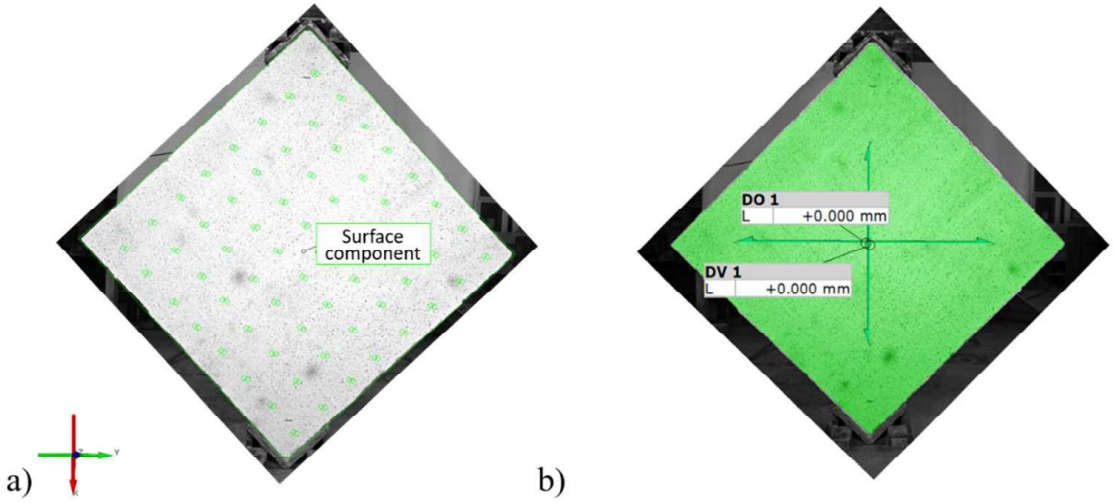


Figure 4.19 Example of DIC components (photos taken during the experimental activities): a) surface component; b) virtual extensimeters

Virtual extensimeters results

The results of the diagonal compression tests are presented in the form of shear stress-vertical strain and shear stress-horizontal strain curves. These results were obtained by processing images acquired using the DIC technique with virtual extensimeters. The graphs are divided into test series and, for each configuration, the data acquired using dial gauges is also shown, denoted by "dg" in parentheses (Figs. 4.20–4.25). Since the envelope of the results obtained for the reference specimens URM are reported in each graph, and a comprehensive comparison of all the curves is provided at the end of the present Section, different scales are adopted for the x-axis to improve the clarity and readability of the curves. Please note that the dial gauges curves are incomplete as the instruments were removed before the end of the test to prevent damage.

Figure 4.20 shows the curves obtained for the unreinforced panels in terms of shear stress versus vertical and horizontal strains. There is good agreement between the curves obtained using the DIC technique and those obtained from the dial gauges. This confirms the reliability of the measurement system and the absence of significant out-of-plane mechanisms during the tests. As

expected, vertical deformations are greater than horizontal ones.

Figure 4.21 shows a comparison of the CM panel reinforced using only the cementitious matrix. The same graph also shows the range corresponding to the experimental results obtained for unreinforced panels. As it can be seen, the system maintains the panel's initial stiffness almost unchanged, while the maximum load capacity increases by around 40%, even without the reinforcing fabric. Once again, the behaviour remains essentially brittle, with a very pronounced post-peak phase characterised by a rapid load drop.

Figure 4.22 shows comparisons for the G_FRCM series, again compared with experimental results for unreinforced panels. For G_FRCM panels without connectors, the failure mode is not typically shear failure; however, the system allows a higher maximum load to be achieved than in the unreinforced configuration. No substantial changes in initial stiffness are observed; however, the reinforced panels begin to exhibit greater deformability after peak stress is reached. This behaviour is even more evident in the G_FRCM+c specimen, indicating that the presence of connectors increases both the deformability and the load-bearing capacity of the panel.

Comparisons relating to the C_FRCM series (Fig. 4.23) indicate that stiffness increases slightly more significantly than strength when compared with glass-fibre-reinforced panels. As in the previous case, the reinforcement system appears to provide the panel with limited additional capacity for deformation. The presence of connectors (C_FRCM+c) does not result in any significant differences compared to the configuration without connectors.

The final comparison relating to the CRM system (Fig. 4.24) shows an increase in both stiffness and load-bearing capacity compared with the unreinforced configuration. The behaviour also exhibits moderate deformation capacity after the maximum load is reached; however, the post-peak phase is characterised by a sudden load drop, with no significant increase in overall deformability.

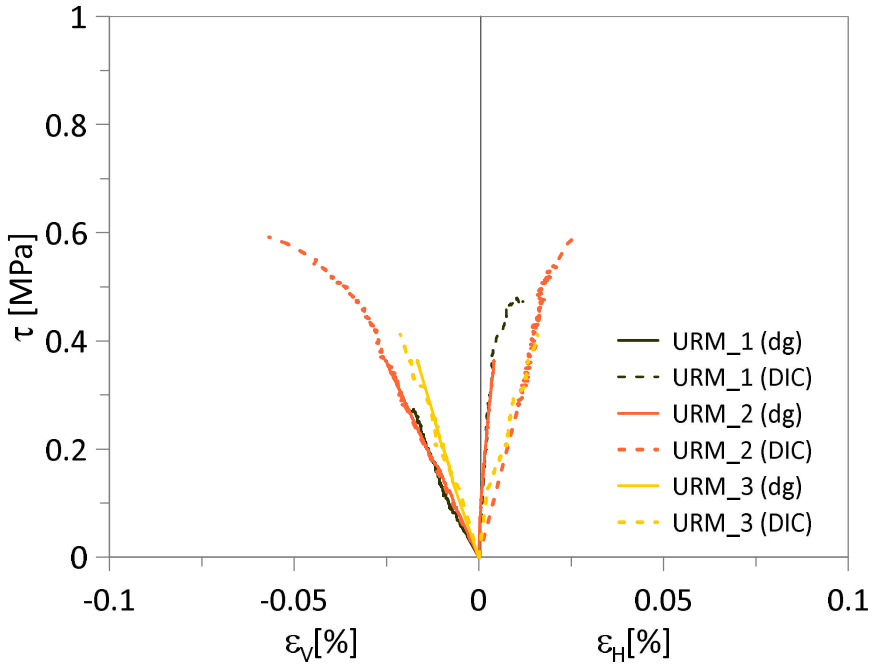


Figure 4.20 Shear Stress-Vertical/Horizontal strain curves of URM series

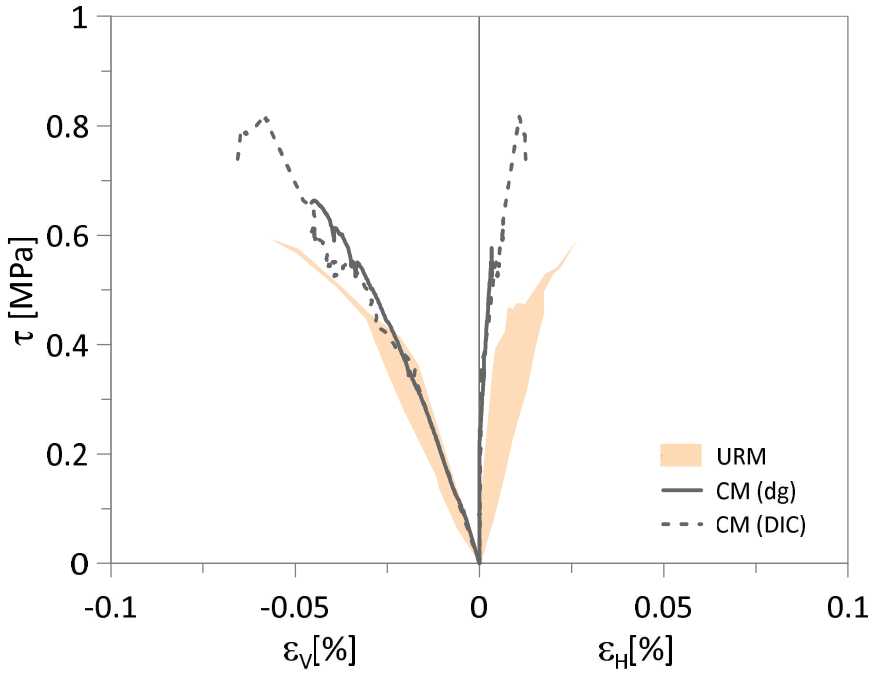


Figure 4.21 Shear stress -Vertical/Horizontal strain curves of the CM panel

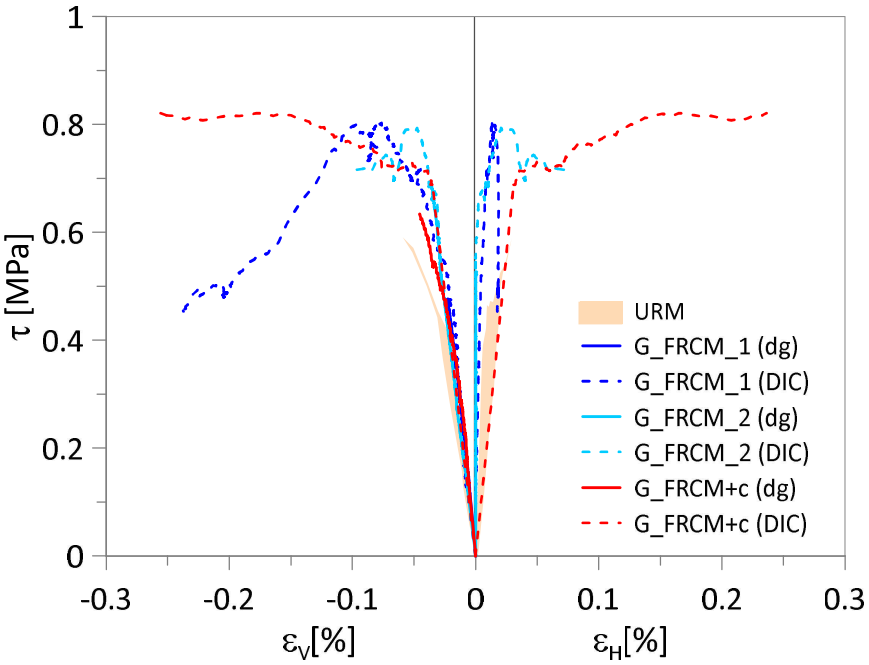


Figure 4.22 Shear stress -Vertical/Horizontal strain curves of G_FRCM series

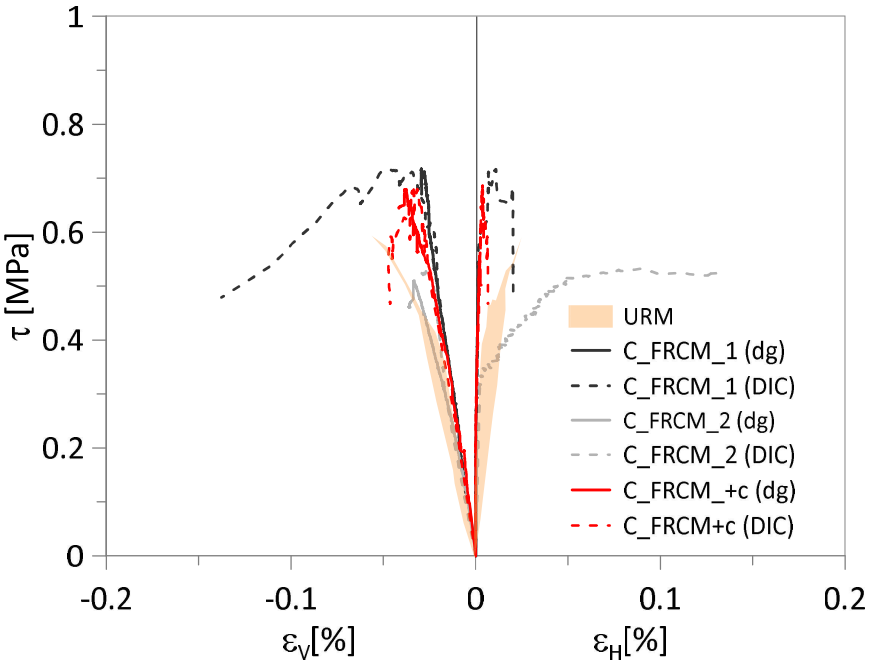


Figure 4.23 Shear stress -Vertical/Horizontal strain curves of C_FRCM series

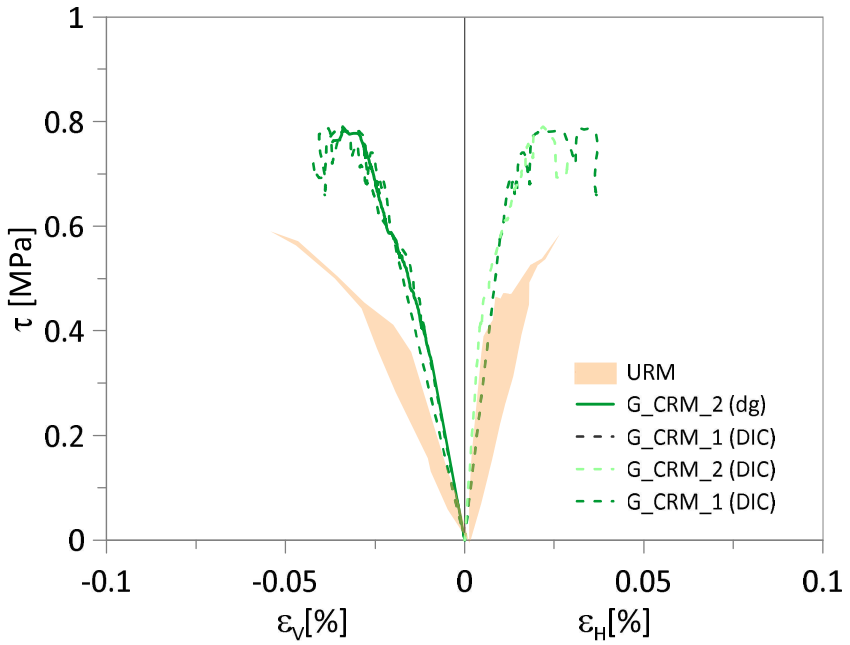


Figure 4.24 Shear stress -Vertical/Horizontal strain curves of G_CRM series

Figure 4.25 shows the shear stress–shear strain diagrams for all the panels for a comprehensive comparison between all the configurations analysed. Shear stresses and shear strains values were calculated using Equations 4.1 and 4.2 respectively. This graph is presented on two different scales: the first allows the differences in shear strain to be seen more clearly, while the second highlights the differences in stiffness and, consequently, in shear modulus G. Overall, the results obtained suggest that the panels belonging to the G_FRCM series exhibited the most favourable behaviour. In all cases analysed, the FRCM matrix showed no signs of detaching from the substrate, suggesting good compatibility between the reinforcement system and the masonry. However, the results also suggest that the mechanical performance of the reinforcement systems exceeds that required by the substrate for the type of masonry used, thereby preventing the full potential of the composite material from being exploited. In terms of stiffness, the greatest increases were observed in the C_FRCM and G_FRCM series, while the panels in the G_FRCM series exhibited the best shear deformability in the nonlinear range.

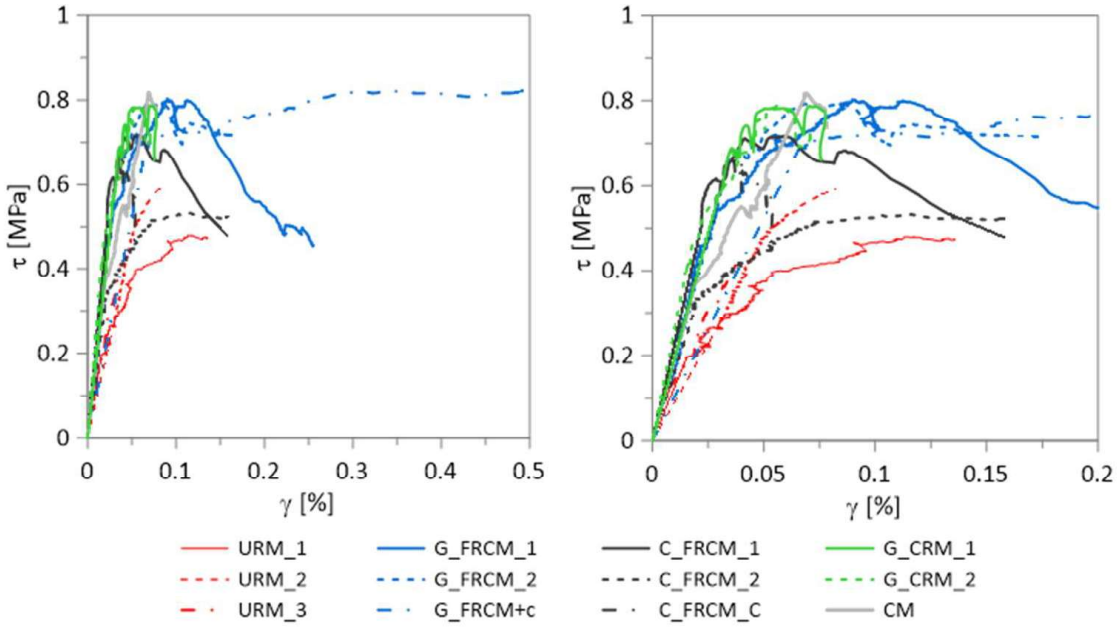


Figure 4.25 Shear stress vs shear strain curves (two different abscissa maximum values are used, for the same data)

Surface component analysis results

Analysing the strain field over the entire surface of the panel produced significant results, enabling the evolution of strains to be correlated with the different load stages applied during the test. Some representative examples of the DIC analysis are shown below, illustrating the evolution of the crack pattern from the pre-peak phase to the post-peak phase (Figs. 4.26–4.29). Figures show a graph in which the evolution of vertical shortening δ_v measured on the specimen surface as a function of the applied load P is plotted. Three points, labelled A, B and C, are identified along the load–vertical shortening curve, corresponding to three selected loading steps. The ε_x strain maps obtained from the DIC analysis at the three loading steps are also shown in the same figure. This provides a way of relating the evolution of the strain distribution to the corresponding loading conditions.

Figure 4.26 shows the results for the unreinforced URM specimen. The panel exhibited a failure mode characterised by cracks developing predominantly

along the mortar joints. Using the DIC technique, it was possible to correlate the evolution of the strain pattern with the various loading stages. This highlights that the first strain concentrations occur at the joints at load values close to 60 kN. As the load increases, these concentrations evolve progressively until the final crack forms across the entire diagonal of the panel. Low amounts of compressive strain are also observable near the upper and lower edges of the panel, at the points of contact with the ends of metal shoes.

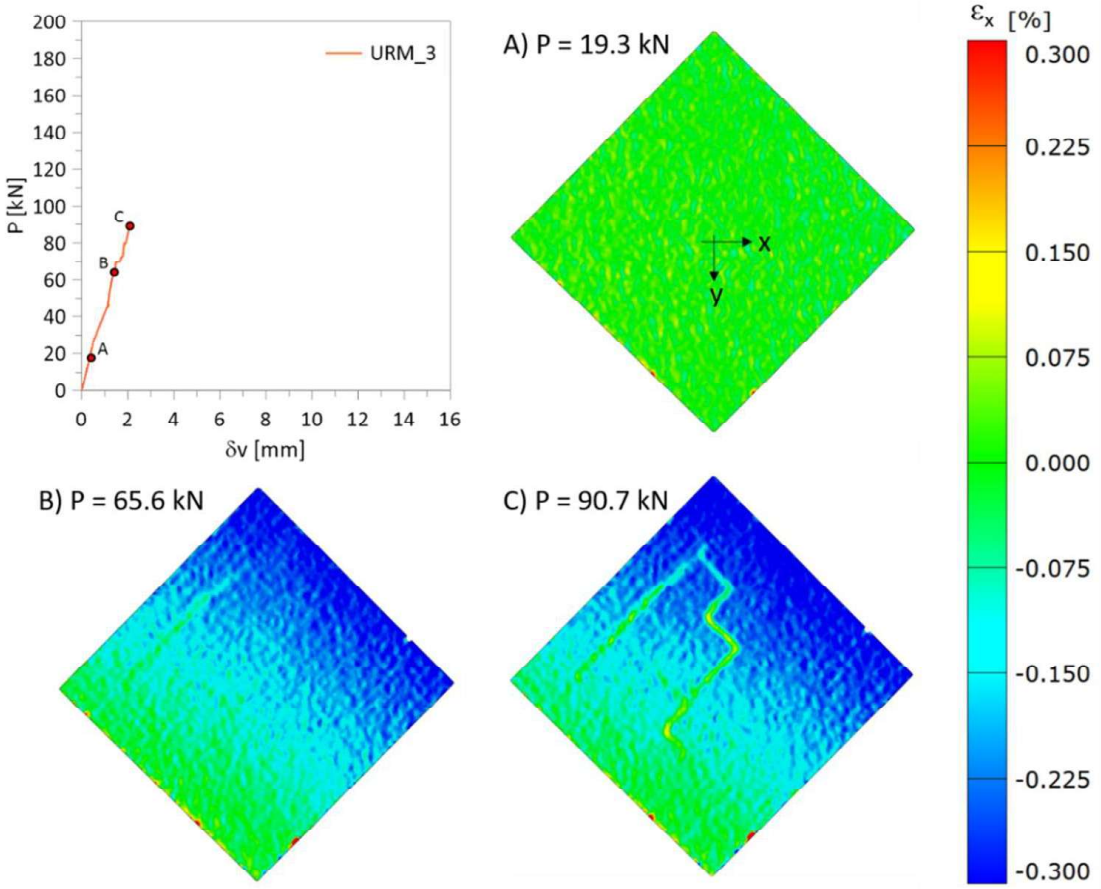


Figure 4.26 Strain pattern of URM_3 specimen

Figure 4.27 shows a summary of the results obtained for the G_FRCM+c panel. In this case, it was particularly significant to monitor the development of cracking on the surface of the reinforcement system. The first cracks in the matrix appear at the end of the initial, almost linear section of the experimental curve. Subsequently, once the maximum load has been reached and exceeded,

the panel continues to deform, and the cracking progressively propagates along the surface of the mortar. The cracks are predominantly aligned along the compressed diagonal of the panel and appear to follow the pattern of the mortar joints in the underlying masonry. Some crushing at toes seems also present.

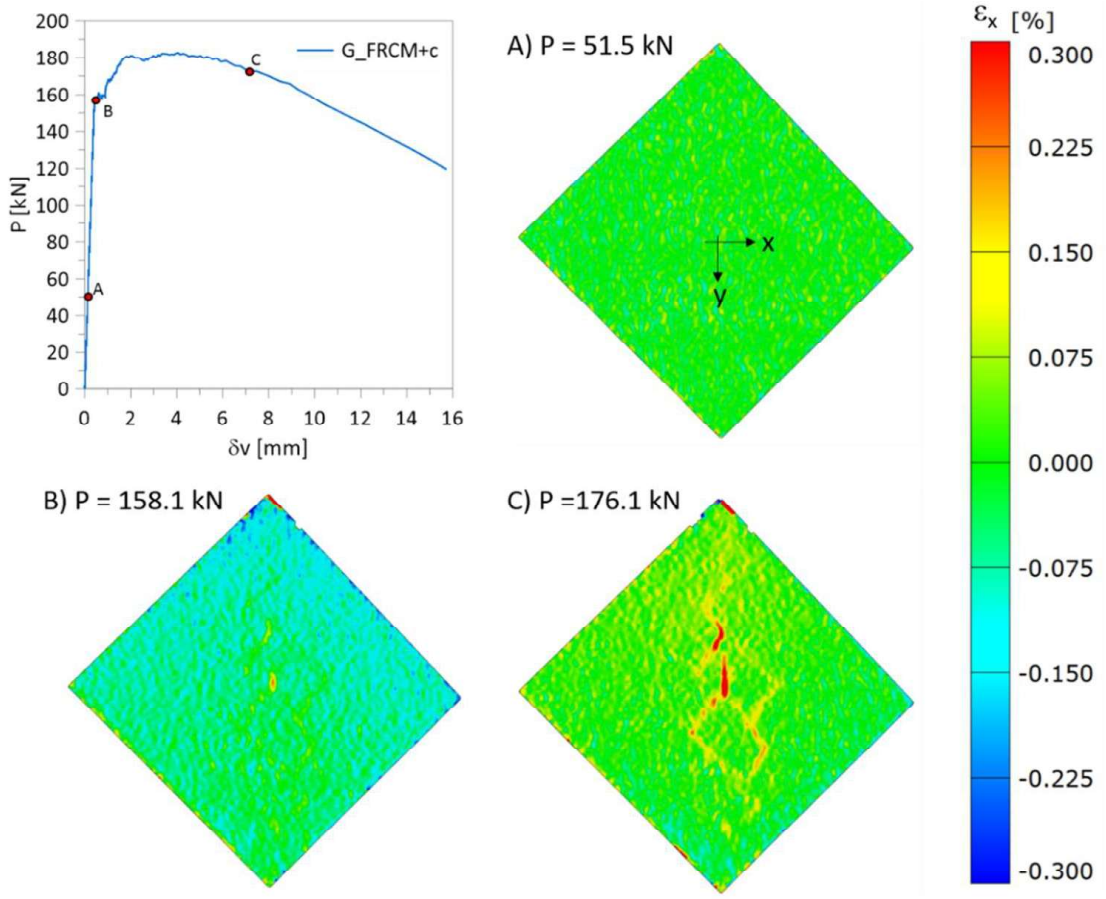


Figure 4.27 Strain pattern of G_FRCM+c specimen

Figure 4.28 shows the results obtained for panel C_FRCM_1. In this case, collapse occurred as a result of the masonry failing under compression. Consequently, it was not possible to observe the formation of a crack pattern on the surface of the reinforcement. However, analysis of the strain field confirmed the absence of surface cracks in the matrix and enabled the area near the edge of the panel where the maximum strain concentration was recorded to be identified more accurately. This area corresponded to the crack in the thickness observed during the test.

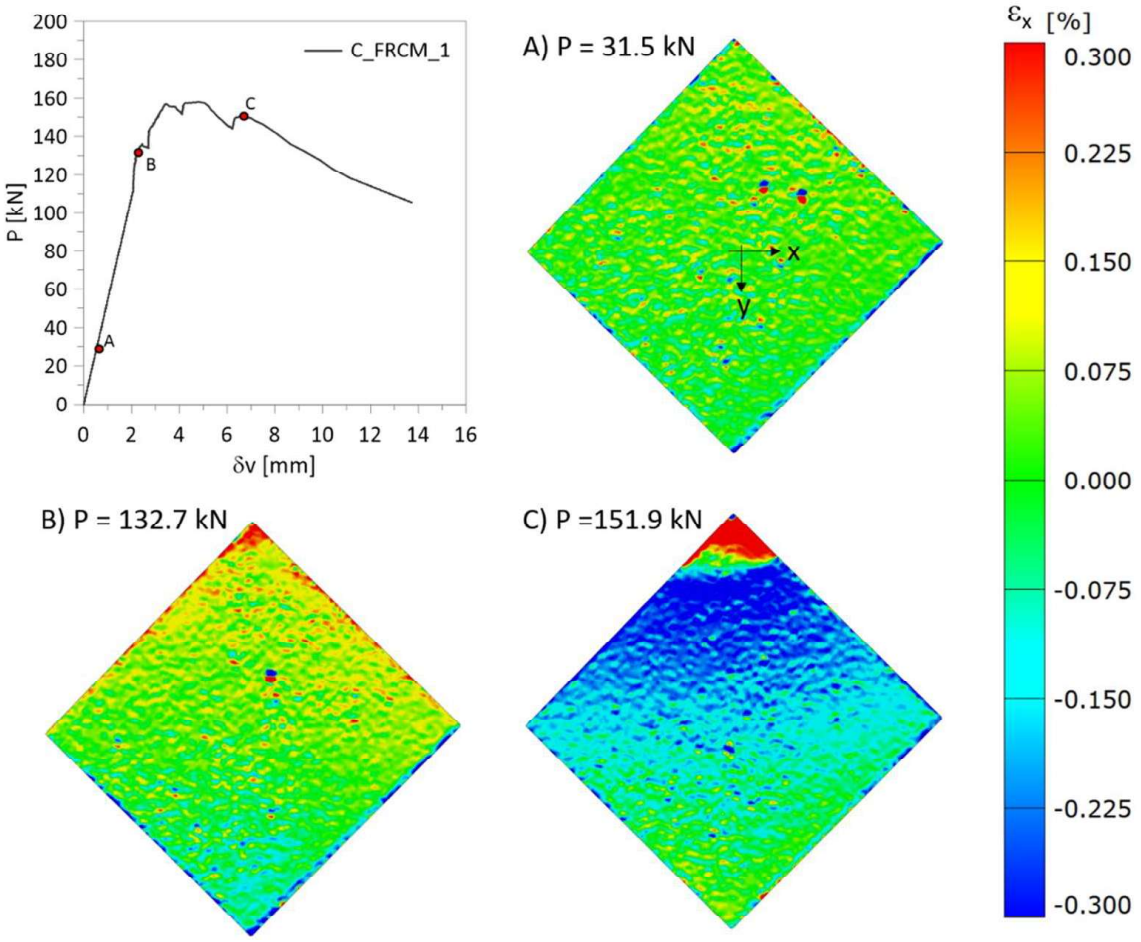


Figure 4.28 Strain pattern of C_FRCM_1 specimen

Similar comments could be made on specimen G_CRM_1, for which the results are shown in Figure 4.29. Once again, the DIC analysis confirmed the absence of cracks on the surface of the reinforcement system. The strain map highlights a zone extending along the entire perimeter of the panel, where the measured strains differ from those observed over the rest of the surface. This zone corresponds to the 2 cm-wide area where the strengthening system was not applied. The difference in the measured strains therefore indicates a different mechanical response between the masonry panel and the strengthened surface, highlighting the interaction between the two. The analysis also enabled the area where the detachment of the reinforcement system began to be identified with greater accuracy, as well as the region of the masonry affected

by compressive failure. It is useful observe that, the DIC technique proved to be an effective tool for interpretation of the experimental results. As well as enabling non-contact measurement of displacements, it allowed monitoring of the crack pattern evolution throughout the entire test. This provided essential support for interpreting collapse mechanisms and validating the conclusions drawn in this study.

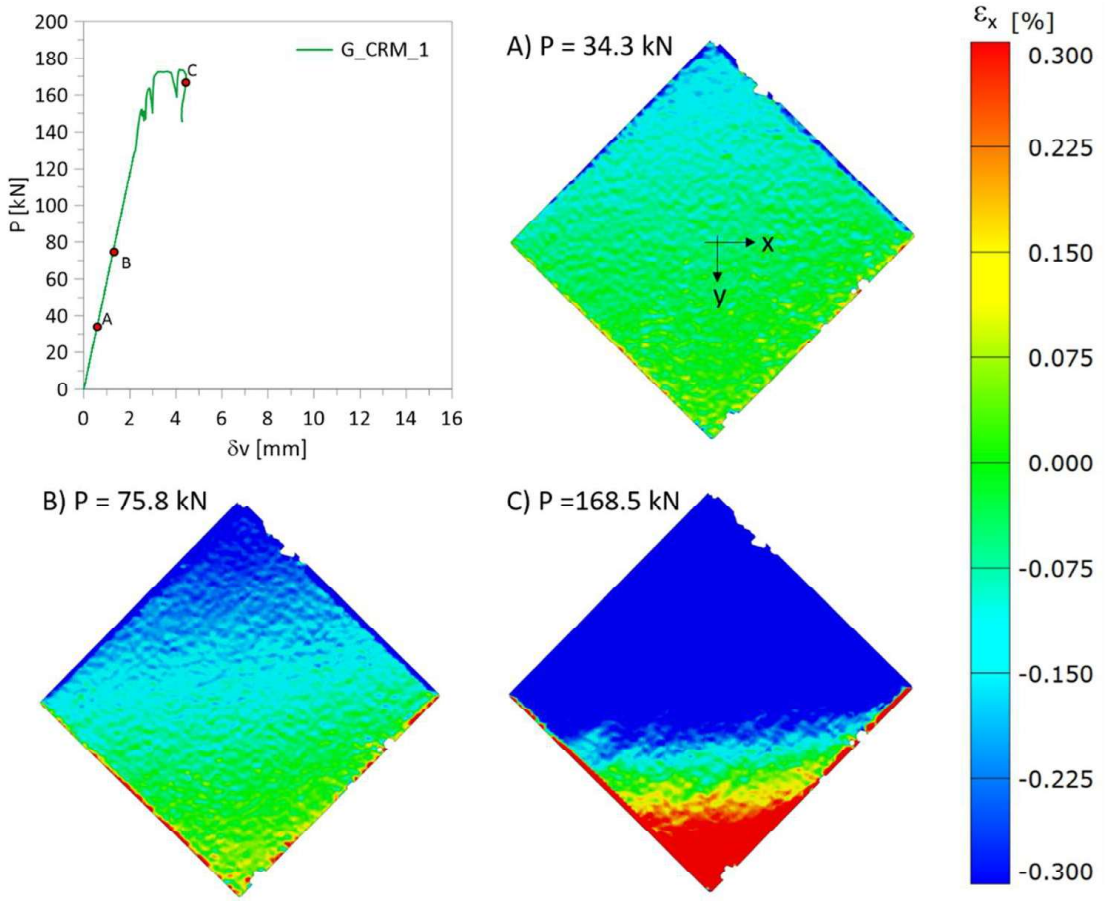


Figure 4.29 Stain pattern of G_CRM_1 specimen

4.5 Comparisons with analytical outcomes

The experimental results were compared with the analytical predictions from the formulations proposed in the current Italian guidelines [18][48][49][18]. In particular, CNR DT 215 [18]is the main Italian technical reference for the design and assessment of FRCM-strengthened structures. Issued by the Italian

National Research Council (CNR), it provides instructions for the design, execution and control of structural strengthening interventions using FRCM composites, including the strengthening of masonry structures. It provides that the shear strength of the reinforced panel $V_{t,R}$ should be evaluated as the sum of two contributions according to the following expression:

$$V_{t,R} = V_t + V_{t,f} \tag{4.3}$$

where V_t is the contribution of the unreinforced masonry and $V_{t,f}$ is the contribution provided by the reinforcement system. The contribution of the unreinforced masonry was determined by applying the formulas outlined in the capacity models for masonry elements as set out in the Italian Technical Standards [48] according to the Italian Circular No. 7/2019 by Ministry of Infrastructure and Transport [49]. To assess differences between experimental and predicted results in the absence of tests, parameters in the formulations were set to values in Tables C8.5.I and C8.5.II of the Italian Circular [49], for masonry of regular soft stone blocks. To calculate the contribution of the reinforcement system, the formulation proposed in CNR DT 215 was adopted:

$$V_{t,f} = \frac{1}{\gamma_{Rd}} n_f t_{Vf} l_f \alpha_f \varepsilon_{fd} E_f \tag{4.4}$$

where:

- γ_{Rd} is the partial model coefficient, assumed to be equal to 2 based on the current state of knowledge;
- $n_f t_{Vf} l_f$ represents the equivalent area of the shear-resistant reinforcement, where n_f is the total number of reinforcement layers applied to both faces of the wall, t_{Vf} is the equivalent thickness of a single layer of fabric, and l_f is the effective dimension of the reinforcement measured orthogonally to the direction of shear;

- α_f is the reduction factor that accounts for the reduction in the tensile strength of the fibres under shear stress, assumed to be 0.8;
- ε_{fd} is the maximum design strain of the fabric;
- E_f is the elastic modulus of the dry fabric.

According to this approach, the shear strength of the reinforced panel is therefore evaluated as the sum of the contributions from the masonry and the FRCM system. Using the mechanical properties stated in the manufacturers' technical data sheets, the contribution of the reinforcement is 284.4 kN for the carbon fabric system and 34.8 kN for the glass fabric system. The obtained values are shown in Table 4.3. A range of values is reported in the column presenting the analytical results, as the contribution of the unstrengthened masonry was calculated based on the values provided in the tables of the Italian Circular No. 7/2019 [49]. These tables provide two limiting values for the relevant masonry properties, resulting in a corresponding range of analytical estimates. The analyses were conducted specifically for FRCM systems, as there are currently no analogous regulatory formulations available for predicting the load-bearing capacity of CRM systems.

Table 4.3 Experimental vs analytical comparisons

ID		Experimental	Analytical	Exp./An.
URM	P_{max} [kN]	110.1	35.1 - 65.9	1.67 - 3.1
	τ_{max} [MPa]	0.46	0.16-0.30	1.67 - 3.1
	G [MPa]	1568	640-800	1.96 - 2.45
C_FRCM	P_{max} [kN]	137.8	319.5 – 350.3	0.39 - 0.43
	τ_{max} [MPa]	0.62	1.45-1.59	0.39 - 0.43
	G [MPa]	2417	-	-
G_FRCM	P_{max} [kN]	176.1	69.9 – 100.7	1.74 - 2.51
	τ_{max} [MPa]	0.80	0.31-0.45	1.74 - 2.51
	G [MPa]	1698	-	-

The comparison shows that the shear strength of unreinforced masonry is generally underestimated by the analytical formulations considered. Although significant, this difference is consistent with the conservative nature that generally characterises the formulations adopted for design purposes.

For reinforced panels, the comparison between the experimental results and the analytical predictions is influenced by the failure mode observed during the tests. In most cases, failure occurred when the compressive strength of the masonry was reached, rather than through the formation of the typical diagonal cracking associated with this type of test. Consequently, the analytical formulations, which are primarily intended to estimate shear capacity, may not be able to fully represent the actual load-bearing mechanism observed experimentally. This is particularly evident for panels reinforced using the C_FRCM system, for which the analytical prediction exceeds the experimental strength. For panels reinforced using the G_FRCM system, however, the analytical formulation provides a conservative estimate compared with the experimental results. In this case, by adding the contribution of the reinforcement system $V_{t,f}$ (Eq. 4.4) to the shear strength of the unreinforced masonry obtained by experimental test (Tab. 4.3), a value of approximately 160 kN is obtained. This value is still lower than the capacity measured experimentally but provides a more reasonable estimate that is more consistent with the results obtained using the formulae set out in the standards.

In the case of the G_FRCM+c panel with mechanical connectors, the formation of the typical diagonal cracks suggests that the comparison with the analytical prediction is more reliable. The conservative nature of the formulation is confirmed here, once again. The observed discrepancy compared to the expected results could also be attributed to the similarity between the compressive strength of the masonry and the shear strength of the reinforced panel, which may have limited the reinforcement system's actual contribution.

This behaviour could be attributed to the relatively low quality of the masonry compared to the performance of the reinforcement, meaning that the masonry's strength could be the limiting factor in the panel's overall response.

Considering the failure modes observed experimentally, a comparison with the compressive strength of the masonry appears to be more appropriate for assessing the actual capacity of the strengthened panels. The CNR DT 215 document states that if the fibres are oriented orthogonally to the shear direction, the shear force applied must not exceed the diagonal compressive strength of the masonry expressed by the following equation:

$$V_{t,c} = 0.25 * f_{md} * t * d_f \quad (4.5)$$

where f_{md} represents the design compressive strength of the masonry, t the wall thickness and d_f the distance between the compressed face of the masonry and the tensile face of the FRCM reinforcement. For this study, assuming a compressive strength of 3.59 MPa, the value of $V_{t,c}$ is 156 kN. However, the prediction remains conservative. In the case of the panel G_FRCM+c, for which no compressive failure of the masonry occurred, the analytical formulation nevertheless provides a limit value that is lower than that obtained experimentally. This comparison therefore confirms the conservative nature of the formula, highlighting that the analytical estimation remains lower than the capacity experimentally observed when the response is not governed by compressive failure of the masonry.

Another aspect to be considered in the CNR DT 215 formulation is that the matrix's contribution is not explicitly considered when evaluating the panel's shear strength. As the experimental results of this study have shown, the matrix plays a fundamental role in the overall behaviour of the reinforcement system and the strength it provides to the panel. These results highlight the importance of accounting for the interaction between the fibres, the matrix and the masonry

substrate when evaluating the strength of composite strengthening systems, as demonstrated by the comparison between the analytical predictions and the experimental observations. Taking these factors into account could enable a more accurate estimation of the strengthening system's contribution to the panel's overall strength.

4.6 Comparisons with the literature database

To verify the consistency of these findings with the results of diagonal compression tests reported in the literature, a collection of experimental data was organised [28]–[36], [72]–[126]. The data were collected and catalogued, along with the main geometric and mechanical parameters affecting the panel's response. A summary of the key data and literature references is provided in Appendix A. Next, these findings are briefly described and some considerations based on the discussion in the previous section are offered.

The database of diagonal compression tests consists of the results of 746 tests performed on unreinforced masonry and masonry reinforced with either mortar or FRCM/CRM systems. For each test, data were collected on the geometry of the specimens, the configuration of the reinforcement system and the mechanical properties of the masonry, fabrics and matrices of the reinforcement systems, as well as the diagonal compression test results. The tests included in the database cover a range of specimen geometries, masonry types and mechanical properties, as well as different strengthening configurations. However, the results were not classified according to specimen geometry, as the comparison was primarily based on normalised and dimensionless quantities, such as shear stress values, which allow the comparison between results obtained from specimens with different geometries. The variability in masonry properties and strengthening configurations was instead considered when interpreting the trends observed

in the database. Following section briefly outlines the main characteristics identified for the various tests collected. For each test characteristic, the percentage of occurrence in the database is reported, calculated relative to the total number of tests.

Figure 4.30 illustrates the types of masonry present in the database of collected test results. This reveals a wide variety of materials, with solid clay bricks and soft rock predominating, while other types account for less than 10% of the total.

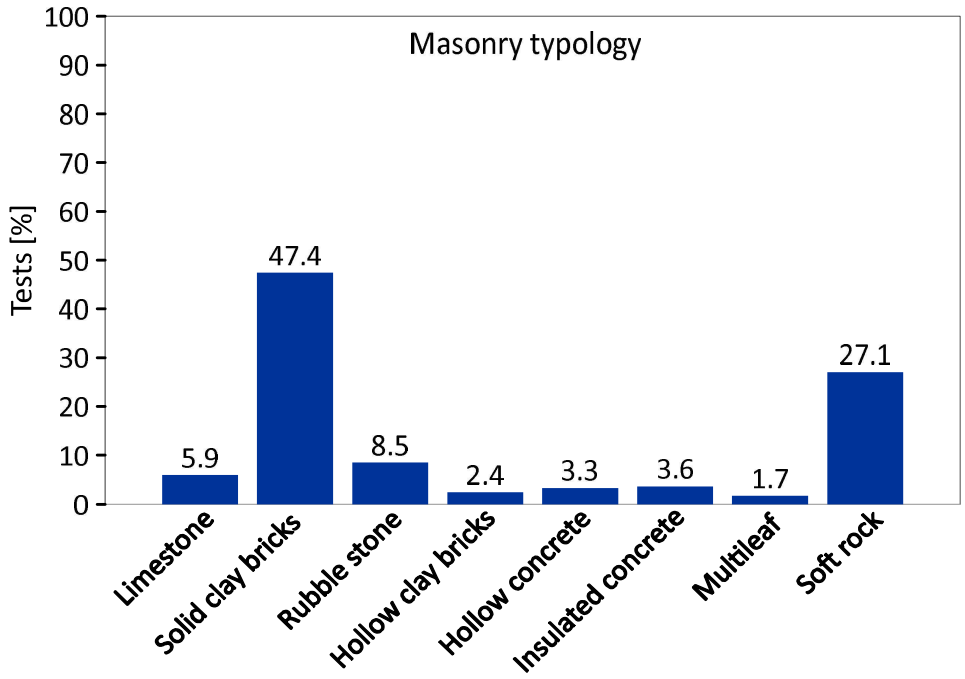


Figure 4.30 Percentage for each masonry type in the database

Figure 4.31 shows how the tests are distributed according to the various reinforcement techniques employed, if applicable (25% are unreinforced, UR, panels). The main percentages (UR, FRCM, CRM, Mortar) reported in blue in the figure refer to the overall number of specimens considered in the study Within each reinforcement category, the percentages reported in grey indicate the distribution of the specimens according to the specific configurations

adopted and are calculated with respect to the total number of specimens belonging to that reinforcement category. Therefore, these percentages provide a more detailed breakdown of the different configurations investigated within each strengthening technique. A small percentage, nearly 10%, is represented by panels in which the reinforcement consists solely of mortar, while the percentages of panels reinforced with FRCM and CRM are similar. The most common configurations are those in which the reinforcement is positioned symmetrically on both surfaces (FRCM 2S and CRM 2S), and a small percentage involves the use of connectors in both single-sided (FRCM 1S+c and CRM 1S+c) and double-sided (FRCM 2S+c and CRM 2S+c) configurations.

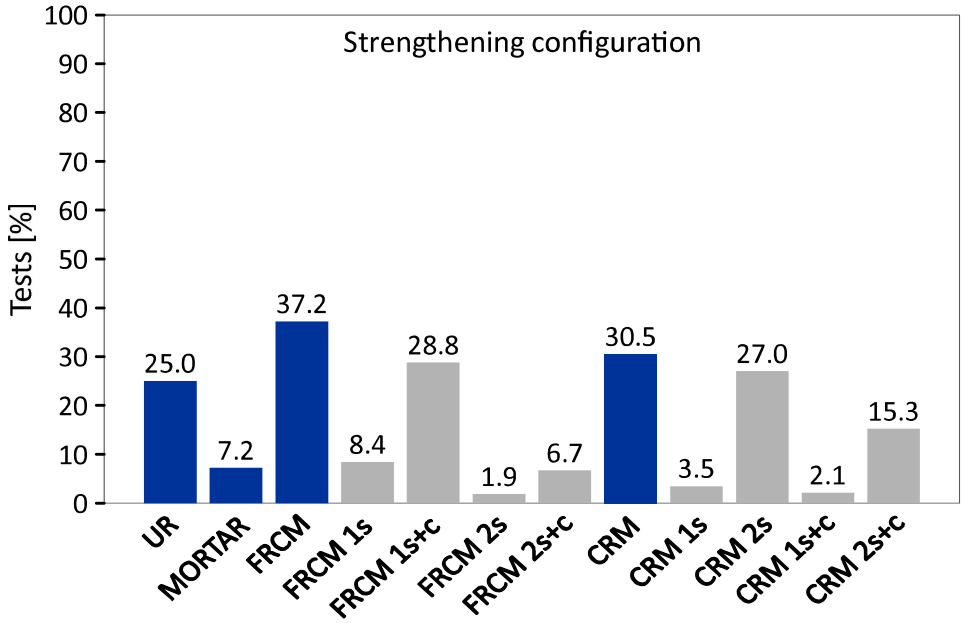


Figure 4.31 Percentage for each strengthening configurations in the database

Figure 4.32 shows the most common types of fibre, with glass being the most popular, followed by basalt and carbon. The 'Others' category includes all fabrics that are not typically used, such as plastic or specially designed fabrics. Several observations were made based on the test results. To ensure consistency and comparability of the results in the following graphs, the τ_0

values (unreinforced) were calculated in accordance with ASTM E519 and the τ_R values (reinforced) according to CNR-DT215. All τ values were calculated based on the cross-sectional area of the masonry excluding the thickness of the reinforcement render. The points denoted by "thesis" in parentheses in the following graphs correspond to the results obtained in the present thesis (Fig.4.33).

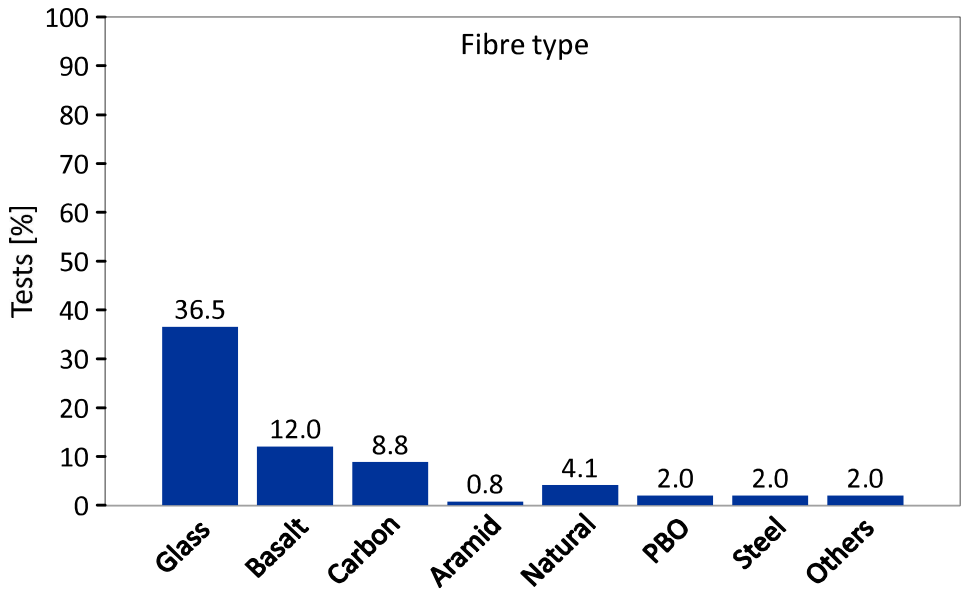


Figure 4.32 Percentage for each fibre type in the database

The first graph (Fig. 4.33a) illustrates the relationship between the reinforcement's contribution and the shear strength of the masonry. The reinforcement contribution is evaluated as the ratio of τ_R to τ_0. The results shown in Fig. 4.33 are derived from the experimental database compiled from the literature, integrated with the results carried out as part of the present thesis. As expected, the results show that reinforcement becomes more effective as the shear strength of the masonry decreases, for low-quality masonry. This trend holds true for panels reinforced with either mortar or FRCM/CRM systems.

The contribution of the reinforcement was plotted against t_{mas}, the thickness

t_{mas} of the masonry to which it was applied (Fig. 4.33b). The analysis of the database confirms the findings reported in the literature: contributions tend to be higher when the masonry thickness is modest [133]. Meanwhile, the contribution appears to gradually decrease as the thickness of the masonry increases. This trend was also observed for panels reinforced with mortar alone, as well as for those using FRCM and CRM.

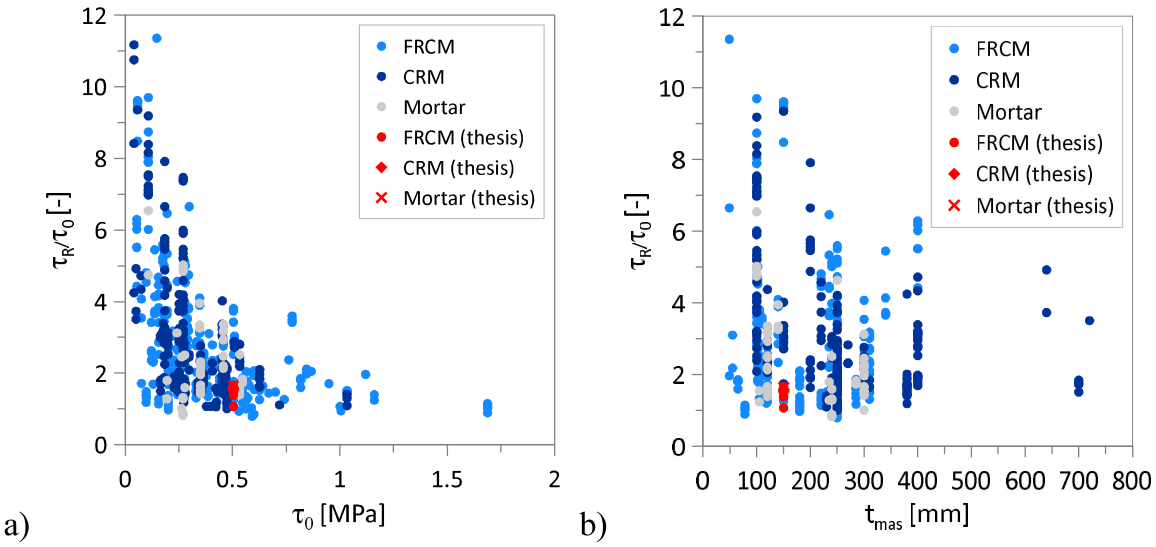


Figure 4.33 Strengthening system effectiveness: a) related to masonry shear strength; b) related to masonry thicknesses

To confirm the hypothesis regarding the contribution of the mortar, the mechanical ratios of fibre ω_f and mortar ω_m were evaluated. These parameters are used in the literature to quantify the reinforcement effect [133] and are calculated using the following expressions:

$$\omega_f = \frac{f_{fu} A_f}{\tau_0 A_{mas}} \tag{4.6}$$

$$\omega_m = \frac{\sqrt{f_{cm}} A_m}{\tau_0 A_{mas}} \tag{4.7}$$

where:

- f_{fu} is the tensile strength of the fibre;

- A_f is the area of the fibre, calculated as the product of n_{side} (i.e. the number of sides to which the reinforcement is applied), n_{layers} (the number of layers per side of the mesh reinforcement), t_{eff} (the equivalent dry thickness of the grid) and L (the length of the masonry panel's edge);
- f_{cm} is the compressive strength of the mortar constituting the matrix;
- A_m is the matrix area, calculated as the product of the matrix thickness, the panel side length L, and the number of sides on which the reinforcement is applied;
- A_{mas} is the area of the masonry, calculated as the product of the thickness and the length of the panel side.

The results obtained were plotted on two s where the y-axis shows the ratio of τ_R and τ_0 (Fig. 4.34) while ω_f (Fig. 4.34a) and ω_m (Fig. 4.34b) are reported on the x-axis. As it can be seen from the trend lines on the graph, the mortar appears to contribute more significantly than the fabric itself. These observations refer to the trends identified from the literature database and therefore provide a broader basis for comparison with the results of the present experimental campaign. In fact, it seems that the strengthening contribution increases more significantly as the mechanical ratio ω_m increases (Fig. 4.34b), while the fibre values are more scattered (Fig. 4.34b). These observations apply to both the FRCM and CRM systems, and, in the case of mortar, to mortar-reinforced panels too.

Subsequently, the analytically estimated values were calculated for the data collected in the database. In this case, the contribution of the reinforcement was only calculated according to CNR DT 215 (Eq. 4.4), and this value was then compared with that obtained experimentally. This experimental value was calculated for each panel as the difference between the value achieved by the reinforced panel and the value of the unreinforced reference panel.

The graph in Fig. 4.35 shows the comparison between the experimental and

theoretical results, differentiated by reinforcement system. The formulation intended for FRCMs was also applied to CRMs. It is evident that there is no concentration of data points around the unit value in the case of FRCM systems; therefore, in some cases the value is overestimated and in others it is underestimated, with highly scattered results. This dispersion can be partly expected due to the heterogeneity of masonry and the conservative nature of the analytical formulations. However, the considerable scatter observed suggests that further investigation is needed, particularly for FRCM systems and, even more importantly, for CRM systems, for which the available experimental evidence is still more limited. Furthermore, it is confirmed that these same formulations are not applicable to the CRM system since, as can be seen from the graph, the results are significantly overestimated in the presence of CRM.

The analyses presented above are based on the experimental database and therefore describe trends observed across the broader body of available experimental evidence. The following analysis instead focuses specifically on the results obtained in the present experimental campaign, with the aim of investigating whether a limit to the effectiveness of the strengthening system can be identified in relation to its mechanical properties.

Based on the results obtained, the regulatory formulation should be updated to account for the mortar's contribution. Further studies are also needed to develop formulations for CRM systems. In-depth studies would be necessary to achieve this. However, in light of the experimental results obtained in this study, the possibility of identifying limits to the mechanical characteristics of the reinforcement beyond which additional strengthening no longer provides a significant benefit to the masonry is investigated. Specifically, the influence of the ratio between the shear modulus G of the reinforcement and the shear modulus G_0 of the masonry on the increase in shear strength was examined.

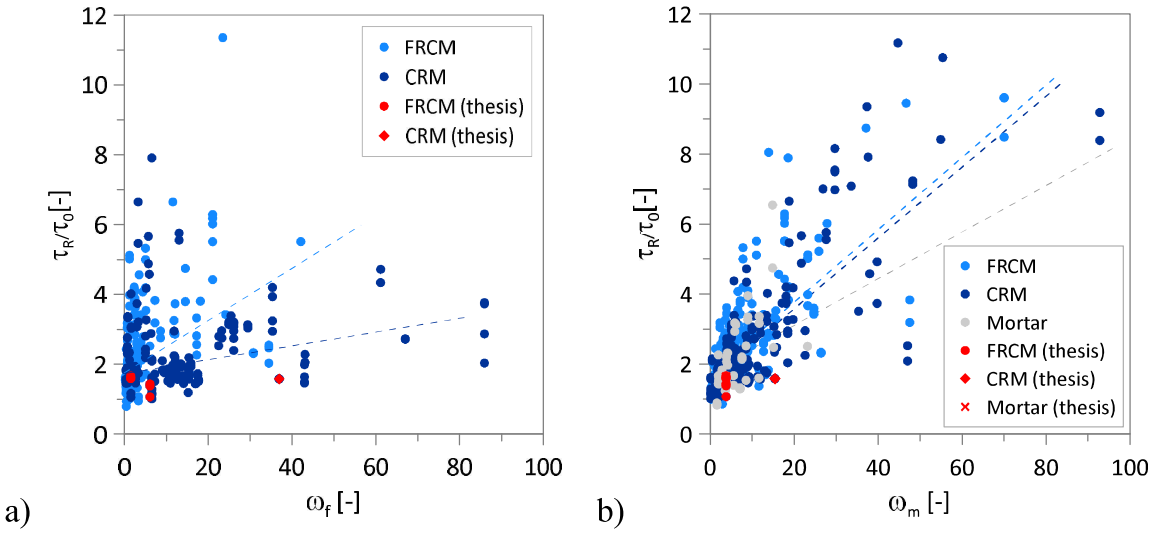


Figure 4.34 Effect of the fibre (a) and mortar (b) mechanical ratios in the shear strength increase

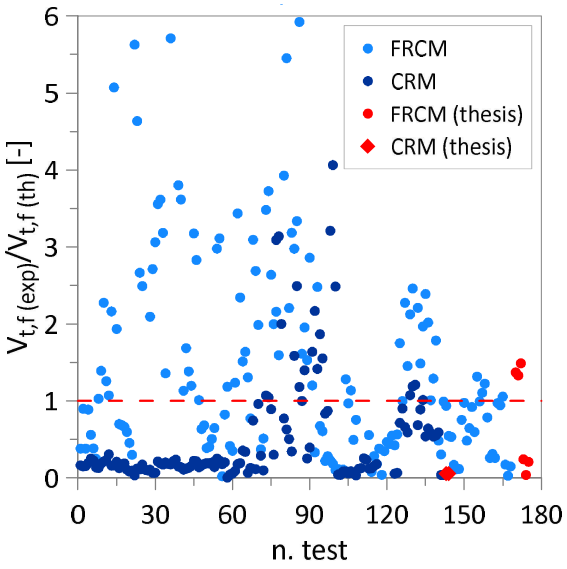


Figure 4.35 Analytical vs Experimental comparisons

Where available, the modulus G_0 was considered to be equal to that obtained from diagonal compression tests. Where not specified, it was calculated based on the elastic modulus E and Poisson's ratio ν [127].An equivalent shear modulus G_R was evaluated for the composite. This was estimated based on the elastic modulus E_R and Poisson's ratio ν, which was assumed to be 0.2. The E_R modulus was calculated according to the theory of composite micromechanics,

which was originally developed for unidirectional fibre-reinforced composites and subsequently used as a homogenization approach for determining equivalent elastic properties [134]. Specifically, the following expression was used:

$$E_R = \frac{E_m}{1 - \sqrt{v_f}\left(1 - \frac{E_m}{E_f}\right)} \tag{4.8}$$

where E_m and E_f are the elastic moduli of the matrix and fibre, respectively, and v_f is the fibre volume fraction.

The results obtained are shown in Figure 4.36 and are correlated with the increase in shear strength. Although the data are highly dispersed and do not reveal a clear correlation between the two quantities, a general trend can be identified, with the greatest increases in strength occurring at shear moduli ratio G_R/G_0 values close to unity. Conversely, as the shear moduli ratio G_R/G_0 increases, the benefit provided by the reinforcement gradually decreases. When considering specifically the experimental results obtained in the present study, the data fall within the region of the diagram characterised by relatively high G_R/G_0 ratios and limited increases in shear strength. This observation is consistent with the broader distribution identified in the literature database, although the present experimental results alone do not allow a direct causal relationship to be established. This behaviour suggests that the effectiveness of the reinforcement depends not only on its absolute strengthening system's shear modulus, but also on the compatibility of deformation between the reinforcement system and the masonry substrate. When the shear modulus of the two materials is comparable, forces are transferred more uniformly at the interface, promoting effective interaction between the reinforcement and the masonry. Conversely, excessive differences in shear modulus can lead to stress concentrations and premature damage to the masonry substrate or interface,

thereby limiting the reinforcement's ability to increase strength effectively. Overall, the comparison between the database and the present experimental results supports the hypothesis that shear stiffness compatibility between the reinforcement system and the masonry substrate may be a relevant factor in determining strengthening effectiveness, while further experimental evidence is required to confirm this relationship.

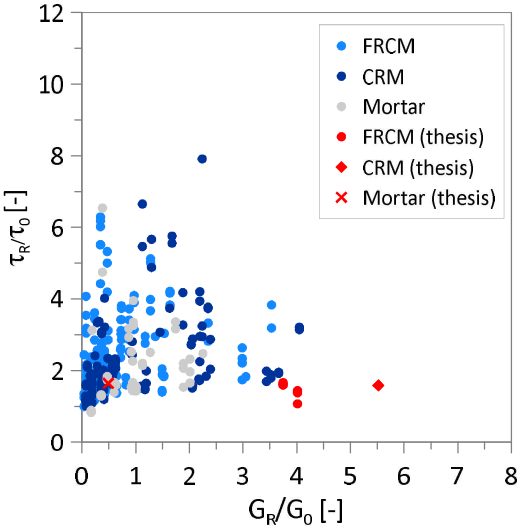


Figure 4.36 Shear strength increase average values related to shear modulus ratio

Chapter 5

Numerical Modelling of Diagonal Compressive Tests

The previous chapter outlined the experimental campaign and its main results, highlighting the mechanical behaviour of structural elements strengthened with composite systems. The experimental study also enabled an analysis of the interaction between the different materials and the failure modes exhibited by the strengthened elements, highlighting the influence of the strengthening systems on their overall structural response. Even if experimentation is a reliable tool for analysing structural behaviour; it does not allow for the direct observation of internal stress and strain evolution, nor does it enable the systematic evaluation of the influence of various parameters. For this reason, the experimental investigation was supplemented by numerical modelling, which was developed as a complementary tool to interpret the experimental results, to understand the mechanisms responsible for the observed response and to support the analysis of the behaviour of the structures under investigation. The modelling process was divided into two phases based on different levels of masonry material representation. In the first phase, a simplified model based on the homogenisation technique was developed. This model was primarily aimed at predicting the overall behaviour of the structure and estimating the collapse load. This information was then used to design the experimental setup and size the testing apparatus.

Once the experimental results were available, a numerical model based on the micro-modelling technique was developed to reproduce the observed behaviour, to analyse the damage mechanisms and interpret the differences between the initial predictions and the experimental evidence. As the homogenisation-based model was only used for preliminary predictions and was it not subsequently calibrated or developed further, the remainder of this chapter will focus solely on the micro-modelling model. This model is the primary numerical tool used to interpret the experimental results and perform the analyses presented in this work.

The numerical model was implemented by using STKO (Scientific ToolKit for OpenSees) [135], which is an advanced pre- and post-processing environment for finite-element modelling of complex structures. The main features of the software used will be summarised in the following sections. Subsequently, the numerical model developed as part of this study will be described, illustrating the modelling assumptions, strategies adopted and calibration process. Finally, the numerical results will be compared with experimental data to evaluate their predictive capability and interpret the mechanisms observed during the experimental tests.

5.1 Overview of STKO and OpenSees

As stated, numerical modelling was developed by using STKO [135] and OpenSees [136]. STKO provides a graphical interface for the open-source OpenSees framework [136], which was developed primarily for the nonlinear analysis of civil engineering structures. The integrated environment allows users to define the model's geometry, to assign materials and elements, to set boundary conditions and analysis procedures, and to manage the visualisation and processing of numerical results. STKO's graphical interface simplifies the

construction of highly complex models while maintaining the full flexibility and computational capabilities of the OpenSees solve.

The modelling environment enables users to define the structure's geometry, generate the finite element mesh, assign material and element mechanical properties, impose boundary conditions and loads, and configure analysis procedures. Once the pre-processing phase is complete, STKO automatically generates Tcl scripts compatible with OpenSees, ensuring the correct translation of the numerical model and its calculation settings. Thanks to its full integration with OpenSees, STKO offers a wide range of finite elements, constitutive models and solution algorithms, enabling the simulation of the linear and nonlinear behaviour of civil engineering structures. These features make the software particularly well-suited to the numerical analyses carried out in this study, which focus on the behaviour of masonry structural elements reinforced with composite systems. In particular, the ability to define nonlinear constitutive models and to adopt different modelling strategies makes it possible to represent, with an appropriate level of detail, the mechanical response of the masonry, the reinforcement system and their interaction. The software also allows for the definition of different load and displacement control strategies, convergence criteria and iterative solution algorithms, depending on the specific requirements of the analysis. These features are particularly important for reproducing the nonlinear response observed experimentally and for studying the evolution of damage and the failure mechanisms of the reinforced elements. The post-processing environment also facilitates the interpretation of numerical results, allowing the visualisation and analysis of quantities such as deformed configurations, displacement and strain fields, stresses, internal forces and material state variables. These features are particularly useful in this study for evaluating the response of the numerical models and comparing it with the experimental results obtained during the

tests. The ability to analyse the development of local damage and the interaction between the masonry substrate and the reinforcement system also provides useful information for interpreting the failure mechanisms observed experimentally and for assessing the effectiveness of the modelling approach adopted.

5.2 Model development

To reproduce the behaviour observed during mechanical testing, the masonry was modelled using a micro-modelling approach. This was done to explicitly represent the main constituents of the masonry, distinguishing the stone elements from the mortar joints and describing their mechanical interaction. Unlike macro-modelling approaches, which treat masonry as a homogeneous material, micro-modelling captures local phenomena that govern the structure's response. These include cracking of the blocks, opening and sliding of mortar joints, and detachment and stress transfer at interfaces between materials. These aspects are particularly relevant when studying the behaviour of masonry panels and evaluating the effectiveness of composite reinforcement systems. While this approach necessitates more detailed discretisation and incurs a greater computational burden than homogenised models, it enables a more realistic representation of damage mechanisms and strength phenomena within the masonry, facilitating a more reliable comparison with experimental evidence.

This study adopted a Continuum Micro-Model approach (Fig. 5.1), modelling both the stone elements and the mortar joints as three-dimensional continua while maintaining an explicit geometric representation of the masonry bond pattern. This approach enables the direct simulation of stress and strain distributions within the various components, as well as the reproduction of the primary collapse mechanisms experimentally observed.

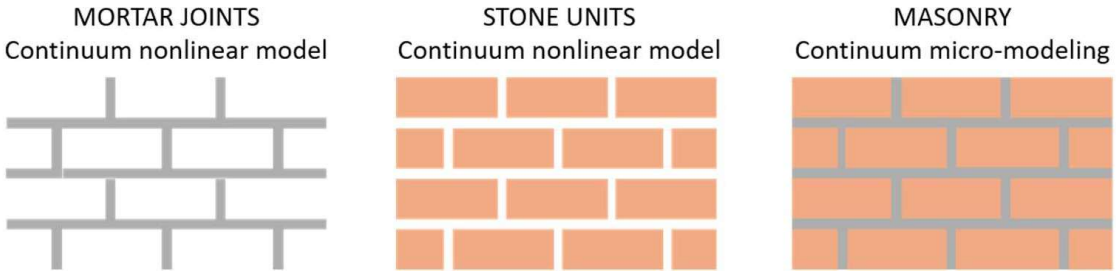


Figure 5.1 Representation of Continuum Micro-Modelling elaborated by the author

In this modelling approach, the primary sources of nonlinearity are concentrated in the constitutive parameters applied to the different masonry components, specifically, the stone elements and mortar joints, while the interface between the two materials is assumed to be perfectly bonded. This implies an absence of opening or sliding phenomena along the block-mortar interface. This assumption represents a simplification of the actual behaviour of masonry, where local opening, sliding and debonding may occur at the stone–mortar interface and may affect the local damage and failure mechanisms. Consequently, the assumption of perfect bonding may influence the numerical prediction of the local response, particularly in the post-peak regime. Nevertheless, it was adopted to maintain the computational efficiency of the model while retaining an explicit representation of the main masonry constituents. Previous continuum micro-modelling approaches have similarly adopted simplified or perfectly bonded interfaces when the primary objective is to reproduce the overall structural response [137]. This approach strikes a balance between the simplicity of homogenised models and the greater detail of detailed micro-models, in which the interface between blocks and mortar is explicitly modelled using contact elements. The continuum micro-model allows for distinct representation of masonry components while reducing the number of parameters required for calibration, primarily linked to the

definition of material constitutive relationships. The possible influence of this assumption is therefore taken into account when interpreting the numerical results, particularly with regard to local interface-related failure mechanisms. With regard to the reinforcement system, the absence of significant cracking of the matrix or delamination at the masonry-reinforcement interface in the experimental evidence obtained in this study led to the decision to adopt a continuous representation using an equivalent homogeneous solid element. The reinforcement was therefore modelled as a single composite material characterised by its own nonlinear constitutive relationship. This approach is capable of representing the overall behaviour of the system without the need for separate modelling of the components (matrix and fabric). This simplification reduces the model's complexity while maintaining an adequate description of the main phenomena.

5.2.1 Geometry, mesh, and boundary conditions

The numerical model was developed by reproducing the geometry of the specimens prepared for diagonal compression tests (Fig. 5.2). Initially, a 2D model was developed to analyse the unreinforced masonry. Four-node quadrilateral *(Quad)* elements were used to discretise the masonry components. The elements were defined under plane-stress conditions and assigned a thickness of 150 mm, corresponding to the actual thickness of the experimental panels.

Two lines representing the dimensions of the metal shoes used in the experimental tests were modelled on the top and bottom edges of the panel. Specific boundary conditions were assigned to each of these lines using the *fix* command: the bottom edge was given a fixed constraint, while the top edge was given a sliding constraint, allowing movement only in the vertical (y) direction. Specific points (selection set) were also defined on the panel's

surface, corresponding to the reference points used to position the dial gauges during the tests. These points were subsequently used to make a direct comparison between the displacements obtained numerically and those measured experimentally. A structured mesh was adopted, with element size of 5 mm. A mesh sensitivity analysis was performed by progressively refining the element size to assess its influence on the numerical response. The results showed that further mesh refinement produced only minor variations in the response, and the adopted mesh was therefore considered sufficiently refined for the analyses presented in this study. The load was applied vertically to the upper shoe, in accordance with the experimental setup, and the analysis was configured for displacement control.

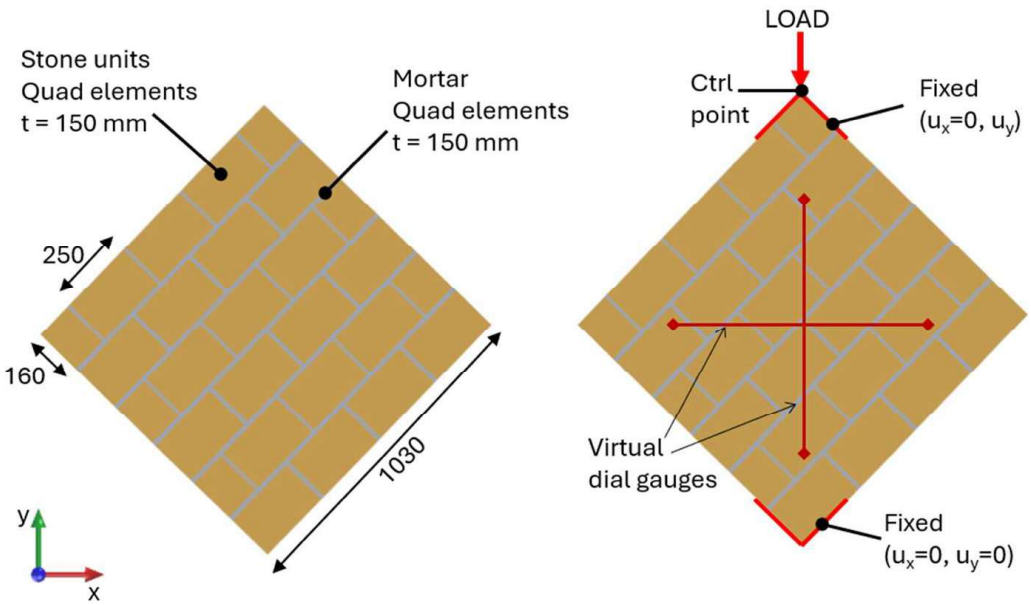


Figure 5.2 Unreinforced masonry 2D model: geometry (dimensions in mm), elements and boundary conditions

For the subsequent analysis of the reinforced panels, the geometric model was extended to a three-dimensional environment (see Fig. 5.3) to better represent the system's overall behaviour and capture the effects resulting from the three-dimensional interaction between the masonry and reinforcement.

The masonry was modelled using Standard Brick (StdBrick) elements for both the stone elements and the mortar joints. This element consists of eight nodes and uses full Gaussian integration with eight integration points (2×2×2), enabling an accurate representation of the three-dimensional stress state and the evolution of damage within the material.

The metal shoe was also modelled in three dimensions using brick elements to reproduce the actual dimensions of the element used during the experimental tests. The boundary conditions were defined analogously to the two-dimensional model, imposing constraints on the lower shoe and leaving only the vertical displacement degree of freedom of the upper shoe unrestricted.

The interaction between the metal shoe and the masonry was modelled using node-to-node interaction to which an equal DOF constraint was subsequently applied to ensure compatibility of displacements between the involved nodes and lock all related degrees of freedom. The reinforcement system was modelled as an equivalent homogeneous solid to which the stdBrick element was assigned, in line with the approach adopted for representing the composite's overall behaviour. The reinforcement layer was then connected to the masonry panel via a node-to-element interaction. Distributed *ZeroLength* elements were assigned to this interaction to represent the behaviour of the interface between the substrate and the reinforcement. The ZeroLength elements were assigned a linear elastic material with a very high elastic modulus in the x- and y-directions. This choice was made to simulate a rigid interface between the masonry substrate and the reinforcement layer, ensuring the transfer of stresses to the reinforcement without introducing significant additional deformation at the interface. Therefore, the ZeroLength elements were not intended to reproduce interface debonding or sliding phenomena, but only to provide the mechanical connection between the masonry and the strengthening layer. The material properties and constitutive parameters

adopted for the numerical model are presented in the following sections.

Four points corresponding to the anchor locations were identified on the surface of the strengthening layer, where dial gauges were installed during the experimental tests. These points were used to define two virtual dial gauges, thereby enabling a direct comparison to be made between the deformations obtained numerically and those measured experimentally.

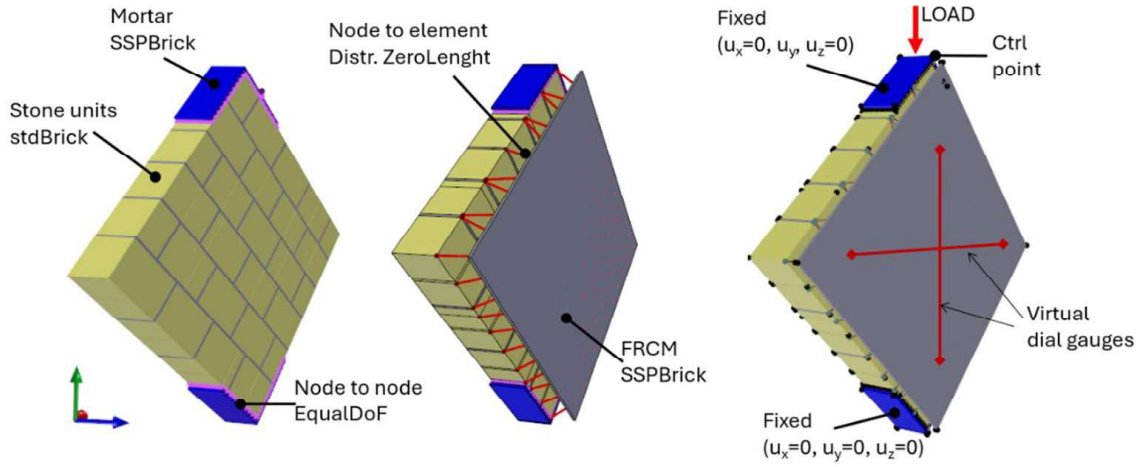


Figure 5.3 Strengthened masonry 3D model: geometry, elements and boundary conditions

The load was applied through the upper shoe so that it was transferred exclusively to the masonry panel and not directly to the reinforcement system, thus replicating the configuration used during the tests.

The numerical analysis was set up under displacement control. The Newton algorithm was used to solve the nonlinear problem, and the Norm Displacement Increment Test was used to define the convergence criterion.

5.2.2 Constitutive models and material parameters

The constitutive model used for the stone units, mortar joints and FRCM system is *ASDConcrete3D* [138]. This three-dimensional, nonlinear constitutive model is implemented in OpenSees to simulate the behaviour of quasi-brittle materials such as concrete and masonry.

The model formulation is based on *Continuum Damage Mechanics* (CDM) and describes the material's behaviour using two independent scalar damage variables: one associated with tension and one with compression. These variables enable the progressive degradation of the material's stiffness to be represented, due respectively to the formation and propagation of cracks and to crushing phenomena.

The stress tensor associated with the tension-compression damage law is defined by the following equation:

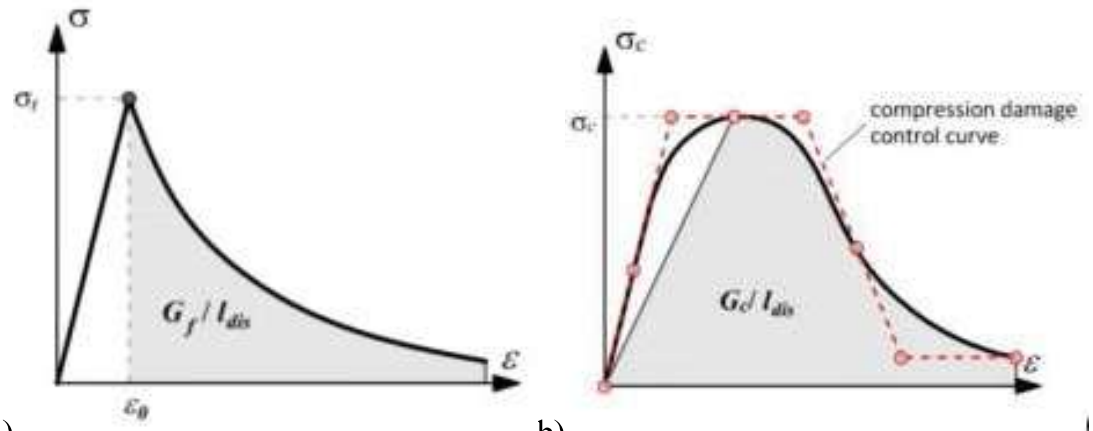
$$\bar{\sigma} = (1 - d^{+})\bar{\sigma}^{+} + (1 - d^{-})\bar{\sigma}^{-} \tag{5.1}$$

where $\bar{\sigma}$ represents the nominal stress tensor, while $\bar{\sigma}^{+}$e $\bar{\sigma}^{-}$ represent the positive and negative components of the effective stress tensor. The variables d^{+}e d^{-} are the damage indices associated with tension and compression, respectively, defined based on the material's constitutive laws. These parameters take values ranging from 0, in the absence of damage, to 1, corresponding to the complete loss of strength.

The model adopts the concept of effective stress, according to which the elastic response of the material is initially defined in the space of effective stresses, while the evolution of damage leads to a progressive reduction in stiffness and strength through the updating of the damage variables.

The initiation and evolution of damage are governed by specific hardening and softening laws, defined separately for tensile and compressive behaviour, allowing the different material responses in the two stress states to be reproduced (Fig. 5.4). In particular, the model allows for the representation of both the phase of increase in load-bearing capacity until the maximum value is reached and the subsequent phase of degradation associated with damage propagation. To ensure consistency between the numerical response and the adopted discretisation scheme, the model introduces an energy regularisation based on fracture energy. This approach reduces the dependence of the

softening response on the size of the finite elements, making the model more suitable for simulating deformation localisation phenomena.



a) b)

Figure 5.4 Representation of the *ASDConcrete3D* uniaxial constitutive models [138]: a) in tension; b) in compression.

These features make the *ASDConcrete3D* model particularly well-suited to simulating the nonlinear behaviour of quasi-brittle materials, enabling a realistic description of crack formation and propagation, progressive stiffness degradation, and strength loss, phenomena typical of masonry and concrete structures.

In this study, the material was defined using the *Concrete 9P preset*, which requires the definition of the following nine parameters:

- f_t is the tensile strength of the material;
- f_{c0} is the compressive stress at the end of the elastic range;
- f_{cp} is the maximum compressive strength of the material;
- f_{cr} is the residual compressive stress;
- e_{cp} is the strain corresponding to the peak compressive stress;
- G_t is the tensile fracture energy;
- G_c is the compressive fracture energy;
- *PScale Tension* is the tensile plasticity scale factor, a variable ranging from 0

to 1;

- *PScale Compression* is the compressive plasticity scale factor, a variable ranging from 0 to 1.

The *IMPLEX* integration option has also been enabled in the model, which is an *IMplicit-EXplicit* mixed integration scheme. This formulation allows for a numerical solution characterized by piecewise linear increments, thanks to the explicit extrapolation of internal variables and the use of a positive-definite tangent matrix, thereby improving the stability of the solution procedure for strongly nonlinear problems.

The calibration of the constitutive parameters was performed based on the results obtained from the experimental characterisation tests conducted on the masonry materials, namely M5PJ mortar, M10 mortar and CMP *calcarenite*. The calibration procedure and the parameters used in the numerical model are described in the following section.

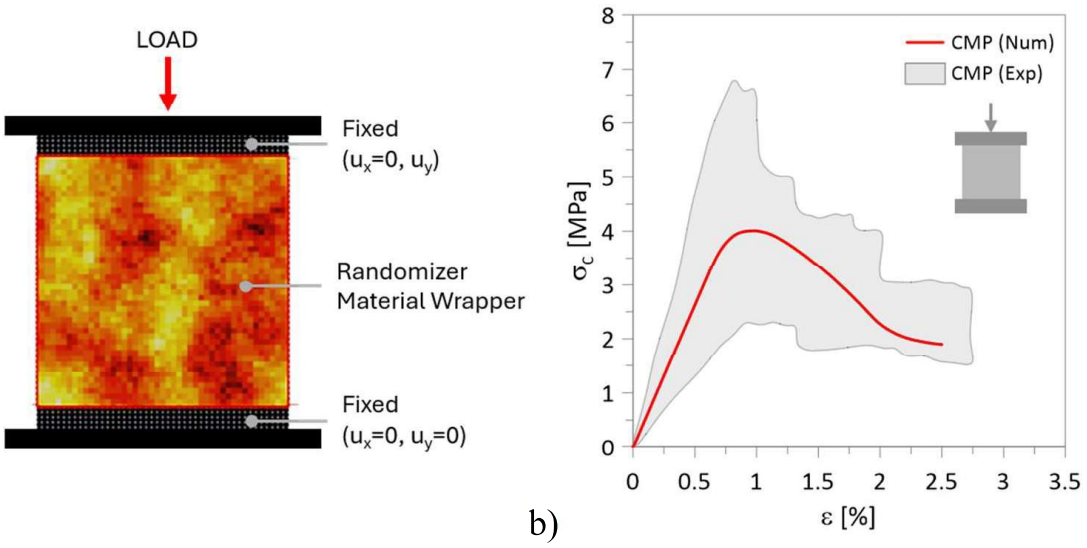
5.3 Model calibration based on experimental data

Calibration of the constitutive models is one of the most complex steps when using nonlinear constitutive models, since not all the required parameters are always available. In such cases, calibration may be performed by comparing the numerical response with experimental results.

In the present study, the materials constituting the masonry were calibrated through the numerical simulation of material characterisation tests, using the results obtained from the experimental campaign as a reference. Specifically, the following tests were numerically simulated: uniaxial compression tests on *calcarenite* and mortar, and three-point bending tests on mortar. The results obtained from these simulations were then used to define and calibrate the constitutive behaviour of the masonry components, i.e. stone units and mortar, which were subsequently assembled in the numerical model to reproduce the

mechanical behaviour of the masonry.

Figure 5.5 shows the results of calibrating the constitutive relationship for calcarenite under compression. Figure 5.5a shows a schematic of the model used. In the material modelling, a Randomizer Material Wrapper was associated with the constitutive model to generate 20 materials characterised by compressive strengths varying around the average compressive strength of *calcarenite* with a standard deviation of 0.2.



a) b)

Figure 5.5 Uniaxial compressive test on CMP *calcarenite* a) numerical model; b) Experimental vs numerical comparisons.

This approach considers the heterogeneous composition of materials such as masonry and concrete since these materials are characterised by natural variations in mechanical properties due to defects, discontinuities and variability in their constituent materials. Using the Randomizer Material Wrapper therefore enables more realistic simulations of structural behaviour, particularly with regard to the initiation and propagation of damage and cracks. The parameters related to behaviour up to the peak strength were calibrated using experimentally obtained values, while fracture energy values in compression G_c and in tension G_t were calibrated using formulations found in

the literature [139] as following:

$$G_c = \frac{32 f_c}{10 + f_c} \qquad [N/mm] \tag{5.1}$$

$$G_t = 0.07 \ln(1 + 0.17\, f_c) \qquad [N/mm] \tag{5.2}$$

where f_c is the compressive strength of the material.

Figure 5.5b shows the numerical-experimental comparison, revealing good agreement between the results.

A similar procedure was followed to calibrate the constitutive relationship of the mortar. In this case, both tensile and flexural tests were simulated (Fig. 5.6). Figure 5.6 shows schematic diagrams of the models used (Figs. 5.6a and 5.6c) and the numerical–experimental comparisons obtained for both simulations (Figs. 5.6b and 5.6d). Once again, good agreement was obtained between the numerical and experimental results.

These comparisons were primarily used to calibrate the compressive behaviour of the material and, in the case of mortar, also its tensile behaviour. They were subsequently implemented within a model developed to simulate the uniaxial compression test on masonry assemblage (Fig. 5.6) for the final definition of the constitutive relationships. The results from the vertical and horizontal dial gauges applied to the specimen during the experimental test (Figs 3.6 and 3.8) were then used to validate the adopted constitutive relationships. The previously calibrated constitutive models showed good agreement with the experimental results, requiring only a slight adjustment to the elastic modulus, a parameter which is often incorrectly estimated during uniaxial compression tests on constituent materials.

The calibrated parameters used in the numerical model of diagonal compression tests are shown in Table 5.1. This summarises the parameters required to calibrate the *ASDConcrete3D* constitutive model, as described in Section 5.2.2.

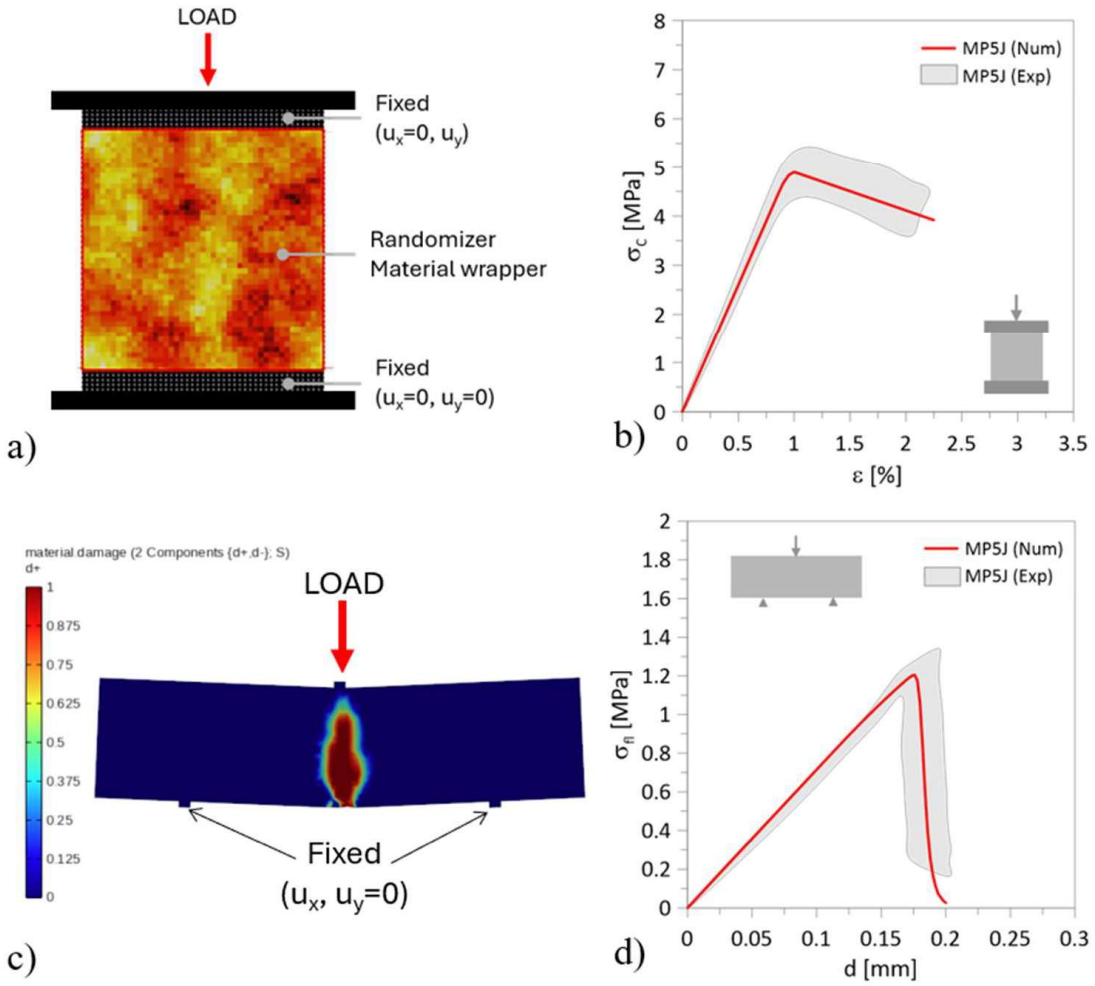


Figure 5.5 Tests on M5PJ mortar a) uniaxial compressive test model; b) Experimental vs numerical comparisons of compressive test; c) three point bending test model; d) Experimental vs numerical comparisons of flexural test

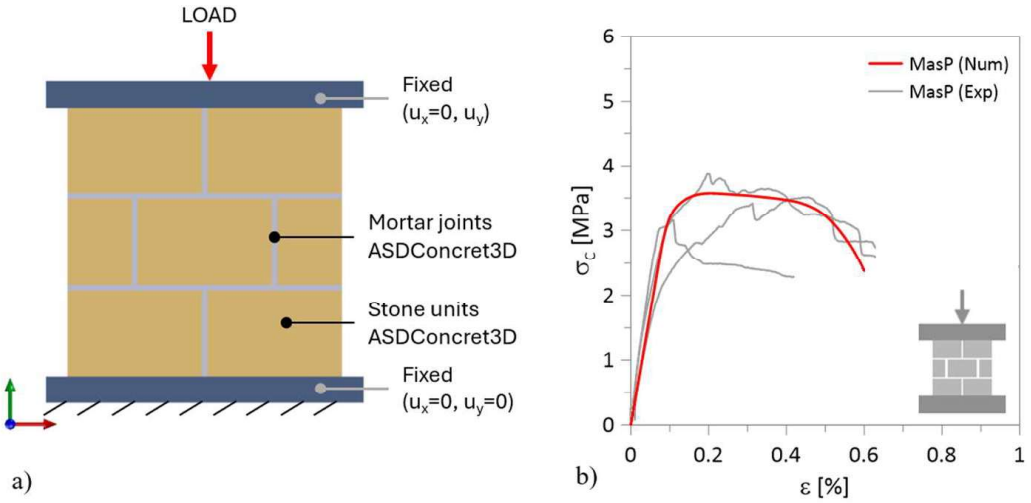


Figure 5.6 Tests on CMP masonry a) uniaxial compressive test model; b) Experimental vs numerical comparisons

Table 5.1 Mechanical parameters calibrated for masonry constituent materials

	E [MPa]	**f_t [MPa]**	**f_{c0} [MPa]**	**f_{cp} [MPa]**	**f_{cr} [MPa]**	**e_{cp} [%]**	**G_t [N/mm]**	**G_c [N/mm]**
CMP	4100	0.41	2.1	4.1	0.05	0.2	0.037	9.3
M5PJ	4900	0.65	4.5	4.9	0.05	0.2	0.042	10.5

The strengthening system was modelled as a homogeneous solid, without explicitly distinguishing, from a geometric point of view, between the fibre and matrix components. Their different mechanical contributions were instead taken into account by defining the constitutive relationship of the equivalent material. The ASDConcrete3D constitutive model was adopted, defined by two distinct contributions. The first describes the compressive behaviour, to which the mechanical properties of the M10P matrix, obtained from material characterisation tests, were assigned. The second describes the tensile behaviour and was defined on the basis of the first bilinear section of the FRCM composite's tensile response [140]. In this way, the numerical model takes account of the distinct contributions of the matrix and the reinforcement, maintaining a homogeneous representation of the reinforcement layer.

Specifically, the mixture rule was used to define the tensile behaviour, considering the strain corresponding to the formation of the first crack in the specimen. In the present case, due to the absence of cracking in the matrix, the final stage of behaviour, in which the strength contribution is entirely provided by the fibre, was not modelled. The two contributions relating to tensile and compressive behaviour were defined separately by setting the *PScale Compressive* and *PScale Tensile* factors to 0, respectively. In the case of the mortar-reinforced panel, only the matrix properties were considered. The parameters introduced into the constitutive relationships are shown in Table 5.2.

Table 5.2 Mechanical parameters for FRCM systems

	E [MPa]	**f_t [MPa]**	**f_{c0} [MPa]**	**f_{cp} [MPa]**	**f_{cr} [MPa]**	**e_{cp} [%]**	**G_t [N/mm]**	**G_c [N/mm]**
Glass +M10P	8140	2.11	-	-	-	-	10.2	-
Carbon +M10P	9340	3.42	-	-	-	-	10.2	
M10P	8000	1.42	8	14.3	0.01	0.3	0.11	2

Specifically, the Glass+M10P and Carbon+M10P rows show the tensile component calibration, and the M10P row shows the complete constitutive relationship. The latter was used to define the compressive behaviour of the two fabric-reinforced panels, and in its complete form to simulate the behaviour of the mortar-reinforced panel. The results obtained from the simulations are presented in the following section.

5.4 Numerical vs experimental results

The diagonal compression tests were simulated numerically, as described in the preceding sections. For brevity, the numerical-experimental comparisons are presented below in terms of the curves obtained from the numerical analysis (Fig. 5.7). The numerical curves obtained from the virtual dial gauges readings on the numerical model, identified by (num), were compared in Figure 5.7 with the full curves obtained from processing the DIC data, identified by (exp). The curves obtained from the numerical model also indicate three loading steps, labelled A, B, and C, for which the results are presented in the subsequent Figures 5.7-5.18.

In general, the numerical model shows good agreement with the experimental results; however, in the case of the reinforced panels, it fails to accurately reproduce the post-peak phase. This could be improved by modelling the reinforcement system in more detail, for example by discretising the matrix

and fibre components separately. This would enable more accurate calibration of the constitutive relationships associated with the materials, as well as better representation of the damage mechanisms and interactions between the different components. Table 5.3 shows a comparison of the numerical results in terms of maximum load P_{max}, maximum shear stress τ_{max} and shear modulus G, alongside a comparison with the previously calculated analytical results (Table 4.3).

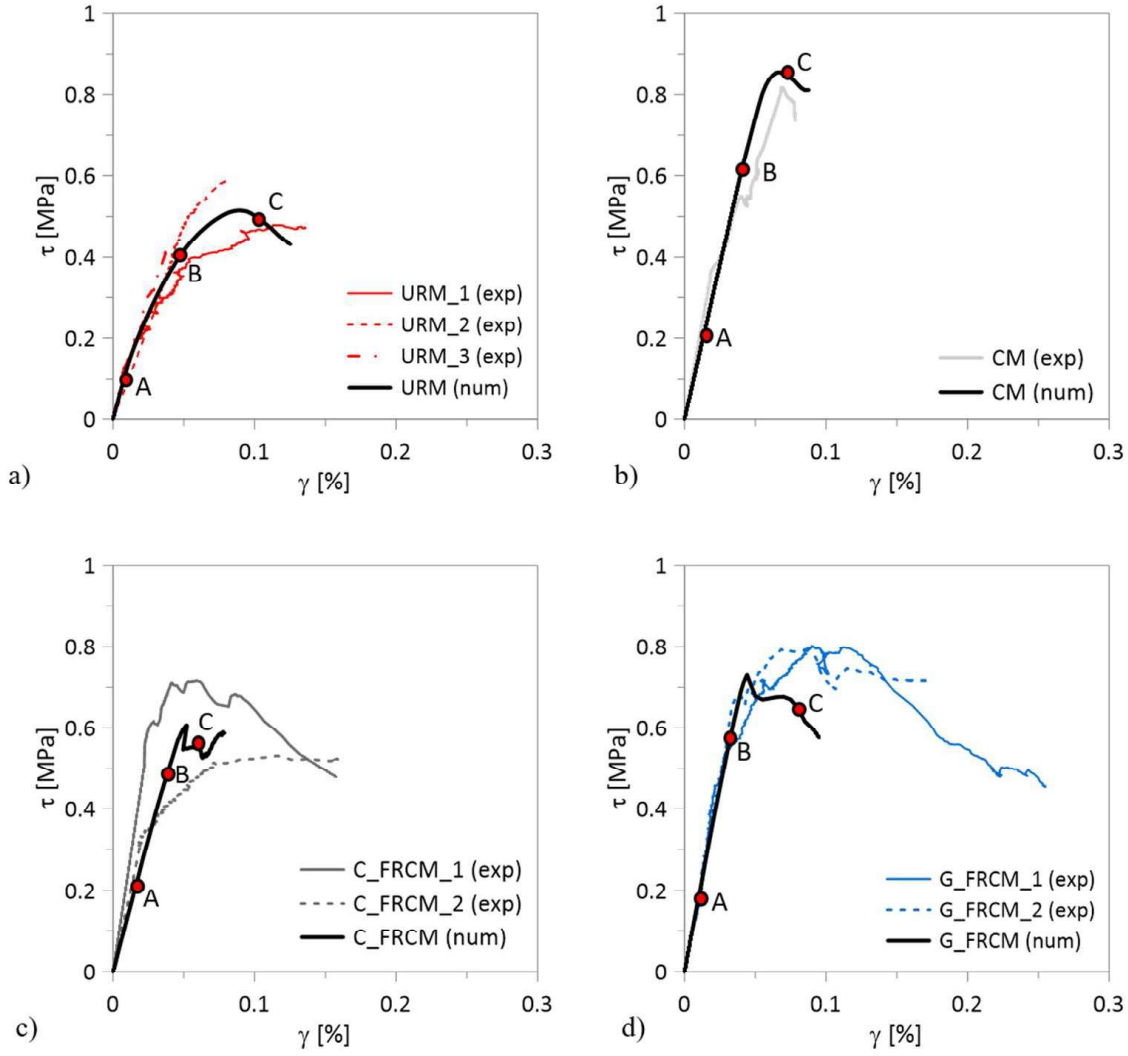


Figure 5.7 Numerical vs experimental comparisons a) URM samples; b) CM samples; c) C_FRCM samples; d) G_FRCM samples.

Table 5.3 Experimental, analytical and numerical comparisons

ID		Experimental	Numerical	Exp./An.	Exp./Num.
URM	P_{max} [kN]	110.1	112.8	1.67 - 3.1	0.98
	τ_{max} [MPa]	0.46	0.51	1.67 - 3.1	0.98
	G [MPa]	1568	1254	1.96 - 2.45	1.25
CM	P_{max} [kN]	180.43	187.6	-	0.96
	τ_{max} [MPa]	0.82	0.85	-	0.96
	G [MPa]	1785	1652	-	1.08
C_FRCM	P_{max} [kN]	137.8	133.2	0.39 - 0.43	1.03
	τ_{max} [MPa]	0.62	0.60	0.39 - 0.43	1.03
	G [MPa]	2417	1322	-	1.82
G_FRCM	P_{max} [kN]	176.1	160.3	1.74 - 2.51	1.09
	τ_{max} [MPa]	0.80	0.73	1.74 - 2.51	1.09
	G [MPa]	1698	1508	-	1.12

The comparison shows that the numerical results are in good agreement with the experimental data in terms of both maximum load and maximum shear stress, as well as the G-modulus. Looking at the final column of the table, which shows the ratio of the experimental to numerical values, it can be seen that these values are close to unity.

Moreover, despite the simplifications adopted, the numerical model can provide a closer representation of the experimental response than the available analytical formulations in some cases. The differences observed can also be attributed to the conservative nature of the analytical formulations, which are intended to provide cautious estimates of the load-bearing capacity. Overall, these results support the suitability of the numerical approach adopted and its ability to capture the main phenomena governing the behaviour of the analysed panels. Some representative post-processing results (Figs. 5.7-5.18) are presented below for selected cases, referring to the three loading steps A, B, and C identified on the curves in Figure 5.7.

For the unreinforced panel, material damage values are shown for both tension (Fig. 5.7) and compression (Fig. 5.8). Examining the trend of tensile damage reveals a typical failure mode characterised by a concentration of stresses along the main diagonal, leading to specimen failure. The model shows a crack crossing the blocks, which is consistent with the experimental failure mode observed in the URM_2 specimen (Fig. 4.10). Conversely, compressive material damage shows an initial concentration of stresses localised at the upper corner where the load is applied.

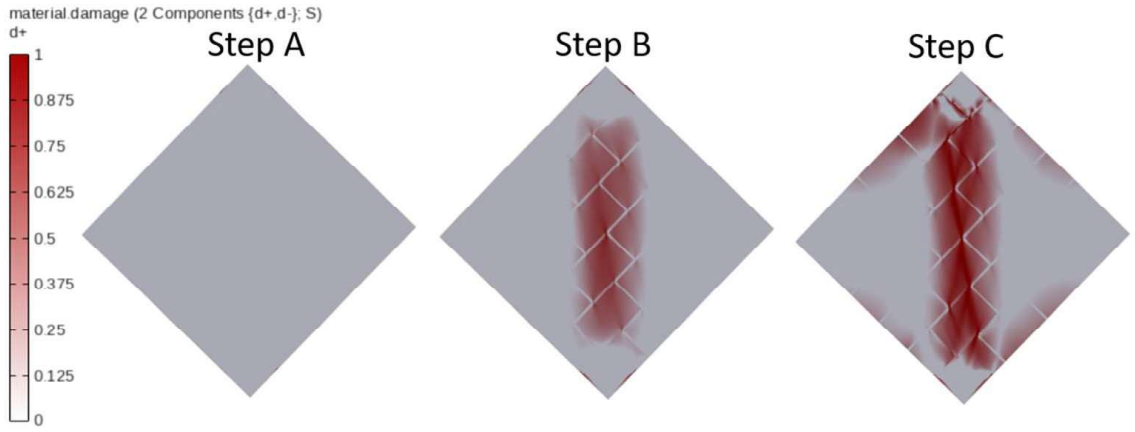


Figure 5.7 Tensile material damage for URM sample

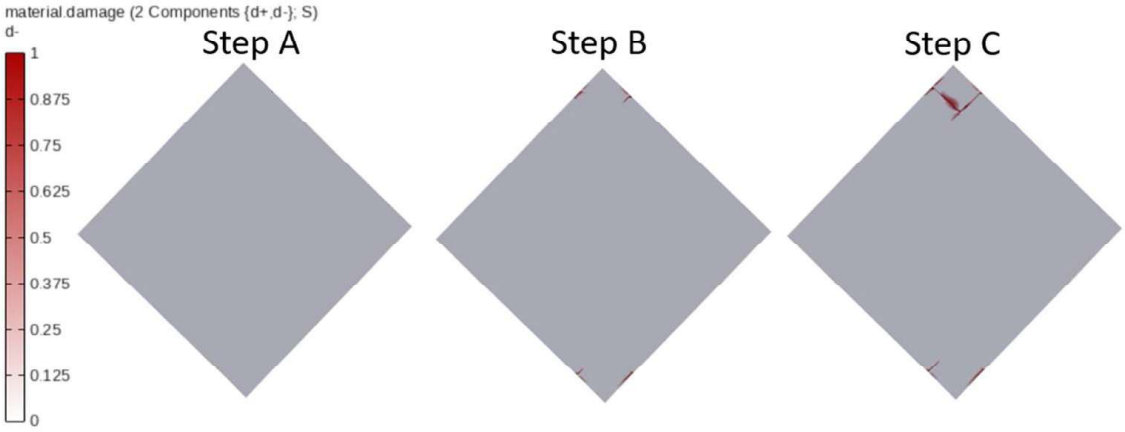


Figure 5.8 Compressive material damage for URM sample

Figures 5.9 and 5.10 are relate to the URM specimen and show the values of the tensile and compressive principal stresses. Once again, a concentration of

stresses is observed along the main diagonal, resulting in the formation of a distinct diagonal crack that propagates through the blocks.

Figures 5.11–5.15 show the simulation results for the G_FRCM series. It is interesting to note in this case that the material damage, both under tension (Fig. 5.11) and under compression (Fig. 5.12), is concentrated within the masonry panel, with no damage observed in the reinforcement layer.

This indicates that the reinforcement exhibited predominantly elastic behaviour, which is consistent with experimental observations in which no cracks were detected on the reinforcement system's surface.

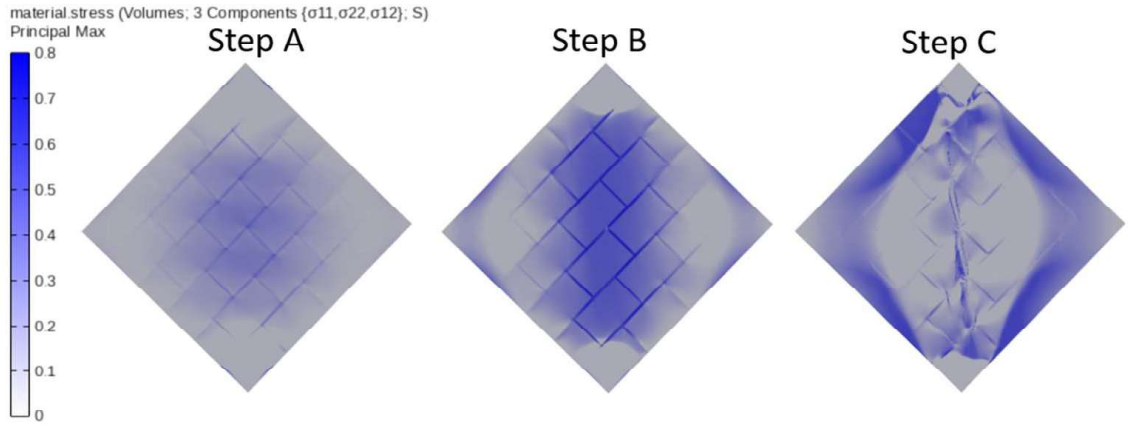


Figure 5.9 Principal tensile material stress for URM sample

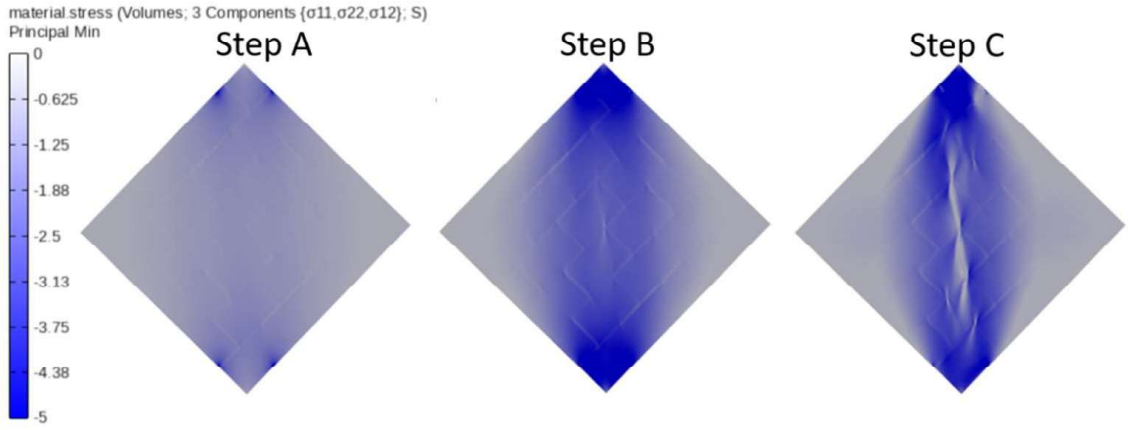


Figure 5.10 Principal compressive material stress for URM sample

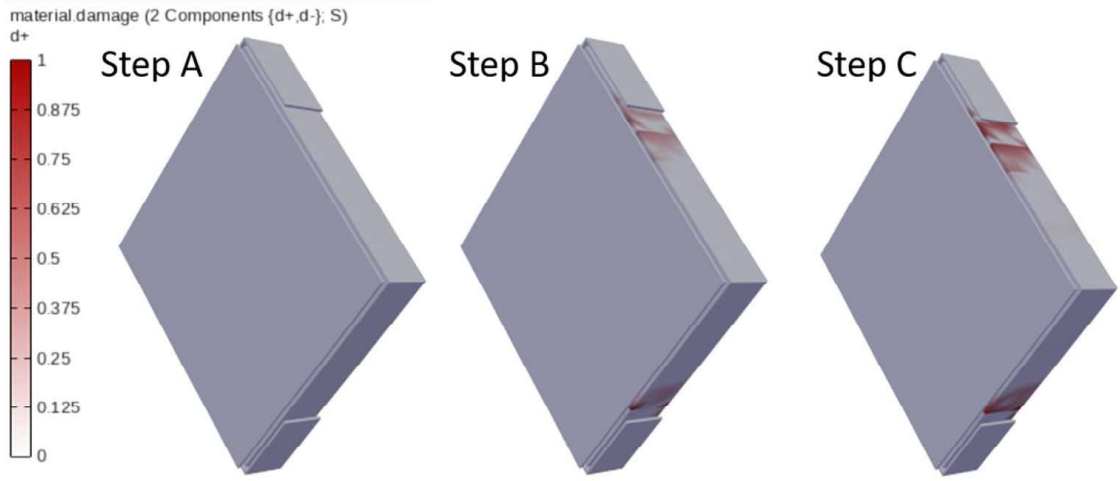


Figure 5.11 Tensile material damage for G_FRCM sample

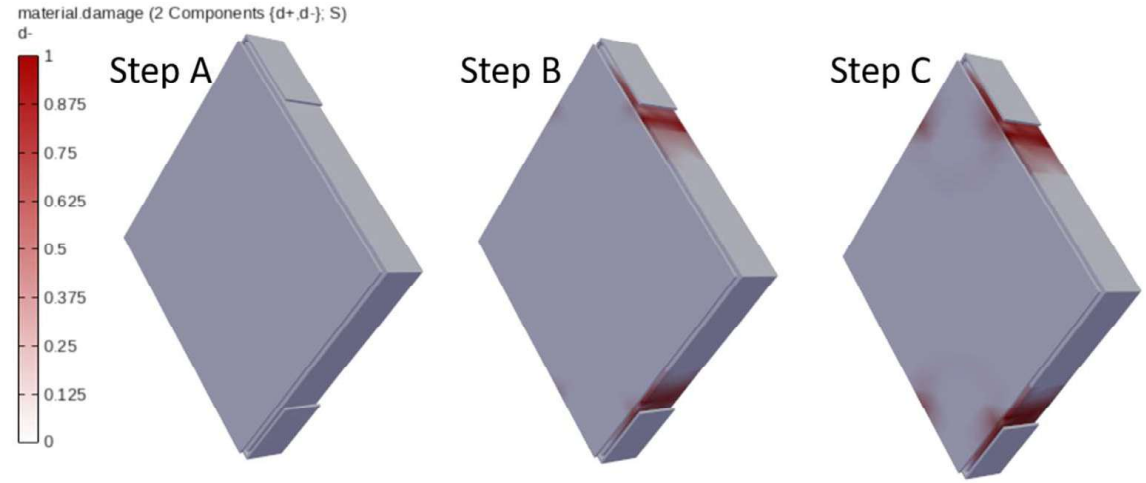


Figure 5.12 Compressive material damage for G_FRCM sample

Similar observations can be made by examining the figures showing the maximum (Fig. 5.13) and minimum (Fig. 5.14) principal strains. It is clear that there are high strains in the thickness of the panel at the upper and lower edges, i.e. in the areas where cracks were observed during the experimental tests.

Figure 5.15 confirms this behaviour by showing the displacements in the z-direction, i.e. perpendicular to the panel's plane. Out-of-plane displacements are observed, with higher values in areas near the top and bottom edges. These areas correspond to those where cracks were observed during the experimental tests.

Figures 5.16, 5.17 and 5.18, on the other hand, show the results for the CM series reinforced with mortar alone. As in the previous case, a concentration of compressive damage localised at the edges of the panel is observed (Fig. 5.16). To further investigate the specimen's internal behaviour, the same results were plotted with the reinforcement layer excluded from the visualisation (Fig. 5.17). This shows the compressive material damage relative to the masonry alone for the same loading steps.

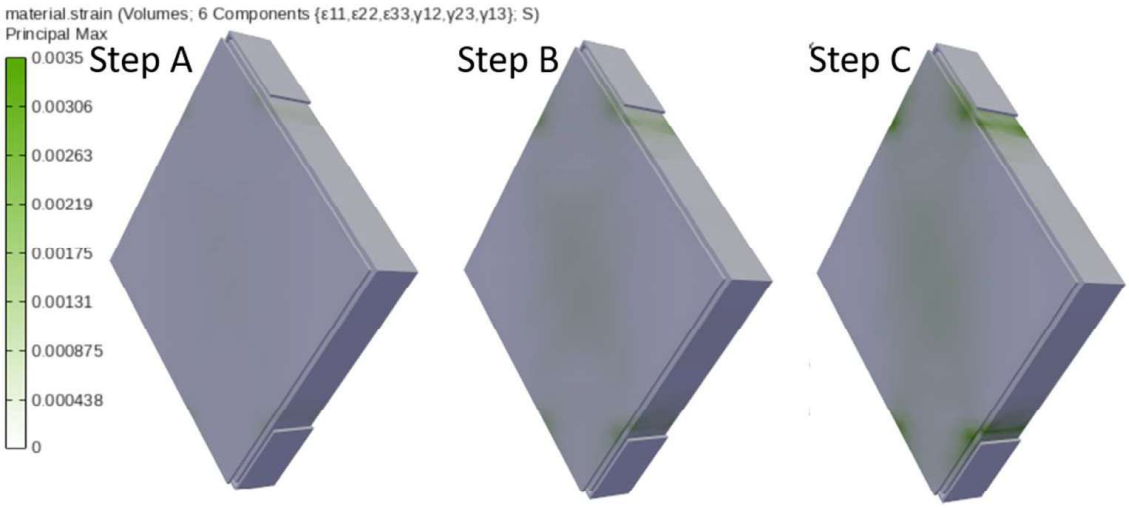


Figure 5.13 Principal tensile material strain for G_FRCM sample

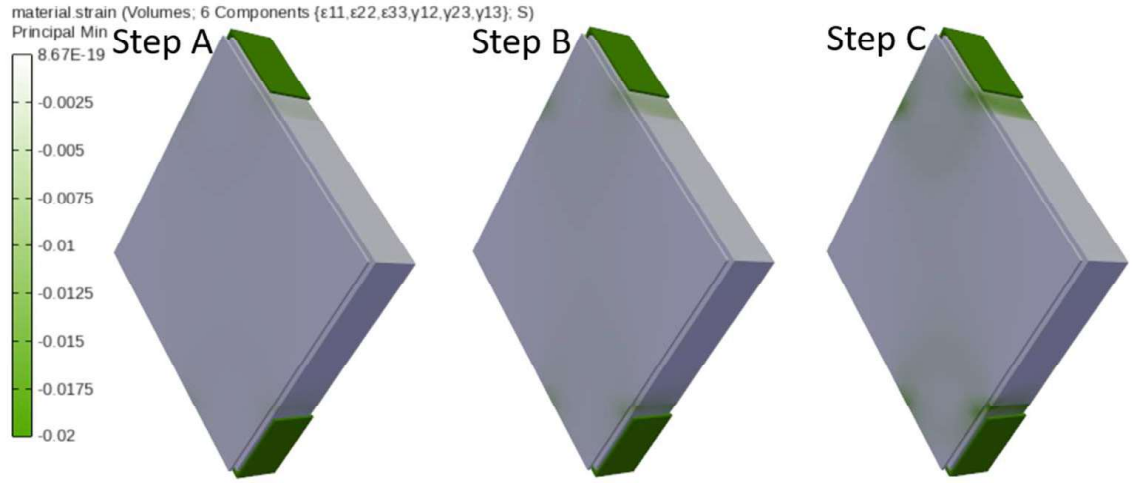


Figure 5.14 Principal compressive material strain for G_FRCM sample

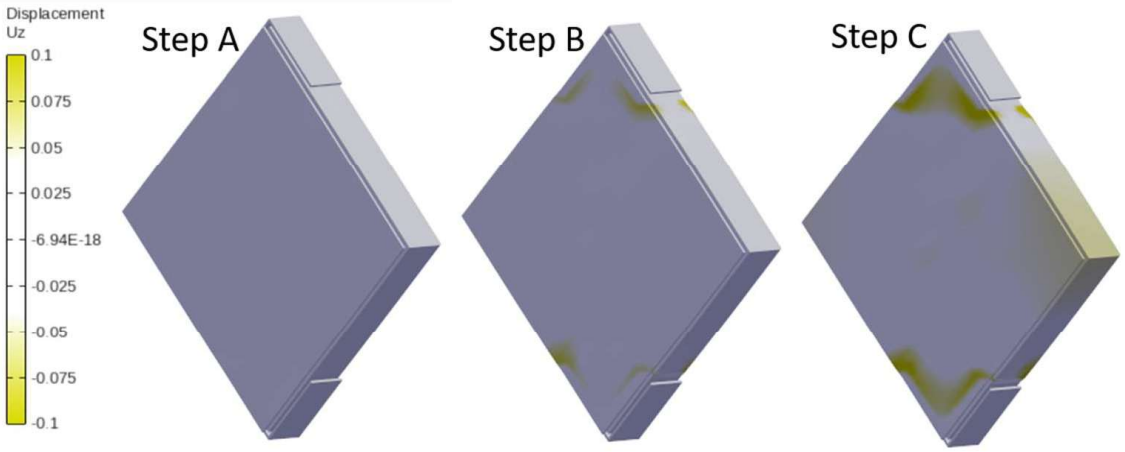


Figure 5.15 Uz displacements for G_FRCM sample

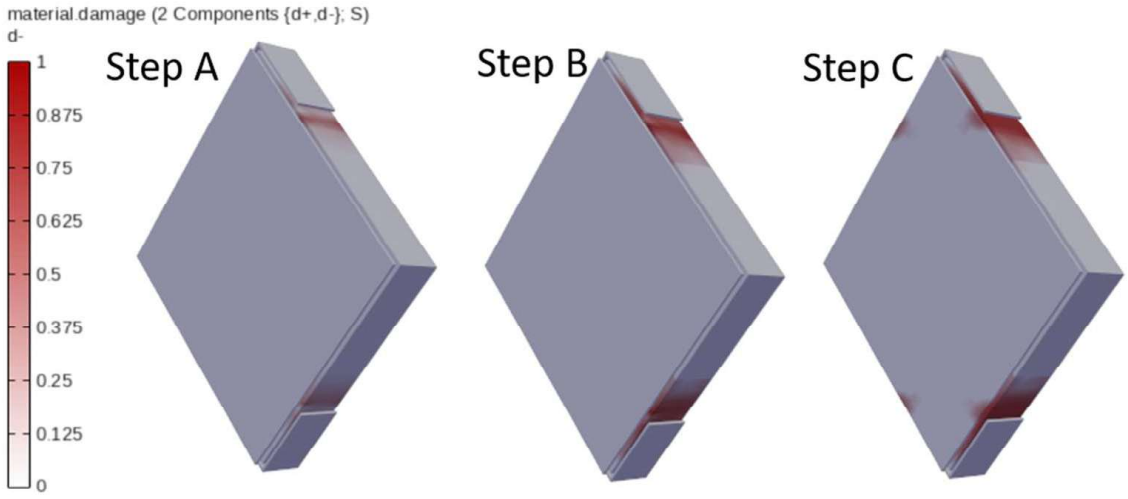


Figure 5.16 Compressive material damage for CM sample

A comparison of Figures 5.16 and 5.17 reveals that the panel is completely damaged internally, with no signs of damage observed in the mortar layer. This result confirms once again that the mortar remained within the elastic range during the test. Figure 5.18 shows the maximum principal strains under tension to confirm this behaviour.

In the colour scale used, blue corresponds to the deformation associated with the tensile strength of the reinforcing mortar, and orange corresponds to the deformation of the underlying masonry. The images depict the same loading steps as in the previous figures.

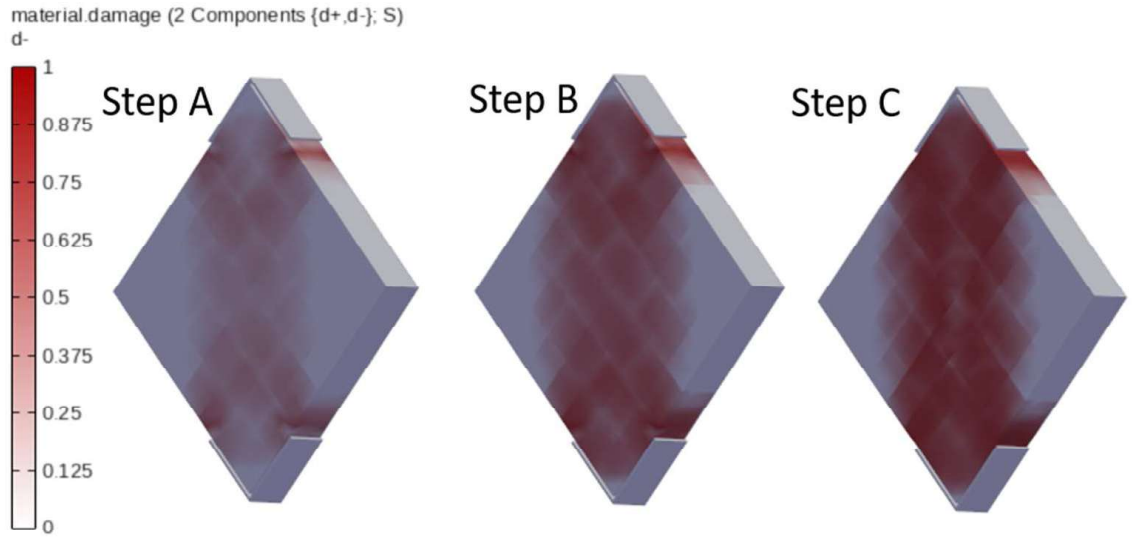


Figure 5.17 Compressive material damage for CM sample on the masonry (hiding mortar layer)

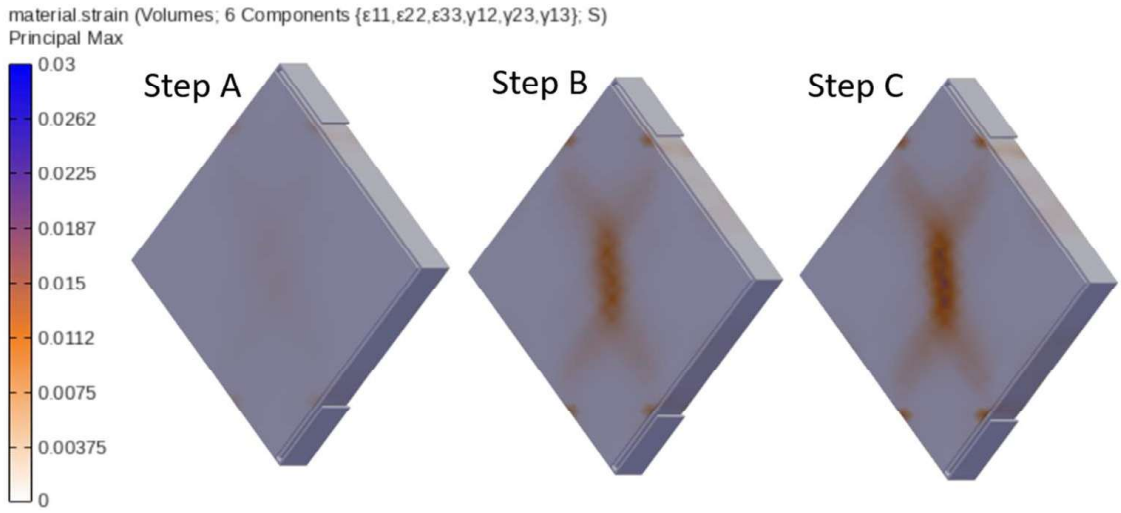


Figure 5.18 Principal tensile material stress for CM sample

Therefore, it can be seen that when the internal masonry reaches the strain corresponding to the peak strength and the damage process begins, the strains in the mortar have not yet reached the value associated with cracking.

This result supports the hypothesis formulated on the basis of the experimental results and the analysis of the correlations, indicating that better interaction

between the materials, in terms of deformation compatibility, is achieved when the strengthening systems have elastic moduli closer to that of the masonry substrate.

5.5 Additional numerical investigations

Further numerical simulations were conducted to investigate the influence of the mechanical properties of the matrix and of the masonry on the contribution of the strengthening system. These additional analyses were motivated by the hypothesis that a masonry substrate with better mechanical properties may allow the strengthening system to contribute more effectively to the overall capacity of the panel. First, a lower elastic modulus was assumed for the mortar, closer to that of the masonry, in order to investigate the effect of a more compatible stiffness between the materials. Subsequently, the compressive strength of the *calcarenite* stone units was varied, followed by another simulation in which the properties of both the stone units and the bedding mortar were modified.

Additional simulations were carried out using the numerical model of the panel reinforced with the G_FRCM system. In the first simulation, the elastic modulus of the strengthening system was reduced from 8140 MPa (Tab. 5.2) to 4500 MPa, in order to obtain a value closer to that of the masonry. The result obtained (Fig. 5.19), expressed in terms of tensile material damage, appears to indicate a more effective interaction between the materials when their deformation response is more compatible. Under these conditions, the strengthening system appears to contribute more effectively to the increase in the shear capacity of the masonry. This result consistent with the observations discussed previously, suggest greater compatibility between the mechanical properties of the masonry and the strengthening system, since it may favour a more effective stresses transfer between the two materials and, a better

contribution of the reinforcement to the overall response of the panel.

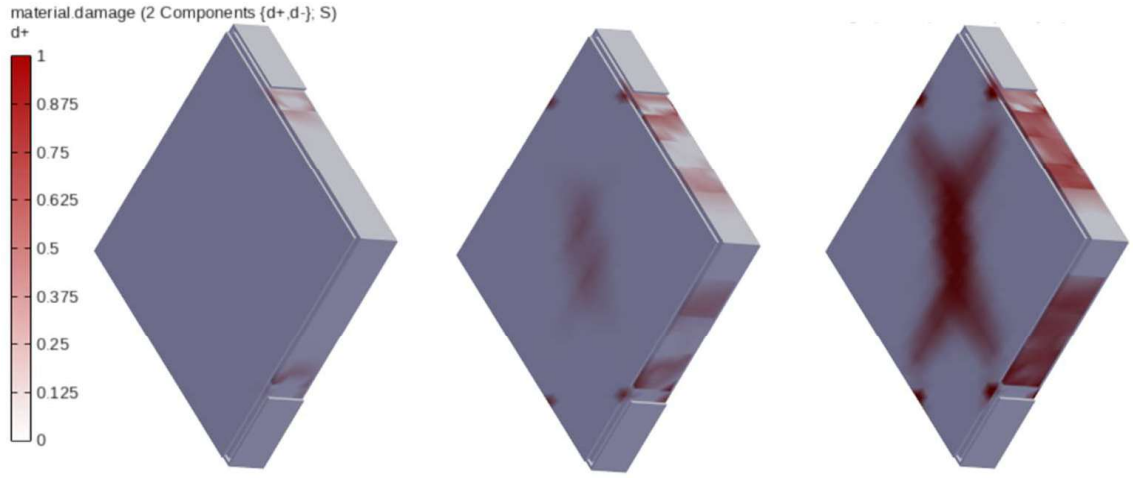


Figure 5.19 Tensile material damage in presence of weak matrix

Based on this initial configuration, further simulations were subsequently carried out by modifying the mechanical properties of the masonry, with the aim of investigating the influence of substrate quality on the contribution of the reinforcement system. In an initial simulation, the compressive strength of the *calcarenite* stone units was varied, while the properties of the reinforcement and the bedding mortar were kept constant. A compressive strength value of 15 MPa was therefore set for the units, corresponding to approximately four times the value of the *calcarenite* used in the experimental campaign and close to the compressive strength values of higher-quality *calcarenite* stone [64][65]. The remaining parameters required to define the constitutive relationship were derived from the compressive strength, using the expressions commonly adopted in the literature [127] [139][140]. The parameters used to define the constitutive behaviour of *calcarenite* are set out in Table 5.4. To facilitate comparison, the table also sets out the parameters for defining the constitutive behaviour of the mortar, as defined above and already shown in Table 4.1. Initially, a numerical simulation was carried out on the unreinforced panel, which was subsequently taken as the reference

configuration to assess the contribution of the reinforcement and the associated failure modes.

Table 5.4 Mechanical parameters for stone units

	E [MPa]	f_t [MPa]	f_{c0} [MPa]	f_{cp} [MPa]	f_{cr} [MPa]	e_{cp} [%]	G_t [N/mm]	G_c [N/mm]
Stone	15000	1.59	11	15	0.05	0.1	0.088	19.2
M5PJ	4900	0.65	4.5	4.9	0.05	0.2	0.042	10.5

Figure 5.20 compares the shear stress–shear strain response curves and the final tensile damage pattern of the unreinforced panel. The latter shows a failure characterised by a mixed sub-vertical crack, which propagated through blocks and mortar joints. A comparison of the overall responses shows an increase in shear capacity for the strengthened configuration.

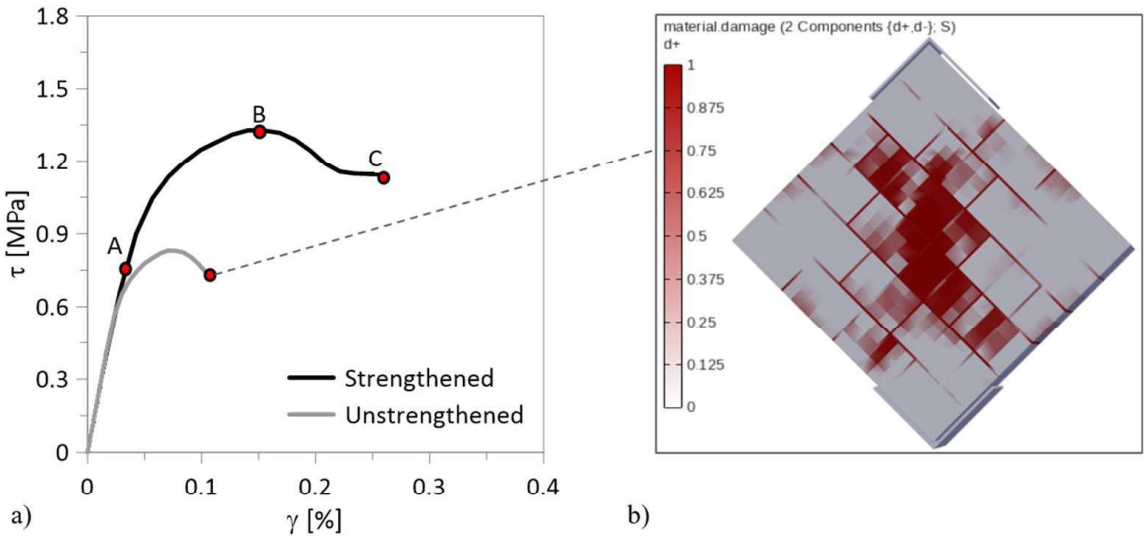


Figure 5.20 Numerical results: a) shear stress vs shear strain curve; b) tensile damage for the unreinforced configuration

Three significant stress states (Points A, B and C) were identified on the curve of the reinforced specimen, and the corresponding stages of tensile damage patterns are illustrated in Figures 5.21 and 5.22. Figure 5.21 shows the

progression of damage visible on the surface of the reinforcement, while in Figure 5.22 this layer has been omitted to allow observation of the damage on the masonry substrate. The analysis reveals effective interaction between the reinforcement system and the masonry substrate, with the progression of damage in the reinforcement closely mirroring the pattern of cracks in the underlying masonry.

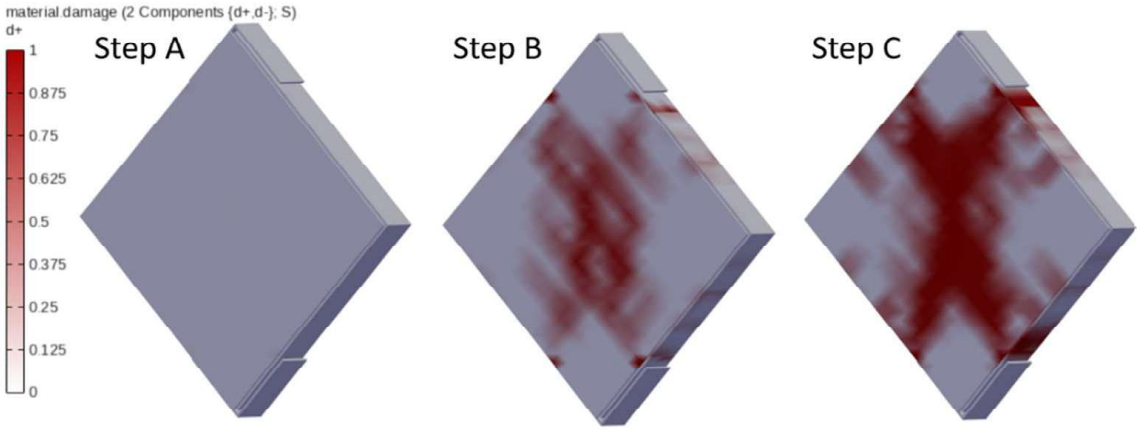


Figure 5.21 Tensile material damage pattern on the FRCM surface

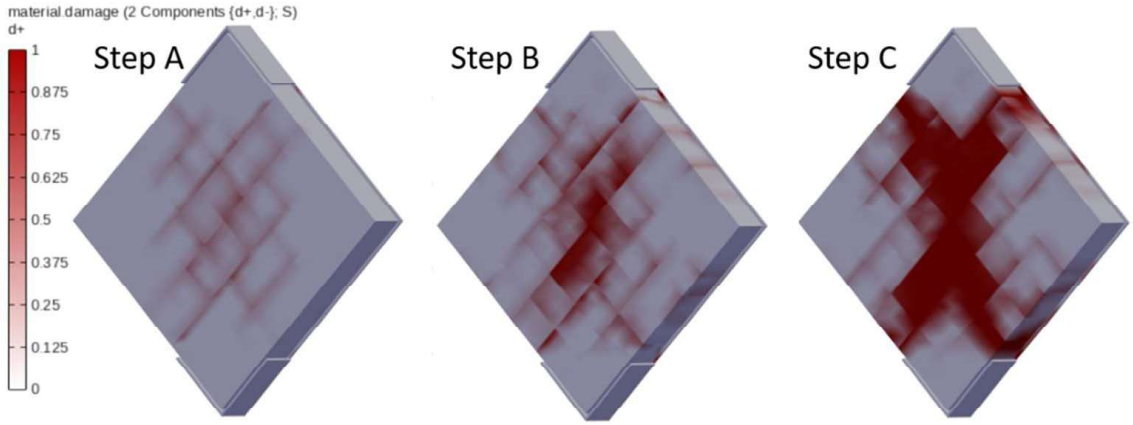


Figure 5.22 Tensile material damage pattern on the masonry (hiding FRCM layer)

Finally, the analysis of the deformation components along the z-axis, i.e. orthogonal to the panel plane, was plotted in Figure 5.23. Although minor

localized deformations are detected, they do not produce significant stress concentrations across the wall thickness, thereby excluding widespread delamination or severe through-thickness cracking. This behaviour differs from that observed in Figure 5.15 which consistently reproduced the results of the experimental test shown in Figure 4.14.

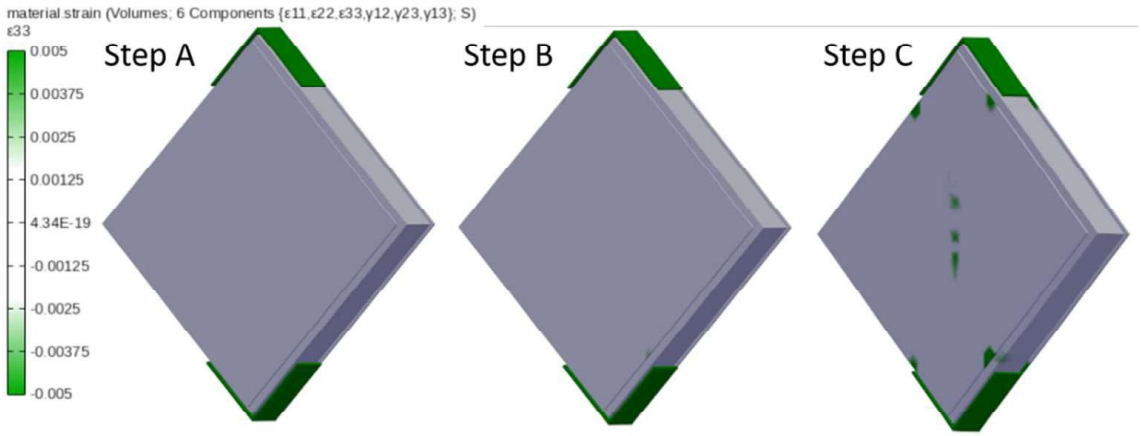


Figure 5.23 Material strain pattern on z-direction

Subsequently, configurations in which the properties of both the stone units and the bedding mortar were enhanced were considered, to represent masonry with better overall mechanical properties. These simulations made it possible to assess whether an increase in the mechanical properties of the masonry could allow greater exploitation of the reinforcement system's contribution and a consequent change in the overall response of the panel.

The parameters used to define the constitutive behaviour of stone units and mortar joints are set out in Table 5.4.

The shear stress-shear strain curves obtained for the unreinforced and reinforced configurations are shown in Figure 5.24, which also illustrates the tensile damage pattern at the end of the test for the unreinforced configuration. In this case, the damage is more widespread, and the cracks also affect the stone units.

Table 5.4 Mechanical parameters for stone units

	E [MPa]	f_t [MPa]	f_{c0} [MPa]	f_{cp} [MPa]	f_{cr} [MPa]	e_{cp} [%]	G_t [N/mm]	G_c [N/mm]
Stone units	15000	1.59	11	15	0.05	0.1	0.088	19.2
Mortar joints	10000	1.2	7	12	0.05	0.1	0.077	17.4

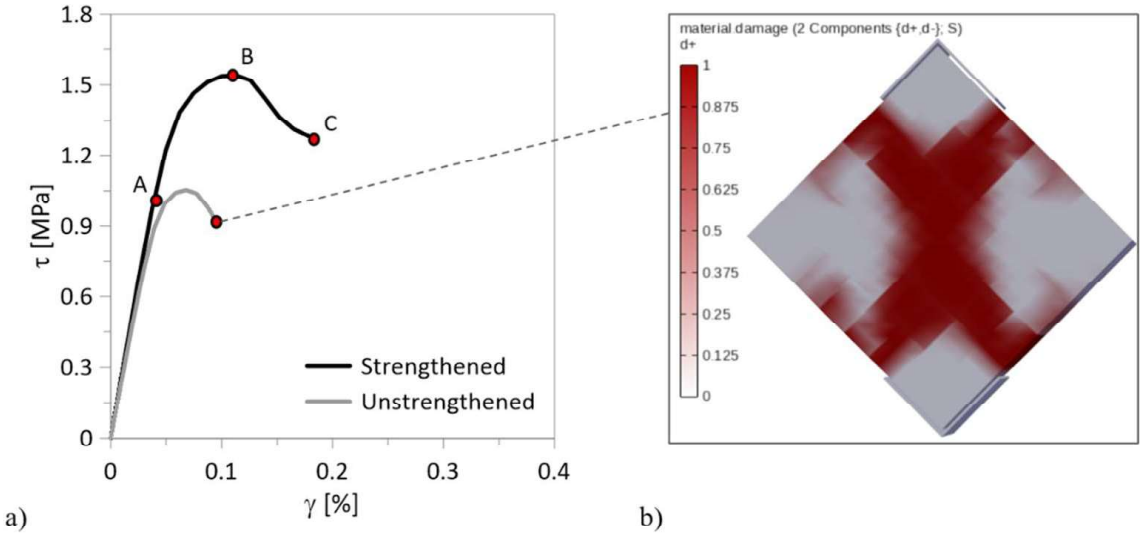


Figure 5.24 Numerical results: a) shear stress vs shear strain curve; b) tensile damage for the unreinforced configuration

Three points, A, B and C, have been identified on the curve for the reinforced configuration, corresponding to the damage patterns shown in Figures 5.25, 5.26 and 5.27. Figures 5.25 and 5.26 show, respectively, the evolution of tensile damage on the surface of the reinforcement and in the masonry layer. In this case too, the reinforcement appears to work effectively with the masonry, promoting a more widespread distribution of damage.

Figure 5.27, on the other hand, shows the deformations in the direction perpendicular to the plane of the panel. At the final loading step, some localised deformations are evident at the shoes, where stress concentrations may occur, and in the central area of the panel, which is characterised by higher stresses.

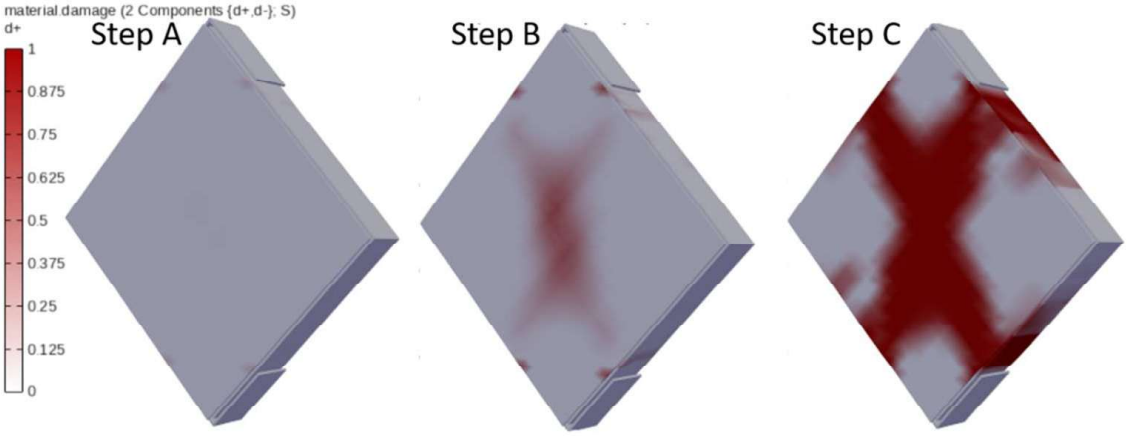


Figure 5.25 Tensile material damage pattern on the FRCM surface

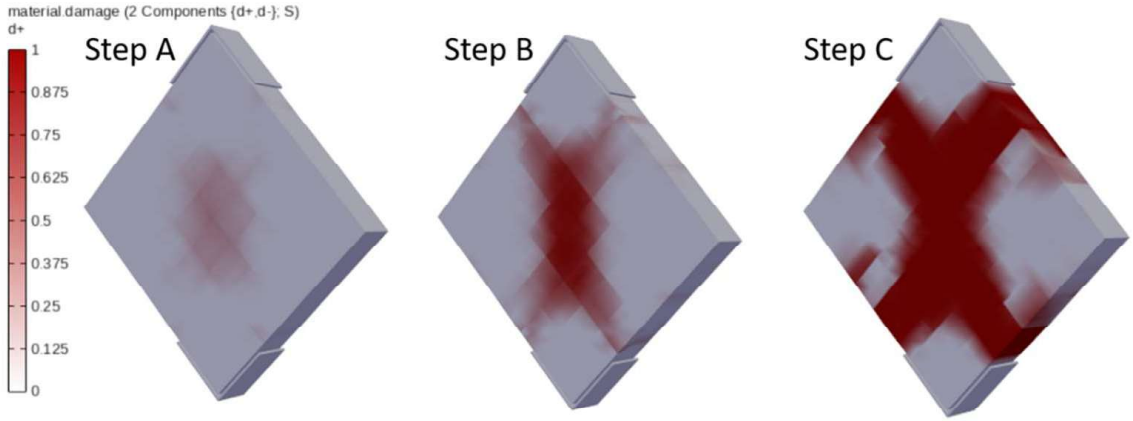


Figure 5.26 Tensile material damage pattern on the masonry (hiding FRCM layer)

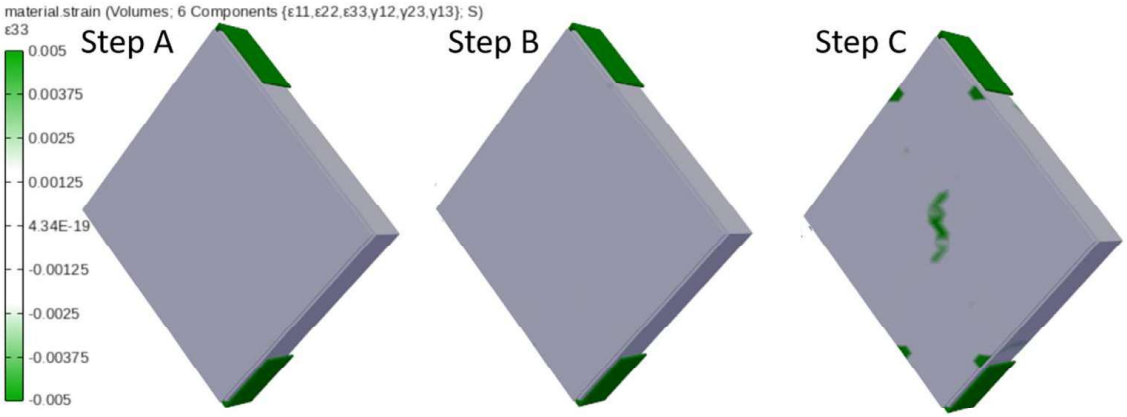


Figure 5.27 Material strain pattern on z-direction

Overall, the simulation results are consistent with the hypothesis formulated based on experimental evidence, which suggests that collapse is governed by compressive failure of the masonry rather than the expected diagonal cracking. While the numerical analyses demonstrate good interaction between the reinforcement and the masonry, they also highlight that the system's response is still strongly influenced by the mechanical properties of the masonry, particularly the stone units. The numerical results therefore suggest that, in the case under investigation, the improvement in performance is not exclusively governed by the capacity of the strengthening system, but by the interaction between the strengthening system and the local characteristics of the masonry, providing a more refined interpretation of the failure of the diagonal cracking mechanism experimentally observed.

Chapter 6

Experimental Campaign on Calcarenite Masonry Vaults

The issue of reinforcing masonry vaults is particularly relevant today, given the increasing focus on preserving our country's historical and cultural heritage. Although the geometry of these structures allows them to withstand high vertical loads, their behaviour under different load conditions and actions can significantly impact their equilibrium and load-bearing capacity. Therefore, it is crucial to identify effective reinforcement techniques that can increase the vaults' load-bearing capacity without compromising their compatibility with the existing structure. In recent decades, various intervention techniques have been investigated, many of which are based on the use of composite materials. When applied to the extrados or intrados of the vault, these materials are able to prevent or delay the opening of hinges, a phenomenon typical of the kinematic collapse mechanisms of vaulted structures, thanks to their mechanism of action. Generally, the idea that inorganic matrix composite materials (FRCM and CRM) are more compatible than polymer matrix systems also apply to vaults, offering a potential solution for reinforcing historic structures. Furthermore, these systems allow for the use of mechanical anchors that can limit debonding, which is particularly important for applications of this type.

However, as previously mentioned, despite the effectiveness of CRM

composites in enhancing the load-bearing capacity and ductility of vaults being proven, the number of experimental studies available in the literature remains limited. In fact, many aspects require further investigation. These include the possibility of adopting different application schemes with various combinations of materials and anchoring systems, and the effectiveness of such systems on vaults with pre-existing damage.

Another critical issue is the compatibility between the strengthening system and the masonry substrate, especially when the masonry consists of materials with poor mechanical properties, such as soft stone, which is commonly found in historical residential buildings. The difference in mechanical properties between the strengthening material and the masonry can influence stress transfer and distribution within the strengthened structure, thereby affecting its overall behaviour.

Additionally, a topic of recent interest is the potential for combining the mechanical performance of the reinforcement system with thermal performance, enabling an integrated approach to seismic and energy retrofitting. In this context, the experimental study presented in this paper aims to improve the understanding of aspects that have not yet been fully explored. The experimental programme was developed to study the effectiveness of CRM systems applied to vault specimens made of soft stone masonry, specifically *calcarenite*. Tests were conducted on three medium-scale vault specimens, which were subjected to load tests with the vertical load applied at one quarter of the span, to simulate an antisymmetric load condition that maximizes bending effects and to promote the development of a collapse mechanism that is clearly identifiable. Different reinforcement configurations were investigated to evaluate the system's effectiveness under conditions of both pre-existing and no initial damage to the vault. Additionally, the distribution of anchors and the restraint conditions of the specimens were

varied. Finally, a CRM system is analysed consisting of a geopolymer matrix, with the aim of identifying a solution that can combine seismic and energy efficiency requirements. To this end, thermal characterisation tests were performed on two specimens: one reinforced with traditional mortar, and one with geopolymer mortar.

The investigation was conducted using the DIC technique to provide a thorough description of the kinematics and the damage evolution that occurred during the tests. A section of the unreinforced vault was also analysed using numerical modelling to gain a deeper understanding of collapse mechanisms.

6.1 Experimental plan

In light of the findings from studies on barrel vaults reinforced with CRM systems, the experimental campaign was designed to analyse the influence of different conditions, such as the presence of pre-existing damage, different connector distributions, the use of two different types of mortar, one traditional and one geopolymer-based, and different constraint conditions. Table 6.1 provides an overview of the specimens, indicating the materials used (Table 3.1), and the configurations adopted for each of them. The first column of the table lists the test identification codes that will be used throughout this document to describe the various tests. The second column shows the sequential number of the sample subjected to each test. The third column provides a description of the system configuration used. Columns four and five list the materials and connectors used for the CRM system, as defined in Table 3.1 and described in Chapter 3. The final column lists, if any, the number and dimensions of the rods used to constrain the system. The vault specimens were constructed using MasV masonry, consisting of CSV *calcarenite* from the *Sabucina* quarry, and M5VJ lime-cement-based bedding mortar. A total of three vault specimens were constructed, on which a total of five tests were

performed: three tests on the first specimen and one test each on the other two specimens.

Table 6.1 Overview of the experimental campaign carried out as part of the present thesis

ID	Vault Spec.	Specimen description	CRM Reinforcement	GFRP connectors	Tie rods
UR/V	1	Unreinforced	-	-	-
REP/V	1	CRM repaired vault	GFRP1+M10V	LS1 distributed	-
REP/V+T	1	CRM repaired vault + tie rods	GFRP1+ M10V	LS1 distributed	4Φ20
R/V+T	2	CRM reinforced vault + tie rods	GFRP2+ M10V	LS2 distributed + end anchorage	2Φ20
R/V_G+T	3	CRM reinforced vault + tie rods	GFRP2+MVG	LS2 distributed + end anchorage	2Φ20

The UR/V test was performed on an unreinforced vault specimen, with the supports simply resting on the base and laterally on the test frame. After undergoing the first test, the same specimen was subsequently reinforced using the CRM system and retested in the REP/V configuration. At the conclusion of that test, rods were added to the system, and the load test was performed again in the REP/V+T configuration. The other two specimens, on the other hand, were fabricated, reinforced and then tested. The type of mortar used as the matrix for the CRM system differs between these specimens as above mentioned. The latter two specimens were also subjected to thermal testing. Specimen 1 differs from specimens 2 and 3 in the distribution of connectors on the surface.

The experimental campaign was characterised by significant complexity, relating both to the construction of the test specimens and the reinforcement system, and to the definition of the test conditions and the monitoring system. For this reason, the experimental campaign was conducted in two progressive phases. Moreover, the Specimen 1 was strengthened with a 40 mm-thick layer

of mortar and was specifically designed to investigate how strengthening system behaves when applied to a previously damaged masonry vault. This configuration was adopted to simulate a repair scenario on an existing damaged vault. This first phase played a crucial role in identifying some issues and informing the adjustments made in preparation for the subsequent tests. The following two tests, conducted in the second phase, used a 30 mm thick layer of mortar and were characterised by different constraint conditions. The difference in thickness is due to the specific configuration of the test specimens, while the definition of the boundary conditions was based on experience gained in the first phase. More detailed descriptions of the configuration of the individual samples will be provided in the following sections.

The relatively limited number of vault specimens tested should be considered when interpreting the influence of the individual parameters investigated. In some cases, more than one parameter was varied simultaneously, such as the matrix type, the presence of pre-existing damage and the connection conditions. Therefore, the differences observed between the tested specimens should be interpreted in relation to the combined effect of the investigated parameters, rather than being attributed exclusively to the variation of a single parameter. Nevertheless, the experimental results provide useful insights into the overall response of the different strengthening configurations and allow the influence of the investigated parameters to be discussed within the specific experimental conditions considered. A larger experimental programme in which individual parameters are varied systematically while keeping the other conditions unchanged would allow their specific effects to be further quantified

6.2 Preliminary studies

The experimental program described above was preceded by a design phase, during which the specimen geometry, test setup, and constraint conditions were

defined. Preliminary analyses were also carried out to design and calibrate the test frame, load cell and instrumentation required for the entire experimental setup.

The initial stage of the study focused on defining the geometry and dimensions of the vault specimens, based on a review of the literature on the construction characteristics of masonry vaults found in the historical heritage of the Mediterranean region. The objective was to identify a geometric configuration that was sufficiently representative of the most common types, while ensuring the feasibility of the experimental tests and the reproducibility of the results.

The choice therefore fell on medium-scale models, which are capable of preserving the main geometric and mechanical characteristics of the actual structures while limiting the challenges related to construction, testing equipment capacity, and available space. Medium-scale models are a widely adopted solution in experimental research on masonry structures because they allow the main resistance and collapse mechanisms typical of full-scale structures to be preserved, provided appropriate criteria for geometric and constructional similarity are met.

The dimensions of the vault (Fig. 6.1) were defined based on the geometric proportions most frequently found in barrel vaults of historic masonry buildings in the Mediterranean region. These are generally characterised by spans ranging from 2 to 5 metres, deflection-to-span ratios in the range of 0.20–0.35 and thicknesses varying between 0.10 and 0.30 metres. The adopted geometry thus reproduces a configuration representative of historical vaults in historical structures. This configuration allows the investigation of damage mechanisms and collapse modes representative of those that may occur in existing masonry vaul.

Accordingly, The vaults were constructed with a radius of 1 m, a thickness of 0.12 m, a span of 1.92 m and a longitudinal lenght of 1.03 m.

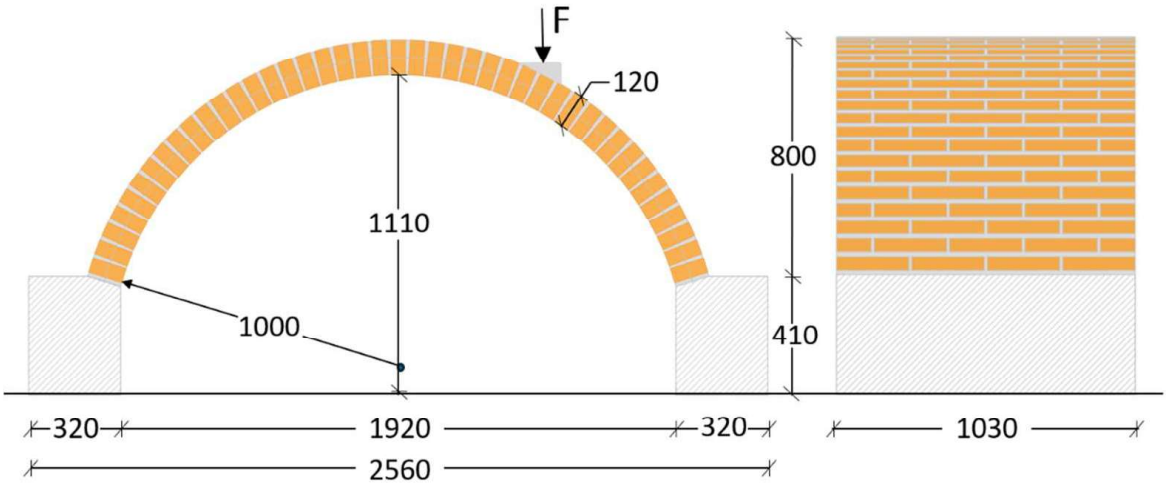


Figure 6.1 Geometry of the vault sample (dimensions expressed in mm)

After defining the geometry of the specimen, theoretical analyses were conducted to study how the vault would behave under a load applied at one quarter of the span. Well-established theories regarding the kinematics of arches were employed for this purpose, as limit analysis [141]. Heyman formalised this approach based on plasticity theory, assuming that masonry can be treated as a perfectly plastic rigid material characterised by unlimited compressive strength, zero tensile strength and an absence of slip between the blocks. Under these conditions, collapse occurs exclusively through the formation of a sufficient number of plastic hinges to transform the structure into a kinematically admissible mechanism. According to the kinematic theorem of limit analysis, the collapse load is less than or equal to that associated with any kinematically admissible mechanism. Therefore, once a possible collapse mechanism has been hypothesised, the limit load can be determined by equating the work done by the applied external forces to that performed by the permanent loads, including the self-weight and any additional surcharge. Of all the admissible mechanisms, the one that yields the minimum collapse multiplier value is the mechanism actually activated by the

structure. In the case of masonry arches, limit analysis enables the identification of hinge locations and collapse kinematics, as well as the corresponding collapse multiplier, providing a reliable estimate of the structure's load-bearing capacity [63][141].

For a preliminary assessment, a simplified numerical model was initially used to identify the kinematics responsible for the vault's collapse. Therefore, an arch with the same geometry as that defined for this experimental campaign was modelled numerically. The arch was modelled using a material exhibiting linear elastic behaviour, and unit load was applied at one quarter of the span. Subsequently, the deformation behaviour was analysed (see Fig. 6.2), which enabled the four-hinge mechanism responsible for the collapse of the arch to be identified for this geometry.

The positions of the four identified hinges were useful for determining the limit load in accordance with the kinematic theorem. This method involves finding the collapse multiplier by taking the minimum of the kinematically admissible multipliers. A kinematically admissible multiplier s is defined as a multiplier of the variable external load for which a kinematic mechanism can be identified that satisfies the condition of equality between the work produced by the fixed load and variable load and the internal work associated with the displacements of the kinematic mechanism, as:

$$L_{f0} + s * L_{fL} = 0 \tag{6.1}$$

where L_{f0} represents the work done by the permanent load, consisting in this case of the vault's own weight, while L_{fL} represents the work done by the external load. Using the theorems of kinematic rods, the centres of absolute rotation C1, C2 and C3 nd the centres of relative rotation C12 and C23 were identified (Fig 6.3).

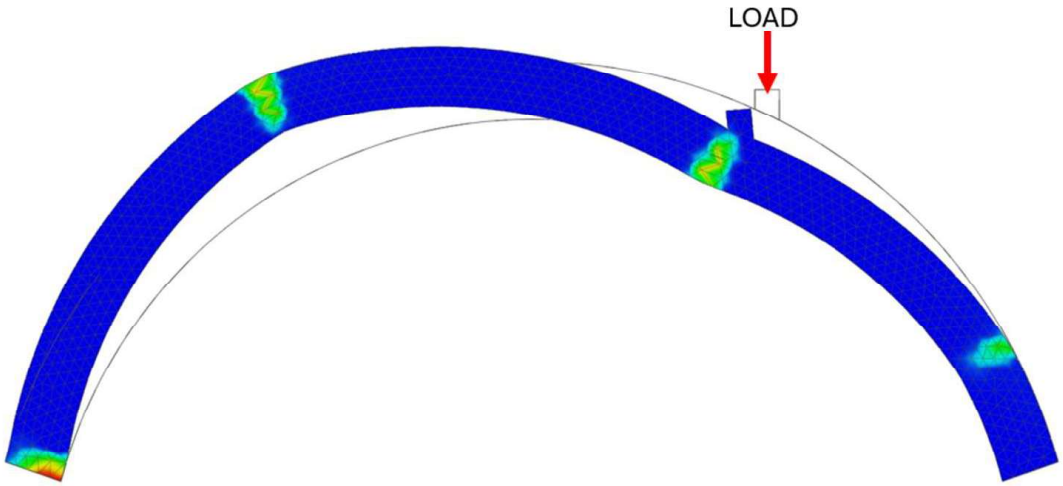


Figure 6.2 Simplified numerical model to estimate the hinges position

Figure 6.3 shows three of the analysed scenarios. For each configuration, the limit load (F) was derived by applying the principle of virtual work. This involved treating the integral of the vault's dead weight as a uniformly distributed load and multiplying it by the virtual displacements associated with each unit.

The limit load F is therefore determined by:

$$F = -\frac{\int_0^L q * \delta_{Pi} dL}{\delta_F} \tag{6.2}$$

where q represents the weight of each block and, δ_{Pi} represents the i^{th} virtual displacement in the x-direction of the individual block, derived from the diagram, δ_F epresents the virtual displacement in the x-direction at the point of application of the external force F. Several limit load values were ultimately identified, from which the minimum value, F_3 = 2.32 kN, was selected and shown in Figure 6.3. This value corresponds to the limit load of the structure and was used as a reference for direct comparison with the capacity curves obtained through numerical modelling, which are described in more detail in Section 6.6.

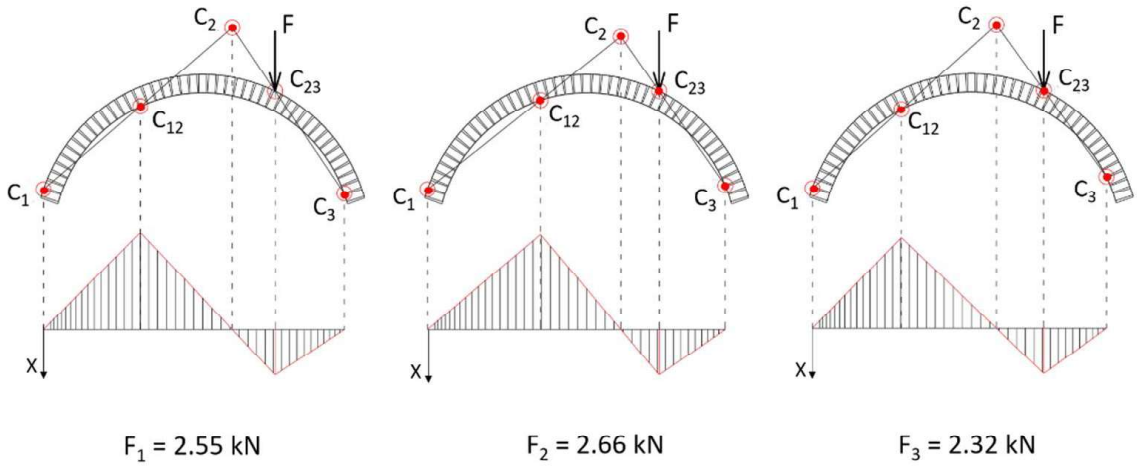


Figure 6.3 Collapse cinematisms hypothesis

6.3 Geometry and construction of masonry vault specimens

Once the geometry had been defined, samples of the masonry barrel vault were prepared. The vault was constructed using the masonry identified in this study as MasV, which consists of CSV *calcarenite* from the *Sabucina* quarry in Sicily and M5VJ bedding mortar. The blocks used to construct the vault measured 120×55×250 mm.

This section describes the procedure for producing the specimens, while subsequent sections present the results of the experimental tests.

6.3.1 Unreinforced Vault sample (Specimen 1, UR/V)

The vaults were constructed using a running bond pattern for the masonry, with mortar joints averaging 1 cm in thickness. Due to the material's high porosity, the blocks had to be saturated with water before laying to prevent them from absorbing the mixing water from the mortar during the setting and hardening stages. A special metal formwork was realized to construct the vault and was subsequently removed before load tests were carried out (Fig. 6.4).

The vault Specimen 1 was constructed with the aim of initially being tested in an unreinforced UR/V configuration and of serving as a basis for comparison with the subsequent reinforced specimens. As shown in Figure 6.4, the

specimen was constructed on concrete support blocks. These elements act as supports for the vault; they simply rest on the base plate and are in contact with the lateral restraint frame. The space between the concrete blocks and the restraint frame was filled with metal plates.

Once the specimen had been constructed, the formwork was removed and the wedge for applying the load was placed (Fig. 6.5). The wedge, positioned at one quarter of the vault's span, was made of concrete and subsequently finished with a thin layer of self-levelling mortar to ensure adequate contact with the metal beam used for the subsequent application of the load during the test.



Figure 6.4 Vault centering and vault realization (photo taken during the experimental activities)



Figure 6.5 Completion of the vault and construction of the support structure for load application (photo taken during the experimental activities)

6.3.2 CRM Repaired vault sample (Specimen 1, REP/V and REP/V+T)

The specimen configurations identified by the codes REP/V and REP/V+T correspond to the Specimen 1. Strengthening system was applied to this specimen after the first load test had been carried out. Holes were drilled into the specimen's surface for installing LS1-type preformed L-shaped connectors. These were drilled to a depth of approximately 80 mm and a diameter of around 16 mm to allow the vinyl ester resin to be inserted for anchoring the connectors. Figure 6.6 shows the applied reinforcement and the layout of the connectors. To allow easier installation of the mesh later on, all the connectors were oriented in the same direction (Fig. 6.7a).

Before applying the reinforcement, the vault's surface was thoroughly cleaned and treated with a water-based acrylic primer to remove residual dust and improve the surface condition of the masonry substrates. Recommended by the manufacturer of the reinforcement system, the product ensures the surface consolidation of the substrate prior to the application of the reinforcement, thereby improving adhesion between the materials. Figure 6.7 shows the reinforcement application process. The connectors were inserted before the first layer of mortar was applied (Fig. 6.7a). After fixing the connectors, the first 20 mm-thick layer of mortar was applied (Fig. 6.7b). The mesh was then positioned to ensure the connectors were correctly inserted within the reinforcement system (Fig. 6.7c). Finally, a second 20 mm-thick layer of mortar was applied until the total reinforcement thickness reached 40 mm (Fig. 6.7d). The resulting configuration is named REP/V. This configuration was then subjected to a load test. Once the test was complete, rods were inserted, resulting in the configuration known as REP/V+T. The rods were inserted into the concrete blocks on which the vault rests. Specifically, four bars with a diameter of 20 mm were installed and anchored to both the inner and outer sides of the support system.

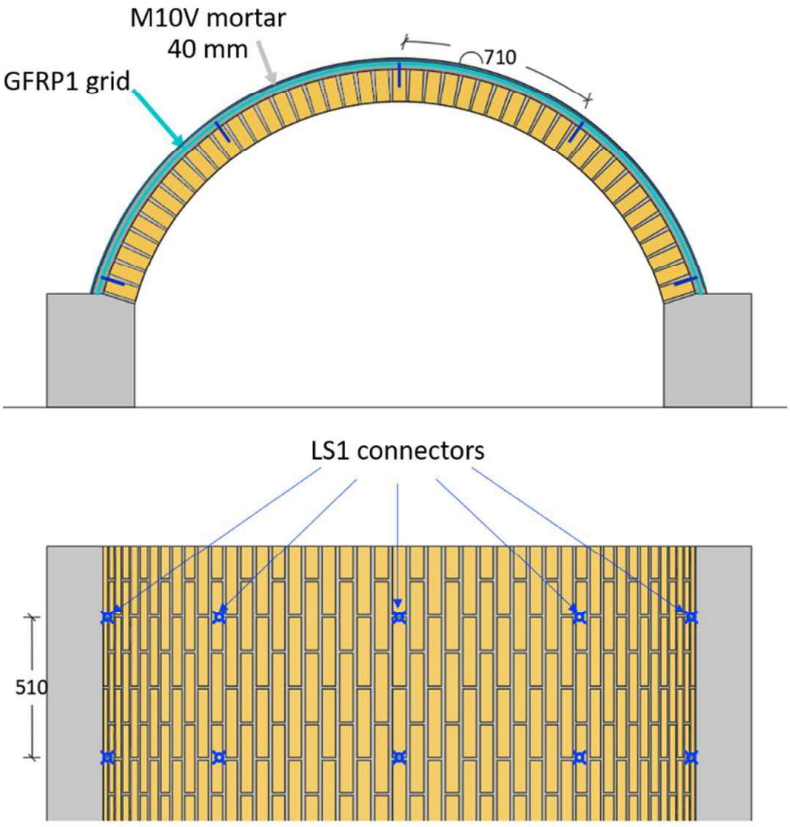


Figure 6.6 Connectors application scheme on strengthened Specimen 1

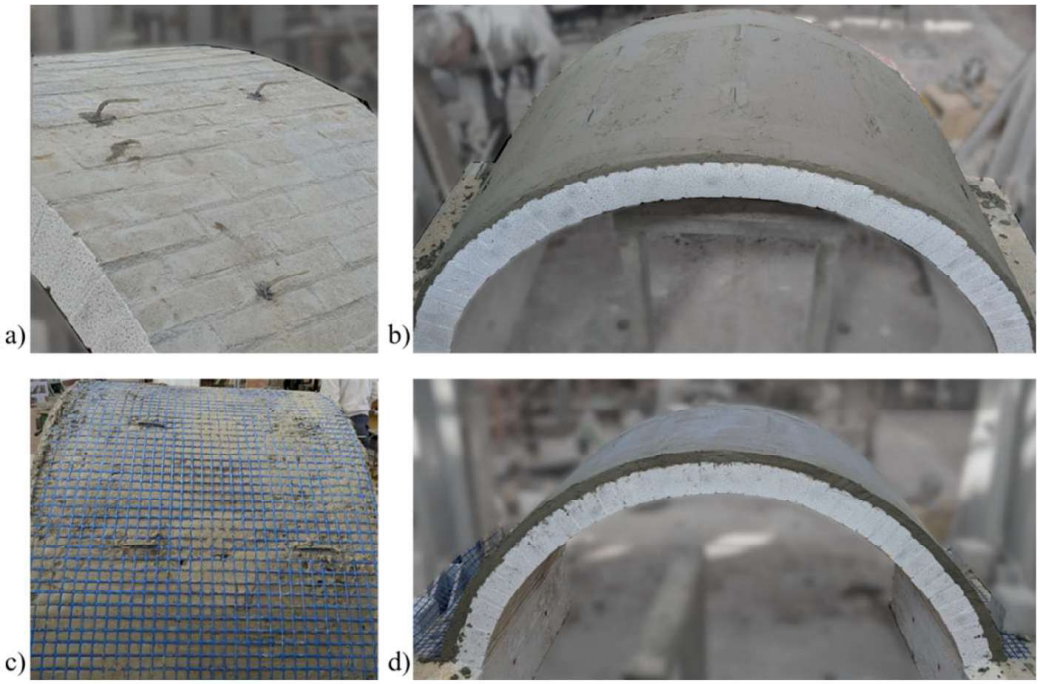


Figure 6.7 CRM application in REP/V configuration (photo taken during the experimental activities): a) LS1 connectors application; b) first layer of M10V mortar; c) GFRP1 grid application; d) second layer of M10V mortar.



Figure 6.8 Tie rods application on REP/V+T configurations and detail on end anchor **(**photo taken during the experimental activities**)**

6.3.3 CRM Reinforced vault samples (Specimen 2, R/V+T and Specimen 3 R/V_G+T)

The configurations adopted for specimens 2 and 3, which were fabricated and directly reinforced using the CRM system, differ from that of the Specimen 1, particularly in terms of the boundary conditions, which were defined taking into account the experience gained during the previous test. The vaults were in fact constructed on reinforced concrete supports connected to a base plate. The latter was anchored, by means of appropriate connections, to the laboratory floor slab, which was 1 m thick. This configuration provided a rigid constraint at the base, preventing both relative displacements between the supports and absolute displacements of the system. Furthermore, rods were installed between the two vertical supports on which the vault rests (Fig. 6.9).

Also in this case, before applying the reinforcement, the vault's surface was thoroughly cleaned and treated with a water-based acrylic primer. The two specimens were fabricated according to the same construction method and differ in terms of the matrix used in the CRM reinforcement system. In the R/V+T configuration, the CRM system consists of a traditional mortar, similar to that used in the previous cases, whilst in the R/V_G+T configuration, the CRM system uses a geopolymer mortar. Holes were drilled into the specimen's surface to accommodate the LS2-type preformed L-shaped connectors. These

were drilled to a depth of around 80 mm and a diameter of around 16 mm to allow the vinyl ester resin, which was used for anchoring, to be injected. The layout of the connectors is shown in Figure 6.9. Compared with the previous configuration, the spacing between the connectors on the vault's surface has been reduced in this case, with two additional rows of connectors featuring reduced spacing introduced near the supports (highlighted in red in Fig. 6.9) in order to avoid premature strengthening system's detachment. To ensure correct installation of the mesh, the connectors were fitted at the same time as the reinforcement was applied by inserting them into the pre-drilled holes.
Figure 6.10 shows the process of applying the reinforcement system.

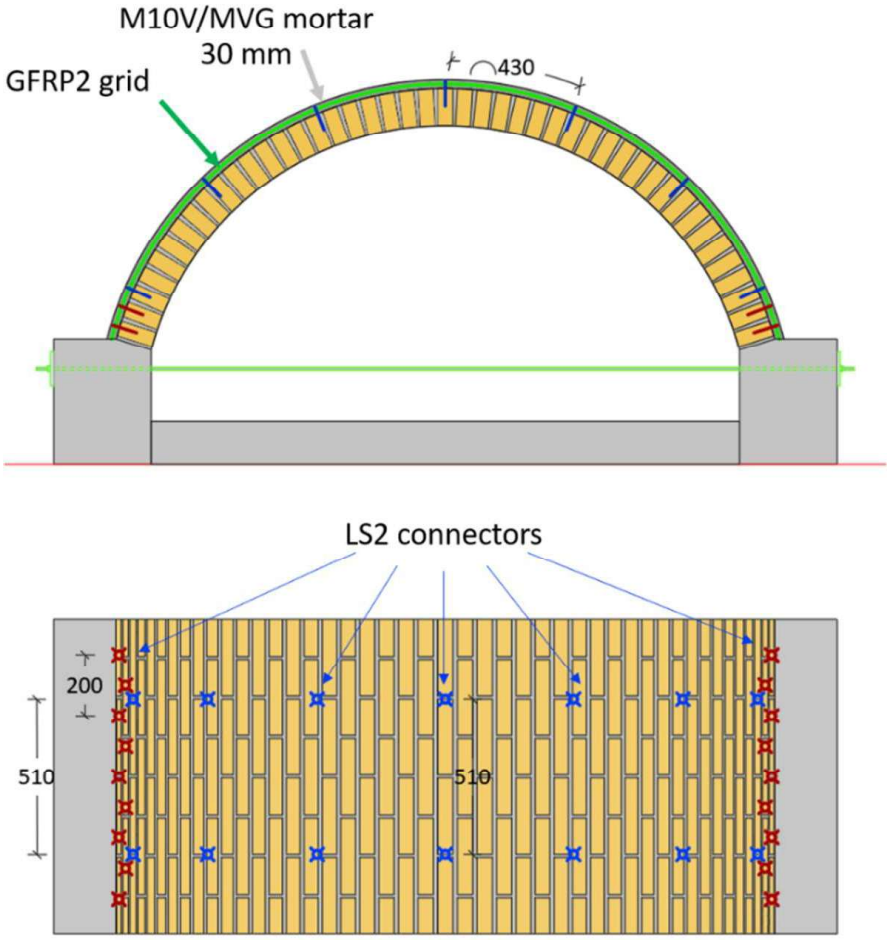


Figure 6.9 System configuration and connectors application scheme on Specimen 2 and 3

After drilling the holes for the connectors and temporarily sealing them (see Fig. 6.10a), the first layer of 15 mm-thick mortar was applied. The GFRP2 mesh was positioned and secured by inserting the connectors into the pre-drilled holes at the same time (Fig. 6.10b). Finally, a second 15 mm-thick layer of mortar was applied and the surface finished to achieve a uniform total reinforcement thickness of 30 mm (Fig. 6.10c). Once prepared, the specimens were anchored to the laboratory's base slab using a base plate and large screws. Figure 6.10c shows the anchoring system at the base of the specimen.

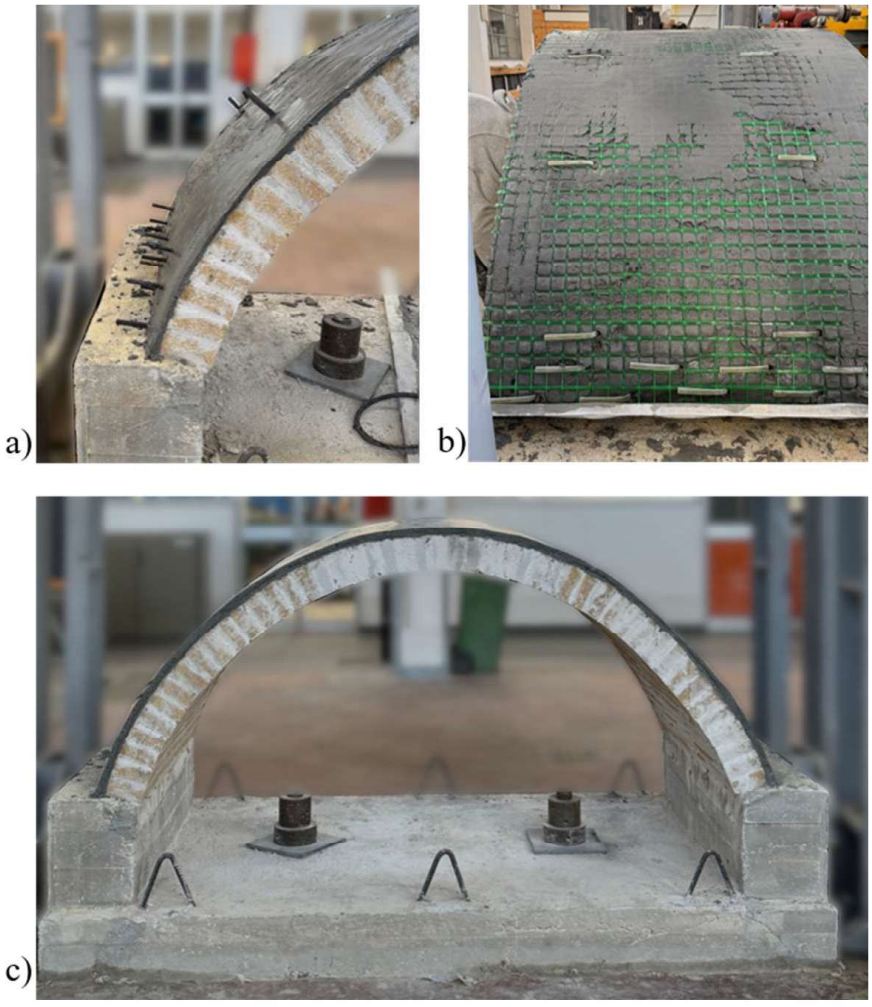


Figure 6.10 CRM application (photo taken during the experimental activities): a) first mortar layer; b) GFRP2 grid and connectors application; c) second mortar layer

6.4 Load test and monitoring setup

All the tests on the vaults were carried out by positioning the specimens within a steel contrast frame that was anchored to the laboratory's strong floor (Fig. 6.11). For Specimen 1 in the UR/V, REP/V and REP/V+T configurations, the concrete base supports were placed in contact with the columns of the steel test frame. Steel plates were inserted at the interface to fill the gap between the concrete supports and the frame. For specimens 2 and 3 in the R/V+T and R/V_G+T configurations, a reinforced concrete slab was constructed to encase the vault's base supports. This slab was subsequently anchored to the strong floor. The load was applied at one quarter of the vault's span along the full length of the vault, to simulate an asymmetric loading condition that would maximise bending effects.

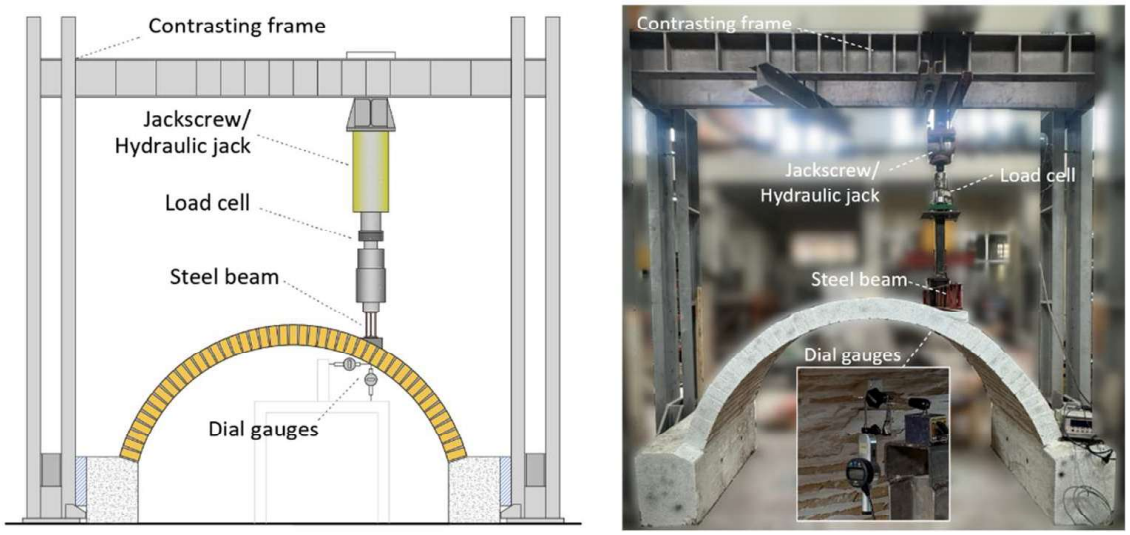


Figure 6.11 Test set up and instrumentation (photo taken during the experimental activities)

All vault specimens were fitted with a concrete wedge that was cast directly onto their surface. The wedge is approximately 10 cm wide and extends across the entire length of the vault. This was necessary in order to accommodate a braced steel beam for the subsequent application of the load. This ensured that

a vertically distributed load was applied uniformly along the entire length of the vault. The load was applied for the various configurations using different jacks and load cells selected according to the expected strength of the specimens under the various test conditions [142]. For the unreinforced vault, a jackscrew with a maximum nominal capacity of 50 kN was used at a displacement rate of 0.4 mm/min. For the reinforced configurations, characterised by higher expected strengths, a manually operated hydraulic jack with a nominal capacity of 200 kN was used.

The appropriate instrumentation was set up to monitor the specimens' behaviour during the test. Two dial gauges were positioned on the intrados of the vault (Fig. 6.11), at the load application point: one to measure horizontal displacements and the other to measure vertical displacements. This allowed to monitor displacements while the load was being applied. Further pairs of dial gauges were installed in the same positions and at other points on the vault to ensure redundancy in the measurements. Figure 6.11 shows a schematic representation of the test setup and depicts one of the specimens (UR/V) within the complete experimental configuration, including the instrumentation.

The 2D-DIC technique was selected as appropriate for the test since the expected displacements occur predominantly along the vertical direction of load application. One of the specimen's surfaces, referred to hereafter as the "front side", was prepared for the application of the technique (Fig. 6.12). The equipment comprised two LED light sources positioned close to the specimen to ensure good image quality and prevent shadows that could interfere with the analysis. The camera was fitted with a 2.3-megapixel, high-resolution sensor with a pixel pitch of 6.00 μm. Due to the size of the sample, it was necessary to minimise the effects of image distortion. For this reason, the camera was positioned 4 m from the front of the sample and 2× magnification was used in the acquisition of the DIC data. Given the sensor resolution and the dimensions

of the acquired images, each pixel corresponds to 0.48 mm of the sample's actual surface. Image acquisition was managed using dedicated software with an acquisition rate of one photograph every three seconds to ensure correct operation of the shutter opening and closing cycles.

The image processing procedure, presented alongside the test results below, was carried out using GOM Correlate software [132]. This procedure is similar to that described for the experimental campaign on the panels (Section 4.4.3). In this case, the analysis was extended to cover the entire specimen surface, including the piers, to monitor any displacements. The entire surface was analysed to assess displacements in the x and y directions and the range of deformations. To define the analysis area, a facet size of 30 pixels and an inter-point distance of 15 pixels were adopted. The point-by-point displacement values obtained from DIC were compared with the measurements taken using dial gauges to verify the correct acquisition and reliability of the data. The following sections present the experimental results relating to the various tests carried out.

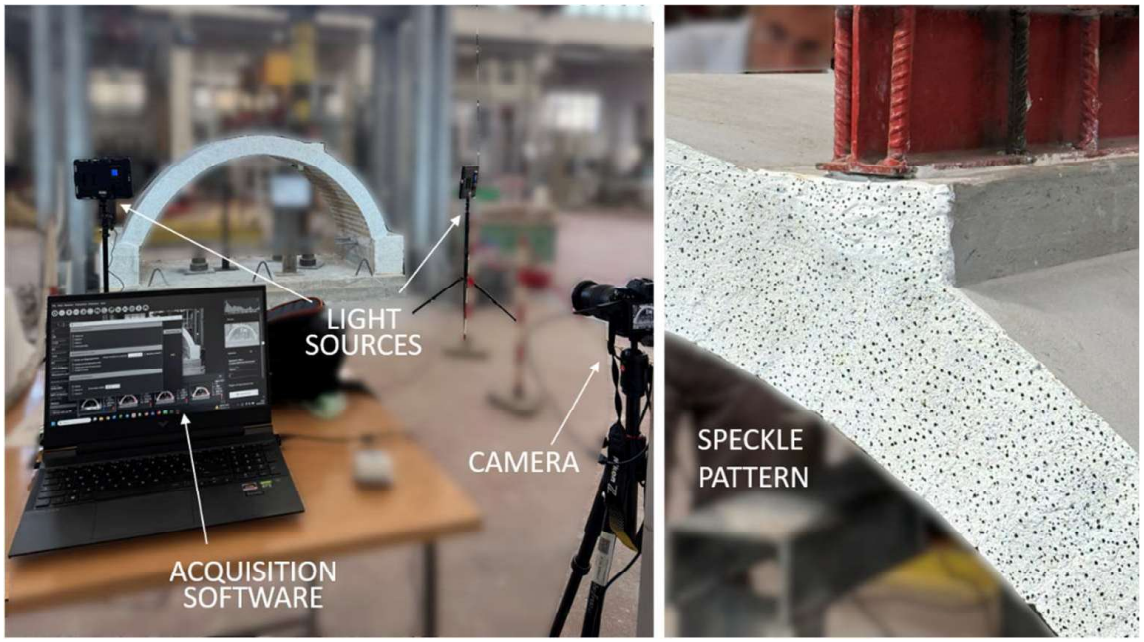


Figure 6.12 DIC arrangment: instrumentation and speckle pattern detail (photos taken during the experimental activities)

6.5 Experimental results on unreinforced vault

The initial test involved the first specimen in the unreinforced UR/V configuration. Prior to conducting the test, a preliminary numerical simulation was carried out to estimate the maximum achievable load and expected behaviour during the test, in addition to the load limit estimation described above. Due to the structure of this thesis, a description of the numerical modelling will be provided in Section 6.6.

The test was conducted applying the load monotonically until the specimen failed. Figure 6.13 shows the overall curve in terms of applied load F and vertical displacement δx, measured at the point of load application. The curve was obtained from measurements taken using a dial gauge positioned on the underside of the vault. It is consistent with the results derived from analysing images acquired using the DIC technique.

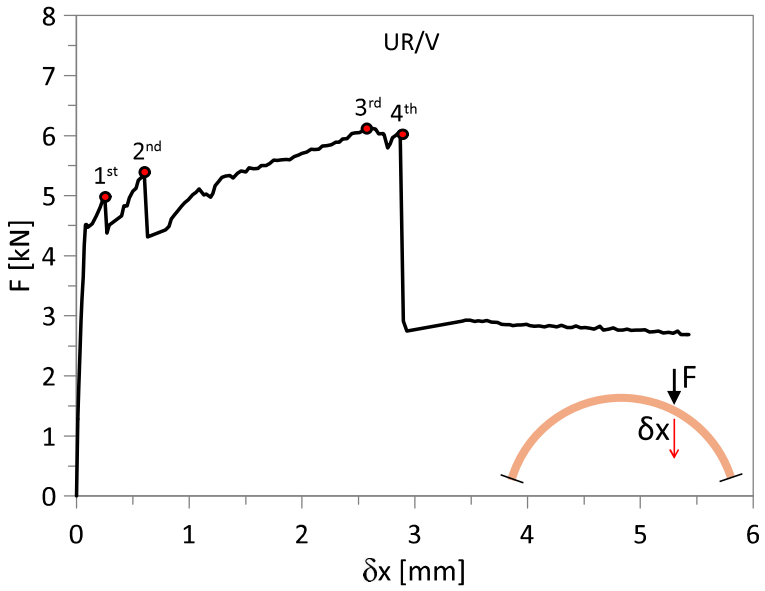


Figure 6.13 Test result on UR/V configuration: vertical load vs vertical displacement curve

The recorded response initially exhibits almost elastic behaviour, with an increasing load up to a value of around 5 kN. This value corresponds to the

formation of the first hinge at the point of load application, where a visible crack opens at the intrados of the vault (1st in Fig. 6.13 and A in Fig. 6.14). After a slight decrease, the load begins to increase again until the second hinge forms in a position that is symmetrical with respect to the first one (2nd in Fig. 6.13 and B in Fig. 6.14). After the two hinges have formed, the curve shows a further reduction in load, followed by an increase. The maximum load value of 6.13 kN, close to the value of about 7.6 kN numerically estimated using the predictive numerical model (following Section 6.6), is reached when the third hinge forms at the base joint on the side opposite the point of load application. This results in the crack opening on the intrados (3rd in Fig. 6.13 and D in Fig. 6.14). Shortly afterwards, the fourth hinge forms at the support on the side where the load is applied (4th in Fig. 6.13 and C in Fig. 6.14). This completes the formation of the four-hinge kinematic system, resulting in the final loss of load-bearing capacity and a reduction in load to approximately 2.9 kN, close to the value of 2.32 kN estimated through limit analysis.

It can be observed that the curve did not fully reflect the expected behaviour. For this type of configuration, an initially almost linear response was expected, followed by a transition to a nonlinear phase characterized by a progressive reduction in stiffness until the peak load was reached. Beyond the peak, a rapid decrease in load was expected until the limit load was attained, as typically observed in tests on arches and vaults undergoing this type of collapse mechanism. In the experimental curve several changes in slope were observed, as well as a relatively extended post-elastic phase. This behaviour was caused by an unexpected displacement identified through the analysis of the DIC data. Horizontal displacements (δy) were detected at the left-hand base support, i.e. on the side opposite where the load was applied (Fig. 6.15). This phenomenon was attributed to the settlement of the steel plates positioned at the interface between the vault supports and the steel contrasting frame.



Figure 6.14 Unreinforced vault (UR/V) damage pattern at the end of the test (photo taken during the experimental activities)

Figure 6.15 shows images of the monitored loading steps (Fig. 6.15a), together with a graph illustrating the evolution of the horizontal and vertical displacements measured below the point of load application over time (Fig. 6.15b). Synchronising the DIC measurements with the load values recorded by

the load cell enabled the horizontal displacements to be correlated with the various levels of applied vertical load via the overall curve.

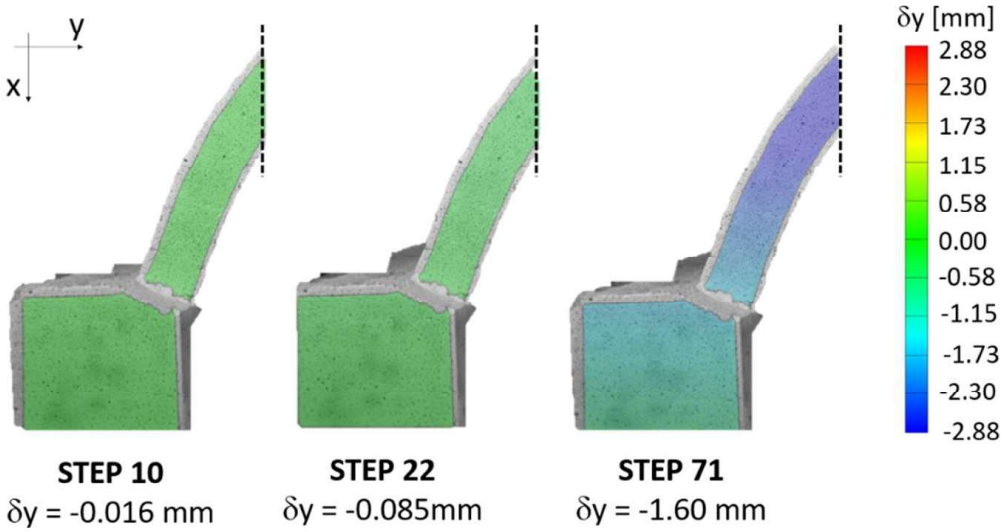
Comparing the data shown in the graphs (Figs. 6.13 and 6.15b) reveals that horizontal displacements begin at the end of the first linear section of the overall curve when the load reaches 4.5 kN, at which point the first change in slope relative to the initial elastic behaviour is observed.

Further vertical displacements occurred as a result of the horizontal displacements observed, which, when combined with the displacements directly induced by the application of the load, contributed to the particular behaviour of the recorded experimental curve. In light of this, although this condition was not initially intended, the test was considered representative of the condition of an existing vault characterised by partial horizontal restraint.

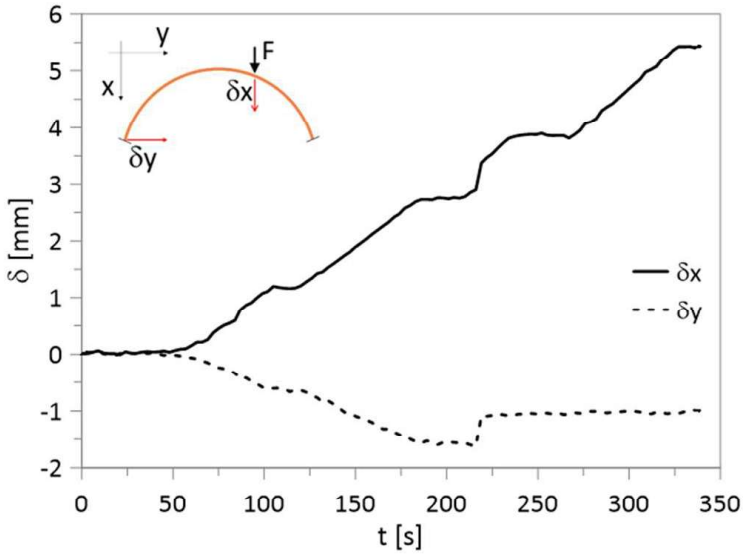
Processing the images acquired by using DIC was also crucial for accurately correlating damage to the vault with the various loading steps. By synchronising the DIC acquisitions with the recorded load values, the entire progressive deformation field was reconstructed in real time (progressive real-time deformation mapping) (Fig. 6.16). The obtained strain pattern allows the formation of hinges on the vault's surface to be identified, confirming the sequence of development of the above-described collapse mechanism. Figure 6.16a corresponds to a load of 5.12 kN. The formation of the first hinge below the point of load application is evident, along with some initial uncertainty regarding cracking. The second hinge forms simultaneously in a position symmetrical to the first. Figure 6.16b corresponds to a load of approximately 5.7 kN. Here, the first two hinges are significantly open, and the formation of a further two hinges at the base of the vault can be observed. Figure 6.16c shows the deformation pattern at the end of the test, when the two hinges at the base are fully formed and the four-hinge collapse kinematic is clearly visible.

The behaviour observed in the vault was subsequently analysed through an

update of the numerical model initially developed in the preliminary phase. Following the experimental test, the numerical analysis was refined based on the observed response, with the aim of interpreting the phenomena identified experimentally. Before describing the experimental results relating to the reinforced vaults, a brief description of the numerical model is provided. This is also useful for explaining the choices made when planning the tests, particularly those related to modifying the constraint conditions.



a)



b)

Figure 6.15 Horizontal displacement *δy* detected during the test on UR/V sample: a) three load steps; b) continuum monitoring during the full test.

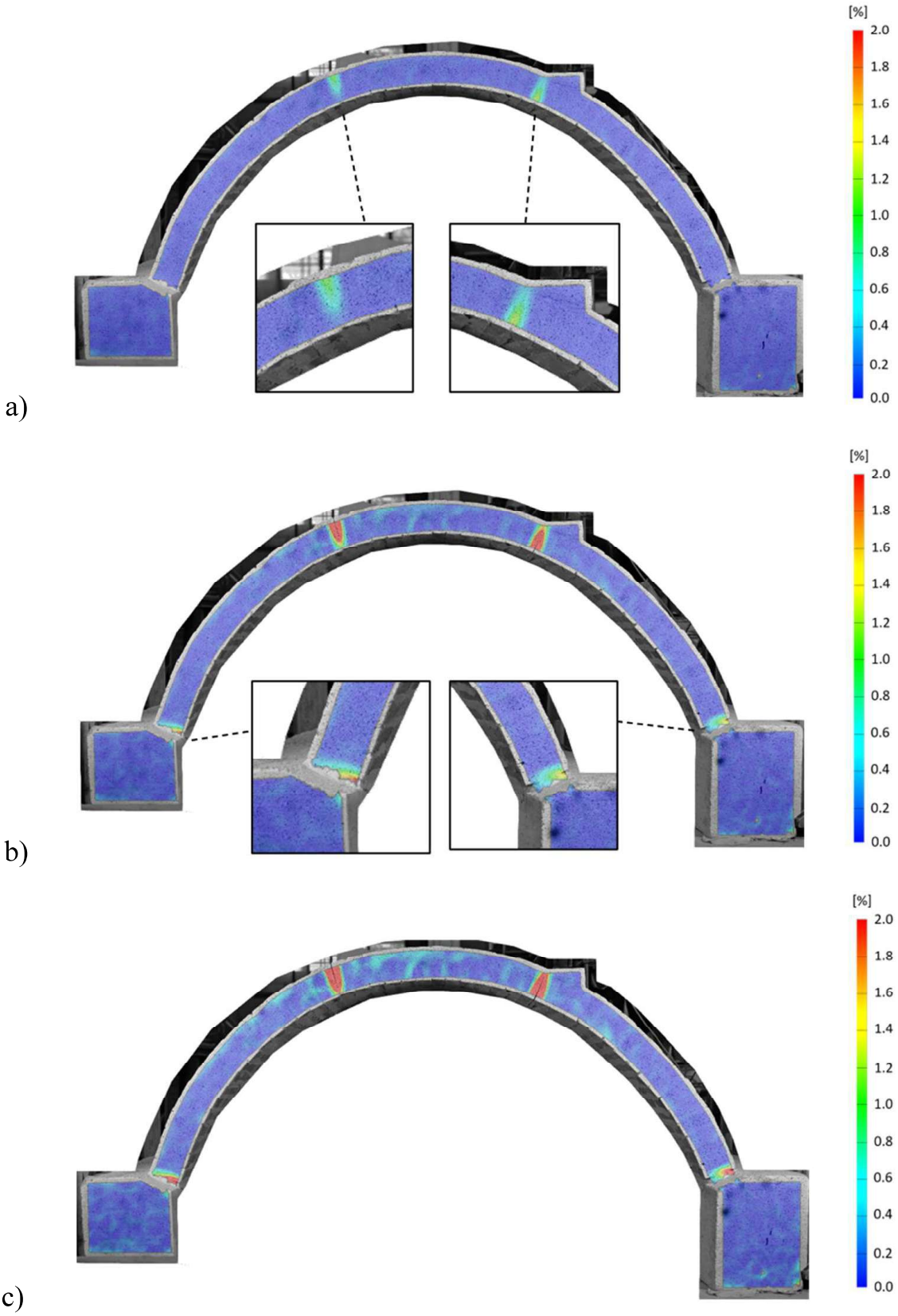


Figure 6.16 DIC strain color patterns for the unreinforced vault configuration (UR/V): a) first and second hinge formation; b) third and fouth hinges formation; c) 4 hinges failure mechanisms at the end of the test

6.6 Numerical modelling of load tests on unreinforced vault

As mentioned, the numerical modelling described here was developed prior to the experimental tests and was used to predict the expected behaviour. The preliminary numerical model was developed in a simplified form using the STKO software [135][136]. Although vaults are three-dimensional structural elements, barrel vaults can be treated as arches due to their geometry, constraints and load-bearing behaviour. Therefore, under the design hypothesis of the present experimental campaign, their behaviour can be interpreted in terms of a one-dimensional equivalent stress state.

The three-dimensional geometry of the vault was represented in the numerical model through an equivalent one-dimensional arch. This simplification was adopted to reproduce the main load-bearing mechanism of the vault while reducing the computational complexity of the model. The equivalent arch was defined based on the geometry and mechanical characteristics of the tested vault and was used to investigate its global response and main collapse mechanism. Although this approach does not explicitly reproduce the three-dimensional interaction between adjacent portions of the vault, it allows the principal longitudinal structural response to be investigated.

The static behaviour of arches is governed by the interaction between the normal force and the bending moment. The bending capacity of the cross-section is influenced by the level of axial force acting on it; in a load test, this varies according to the applied load. Therefore, it is essential to correctly represent the interaction between the axial force N and the bending moment M in static analyses under nonlinear conditions. Based on these considerations, a simplified modelling approach can be adopted in the nonlinear domain, whereby the arch surface is discretised using beam elements. This study uses 1D force-based beam elements. This formulation is based on interpolating

internal forces and integrating the response of cross-sections along the element. This allows for an accurate representation of nonlinear behaviour. The vault was discretized in 20 elements, and each element was modelled using fibre cross-sections to reproduce the N-M interaction in the nonlinear regime (see Fig. 6.17). The cross-section was therefore subdivided into 20 fibres. The cross-section was defined using three integration points and the Gauss–Lobatto integration rule.

The vault was modelled by treating the masonry as a homogenised material and combining the *calcarenite* and bedding mortar to create a single equivalent material.

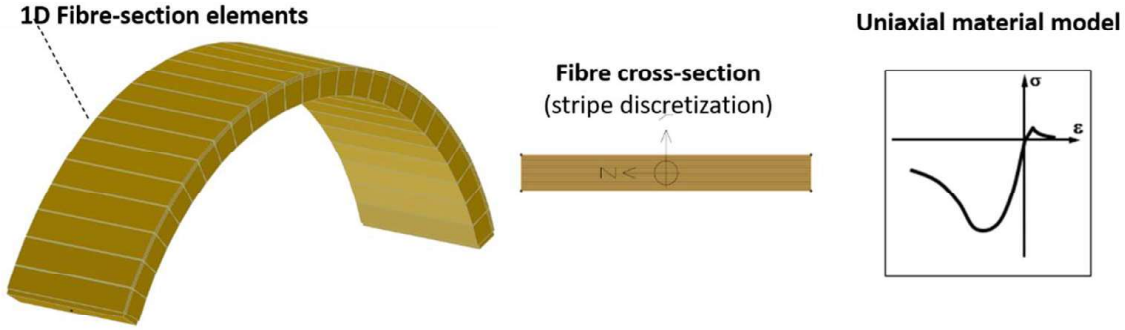


Figure 6.17 View and details of the unreinforced vault model

The constitutive model used is *ASDConcrete1D*, which has a one-dimensional formulation similar to *ASDConcrete3D*, previously described in Section 5.2.2. It enables the simulation of crack formation and subsequent crack propagation, which are typical phenomena of brittle materials. The mechanical properties associated with each fibre are shown in Table 6.2 and were defined based on the results of the characterisation tests (Tab. 3.9).

Table 6.2 Masonry mechanical parameters used for numerical modelling

E_m [MPa]	f_{cm}[MPa]	f_{tm} [MPa]	G_t [N/mm]	G_c [N/mm]
5580	7.62	0.075	0.04	8

To define the constitutive relationship, the elastic modulus E_m, compressive strength f_{cm}, tensile strength f_{tm} and fracture energy G_c and G_t of the masonry had to be determined. The elastic modulus E_m and compressive strength f_{cm} were taken as the values obtained from experimental tests (Tab. 3.9). The tensile strength f_{tm} was set at approximately one-tenth of the compressive strength. The fracture energies were calibrated starting from the expressions proposed in the literature [139]. The ends of the vault were fully constrained using the 'fix' command. The load was applied vertically at a point corresponding to one quarter of the span, in accordance with the experimental procedure. A static analysis under displacement control was set up.

6.6.1 Numerical vs Experimental comparisons

Figure 6.18 shows the results obtained from the predictive numerical modelling described above. This graph compares the results of the numerical model with the experimental curve described earlier. Furthermore, the limit load value of 2.32 kN, which was calculated during the preliminary study phase, is indicated by a red dotted line.

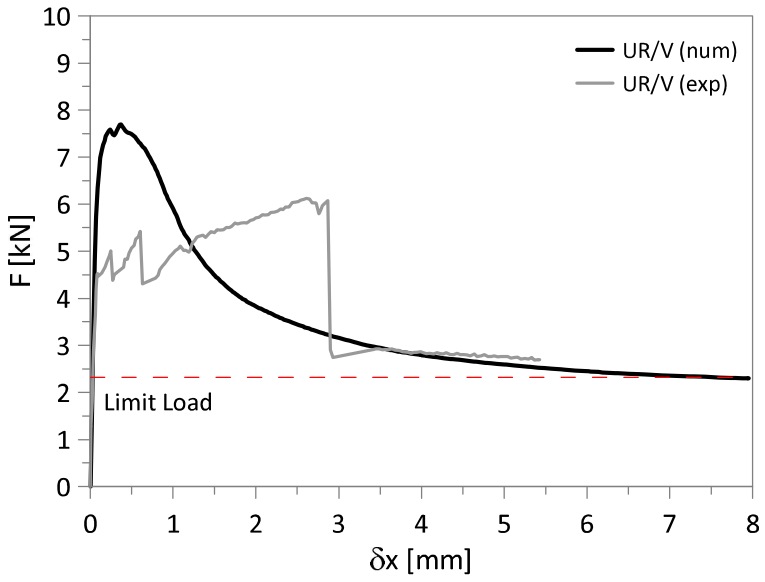


Figure 6.18 Experimental vs numerical comparison for UR/V vault

Examining the numerical results, it can be seen that the curve initially exhibits an elastic phase until the maximum load of 6.5 kN is reached. This is followed by a nonlinear phase, during which the load continues to increase until the maximum load of 7.6 kN is reached, then followed by a gradual reduction in load until the estimated limit load is reached. This result, obtained during the preliminary prediction phase, is consistent with the expected behaviour and that typically observed in barrel vaults subjected to load configurations of this type. The numerical result was then compared with that obtained from the experimental test, immediately highlighting the difference between the two curves, while the difference relating to the peak value, although overestimated by the numerical model, is within an acceptable order of magnitude. The difference between the two trends, the numerical trend representing the expected behaviour and the experimental trend observed during the test, can be attributed to the considerations regarding the displacements exhibited by the supports during the load test described above. Consequently, the type of constraint imposed in the numerical model is excessively rigid and does not fully represent the actual conditions that occurred during the test.

6.6.2 Calibration and model updating

In light of the observed behaviour, the numerical model was updated to account for the experimental response and to verify the assumptions made in interpreting the test results. An attempt was made to reproduce the yielding constraint condition by introducing a deformable horizontal constraint at the base of the model, on the side opposite the point at which the load was applied. To this end, a *ZeroLength* element was introduced in the horizontal direction on the left side, where horizontal displacement was observed during the test.

In order to define the constraint correctly, a stress–strain constitutive law was introduced that could simulate the behaviour of the constraint itself. The

horizontal displacements measured by processing the DIC results were taken into account to this end, and a time-varying horizontal force was associated with these values. This was calculated as a ratio between the applied load and the horizontal reaction obtained numerically, which was assumed to be constant as a first approximation. This relationship was then used to define the horizontal reaction transmitted to the support based on the load applied during the test. This made it possible to define the constitutive relationship shown in Figure 6.19.

The graph shows two curves: the grey curve is obtained from the experimental data, synchronising forces and horizontal displacements measurements using their respective time records; the black curve represents the simplified bilinear curve associated with the *ZeroLength* element in the numerical model.

Figure 6.20 shows the UR/V (num, ZL) curve in red. This corresponds to the result obtained by correcting the constraint in the numerical model. Plotted alongside this are the previous curve obtained from the UR/V (num) model and the experimental UR/V(exp) curve. As the comparison shows, this update enabled the model to simulate the experimental result with good accuracy. This confirms the validity of the model, albeit a simplified one, and the hypotheses put forward regarding the cause of the behaviour that differed from what was expected.

Figure 6.21 shows a graphical comparison of the strain pattern obtained using DIC and the tensile damage obtained from the numerical model. Once again, there is good agreement between the two results, i.e. strain pattern from DIC and damage plot from numerical model, confirming the validity of the modelling and the assumptions underlying the interpretation of the observed behaviour. The slight differences observed in the position of the hinges may be attributed to the assumptions and simplifications adopted in the numerical model, as well as to physical phenomena occurring in the real structure, such

as friction at the interface between the masonry and the concrete at the springing plane.

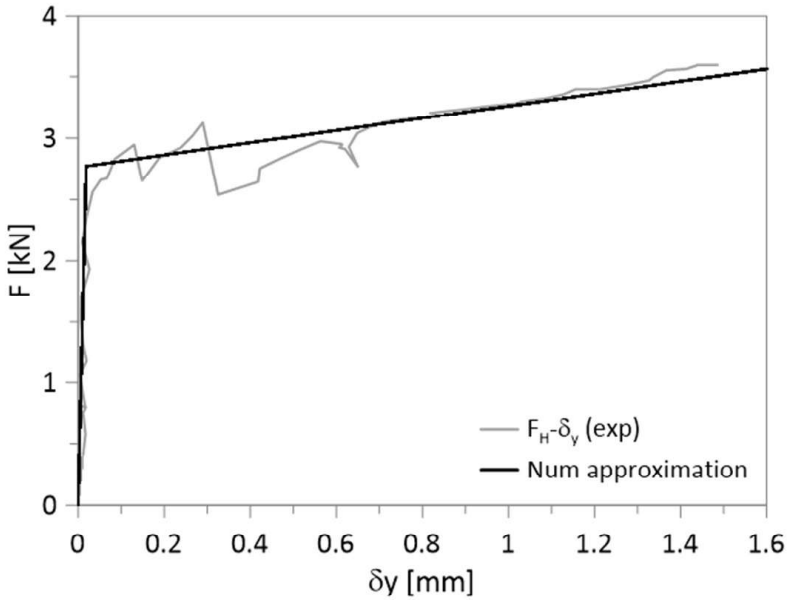


Figure 6.19 Experimental horizontal force-displacement response and numerical approximation

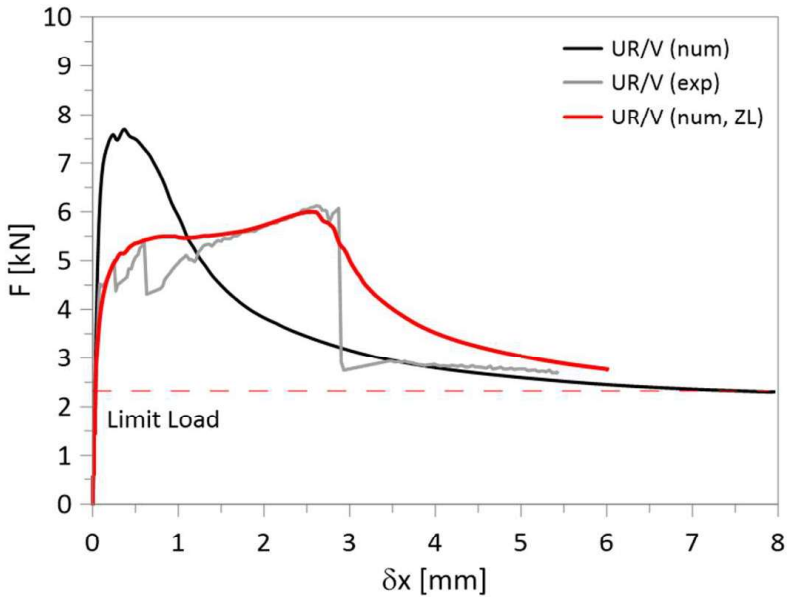


Figure 6.20 Comparison between experimental and numerical pre- and post-diction force displacement curves

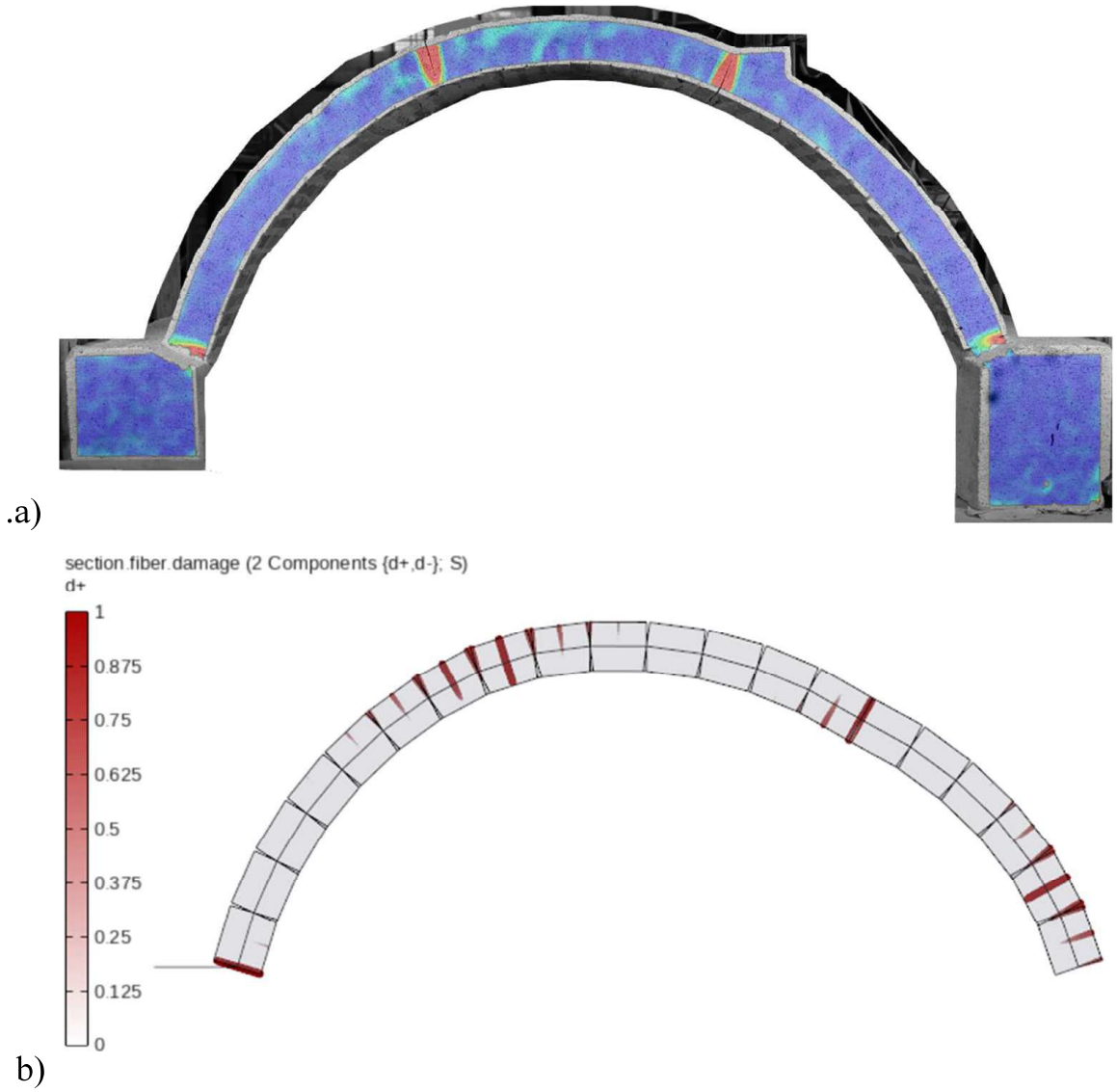


Figure 6.21 Position of the hinges after test on UR/V configuration: a) Experimental strain pattern (DIC); b) Numerical section fibre tensile damage

6.7 Experimental results on strengthened vault samples

Subsequent tests on the vaults were developed and organised based on the experimental and numerical results obtained in the previous test, as described below. In particular, the constraint conditions adopted for the following two tests were selected based on the considerations arising from the experimental observations and their numerical interpretation discussed above. The results obtained from these tests will then be compared with those of the previous test,

in order to highlight the differences in the structural response associated with the different conditions adopted.

6.7.1 CRM Repaired vault sample (REP/V and REP/V+T)

Specimen 1 was repaired using the CRM system (GFRP1 grid, M10V matrix and LS1 connectors) in its damaged state resulting from the test carried out in the UR/V configuration, and it was then tested in the configuration identified as REP/V. The test followed the same loading protocol as the previous test, with the same boundary conditions. In this case, however, steel plates were positioned at the interface between the supports and the contrasting frame. Figure 6.22 shows the curve obtained in terms of applied load versus vertical displacement, alongside the corresponding curve for the UR/V configuration in order to compare the results.

The repaired specimen initially exhibited an almost linear behaviour, with a slightly different slope compared with the previous test, due to the introduction of the reinforcement and the consequent increase in the vault thickness. This difference is not clearly visible in the figure, as the curves appear to overlap during the initial stage. The load then continued to increase until reaching a value of approximately 12.1 kN. From this point onwards, horizontal displacements of the concrete block began to occur on the side opposite the load application point, as the restraint system was unable to completely prevent these displacements, particularly under the higher load levels reached during the test. As expected, and similarly to the previous case, the curve then followed an almost horizontal trend. The crack, which was already open at the intrados at the point of load application (C in Fig. 6.23), became apparent from the first loading steps onwards.

Conversely, the CRM system repairs the hinge that had previously formed in a symmetrical position on the upper surface. Instead, cracks have developed in

the mortar at this point (B in Fig. 6.23). The overall curve subsequently increased until the maximum load of 15.9 kN was reached, after which there was a loss of load due to debonding of the FRCM at the left-hand end of the specimen (A in Fig. 6.23).

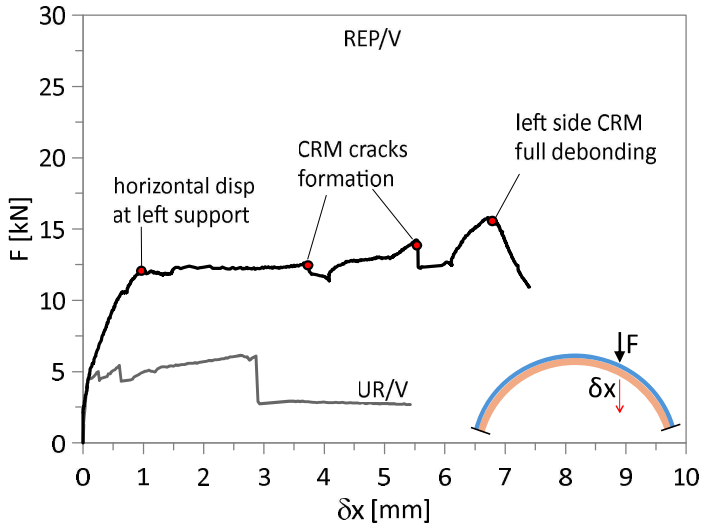


Figure 6.22 Repaired vault (REP/V) test results and comparison with UR/V

At this support point, a composite mechanism developed involving the first two rows of blocks, accompanied by corner crushing of the third row and shear sliding. These phenomena can be seen in Figure 6.24, trough DIC strain pattern. Figure 6.24a shows the re-opening of the first hinge at the point of load application. This was followed by cracking in the upper-surface reinforcement at a symmetrical position and CRM debonding (Fig. 6.24b). Figure 6.24c shows the progression of damage at the end of the test, with the hinges fully open and complete CRM debonding at the support, as well as widespread cracking on the upper surface of the specimen.

Despite these phenomena, applying CRM reinforcement to a damaged specimen increased its load-bearing capacity in terms of both maximum sustained load and ultimate displacement. In fact, the REP/V specimen achieved a load value approximately double that of the UR/V configuration,

with a displacement also approximately double that of the previous case. The failure mode confirmed that the load-bearing capacity of the arch was influenced by both the horizontal displacement of the support and the debonding of the CRM. At the end of the test, four metal rods with 20 mm diameter bars were inserted to the same vault, to prevent the small horizontal displacements also recorded during this test. These were designed according to the expected load magnitude to ensure a secure connection and minimal deformation.



Figure 6.23 Repaired vault (REP/V) damage pattern at the end of the test (photo taken during the experimental activities)

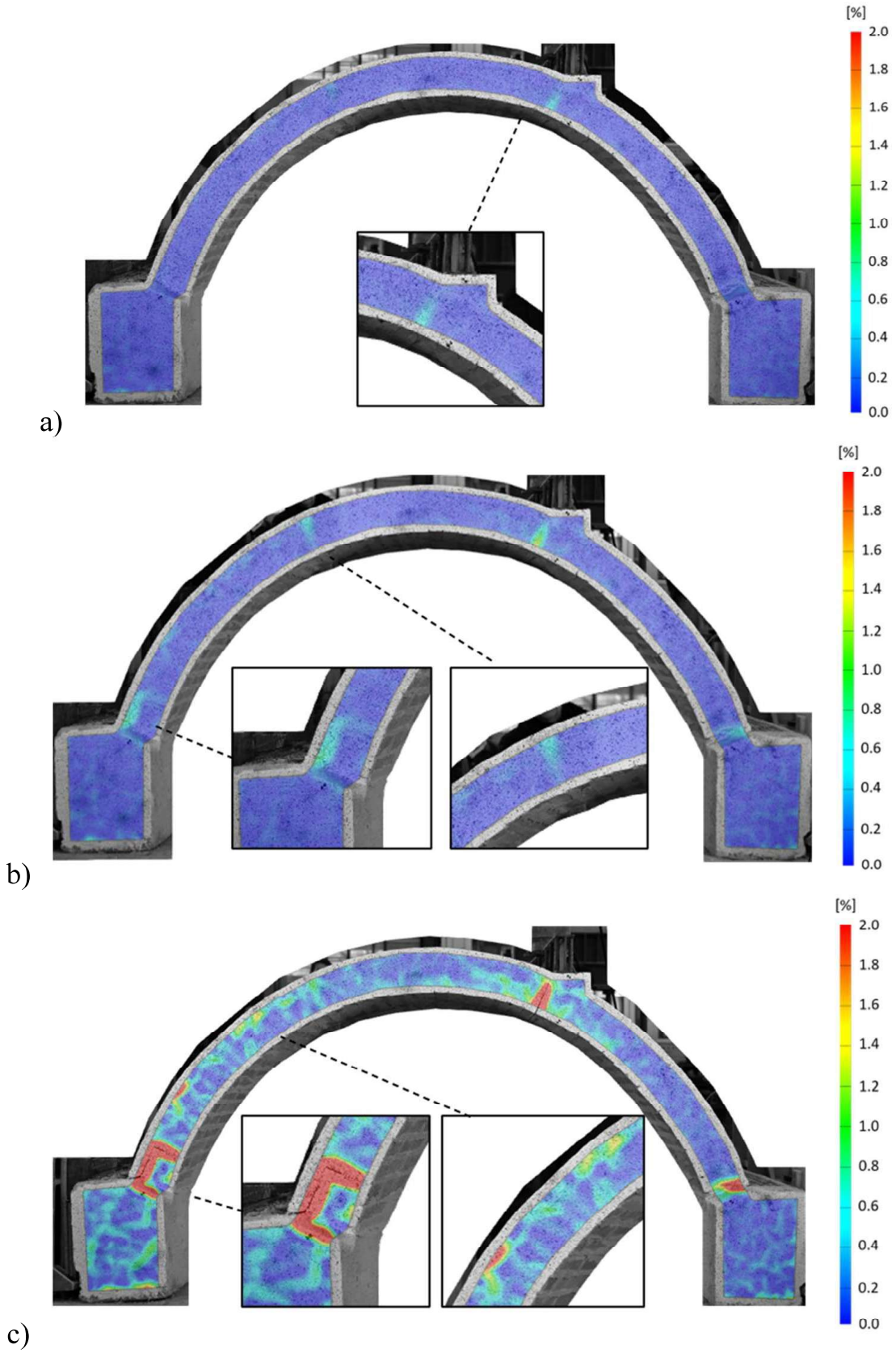


Figure 6.24 DIC strain color patterns for the Repaired vault configuration (REP/V): a) first hinge re-opening; b) cracking formation near repaired hinge and delamination onset; c) CRM full debonfing and widespreas cracking on the surface

The vault was then tested in the REP/V+T configuration. It exhibited damage resulting from the previous REP/V configuration test, to which the metal rods had been added. The results obtained during the test are shown in Figure 6.25, where they are compared with the two curves corresponding to the previous configurations. Firstly, as expected due to the pre-existing damage in the specimen, it can be seen that the initial stiffness is lower than in previous tests. This behaviour is due to the presence of already-opened hinges, debonding of the CRM, and widespread cracking of the matrix on the upper surface.

The behaviour observed in previous stages, characterised by a change in the curve's slope due to horizontal displacements of the supports, did not occur in this case. This demonstrates the effectiveness of the chain system in limiting such movements. The curve was found to be almost linear, with small drops in load associated with the formation of various cracks on the upper surface of the CRM matrix. The load increased until it reached a maximum value of 23.4 kN, after which there was a rapid drop of load.

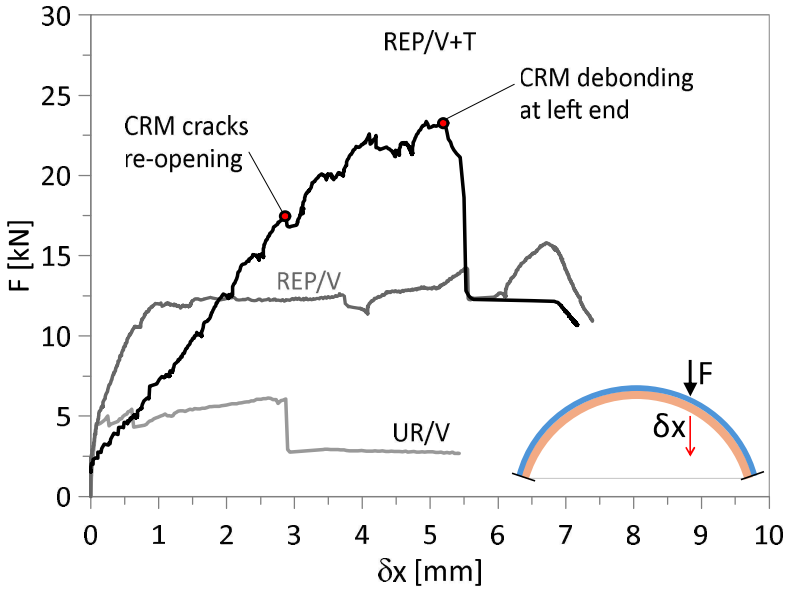


Figure 6.25 Repaired vault with tie rods (REP/V+T) test results and comparison with UR/V and REP/V

At this stage, the CRM had completely debonded on the left-hand side of the vault (B and C in Fig. 6.26). In this case, the debonding affected a larger area of the reinforced surface, extending to the blocks in the fifth course. The composite mechanism previously observed became more pronounced, leading to increased relative slippage between the blocks and localised crushing at the third course. However, the position of the hinges and the pattern of widespread cracking showed no significant changes compared with the REP/V configuration.

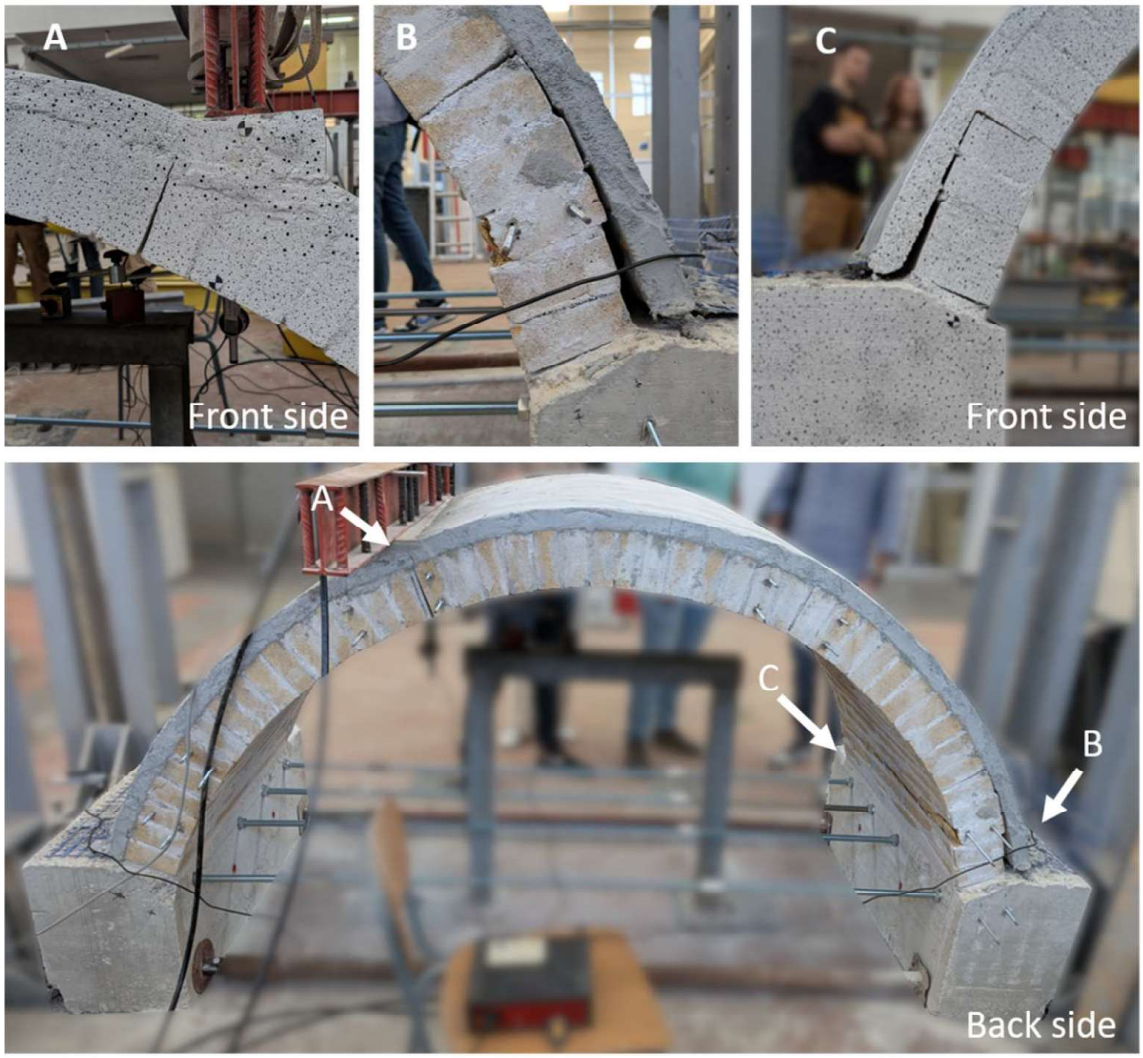


Figure 6.26 Repaired vault with tie rods (REP/V+T) damage pattern at the end of the test (photo taken during the experimental activities)

The results obtained were consistent with expectations, as the restraint conditions are known to significantly influence the structural response of masonry vaults. Despite the presence of pre-existing damage resulting from the previous REP/V test, the REP/V+T configuration achieved a maximum load value almost double that of the REP/V configuration and approximately four times higher than that of the unreinforced UR/V configuration. However, this comparison must be interpreted qualitatively, given that the specimen subjected to the REP/V+T test exhibited significant damage, including partially open joints, widespread CRM matrix cracking and partial reinforcement detachment. Despite these unfavourable initial conditions, installing the rods significantly altered the system's overall behaviour, limiting the horizontal displacements of the supports and increasing the vault's residual load-bearing capacity.

6.7.2 Traditional CRM reinforced vault sample (R/V+T)

The Specimen 2 was constructed in the R/V+T configuration and subsequently reinforced prior to the test. In this case, the CRM system comprises a 30 mm layer of traditional M10P mortar, GFRP2 mesh and LS2-type connectors. The main difference compared with previous cases concerns the restraint conditions: the vault supports were incorporated into a suitably dimensioned reinforced concrete slab and subsequently restrained to the strong floor. Furthermore, two rods with 20 mm diameter bars were installed to prevent horizontal displacement of the system. The test was designed to simulate the behaviour of an undamaged real vault characterised by rigid constraints and reinforced using a CRM system. A different distribution of connectors was adopted compared with the previous configurations, with the aim of preventing the debonding of the CRM system at the edge of the specimen, which had occurred in previous tests. The test was carried out using the same loading

protocol as in previous cases of strengthened vault. In this case, the load cell with a higher capacity was adopted in view of the higher loads expected during the test. Figure 6.27 shows the overall response curve in terms of force–vertical displacement, alongside the curves for the previous configurations. The behaviour can be characterised as an initial almost linear section up to a load of about 37 kN, followed by a nonlinear phase up to the of approximately 43 kN. This corresponds to the formation of the first hinge on the underside at the point of load application, as shown in Figure 6.28a.

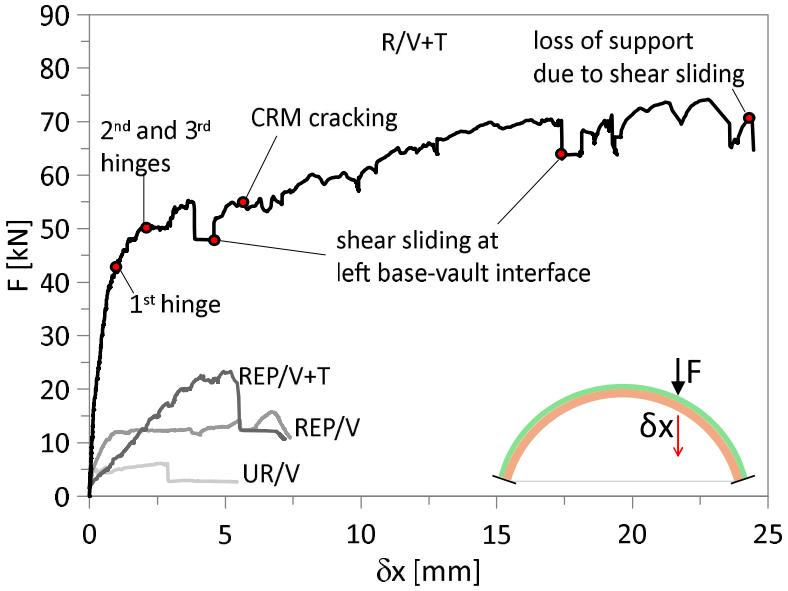


Figure 6.27 Reinforced vault with traditional CRM matrix (R/V+T) test results and comparison with UR/V, REP/V and REP/V+T

As the load increased further, the second and third hinges formed at the two supports (Fig. 6.28b). The load then increased further, reaching values close to 55 kN. At this point, the left support (opposite the side where the load was applied) began to slip, followed by cracking of the CRM on the upper surface (Figs. 6.28c, 6.29). The area affected by cracking extends for approximately 1 m, corresponding to about one-third of the vault's span. This region can be interpreted as the length of the plastic hinge that developed on the upper surface.

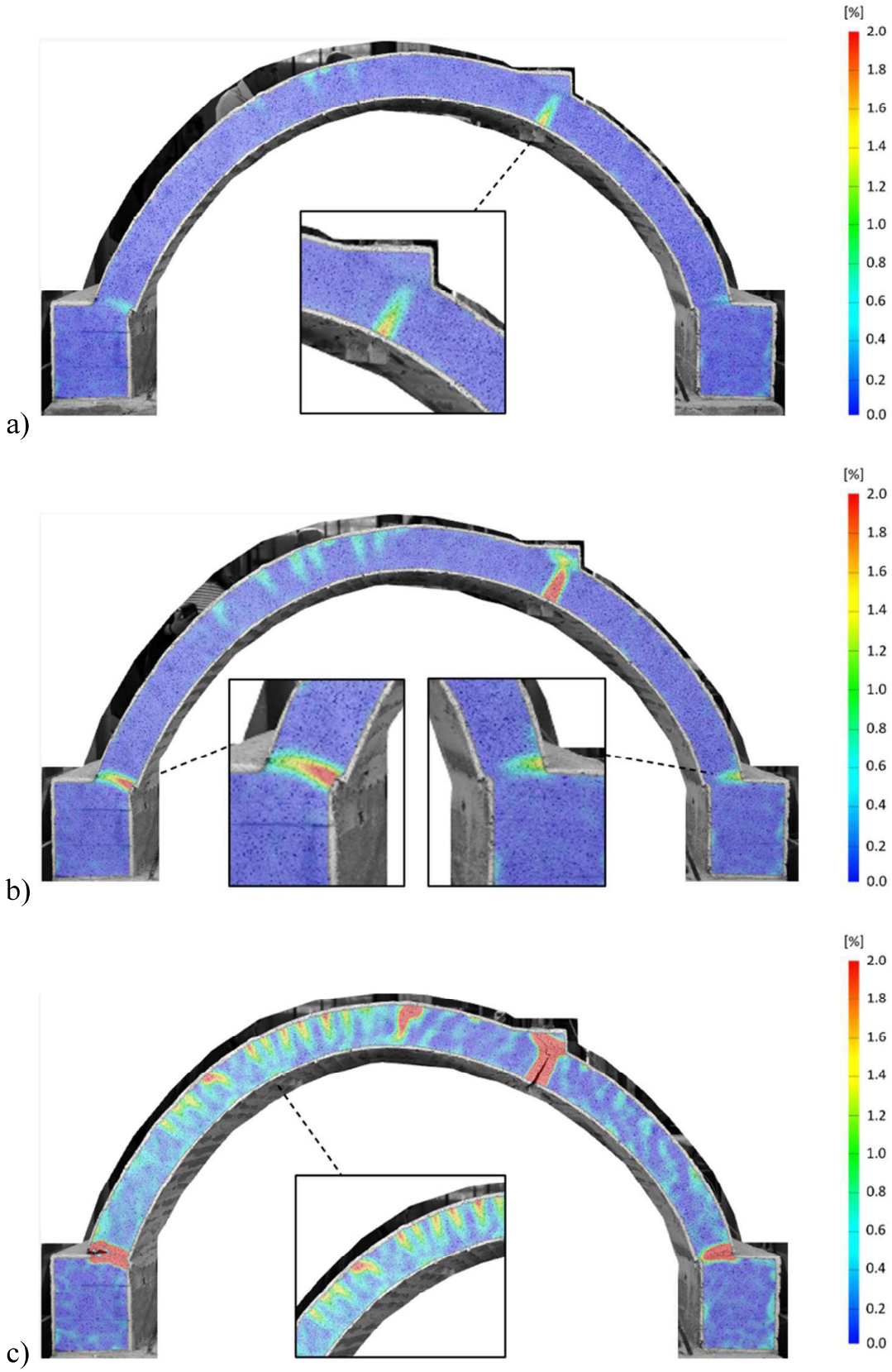


Figure 6.28 DIC strain color patterns for the Reinforced vault configuration (R/V+T): a) first hinge formation; b) hinge formation at the base joints; c) extrados cracking stabilization and overall damage strain pattern at the upcoming collapse



Figure 6.29 Reinforced vault with traditional CRM matrix (R/V+T) damage pattern at the end of the test (photo taken during the experimental activities)

The extent of the cracking, which occurred without any significant loss of load-bearing capacity, indicates the effective activation of the GFRP mesh. Given the results obtained, it is reasonable to conclude that the high capacity is also associated with the full activation of the CRM reinforcement, facilitated by the improved anchoring system near the base of the vault that prevented debonding at the base edge of the specimen.

The system continued to bear the load until the next loss of capacity occurred at around 70 kN. At this point, further slippage at the support occurred. The

maximum load of around 74 kN was then reached, after which a complete loss of contact between the arch and the support occurred due to shear sliding.
Figure 6.29 shows images of the specimen's damaged configuration at the end of the test. These reveal widespread cracking on the upper surface and slippage at the base, which led to the specimen's collapse. Due to the different constraint conditions and initial damage compared to previous cases, a direct comparison with the results obtained for the other configurations is not possible. However, based on the experimental results, it is possible to draw some qualitative conclusions. Compared with the unreinforced UR/V configuration, the R/V+T configuration resulted in an approximately 12 times increase in maximum load and an almost 8 times increase in displacement capacity. The reinforcement system's contribution is clearly even more significant than when the CRM was applied to an already damaged configuration.

6.7.3 Geopolymer CRM reinforced vault sample (R/V_G+T)

The Specimen 3 was constructed and tested in the R/V_G+T configuration. It was fabricated in the same way as the R/V+T specimen, with rigid supports and metal rods added. The difference from the previous case concerns the CRM system matrix, which consists of geopolymer mortar in this instance. The test conditions are equal to those of the previous configuration.
The results obtained for this configuration are shown in Figure 6.30, alongside those of previous tests. The curve exhibits an initial, almost linear section characterised by slightly lower stiffness than that observed for the R/V+T configuration. Following a nonlinear phase, the first hinge forms below the point of load application at a load of approximately 24 kN, marking a change in the slope of the curve. As can be seen from the strain patterns in Figure 6.31a, shear sliding begins at the left support at the same load value, which is responsible for the observed change in slope. The load then increased linearly

until reaching 48 kN, at which point significant sliding first occurred at the base (Fig. 6.31b). At the same time, a second hinge formed at the right support and incipient cracking of the CRM matrix was evident on the upper surface. Following the load drop, the test continued with an increase in load. Two further instances of slippage were observed, as indicated in Figure 6.30 and shown in Figure 6.31c. At this stage, cracking of the matrix on the upper surface was also evident. This cracking pattern resembles that observed in the R/V+T configuration, with widespread cracking extending over an area of approximately 1 m. After the final load drop, the load was increased until reaching a maximum value of 61.6 kN, at which point there was a complete loss of support due to shear sliding.

Figure 6.32 shows a complete overview of the damage at the end of the test. In this configuration, the cracking pattern that developed at the end of the test is clearly visible, as is the mechanism that led to the vault's collapse. The maximum load reached is slightly lower than that obtained in the R/V+T configuration, in which a CRM matrix consisting of traditional mortar was used.

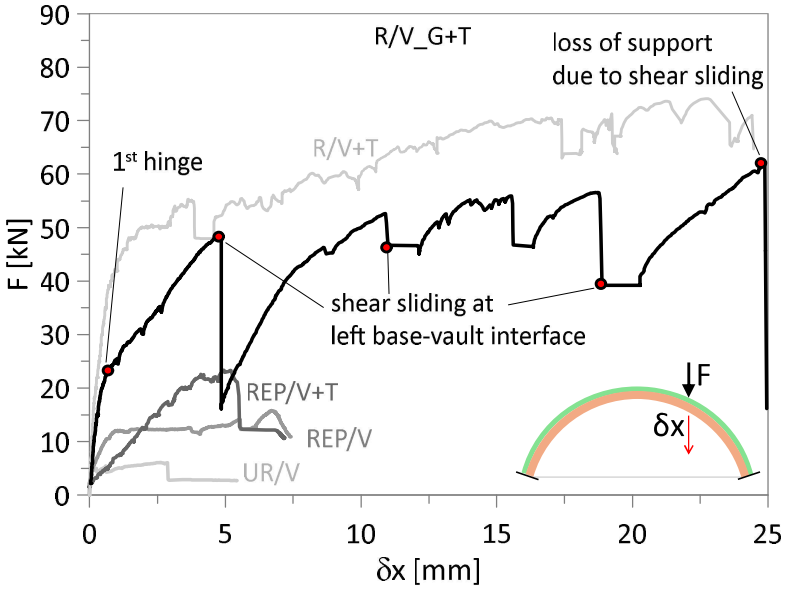


Figure 6.30 Reinforced vault with geoplymer CRM matrix (R/V_G+T) test results and comparison with UR/V, REP/V, REP/V+T and R/V+T

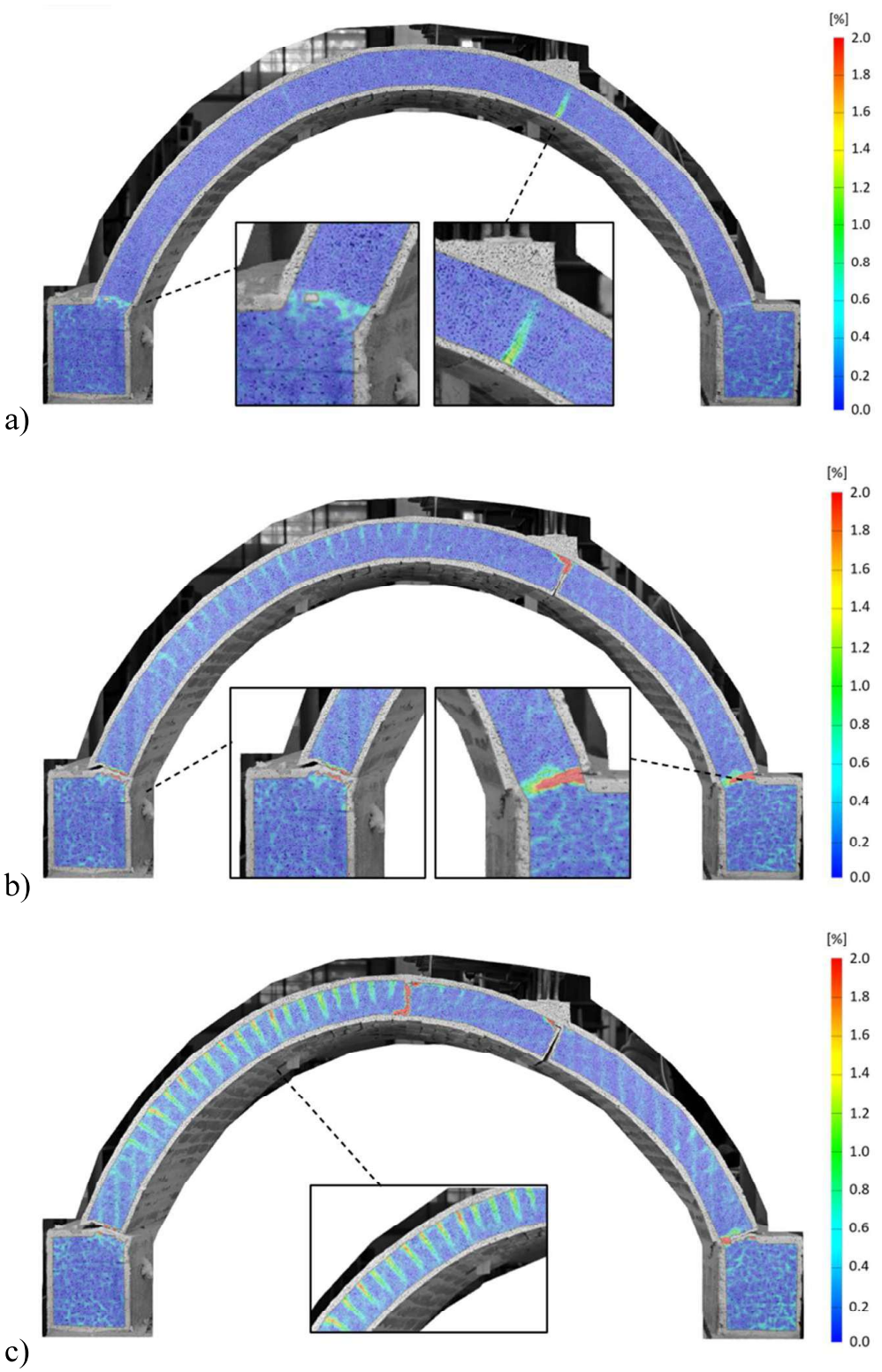


Figure 6.31 DIC strain color patterns for the reinforced vault configuration (R/V_G+T): a) first hinge formation; b) hinge formation and sliding at the base joints; c) extrados cracking stabilization and overall damage strain pattern at the upcoming collapse

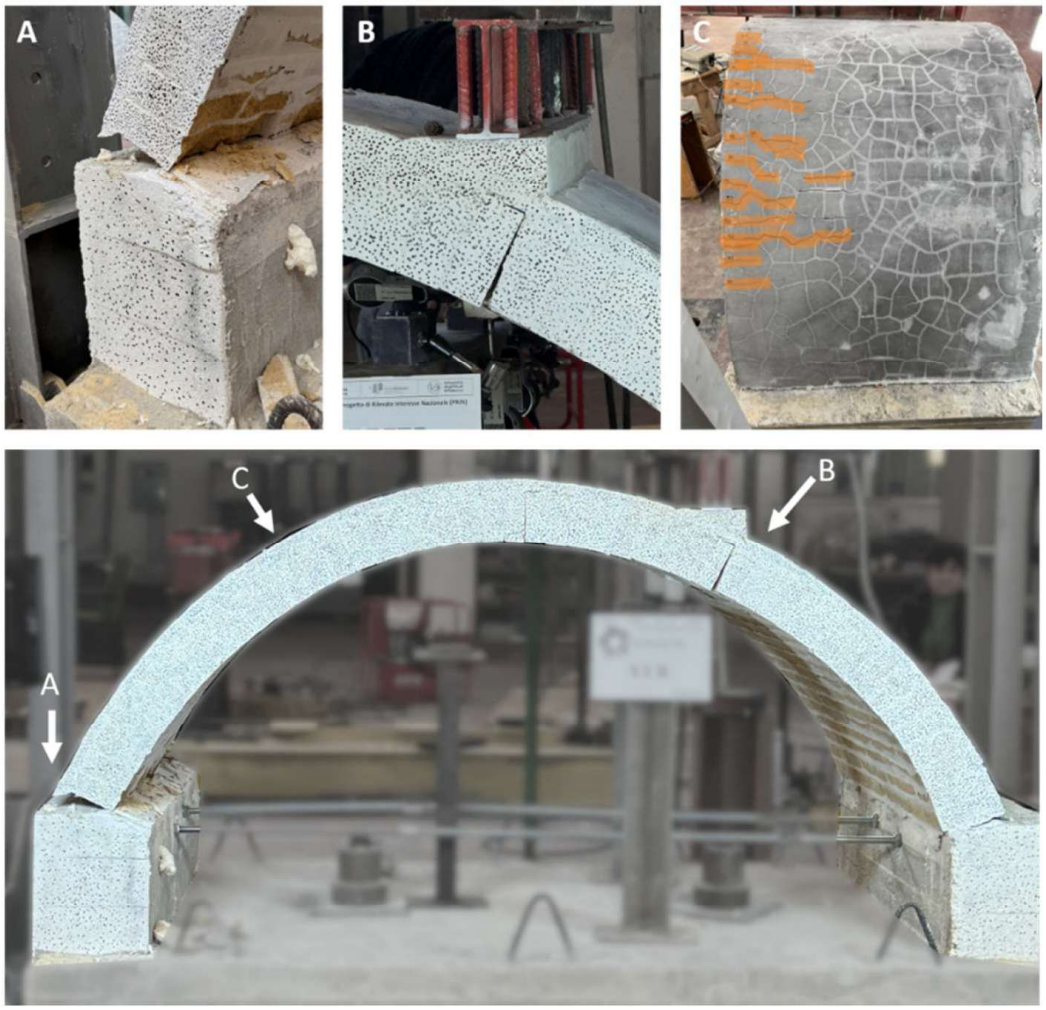


Figure 6.32 Reinforced vault with geopolymer CRM matrix (R/V_G+T) damage pattern at the end of the test (photo taken during the experimental activities)

6.8 Comparisons and discussion of the results

Table 6.3 summarises the results obtained for all vault specimens in terms of the maximum load and displacement achieved and the failure mechanism exhibited by each specimen. In general, the experimental campaign enabled the load-bearing capacity of vaults with different configurations to be compared. This included the unreinforced case, the repaired case, the repaired case subsequently fitted with tie rods and, finally, two vaults reinforced from scratch using a CRM system and tie rods.

Table 6.3 Experimental results of load test on vaults

ID	Description	F_{max} [kN]	$\delta_{x,u}$ [mm]	Failure mode
UR/V	Unreinforced vault	6.1	2.90	4-hinge mechanisms
REP/V	CRM repaired vault	15.9	6.50	4-hinge mechanism + CRM debonding
REP/V+T	CRM repaired vault + steel tie rods	23.4	5.15	4-hinge mechanism + extended CRM debonding
R/V+T	CRM (traditional matrix) reinforced vault + double anchoring + steel tie rods	74.0	22.50	Base shear sliding, loss of support
R/V_G+T	CRM (geopolymer matrix) reinforced vault + double anchoring + steel tie rods	61.6	24.90	Base shear sliding, loss of support

Analysis of the results in Table 6.3 shows that applying the CRM to the vault's extrados significantly increases both its load-bearing and deformation capacities. In particular, the reinforcement system effectively delays the formation of the fourth hinge with opening at the extrados, which triggers the vault's collapse mechanism.

A significant increase in load-bearing capacity was even observed in specimens characterised by pre-existing damage, confirming the effectiveness of the CRM system in the repair and consolidation of compromised structures. The R/V+T configuration was found to deliver the best performance, thanks to a combination of favourable factors, including the absence of initial damage, stiffer constraints and an improved anchoring system. These factors allowed for more effective stress transfer between the reinforcement and the wall structure.

Another important consideration is the use of geopolymer mortar as the matrix for the CRM system. The results show that, mechanically, this solution enables performance comparable to that achieved with CRM systems using traditional

matrices. This highlights the potential of these materials for reinforcing existing heritage buildings during restoration and regeneration.

6.9 Thermal test on CRM reinforced vault samples

Prior to the mechanical tests, the last two vault configurations (R/V+T and R/V_G+T) were subjected to thermal tests to compare the contribution of the traditional and geopolymer matrices to the thermophysical behaviour of the reinforcement system. These tests were conducted by the Institute for Construction Technologies of the National Research Council of Italy (ITC-CNR), at the Materials and Structures Laboratory of the Department of Engineering at the University of Palermo.

To assess the thermophysical behaviour of the reinforced vaults, thermal tests were developed under controlled conditions to compare the thermal response of the different reinforcement configurations. The test set-up is shown in Figure 6.33. Thermal loading was applied to the intrados using a system comprising eight infrared halogen lamps capable of providing a controlled, uniform heat flux across the inner surface of the vault (Fig. 6.33a). The radiation source was kept active throughout the test to induce a thermal gradient between the intrados and extrados surfaces of the element. Temperature changes were monitored using two sensors, one installed on the intrados of the vault and the other on its upper surface (Fig. 6.33b). Thanks to continuous data acquisition, it was possible to analyse the temporal evolution of the thermal field throughout the entire test duration and compare the response of the two different reinforcement configurations.

In order to minimise heat exchange with the external environment and encourage predominantly one-dimensional heat flow through the thickness of the vault (Fig. 6.33c), the sides of the specimen were sealed with 80 mm-thick extruded polystyrene (XPS) panels, which offer high thermal resistance. This

reduced lateral heat loss, concentrating heat transfer perpendicular to the vault's surface.

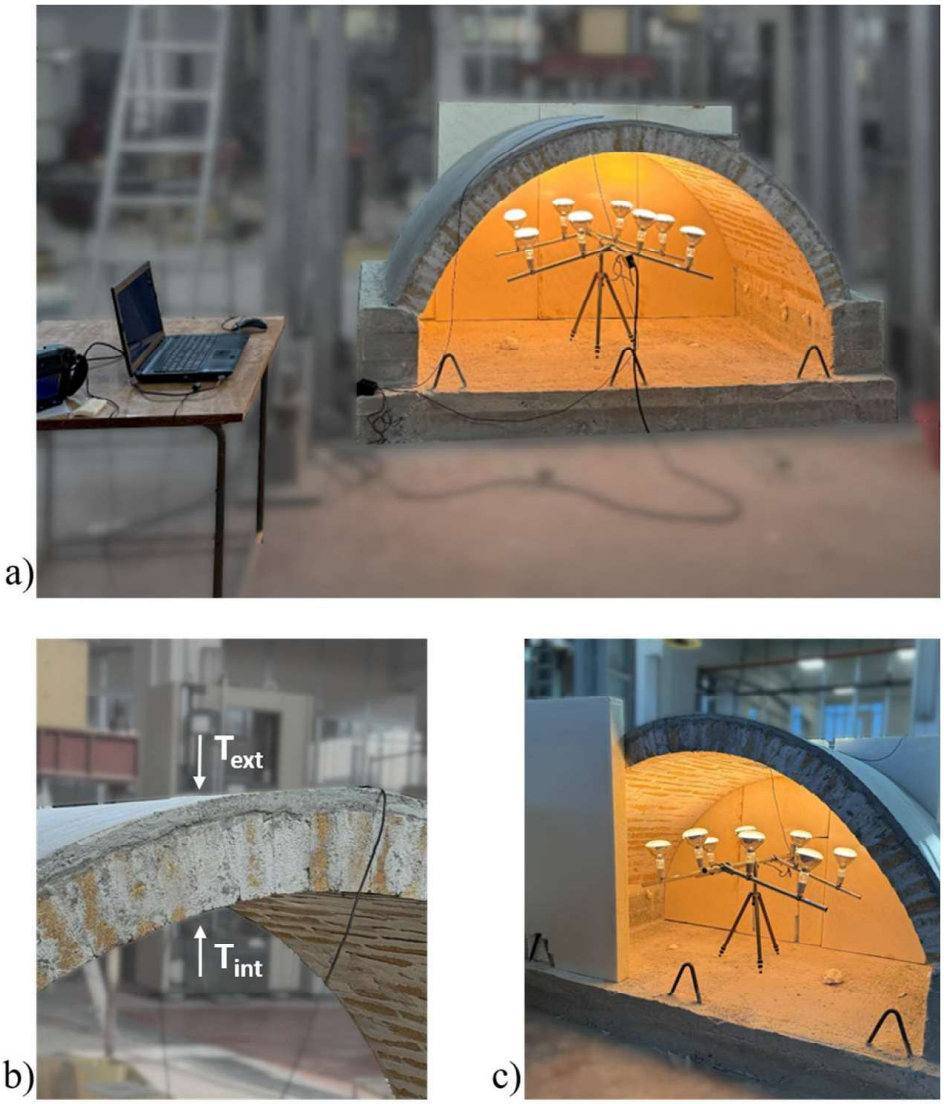


Figure 6.33 Thermal test arrangement and instrumentation (photo taken during the experimental activities)

The test was divided into two distinct phases. In the first phase (heating), the infrared lamps remained operational until the target thermal state was reached, enabling the propagation of heat through the vault's thickness to be evaluated. In the second phase (cooling or thermal dissipation), the lamps were switched off and temperature monitoring continued until the specimen gradually

returned to equilibrium with the ambient conditions. Analysis of the cooling phase enabled the vault's capacity to dissipate accumulated heat to be assessed, providing further information on the thermal inertia and thermophysical behaviour of the various reinforcement configurations.

A comparative analysis of the temperatures recorded during both phases enabled the influence of the reinforcement system on the vault's thermal behaviour to be evaluated. In particular, the evolution of the temperature difference between the intrados and extrados during both heating and cooling was used as an indicator of the system's effectiveness in limiting heat transfer and modifying the element's thermal response.

The absolute values of the thermophysical properties and parameters derived from the experimental tests are not reported here, as these are the subject of another research project and cannot be disclosed at this time. Therefore, the discussion of the results is based on percentage changes and observed trends, which are sufficient for the purposes of the comparative analysis.

The experimental tests showed that the CRM system with a geopolymer matrix improves the vault's thermal performance by approximately 20% compared to the CRM system with traditional mortar. This suggests that the nature of the composite matrix affects not only the mechanical behaviour of the reinforcement but also the thermophysical properties of the masonry element.

Calcarenite stone CSV has thermal conductivity of 1.76 W/mK, (Table 3.8) and results in limited resistance to heat flow. The geopolymer CRM system consists of a 30 mm thick layer of mortar with a thermal conductivity ranging from 0.20 to 0.32 W/mK [71], which is significantly lower than that of the existing masonry. In terms of thermal resistance, the geopolymer layer makes a notable contribution to the overall stratigraphy, with a resistance that is comparable to, and in some cases may exceed, that of the existing masonry. Despite accounting for only 25% of the element's total thickness, the CRM

coating therefore has a measurable influence on the vault's overall thermal behaviour.

The observed experimental improvement can therefore initially be attributed to the lower thermal conductivity of the geopolymer matrix, which increases the element's overall thermal resistance and reduces the heat flux through the cross-section. However, it should be noted that the overall thermal performance depends on the combined properties of the stratigraphy, rather than the thermal conductivity of the individual materials alone. Therefore, the measured benefit reflects the interaction between the characteristics of the existing masonry, the CRM system, and the test conditions.

From a design perspective, the results obtained are of particular interest because they demonstrate how the selection of the CRM system matrix can achieve structural improvement and energy performance optimisation simultaneously. This is particularly relevant for historic buildings, where the selection of reinforcement materials should not only increase the structure's load-bearing capacity and ductility, but also contribute to reducing heat transfer through the reinforced masonry element. The measured thermal performance should, however, be distinguished from the overall energy performance of the building, which depends on several additional factors, including the characteristics of the building envelope, its geometry, boundary conditions, climatic conditions and operational conditions. Within this context, the proposed integrated approach can contribute to improving both the structural and thermal performance of the strengthened masonry element, while remaining compatible with conservation principles.

Chapter 7

General Discussion and Conclusions

7.1 Summary of the main findings

This study analysed the mechanical behaviour of masonry elements reinforced with inorganic matrix composite systems, with a focus on FRCM and CRM solutions, using an integrated experimental, analytical and numerical approach. The main objective was to improve understanding of the mechanisms that govern the effectiveness of these reinforcement systems by moving beyond an evaluation based solely on the properties of individual components to consider the overall behaviour of the interaction between masonry, matrix and reinforcement. The research addressed this objective through the experimental investigation of masonry panels and barrel vaults, the analysis of an extended experimental database, the assessment of existing analytical formulations, and the development of numerical models to interpret the observed structural response.

The experimental campaign was aimed at investigating the use of FRCM and CRM systems for the strengthening of historic masonry structures, which may require strengthening intervention as a result of changes in their loading conditions. Considering the historic masonry heritage of the Mediterranean region, *calcarenite* stone masonry was selected as a representative material due to its widespread use in traditional construction. The experimental programme

then focused on two main categories of structural elements identified through the analysis of historic buildings: vertical masonry elements, represented by panels, whose vulnerability is commonly associated with increases in shear actions, and horizontal structural elements, represented in the present study by masonry barrel vaults, whose structural response may be significantly affected by changes in their boundary conditions. Two types of *calcarenite stone*, characterised by different mechanical properties and representative of different construction contexts, were therefore investigated in the two experimental programmes.

With regard to the objective of assessing the effectiveness of FRCM and CRM systems in improving the shear response of masonry panels, the experimental campaign on diagonal compressive test on panels made it possible to characterise the behaviour of both unreinforced and reinforced configurations using different FRCM and CRM systems. The main mechanisms responsible for the increase in shear capacity were highlighted. The results showed that both systems can significantly improve the masonry's response, though the contribution of the reinforcement cannot be interpreted solely in terms of the fabric's strength capacity. The effectiveness of the intervention stems from the combined action of the masonry, matrix and fibrous components, as well as their ability to develop a compatible response to deformation. These results therefore confirm that the effectiveness of the strengthening system cannot be assessed solely on the basis of the mechanical properties of the fibre layer, but must be considered as the result of the interaction between the masonry, matrix and fibre layer.

With regard to the objective of assessing the applicability and predictive capability of existing analytical formulations, a comparison of experimental results with available analytical formulations has revealed significant limitations in current design approaches. In particular, procedures that simply

add together the contributions of the masonry and the reinforcement do not always reproduce the observed experimental behaviour. While the approach currently provided by the Italian guidelines offers conservative estimates for some unreinforced configurations, the results obtained for reinforced systems have highlighted aspects that require further investigation, particularly in relation to the representation of the actual contribution of composite strengthening systems. This behaviour can be primarily attributed to the contribution of the matrix, stress transfer mechanisms, and mechanical compatibility between the reinforcement and substrate. The results therefore indicate that more comprehensive formulations are required, particularly those capable of accounting for the contribution of the matrix and the interaction between the different components of the strengthening system.

To investigate the main parameters governing the effectiveness of the strengthening systems and to extend the evidence beyond the results obtained in the present experimental campaign, analysing an extensive database of 746 experimental results from the literature made it possible to generalise the observations obtained during the experimental campaign. The results showed that reinforcement systems are generally more effective for masonry with low mechanical properties and thin thicknesses, while the contribution of the reinforcement decreases as the substrate's strength and stiffness increase. Furthermore, analysis of the mechanical relationships between the reinforcement and the masonry revealed a stronger correlation between increased load-bearing capacity and matrix properties than reinforcement characteristics, highlighting the matrix's active role in composite system behaviour. These results further support the relevance of considering the matrix as an active component of the strengthening system rather than merely as a medium for transferring stresses to the reinforcement.

The analysis also investigated mechanical compatibility between the strengthening system and the masonry substrate by comparing their shear stiffness through the ratio between the shear modulus of the strengthening system and that of the masonry. The results indicated that the greatest increases in shear strength were generally associated with values of the ratio closer to unity, whereas higher ratios were associated with more limited strengthening effectiveness. Although the available data do not allow a definitive threshold for mechanical compatibility to be established, these observations suggest that the relative stiffness of the strengthening system and the masonry may play a role in determining the effectiveness of the intervention. This finding provides an initial indication of the potential relevance of mechanical compatibility as a parameter for evaluating strengthening effectiveness, while further experimental evidence is required to establish quantitative criteria.

Regarding the objective of using numerical modelling to interpret the experimentally observed behaviour, numerical modelling developed using the STKO/OpenSees framework further contributed to interpreting the experimental results. A continuous micro-modelling model was developed and calibrated by simulating characterisation tests on the constituent materials, enabling the nonlinear behaviour of the masonry and reinforcement systems to be reproduced. Comparing the numerical and experimental results showed good agreement in terms of maximum load, shear strength and global stiffness. The numerical predictions were generally closer to the experimental results than the available analytical formulations. Damage analysis obtained from numerical post-processing also enabled the mechanisms responsible for the structural response to be identified. In the unreinforced panels, the model correctly reproduced the formation of diagonal cracks through the stone elements. In the reinforced panels, however, the damage was predominantly localised in the masonry, with limited activation of the reinforcement. This

result confirms that, in the configurations investigated, the improvement in response does not necessarily stem from reaching the structural capacity of the masonry, but rather from the change in the stress state of the masonry and the improved distribution of stresses induced by the composite system. The numerical results therefore provided further evidence that the strengthening effect should be interpreted in terms of the modification of the stress state and stress-transfer mechanisms within the masonry rather than solely in terms of the direct mobilisation of the reinforcement.

With regard to the objective of investigating the structural behaviour of CRM-reinforced masonry barrel vaults and the influence of matrix type, pre-existing damage and connection conditions, five tests were carried out on masonry barrel vaults made of *calcarenite* and subjected to an asymmetric vertical load applied at one-quarter of the span. The research analysed the behaviour of masonry barrel vaults, with particular reference to the application of CRM systems as a solution for structural consolidation and integrated performance improvement. This part of the research has expanded the available knowledge on the use of CRM systems in vaulted elements, for which experimental results in literature are limited compared to other applications. The experimental campaign conducted on the vaults made it possible to evaluate the effectiveness of the CRM system under different conditions, considering the influence of the matrix type, the presence of pre-existing damage, and the configuration of the connection systems. The results showed that reinforcement using CRM systems can modify the structural behaviour of the vault, influencing the load-bearing mechanism and the capacity to redistribute loads after the onset of major damage mechanisms. However, the effectiveness of the intervention was found to depend closely on proper interaction between the reinforcement system, the existing masonry and the boundary conditions. One particularly significant aspect, which was already known and confirmed

by the experimental campaigns in literature, concerns the role of constraint conditions between strengthening system and substrate in the behaviour of reinforced vaults. This result highlights the fact that evaluating the effectiveness of a CRM system applied to vaulted elements requires an accurate representation of the interaction between the vault and the supporting structure, as the overall behaviour does not depend exclusively on the mechanical properties of the reinforcement and the masonry.

The numerical investigation of the vaults was aimed at further assessing the influence of boundary conditions and at determining whether their effect could be reproduced through an appropriate representation of the support conditions. Numerical modelling developed to interpret the experimental results confirmed this finding. The initial model, which used a homogenised representation of the masonry and a fibre-based formulation, reproduced the nonlinear behaviour typical of arches, but it overestimated the load-bearing capacity due to the assumption of perfectly rigid constraints.

Introducing a deformable horizontal constraint, calibrated based on experimentally measured displacements using DIC, enabled a closer alignment of numerical and experimental results. This allowed both the force-displacement response and the observed damage pattern to be reproduced.

Finally, with regard to the objective of investigating the potential of CRM systems as integrated solutions for structural and thermal improvement, studying the vaults also provided an opportunity to explore the potential of CRM systems as multifunctional solutions for masonry buildings. Thermal tests conducted on the reinforced configurations demonstrated that the application of CRM with geopolymer matrix not only improves the structural response in terms of load bearing and displacement capacity but also improves the thermal performance of the tested masonry element. This aspect is an original contribution of the research and aligns with the current objectives of

the scientific community, as it highlights the possibility of using consolidation systems that are compatible with historic heritage as part of integrated structural and thermal retrofitting strategies.

7.2 Recommendations and future research directions

The results obtained highlight the need for more comprehensive design procedures to evaluate the effectiveness of FRCM and CRM systems. In particular, further consideration could be given to the contribution of the matrix and to the overall behaviour of the composite system arising from the interaction between the fabric, matrix and masonry.

The experimental database should be further expanded, particularly for CRM systems and for masonry characterised by different mechanical properties. Larger experimental campaigns would allow a greater number of specimens to be tested under comparable conditions and would provide a more robust basis for identifying generalised trends. In particular, systematic test programmes in which individual parameters are varied while the other conditions are kept constant would help to better isolate the effects of matrix properties, reinforcement percentage, number of layers, connector characteristics and anchoring conditions. This approach would also provide a more reliable basis for assessing the interaction between these parameters and their influence on the overall strengthening effectiveness.

The concept of mechanical compatibility identified in this research represents a potentially innovative parameter for the preliminary evaluation of reinforcement solutions. However, further experimental and numerical studies are required to establish quantitative criteria and possible limit values for incorporation into design procedures.

From a numerical standpoint, the results have demonstrated the potential of simplified advanced nonlinear models as useful tools for interpreting the

phenomena experimentally observed. The need for further development is particularly evident in relation to the representation of the strengthening system and the interaction with the masonry. Further developments could focus on more detailed modelling of FRCM and CRM systems, including a more explicit representation of the matrix and reinforcement, as well as on the refinement of interface models to improve the prediction of post-peak behaviour and damage mechanisms.

Regarding vaulted structures, the relatively limited number of specimens investigated and the simultaneous variation of different parameters indicate the need for larger and more systematic experimental campaigns. Further research should focus on developing models that can represent realistic restraint conditions by taking into account the deformability of supports, friction phenomena and interaction with adjacent structural elements. Additional tests involving different boundary conditions would be particularly useful to quantify the influence of the support conditions on the structural response and to distinguish their effects from those associated with the strengthening configuration. This is particularly important for historic structures, where boundary conditions are often poorly understood yet can significantly impact the overall response.

Further study is also needed to evaluate the integrated thermomechanical behaviour of CRM systems and their application to other structural elements.

Future investigations should analyse the impact of various matrices, reinforcement configurations and environmental conditions with the objective of devising evaluation procedures that can consider structural and energy improvements simultaneously.

Finally, a key prospect for the future is to extend the developed methodologies to the study of more complex masonry structures and vaults reinforced with CRM and FRCM systems. Integrating experimentation with advanced

monitoring techniques such as DIC, numerical modelling and the analysis of large databases is a promising strategy for developing more reliable methodologies for assessing and designing interventions on historic masonry structures. In this context, the combination of larger experimental datasets, systematic parametric testing and advanced numerical modelling would provide a more robust basis for translating the findings of the present study into generalised assessment and design procedures.

Appendix A

The following table lists the bibliographical references and main characteristics of the experimental data collected in the database used for this study. The first column shows the bibliographical reference and the second shows the sample code as identified within the experimental campaign by the authors. For masonry, the parameters given are the thickness *t,* the edge length of the tested panel L and compressive strength f_c. Where compressive strength was unavailable, it was evaluated using the EuroCode 6 formulae based on the block and mortar characteristics [127].

For the reinforcement system, the sample configuration is specified, distinguishing between unreinforced masonry (UR), masonry reinforced with mortar only (Mortar), FRCM systems, and CRM systems. For each configuration, the next column indicates the type of fibre used in the fabric or mesh: carbon, AR glass, glass, basalt, GFRP, steel mesh, hemp, aramid, polymer, polypropylene (PP). The following column describes the type of matrix: cementitious (C), lime-based (L), lime-cement (LC), polymer (P), geopolymer (G) or alkali-activated (AA). Where data are not available, the cell is marked 'not declared' (n.d.). The last column of the table shows the results of the diagonal compressive tests (DCT), indicating the maximum shear stress τ_{max} recorded during the test, evaluated in accordance with ASTM E519.

The database combines experimental results obtained from different types of masonry, specimen geometries, reinforcement configurations and experimental campaigns. This heterogeneity has been taken into account when interpreting the trends identified from the data collected. The results were not systematically categorised according to specimen geometry, as the analyses were primarily conducted on the basis of normalised and dimensionless quantities, such as stress values and ratios between parameters, which allow for the comparison of results obtained from specimens with different

geometries. Differences in the properties of the masonry and in the reinforcement configurations were, however, taken into account through the calculation of the parameters used in the subsequent analyses and correlations. In this way, it was possible to maintain a broad representation of the available experimental evidence, whilst taking into account the characteristics of the different systems and their respective substrates when interpreting the results. Differences in test procedures and experimental conditions were also considered in the interpretation of the results. The correlations identified should therefore be understood as general trends emerging from the body of available experimental evidence, rather than as relationships independent of the specific test conditions.

REF.	**ID**	**Masonry**			**Strengthening system**			**DCT res.**
		t	L	f_c	Conf.	Fibre type	Matrix type	τ_{max}
		mm	mm	[MPa]	-	-	-	[MPa]
[73]	PM1	105	467.5	28.6	UR	n.d.	C	0.97
	PM2	105	467.5	28.6	UR	n.d.	C	0.50
	PM3	105	467.5	28.6	Mortar	n.d.	C	0.78
	PM4	105	467.5	28.6	Mortar	Carbon	C	0.62
	PM5	105	467.5	28.6	FRCM	Carbon	C	0.67
	PM6	105	467.5	28.6	FRCM	Carbon	C	0.89
	PM7	105	467.5	28.6	FRCM	Carbon	C	1.44
	PM8	105	467.5	28.6	FRCM	Carbon	C	1.27
	PM9	105	467.5	28.6	FRCM	Carbon	C	1.88
	PM10	105	467.5	28.6	FRCM	Carbon	n.d.	1.92
	PM11	105	467.5	28.6	FRCM	n.d.	n.d.	1.73
[74]	P#1	250	1030	2.3	UR	n.d.	n.d.	0.22
[74]	P#2	250	1030	2.3	UR	n.d.	n.d.	0.35
	P#3	250	1030	2.3	UR	n.d.	C	0.21
	P#4	250	1030	2.3	UR	AR glass	C	0.19
	PS#1	250	1030	2.3	FRCM	AR glass	C	0.54
	PS#2	250	1030	2.3	FRCM	AR glass	C	0.64

REF.	ID	Masonry			Strengthening system			DCT res.
		t	L	f_c	Conf.	Fibre type	Matrix type	τ_{max}
		mm	mm	[MPa]	-	-	-	[MPa]
	PS#3	250	1030	2.3	FRCM	AR glass	C	0.57
	PS#4	250	1030	2.3	FRCM	AR glass	C	0.42
	PT#1	250	1030	2.3	FRCM	AR glass	C	0.35
	PT#2	250	1030	2.3	FRCM	AR glass	C	0.46
	PT#3	250	1030	2.3	FRCM	AR glass	n.d.	0.50
	PT#4	250	1030	2.3	FRCM	n.d.	n.d.	0.34
[75]	1	400	1200	1.3	UR	n.d.	n.d.	0.07
	2	400	1200	1.3	UR	n.d.	C	0.05
	3	400	1200	1.3	UR	Carbon	C	0.05
	4	400	1200	1.3	FRCM	Carbon	C	0.34
	5	400	1200	1.3	FRCM	Carbon	C	0.33
	6	400	1200	1.3	FRCM	Carbon	C	0.32
	7	400	1200	1.3	FRCM	Carbon	C	0.30
	8	400	1200	1.3	FRCM	Carbon	n.d.	0.24
	9	400	1200	1.3	FRCM	n.d.	n.d.	0.30
[76]	P1	310	1230	3.6	UR	n.d.	n.d.	0.21
	P2	310	1230	3.6	UR	n.d.	n.d.	0.19
	P3	310	1230	3.6	UR	GFRP	n.d.	0.27
	PR1	310	1230	3.6	FRCM	GFRP	n.d.	0.45
	PR2	310	1230	3.6	FRCM	GFRP	n.d.	0.41
	PRF1	310	1230	3.6	FRCM	GFRP	n.d.	0.53
	PRF2	310	1230	3.6	FRCM	GFRP	n.d.	0.51
	PRR1	310	1230	3.6	FRCM	GFRP	n.d.	0.71
	PRR2	310	1230	3.6	FRCM	n.d.	n.d.	0.68
[77]	IP-CMU-Control-1	102	1220	19.0	UR	n.d.	n.d.	0.47
	IP-CMU-Control-2	102	1220	19.0	UR	n.d.	C	0.46
	IP-CMU-Control-3	102	1220	19.0	UR	carbon	C	0.38
	IP-CMU-1-Ply-1	102	1220	19.0	FRCM	carbon	C	0.95
	IP-CMU-1-Ply-2	102	1220	19.0	FRCM	carbon	C	0.79

Continued on the next page

REF.	ID	Masonry			Strengthening system			DCT res.
		t	L	f_c	Conf.	Fibre type	Matrix type	τ_{max}
		mm	mm	[MPa]	-	-	-	[MPa]
	IP-CMU-1-Ply-3	102	1220	19.0	FRCM	carbon	C	0.82
	IP-CMU-4-Ply-1	102	1220	19.0	FRCM	carbon	C	1.05
	IP-CMU-4-Ply-2	102	1220	19.0	FRCM	carbon	n.d.	1.02
	IP-CMU-4-Ply-3	102	1220	19.0	FRCM	n.d.	n.d.	1.03
	IP-CL-Control-1	102	1220	24.0	UR	n.d.	n.d.	0.29
	IP-CL-Control-2	102	1220	24.0	UR	n.d.	C	0.28
	IP-CL-Control-3	102	1220	24.0	UR	carbon	C	0.26
	IP-CL-1-Ply-1	102	1220	24.0	FRCM	carbon	C	0.62
	IP-CL-1-Ply-2	102	1220	24.0	FRCM	carbon	C	0.76
	IP-CL-1-Ply-3	102	1220	24.0	FRCM	carbon	C	0.67
	IP-CL-4-Ply-1	102	1220	24.0	FRCM	carbon	C	1.40
	IP-CL-4-Ply-2	102	1220	24.0	FRCM	carbon	n.d.	1.27
	IP-CL-4-Ply-3	102	1220	24.0	FRCM	n.d.	n.d.	1.30
	P1	250	1000	1.9	UR	n.d.	L	0.14
	P2	250	1000	1.9	UR	glass	L	0.17
	PGG1	250	1000	1.9	FRCM	glass	L	0.44
	PGG2	250	1000	1.9	FRCM	glass	C	0.53
[78]	PGG3	250	1000	1.9	FRCM	glass	C	0.58
	PGG1C	250	1000	1.9	FRCM	glass	C	0.65
	PGG2C	250	1000	1.9	FRCM	glass	L	0.66
	PGG3C	250	1000	1.9	FRCM	basalt	n.d.	0.60
	PBB1	250	1000	1.9	FRCM	n.d.	n.d.	0.39
	P1	310	1200	1.8	UR	n.d.	n.d.	0.21
	P2	310	1200	1.8	UR	n.d.	L	0.16
	P3	310	1200	1.8	UR	glass	L	0.23
	PG1	310	1200	1.8	FRCM	glass	L	0.46
[78]	PG2c	310	1200	1.8	FRCM	glass	L	0.42
	PG1c	310	1200	1.8	FRCM	glass	L	0.55
	PG2c	310	1200	1.8	FRCM	glass	L	0.54
	PGG1	310	1200	1.8	FRCM	glass	n.d.	0.62
	PGG2	310	1200	1.8	FRCM	n.d.	L	0.60

REF.	ID	Masonry			Strengthening system			DCT res.
		t	L	f_c	Conf.	Fibre type	Matrix type	τ_{max}
		mm	mm	[MPa]	-	-	-	[MPa]
	P1	250	1250	2.3	UR	basalt	L	0.12
	P1BB	250	1250	2.3	FRCM	basalt	L	0.32
	P2BB	250	1250	2.3	FRCM	glass	L	0.42
	P1GG	250	1250	2.3	FRCM	glass	n.d.	0.31
	P2GG	250	1250	2.3	FRCM	n.d.	n.d.	0.29
	CD-02-U-OR	480	1200	n.d.	UR	n.d.	n.d.	0.04
	CD-06-U-OR	600	1200	n.d.	UR	n.d.	C	0.04
	CD-09-S-OR	280	1200	n.d.	UR	glass	C	0.04
	CD-07-U-IP	570	1200	n.d.	CRM	glass	C	0.34
	CD-08-U-IR	565	1200	n.d.	CRM	glass	C	0.44
[79]	CD-10-U-IR	700	1200	n.d.	CRM	glass	n.d.	0.46
	CD-11-S-1P	380	1200	n.d.	CRM	n.d.	C	0.17
	CD-11-A-OR	620	1200	n.d.	UR	glass	C	0.05
	CD-12-P-IP	720	1200	n.d.	CRM	glass	C	0.18
	CD-13-P-IP	640	1200	n.d.	CRM	glass	n.d.	0.25
	CD-14-P-IP	640	1200	n.d.	CRM	n.d.	n.d.	0.19
	ABI-01 a	220	1200	5.9	UR	n.d.	n.d.	0.15
	ABI-02 b	220	1200	5.6	UR	glass	P	0.10
	TMI-03 a	220	1200	5.9	FRCM	glass	n.d.	0.18
	TMI-04 a	220	1200	5.9	FRCM	glass	P	0.20
[80]	TMI-05 a	220	1200	5.9	FRCM	glass	n.d.	0.69
	TMI-06 a	220	1200	5.9	FRCM	glass	n.d.	0.72
	TMI-07 b	220	1200	5.6	FRCM	glass	n.d.	0.15
	TMI-08 b	220	1200	5.6	FRCM	glass	n.d.	0.13
	TMI-09 b	220	1200	5.6	FRCM	glass	n.d.	0.14
	TMI-10 b	220	1200	5.6	FRCM	glass	n.d.	0.12
[80]	TMI-11 b	220	1200	5.6	FRCM	glass	n.d.	0.45
	TMI-12 b	220	1200	5.6	FRCM	n.d.	n.d.	0.47
	ref_01	110	990	2.5	UR	n.d.	n.d.	0.75
	ref_02	110	990	2.5	UR	n.d.	C	0.63
	ref_03	110	990	2.5	UR	carbon	C	0.95
[81]	FRMcom_01	110	990	2.5	FRCM	carbon	C	2.66
	FRMcom_02	110	990	2.5	FRCM	carbon	n.d.	2.72
	FRMcom_03	110	990	2.5	FRCM	n.d.	n.d.	2.80
[82]	B2A-1	250	1160	7.0	UR	n.d.	LC	0.52

Continued on the next page

REF.	ID	Masonry			Strengthening system			DCT res.
		t	L	f_c	Conf.	Fibre type	Matrix type	τ_{max}
		mm	mm	[MPa]	-	-	-	[MPa]
	B2A-2	250	1160	7.0	UR	GFRP	LC	0.41
	B2A-F33S-1	250	1160	7.0	CRM	GFRP	LC	0.95
	B2A-F33S-2	250	1160	7.0	CRM	GFRP	LC	0.91
	B2A-F66S-1	250	1160	7.0	CRM	GFRP	LC	0.91
	B2A-F66S-2	250	1160	7.0	CRM	GFRP	LC	1.02
	B2A-F99S-1	250	1160	7.0	CRM	GFRP	LC	1.03
	B2A-F99S-2	250	1160	7.0	CRM	Steel mesh	LC	0.98
	B2A-S150-1	250	1160	7.0	CRM	Steel mesh	LC	0.79
	B2A-S150-2	250	1160	7.0	CRM	Steel mesh	LC	0.83
	B2A-S200-1	250	1160	7.0	CRM	Steel mesh	n.d.	0.99
	B2A-S200-2	250	1160	7.0	CRM	n.d.	n.d.	0.97
	B2C-1	250	1160	7.1	UR	n.d.	LC	0.67
	B2C-2	250	1160	7.1	UR	GFRP	LC	0.58
	B2C-F33S-1	250	1160	7.1	CRM	GFRP	LC	1.03
	B2C-F33S-2	250	1160	7.1	CRM	GFRP	LC	1.01
	B2C-F66S-1	250	1160	7.1	CRM	GFRP	LC	1.16
	B2C-F66S-2	250	1160	7.1	CRM	GFRP	LC	1.23
	B2C-F99S-1	250	1160	7.1	CRM	GFRP	n.d.	1.14
	B2C-F99S-2	250	1160	7.1	CRM	n.d.	n.d.	1.32
	B3A-1	380	1160	7.0	UR	n.d.	LC	0.42
	B3A-2	380	1160	7.0	UR	GFRP	LC	0.50
	B3A-F33S-1	380	1160	7.0	CRM	GFRP	LC	0.77
	B3A-F33S-2	380	1160	7.0	CRM	GFRP	LC	0.77
	B3A-F66S-1	380	1160	7.0	CRM	GFRP	LC	0.85
	B3A-F66S-2	380	1160	7.0	CRM	GFRP	LC	0.70
	B3A-F66D-1	380	1160	7.0	CRM	GFRP	LC	0.88
	B3A-F66D-2	380	1160	7.0	CRM	GFRP	LC	0.92
	B3A-F99D-1	380	1160	7.0	CRM	GFRP	LC	0.73
	B3A-F99D-2	380	1160	7.0	CRM	Steel mesh	LC	0.66
	B3A-S150-1	380	1160	7.0	CRM	Steel mesh	n.d.	0.80
	B3A-S150-2	380	1160	7.0	CRM	n.d.	n.d.	0.65
	B3B-1	380	1160	6.9	UR	n.d.	LC	0.39

REF.	ID	Masonry			Strengthening system			DCT res.
		t	L	f_c	Conf.	Fibre type	Matrix type	τ_{max}
		mm	mm	[MPa]	-	-	-	[MPa]
	B3B-2	380	1160	6.9	UR	GFRP	LC	0.46
	B3B-F99D-1	380	1160	6.9	CRM	GFRP	n.d.	0.66
	B3B-F99D-2	380	1160	6.9	CRM	n.d.	n.d.	0.51
	IA-1	380	1160	7.0	UR	n.d.	LC	0.36
	IA-2	380	1160	7.0	UR	GFRP	LC	0.32
	IA-F66S-1	380	1160	7.0	CRM	GFRP	LC	0.57
	IA-F66S-2	380	1160	7.0	CRM	GFRP	LC	0.54
	IA-F99S-1	380	1160	7.0	CRM	GFRP	n.d.	0.59
	IA-F99S-2	380	1160	7.0	CRM	n.d.	n.d.	0.50
	IB-1	380	1160	6.9	UR	n.d.	LC	0.28
	IB-2	380	1160	6.9	UR	GFRP	LC	0.27
	IB-F33S-1	380	1160	6.9	CRM	GFRP	LC	0.47
	IB-F33S-2	380	1160	6.9	CRM	GFRP	LC	0.48
	IB-F66S-1	380	1160	6.9	CRM	GFRP	n.d.	0.40
	IB-F66S-2	380	1160	6.9	CRM	n.d.	n.d.	0.41
	RA-1	400	1160	0.6	UR	n.d.	LC	0.21
	RA-2	400	1160	0.6	UR	GFRP	LC	0.19
	RA-F33S-1	400	1160	0.6	CRM	GFRP	LC	0.59
	RA-F33S-2	400	1160	0.6	CRM	GFRP	LC	0.55
	RA-F66S-1	400	1160	0.6	CRM	GFRP	LC	0.51
	RA-F66S-2	400	1160	0.6	CRM	GFRP	LC	0.56
	RA-F66D-1	400	1160	0.6	CRM	GFRP	n.d.	0.63
	RA-F66D-2	400	1160	0.6	CRM	GFRP	n.d.	0.61
	RB-1	400	1160	0.6	CRM	GFRP	LC	0.18
	RB-2	400	1160	0.6	CRM	GFRP	LC	0.18
	RB-F66S-1	400	1160	0.6	CRM	GFRP	n.d.	0.56
	RB-F66S-2	400	1160	0.6	CRM	n.d.	n.d.	0.60
	B2A-1	250	1160	7.0	UR	n.d.	n.d.	0.52
	B2A-2	250	1160	7.0	UR	GFRP	n.d.	0.41
	B2A-N-1	250	1160	7.0	CRM	GFRP	n.d.	0.89
	B2A-N-2	250	1160	7.0	CRM	GFRP	n.d.	0.87
[83]	B2A-M-1	250	1160	7.0	CRM	GFRP	n.d.	0.77
	B2A-M-2	250	1160	7.0	CRM	GFRP	n.d.	0.81
	B2A-Z-1	250	1160	7.0	CRM	GFRP	n.d.	0.84
	CF-L-2	400	1160	0.5	CRM	n.d.	n.d.	0.35
	CA-1	400	1160	0.6	UR	n.d.	n.d.	0.17

Continued on the next page

REF.	ID	Masonry			Strengthening system			DCT res.
		t	L	f_c	Conf.	Fibre type	Matrix type	τ_{max}
		mm	mm	[MPa]	-	-	-	[MPa]
	CA-2	400	1160	0.6	UR	GFRP	n.d.	0.19
	CA-M-1	400	1160	0.6	CRM	GFRP	n.d.	0.58
	CA-M-2	400	1160	0.6	CRM	n.d.	n.d.	0.57
	CF-1	400	1160	0.5	UR	n.d.	n.d.	0.07
	CF-2	400	1160	0.5	UR	GFRP	n.d.	0.08
	CF-L-1	400	1160	0.5	CRM	n.d.	n.d.	0.32
	R4D-1	400	1160	0.7	UR	GFRP	n.d.	0.36
	R4D-N-1	400	1160	0.7	CRM	GFRP	n.d.	0.65
	R4D-N-2	400	1160	0.7	CRM	GFRP	n.d.	0.69
	R4D-M-1	400	1160	0.7	CRM	GFRP	n.d.	0.71
	R4D-M-2	400	1160	0.7	CRM	GFRP	n.d.	0.70
	R4D-Z-1	400	1160	0.7	CRM	GFRP	n.d.	0.72
	R4D-Z-2	400	1160	0.7	CRM	n.d.	n.d.	0.61
	R7E-1	700	1160	0.7	UR	n.d.	n.d.	0.38
	R7E-2	700	1160	0.7	UR	GFRP	n.d.	0.33
	R7E-M-1	700	1160	0.7	CRM	GFRP	n.d.	0.61
	R7E-M-2	700	1160	0.7	CRM	GFRP	n.d.	0.65
	R7E-Z-1	700	1160	0.7	CRM	GFRP	n.d.	0.54
	R7E-Z-2	700	1160	0.7	CRM	n.d.	n.d.	0.62
[84]	DC_CON	55	800	51.0	UR	glass	n.d.	0.39
	DC_1L	55	800	5.7	FRCM	glass	n.d.	0.85
[84]	DC_2L	55	800	5.7	FRCM	n.d.	n.d.	1.21
[36]	NYT-P1	250	1200	2.3	UR	n.d.	P	0.37
	NYT-P2	250	1200	2.3	UR	hemp	P	0.30
	NYT-HFC_PT	250	1200	2.3	FRCM	hemp	L	0.57
	NYT-HFC_PT_2	250	1200	2.3	FRCM	hemp	L	0.67
	NYT-HFC_MW	250	1200	2.3	FRCM	hemp	n.d.	0.95
	NYT-HFC_MW_2	250	1200	2.3	FRCM	hemp	n.d.	0.92
	C-P	250	1180	3.4	UR	hemp	P	0.12
	C-P2	250	1180	3.4	UR	hemp	P	0.24
	C-HFC_PT	250	1180	3.4	FRCM	hemp	L	0.90
	C-HFC_PT_2	250	1180	3.4	FRCM	hemp	L	0.97
	C-HFC_MW	250	1180	3.4	FRCM	hemp	n.d.	0.92

REF.	ID	Masonry			Strengthening system			DCT res.
		t	L	f_c	Conf.	Fibre type	Matrix type	τ_{max}
		mm	mm	[MPa]	-	-	-	[MPa]
	C-HFC_MW_2	250	1180	3.4	FRCM	n.d.	n.d.	0.98
[85]	35-UR	250	1200	4.3	UR	n.d.	L	0.48
	36-UR	250	1200	4.3	UR	glass	L	0.47
	31-RO	250	1200	4.3	CRM	glass	L	0.48
	32-RO	250	1200	4.3	CRM	glass	L	0.54
	33-D	250	1200	4.3	CRM	glass	n.d.	0.56
	34-D	250	1200	4.3	CRM	glass	n.d.	0.61
	37-R2	250	1200	4.3	CRM	glass	L	0.74
	38-R2	250	1200	4.3	CRM	glass	L	0.77
	39-C	250	1200	4.3	CRM	glass	n.d.	1.02
	40-C	250	1200	4.3	CRM	n.d.	n.d.	0.99
[86]	UPD1	250	1000	2.7	UR	n.d.	L	0.40
	UPD2	250	1000	2.7	UR	basalt	L	0.37
	RPS1	250	1000	2.7	FRCM	basalt	L	0.60
	RPS2	250	1000	2.7	FRCM	basalt	L	0.52
	RPS3	250	1000	2.7	FRCM	basalt	L	0.53
	RPD1	250	1000	2.7	FRCM	basalt	n.d.	0.62
	RPD2	250	1000	2.7	FRCM	n.d.	n.d.	0.63
[32]	URM_01	120	1210	7.3	UR	n.d.	L	1.23
[32]	URM_02	120	1210	7.4	UR	carbon	L	1.09
	CFRCM	120	1210	7.5	FRCM	glass	n.d.	1.62
	GFRCM	120	1210	7.6	FRCM	n.d.	n.d.	1.44
[31]	T1	250	1200	2.2	UR	n.d.	n.d.	0.31
	T2	250	1200	2.2	UR	n.d.	n.d.	0.24
	T3	250	1200	2.2	UR	n.d.	n.d.	0.29
	T4	250	1200	2.2	UR	n.d.	n.d.	0.22
	T5	250	1200	2.2	UR	n.d.	P L	0.23
	T6	250	1200	2.2	UR	glass	P L	0.23
	T_G_M1_s1	250	1200	2.2	CRM	glass	P L	0.58
	T_G_M1_s2	250	1200	2.2	CRM	glass	P L	0.73
	T_G_M1_a1	250	1200	2.2	CRM	glass	P L	0.40
	T_G_M1_a2	250	1200	2.2	CRM	glass	P L	0.43
	T_G_M2_s1	250	1200	2.2	CRM	glass	P L	0.64
	T_G_M2_s2	250	1200	2.2	CRM	hemp	P L	0.82
	T_H_M1_s1	250	1200	2.2	FRCM	hemp	L	0.51

Continued on the next page

REF.	ID	Masonry			Strengthening system			DCT res.
		t	L	f_c	Conf.	Fibre type	Matrix type	τ_{max}
		mm	mm	[MPa]	-	-	-	[MPa]
	T_H_M1_s2	250	1200	2.2	FRCM	hemp	L	0.60
	T_H_M4_s1	250	1200	2.2	FRCM	hemp	n.d.	1.01
	T_H_M4_s2	250	1200	2.2	FRCM	n.d.	n.d.	0.97
	CB1	250	1180	3.4	UR	n.d.	P L	0.26
	CB2	250	1180	3.4	UR	hemp	P L	0.32
	CB_H_M1_s1	250	1180	3.4	FRCM	hemp	L	0.80
	CB_H_M1_s2	250	1180	3.4	FRCM	hemp	L	0.86
	CB_H_M4_s1	250	1180	3.4	FRCM	hemp	n.d.	1.02
	CB_H_M4_s2	250	1180	3.4	FRCM	n.d.	n.d.	0.96
[87]	S1-NR-1	100	1250	4.4	UR	n.d.	L	0.12
	S1-NR-2	100	1250	4.4	UR	glass	L	0.10
	S1-FB8-1	100	1250	4.4	CRM	glass	L	0.75
	S1-FB8-2	100	1250	4.4	CRM	glass	L	0.88
	S1-FB13-1	100	1250	4.4	CRM	glass	C	0.77
	S1-FB13-2	100	1250	4.4	CRM	glass	C	0.78
	S1-FB25-1	100	1250	4.4	CRM	glass	L	0.90
	S1-FB25-2	100	1250	4.4	CRM	glass	L	0.99
	S1-FBSC-1	100	1250	4.4	CRM	glass	L	0.81
	S1-FBSC-2	100	1250	4.4	CRM	n.d.	L	0.81
[87]	S1-FB-8SR-1	100	1250	4.4	Mortar	n.d.	eco-L	0.70
	S1-FB-8SR-2	100	1250	4.4	Mortar	glass	eco-L	0.51
	S1-FBML-1	100	1250	4.4	CRM	glass	L	0.76
	S1-FBML-2	100	1250	4.4	CRM	glass	L	0.75
	S1-FRCM-A1	100	1250	4.4	FRCM	glass	C	0.85
	S1-FRCM-A2	100	1250	4.4	FRCM	aramid	C	1.05
	S1-FRCM-B1	100	1250	4.4	FRCM	aramid	C	0.85
	S1-FRCM-B2	100	1250	4.4	FRCM	glass	C	0.94
	S1-FRCM-C1	100	1250	4.4	FRCM	glass	L	0.65
	S1-FRCM-C2	100	1250	4.4	FRCM	n.d.	L	0.87
	D1-NR-1	150	1250	6.1	UR	n.d.	n.d.	0.05
	D1-NR-2	150	1250	6.1	UR	glass	n.d.	0.07
	D1-FB8-1	150	1250	6.1	CRM	glass	L	0.53
	D1-FB8-2	150	1250	6.1	CRM	glass	L	0.53
	D1-FRCM-A1	150	1250	6.1	FRCM	glass	C	0.53
	D1-FRCM-A2	150	1250	6.1	FRCM	aramid	C	0.55
	D1-FRCM-B1	150	1250	6.1	FRCM	aramid	C	0.54

REF.	ID	Masonry			Strengthening system			DCT res.
		t	L	f_c	Conf.	Fibre type	Matrix type	τ_{max}
		mm	mm	[MPa]	-	-	-	[MPa]
	D1-FRCM-B2	150	1250	6.1	FRCM	glass	C	0.48
	D1-FRCM-C1	150	1250	6.1	FRCM	glass	n.d.	0.55
	D1-FRCM-C2	150	1250	6.1	FRCM	n.d.	C	0.55
[88]	C	78	347	7.3	UR	glass	C	1.69
	D-N	78	347	7.3	FRCM	glass	C	1.73
	D-A	78	347	7.3	FRCM	glass	C	1.51
	S-N	78	347	7.3	FRCM	glass	n.d.	1.78
	S-A	78	347	7.3	FRCM	n.d.	n.d.	1.94
[89]	P	250	1200	n.d.	UR	n.d.	n.d.	0.14
	PS	250	650	n.d.	UR	steel	n.d.	0.12
	FC	250	650	n.d.	FRCM	n.d.	n.d.	0.62
	PP	250	650	n.d.	Mortar	glass	n.d.	0.60
	TII	250	650	n.d.	FRCM	glass	n.d.	0.48
	TI1	250	650	n.d.	FRCM	glass	n.d.	0.31
	TI2	250	650	n.d.	FRCM	n.d.	L	0.32
[28]	URM	120	1200	5.0	UR	carbon	L	0.60
	C_FRCM_S_A	120	1200	5.1	FRCM	carbon	L	1.17
[28]	C_FRCM_S	120	1200	5.2	FRCM	carbon	L	1.16
	C_FRCM_U_A	120	1200	5.3	FRCM	glass	L	0.93
	G_FRCM_S_A	120	1200	5.5	FRCM	glass	n.d.	1.23
	G_FRCM_S	120	1200	5.6	FRCM	n.d.	n.d.	1.24
[90]	WA1	150	1055	3.5	UR	glass	n.d.	0.51
	WG2	150	1055	3.5	CRM	basalt	n.d.	1.38
	WB3	150	1055	3.5	FRCM	basalt	n.d.	1.50
	WB4	150	1055	3.5	FRCM	glass	n.d.	1.55
	WG5	150	1055	3.5	CRM	carbon	n.d.	1.39
	WC6	150	1050	3.5	CRM	carbon	n.d.	1.47
	WC7	150	1065	3.5	CRM	n.d.	n.d.	0.80
[91]	W1	250	1200	6.1	UR	n.d.	n.d.	0.45
	W2	250	1200	6.1	UR	n.d.	C	0.47
	W3	250	1200	6.1	UR	glass	C	0.35
	W4_GFRP	250	1200	6.1	CRM	glass	C	0.66
	W5-GFRP	250	1200	6.1	CRM	glass	n.d.	0.49

Continued on the next page

REF.	ID	Masonry			Strengthening system			DCT res.
		t	L	f_c	Conf.	Fibre type	Matrix type	τ_{max}
		mm	mm	[MPa]	-	-	-	[MPa]
	W6-GFRP	250	1200	6.1	CRM	n.d.	n.d.	0.45
[92]	T1C-1	150	1045	17.2	UR	n.d.	n.d.	0.51
	T2C-2	200	1050	17.2	UR	glass	n.d.	0.39
	T1F-3	150	1050	17.2	CRM	glass	n.d.	1.39
	T1F-4	150	1070	17.2	CRM	carbon	n.d.	1.37
	T1F-5	150	1060	17.2	CRM	carbon	n.d.	1.45
	T1F-6	150	1075	17.2	CRM	basalt	n.d.	0.79
	T1F-7	150	1050	17.2	CRM	basalt	n.d.	1.51
	T1F-8	150	1070	17.2	CRM	basalt	n.d.	1.52
	T1F-9a	150	1050	17.2	CRM	glass	n.d.	1.82
	T2F-10	200	1035	16.8	CRM	glass	n.d.	0.96
	T2F-11	200	1040	16.8	CRM	carbon	n.d.	0.87
	T2F-12	200	1040	16.8	CRM	carbon	n.d.	0.88
	T2F-13	200	1040	16.8	CRM	basalt	n.d.	0.74
	T2F-14	200	1050	16.8	CRM	basalt	n.d.	0.86
	T2F-15	200	1050	16.8	CRM	basalt	n.d.	1.09
	T2F-16	200	1040	16.8	CRM	n.d.	n.d.	1.06
[93]	W1-A-1	220	1040	2.9	UR	n.d.	n.d.	0.10
	W2-A-2	200	1050	3.6	UR	glass	n.d.	0.27
	W1-G-3	220	1040	2.9	CRM	glass	n.d.	0.60
	W1-G-4	220	1040	2.9	CRM	carbon	n.d.	0.77
	W1-C-5	220	1040	2.9	CRM	carbon	n.d.	0.41
	W1-C-6	220	1040	2.9	CRM	basalt	n.d.	0.54
	W1-B-7	220	1040	2.9	CRM	basalt	n.d.	0.57
	W1-B-8	220	1040	2.9	CRM	basalt	n.d.	0.69
	W1-B-9*	220	1040	2.9	CRM	glass	n.d.	0.84
	W2-G-10	200	1050	3.6	CRM	glass	n.d.	1.04
	W2-G-11	200	1050	3.6	CRM	carbon	n.d.	0.90
	W2-C-12	200	1050	3.6	CRM	carbon	n.d.	1.02
	W2-C-13	200	1050	3.6	CRM	basalt	n.d.	1.06
	W2-B-14	200	1050	3.6	CRM	basalt	n.d.	1.01
	W2-B-15	200	1050	3.6	CRM	basalt	n.d.	1.23
	W2-B-16*	200	1050	3.6	CRM	n.d.	L	1.46
[94]	DW	300	1000	6.0	UR	glass	L	0.08
	DW_G-TRCM	300	1000	6.0	FRCM	glass	L	0.27

REF.	ID	Masonry			Strengthening system			DCT res.
		t	L	f_c	Conf.	Fibre type	Matrix type	τ_{max}
		mm	mm	[MPa]	-	-	-	[MPa]
	DW_Gc-TRM	300	1000	6.0	FRCM	glass	n.d.	0.31
	DW_G-TRM-NSM	300	1000	6.0	FRCM	n.d.	n.d.	0.13
[95]	UR2-1	250	1030	4.2	UR	n.d.	n.d.	0.33
	UR2-2	250	1030	4.2	UR	n.d.	L	0.20
	UR2-3	250	1030	4.2	UR	glass	L	0.29
	R2s-1	250	1030	4.2	CRM	glass	L	0.50
	R2s-2	250	1030	4.2	CRM	glass	L	0.39
	R2s-3	250	1030	4.2	CRM	glass	L	0.34
	R2s-4	250	1030	4.2	CRM	glass	L	0.32
	R2s-th	250	1030	4.2	CRM	glass	L	0.48
	R2d-1	250	1030	4.2	CRM	glass	L	0.65
	R2d-2	250	1030	4.2	CRM	glass	n.d.	0.70
	R2d-3	250	1030	4.2	CRM	n.d.	L	0.74
	UR1-1	120	1030	4.2	UR	glass	n.d.	0.20
	R1s-1	120	1030	4.2	CRM	n.d.	L	0.86
[95]	URh-1	250	1200	3.1	UR	glass	n.d.	0.72
	Rhs-1	250	1200	3.1	CRM	n.d.	n.d.	0.80
[96]	CW1*	100	600	2.2	UR	n.d.	n.d.	0.28
	CW2	100	600	2.2	UR	n.d.	n.d.	0.27
	CW3	100	600	2.2	UR	n.d.	n.d.	0.26
	C1	100	600	2.2	UR	n.d.	n.d.	0.42
	C2	100	600	2.2	UR	n.d.	n.d.	0.41
	C3	100	600	2.2	UR	-	n.d.	0.39
	M1	100	600	2.2	Mortar	-	n.d.	1.31
	M2	100	600	2.2	Mortar	-	n.d.	1.36
	M3	100	600	2.2	Mortar	steel	n.d.	1.34
	SM1	100	600	2.2	CRM	steel	n.d.	1.47
	SM2	100	600	2.2	CRM	steel	n.d.	1.44
	SM3	100	600	2.2	CRM	polymer	n.d.	1.41
	PM1	100	600	2.2	CRM	polymer	n.d.	1.60
	PM2	100	600	2.2	CRM	polymer	n.d.	1.62
	PM3	100	600	2.2	CRM	glass	n.d.	1.40
	GM1	100	600	2.2	CRM	glass	n.d.	2.02

Continued on the next page

REF.	ID	Masonry			Strengthening system			DCT res.
		t	L	f_c	Conf.	Fibre type	Matrix type	τ_{max}
		mm	mm	[MPa]	-	-	-	[MPa]
	GM2	100	600	2.2	CRM	glass	n.d.	2.00
	GM3	100	600	2.2	CRM	steel	n.d.	1.99
	S1	100	600	2.2	Steel	steel	n.d.	0.97
	S2	100	600	2.2	Steel	steel	n.d.	0.90
	S3	100	600	2.2	Steel	green plastic	n.d.	0.97
	PL1	100	600	2.2	CRM	green plastic	n.d.	1.09
	PL2	100	600	2.2	CRM	green plastic	n.d.	1.01
	PL3	100	600	2.2	CRM	orange plastic	n.d.	1.05
	PS1	100	600	2.2	CRM	orange plastic	n.d.	1.24
	PS2	100	600	2.2	CRM	orange plastic	n.d.	1.10
	PS3	100	600	2.2	CRM	PP	n.d.	1.13
[96]	4P1	100	600	2.2	CRM	PP	n.d.	0.83
	4P2	100	600	2.2	CRM	PP	n.d.	0.74
	4P3	100	600	2.2	CRM	PP	n.d.	0.65
	6P1	100	600	2.2	CRM	PP	n.d.	0.87
	6P2	100	600	2.2	CRM	PP	n.d.	0.86
	6P3	100	600	2.2	CRM	n.d.	n.d.	0.80
[97]	UW	110	1200	7.4	UR	n.d.	n.d.	0.03
	1NRW15	110	1200	7.4	Mortar	n.d.	n.d.	0.44
	1NRW25	110	1200	7.4	Mortar	Glass	n.d.	0.60
	1GRWN15_1	110	1200	7.4	FRCM	Glass	n.d.	0.48
	1GRWN15_2	110	1200	7.4	FRCM	Glass	n.d.	0.70
	1GRWN25_1	110	1200	7.4	FRCM	Glass	n.d.	0.58
	1GRWN25_2	110	1200	7.4	FRCM	Glass	n.d.	1.13
	2GRWN15	110	1200	7.4	FRCM	Glass	n.d.	1.54
	2GRWN25_1	110	1200	7.4	FRCM	Glass	n.d.	1.90
	2GRWN25_2	110	1200	7.4	FRCM	n.d.	n.d.	1.63
[98]	UPD1	250	960	6.9	UR	n.d.	n.d.	0.45
	UPD2	250	960	6.9	UR	n.d.	L	0.60
	UPD3	250	960	6.9	UR	basalt	L	0.64
	RPS1	250	960	6.9	FRCM	basalt	L	0.56
	RPS2	250	960	6.9	FRCM	basalt	L	0.70

REF.	ID	Masonry			Strengthening system			DCT res.
		t	L	f_c	Conf.	Fibre type	Matrix type	τ_{max}
		mm	mm	[MPa]	-	-	-	[MPa]
	RPS3	250	960	6.9	FRCM	basalt	L	0.76
	RPD1	250	960	6.9	FRCM	basalt	L	0.76
	RPD2	250	960	6.9	FRCM	basalt	n.d.	0.73
	RPD3	250	960	6.9	FRCM	n.d.	n.d.	1.15
[99]	REF 1	118	1155	n.d.	UR	n.d.	n.d.	0.19
	REF 2	118	1145	n.d.	UR	n.d.	n.d.	0.30
	REF 3	118	1150	n.d.	UR	basalt	n.d.	0.24
	BTF-A 1	118	1160	n.d.	FRCM	basalt	n.d.	1.11
	BTF-A 2	118	1155	n.d.	FRCM	basalt	n.d.	1.05
	BTF-A 3	118	1165	n.d.	FRCM	basalt	n.d.	0.96
	BTC-A 1	118	1155	n.d.	FRCM	basalt	n.d.	1.05
	BTC-A 2	118	1160	n.d.	FRCM	basalt	n.d.	1.03
	BTC-A 3	118	1170	n.d.	FRCM	basalt	n.d.	0.93
[99]	BTG-B 1	118	1150	n.d.	FRCM	basalt	n.d.	1.81
	BTG-B 2	118	1160	n.d.	FRCM	basalt	n.d.	1.77
	BTG-B 3	118	1160	n.d.	FRCM	basalt	n.d.	1.62
	BTC-N x	118	1150	n.d.	FRCM	basalt	n.d.	0.95
	BTC-N #	118	1150	n.d.	FRCM	n.d.	n.d.	1.07
[100]	URM-1	100	520	3.7	UR	n.d.	n.d.	0.18
	URM-2	100	520	3.7	UR	Glass	n.d.	0.19
	RF-A-1	100	520	3.7	FRCM	Glass	n.d.	0.62
	RF-A-2	100	520	3.7	FRCM	Glass	n.d.	0.65
	RF-A-3	100	520	3.7	FRCM	Glass	n.d.	0.52
	RF-S-1	100	520	3.7	FRCM	Glass	n.d.	0.91
	RF-S-2	100	520	3.7	FRCM	Glass	n.d.	0.96
	RF-S-3	100	520	3.7	FRCM	n.d.	n.d.	0.76
[33]	DW_110_control	270	830	6.7	UR	Glass	n.d.	0.27
	DW_110_G_1	270	830	6.7	CRM	Glass	n.d.	0.78
	DW_110_G_2	270	830	6.8	CRM	Glass	n.d.	0.64
	DW_110_G_3	270	830	6.8	CRM	n.d.	n.d.	0.63
[29]	URM_1	250	1200	2.3	UR	n.d.	n.d.	0.31
	URM_2	250	1200	2.3	UR	n.d.	n.d.	0.24
	URM_3	250	1200	2.3	UR	n.d.	n.d.	0.23
	URM_4	250	1200	2.3	UR	n.d.	n.d.	0.23
	URM_5	250	1200	2.3	UR	n.d.	C L	0.29

Continued on the next page

REF.	ID	Masonry			Strengthening system			DCT res.
		t	L	f_c	Conf.	Fibre type	Matrix type	τ_{max}
		mm	mm	[MPa]	-	-	-	[MPa]
[29]	URM_6	250	1200	2.3	UR	Glass	C L	0.22
	G30cl_1_1	250	1200	2.3	CRM	Glass	C L	0.37
	G30cl_1_2	250	1200	2.3	CRM	Glass	C L	0.37
	G30cl_2_1	250	1200	2.3	CRM	Glass	L	0.95
	G30cl_2_2	250	1200	2.3	CRM	Glass	L	0.94
	G30l_1_1	250	1200	2.3	CRM	Glass	L	0.41
	G30l_1_2	250	1200	2.3	CRM	Glass	L	0.50
	G30l_2_1	250	1200	2.3	CRM	Glass	C L	0.72
	G30l_2_2	250	1200	2.3	CRM	Glass	C L	0.51
	G40cl_1_1	250	1200	2.3	CRM	Glass	C L	0.38
	G40cl_1_2	250	1200	2.3	CRM	Glass	C L	0.39
	G40cl_2_1	250	1200	2.3	CRM	Glass	L	1.06
	G40cl_2_2	250	1200	2.3	CRM	Glass	L	0.99
	G40l_1_1	250	1200	2.3	CRM	Glass	L	0.38
	G40l_1_2	250	1200	2.3	CRM	Glass	L	0.39
	G40l_2_1	250	1200	2.3	CRM	Glass	n.d.	0.74
	G40l_2_2	250	1200	2.3	CRM	n.d.	n.d.	0.82
[34]	1L_C_a	140	1280	3.4	UR	n.d.	n.d.	0.36
	1L_C_b	140	1280	3.4	UR	n.d.	L	0.33
	1L_C_c	140	1280	3.4	UR	basalt	L	0.35
	1L_1FRCM_a	140	1280	3.4	FRCM	basalt	L	1.08
	1L_1FRCM_b	140	1280	3.4	FRCM	basalt	L	0.81
	1L_1FRCM_c	140	1280	3.4	FRCM	basalt	L	0.99
	1L_2FRCM_a	140	1280	3.4	FRCM	basalt	L	1.09
	1L_2FRCM_b	140	1280	3.4	FRCM	basalt	L	1.42
	1L_2FRCM_c	140	1280	3.4	FRCM	n.d.	L	1.35
	1L_2FRM_a	140	1280	3.4	Mortar	n.d.	L	1.16
	1L_2FRM_b	140	1280	3.4	Mortar	n.d.	n.d.	1.37
	1L_2FRM_c	140	1280	3.4	Mortar	n.d.	n.d.	1.13
	2L_C_a	285	1280	3.4	UR	n.d.	n.d.	0.70
	2L_C_b	285	1280	3.4	UR	n.d.	L	0.54
	2L_C_c	285	1280	3.4	UR	basalt	L	0.40
	2L_1FRCM_a	285	1280	3.4	FRCM	basalt	L	0.74
	2L_1FRCM_b	285	1280	3.4	FRCM	basalt	L	0.89
	2L_1FRCM_c	285	1280	3.4	FRCM	basalt	L	0.64
	2L_2FRCM_a	285	1280	3.4	FRCM	basalt	L	0.87

REF.	ID	Masonry			Strengthening system			DCT res.
		t	L	f_c	Conf.	Fibre type	Matrix type	τ_{max}
		mm	mm	[MPa]	-	-	-	[MPa]
	2L_2FRCM_b	285	1280	3.4	FRCM	basalt	L	0.80
	2L_2FRCM_c	285	1280	3.4	FRCM	n.d.	L	1.02
	2L_2FRM_a	285	1280	3.4	Mortar	n.d.	L	1.00
	2L_2FRM_b	285	1280	3.4	Mortar	n.d.	n.d.	0.96
	2L_2FRM_c	285	1280	3.4	Mortar	n.d.	n.d.	0.95
[101]	CD_A_URM	250	1200	4.0	UR	basalt	n.d.	0.59
	CD_A-crack_BFRCM	250	1200	4.0	FRCM	n.d.	n.d.	0.47
	CD_B_URM	250	1100	4.2	UR	basalt	n.d.	0.53
[101]	CD_B-crack_BFRCM	250	1100	4.2	FRCM	basalt	n.d.	0.50
	CD_B_BFRCM	250	1100	4.2	FRCM	n.d.	L	0.78
[30]	URM	250	1290	4.0	UR	basalt	L	0.27
	FRCM_M15_SP15	250	1290	4.0	FRCM	basalt	L	0.63
	FRCM_M20_SP10	250	1290	4.0	FRCM	glass	L	0.68
	CRM_M10_SP30	250	1290	4.0	CRM	glass	n.d.	0.72
	CRM_M15_SP30	250	1290	4.0	CRM	n.d.	n.d.	0.91
[102]	URM	110	900	5.2	UR	n.d.	n.d.	0.81
	URM	110	900	5.2	UR	carbon	n.d.	0.88
	Carbon	110	900	5.2	FRCM	basalt	n.d.	1.79
	2 ply-basalt	110	900	5.2	FRCM	basalt	n.d.	1.67
	4-ply-basalt	110	900	5.2	FRCM	n.d.	n.d.	1.71
[103]	5NR	340	1200	0.6	UR	n.d.	n.d.	0.14
	6NR	340	1200	0.6	UR	glass	n.d.	0.13
	1R-GC	340	1200	0.6	FRCM	glass	n.d.	0.75
	2RG	340	1200	0.6	FRCM	glass	n.d.	0.51
	3RGC	340	1200	0.6	FRCM	glass	n.d.	0.50
	4RG	340	1200	0.6	FRCM	n.d.	n.d.	0.57
[104]	W-U-1	120	1000	3.2	UR	n.d.	n.d.	0.49
	W-U-2	120	1000	3.2	UR	n.d.	n.d.	0.42
	W-SM-1	120	1000	3.2	Mortar	n.d.	n.d.	1.01
	W-SM-2	120	1000	3.2	Mortar	n.d.	n.d.	0.98

Continued on the next page

REF.	ID	Masonry			Strengthening system			DCT res.
		t	L	f_c	Conf.	Fibre type	Matrix type	τ_{max}
		mm	mm	[MPa]	-	-	-	[MPa]
[104]	W-DM-1	120	1000	3.2	Mortar	n.d.	n.d.	
	W-DM-2	120	1000	3.2	Mortar	n.d.	n.d.	1.13
	W-SE-1	120	1000	3.2	Mortar	n.d.	n.d.	1.34
	W-SE-2	120	1000	3.2	Mortar	n.d.	n.d.	1.45
	W-DE-1	120	1000	3.2	Mortar	n.d.	n.d.	1.44
	W-DE-2	120	1000	3.2	Mortar	carbon glass	n.d.	1.53
	W-SC1-1	120	1000	3.2	FRCM	carbon glass	n.d.	1.35
	W-SC1-2	120	1000	3.2	FRCM	carbon glass	n.d.	1.26
	W-DC1-1	120	1000	3.2	FRCM	carbon glass	n.d.	1.29
	W-DC1-2	120	1000	3.2	FRCM	n.d.	n.d.	1.52
[105]	C_a	300	1200	0.8	UR	n.d.	n.d.	0.27
	C_b	300	1200	0.8	UR	n.d.	n.d.	0.33
	C_c	300	1200	0.8	UR	glass	n.d.	0.44
	2FRCM_a	300	1200	0.8	CRM	glass	n.d.	0.88
	2FRCM_b	300	1200	0.8	CRM	glass	n.d.	0.97
	2FRCM_c	300	1200	0.8	CRM	n.d.	n.d.	0.81
	2FRM-A_a	300	1200	0.8	Mortar	n.d.	n.d.	0.69
	2FRM-A_b	300	1200	0.8	Mortar	n.d.	n.d.	0.58
	2FRM-A_c	300	1200	0.8	Mortar	n.d.	n.d.	0.81
	2FRM-B_a	300	1200	0.8	Mortar	n.d.	n.d.	0.72
	2FRM-B_b	300	1200	0.8	Mortar	n.d.	n.d.	0.77
	2FRM-B_c	300	1200	0.8	Mortar	glass	n.d.	0.54
	1FRCM_a	300	1200	0.8	CRM	glass	n.d.	0.51
	1FRCM_b	300	1200	0.8	CRM	glass	n.d.	0.64
	1FRCM_c	300	1200	0.8	CRM	n.d.	n.d.	0.55
	1FRM-A_a	300	1200	0.8	Mortar	n.d.	n.d.	0.50
	1FRM-A_b	300	1200	0.8	Mortar	n.d.	n.d.	0.54
	1FRM-A_c	300	1200	0.8	Mortar	n.d.	n.d.	0.53
	1FRM-B_a	300	1200	0.8	Mortar	n.d.	n.d.	0.79
	1FRM-B_b	300	1200	0.8	Mortar	n.d.	n.d.	0.58
	1FRM-B_c	300	1200	0.8	Mortar	n.d.	n.d.	0.50
[35]	USW-1	120	1030	4.1	UR	n.d.	n.d.	0.38
	USW-2	120	1030	4.1	UR	n.d.	L	0.42

REF.	ID	Masonry			Strengthening system			DCT res.
		t	L	f_c	Conf.	Fibre type	Matrix type	τ_{max}
		mm	mm	[MPa]	-	-	-	[MPa]
	USW-3	120	1030	4.1	UR	flax	L	0.30
	SW-1L-1	120	1030	4.1	FRCM	flax	L	0.94
	SW-1L-2	120	1030	4.1	FRCM	flax	L	0.83
	SW-1L-3	120	1030	4.1	FRCM	flax	L	0.62
	SW-2L-1	120	1030	4.1	FRCM	flax	L	0.93
	SW-2L-2	120	1030	4.1	FRCM	flax	n.d.	0.74
	SW-2L-3	120	1030	4.1	FRCM	n.d.	n.d.	0.90
[106]	URM_1	310	1270	6.5	UR	n.d.	n.d.	0.32
	URM_2	310	1270	6.5	UR	steel	n.d.	0.21
	URM_1_R	310	1270	6.5	CRM	steel	n.d.	0.49
	URM_2_R	310	1270	6.5	CRM	n.d.	L	0.43
[107]	UM	120	1030	4.3	UR	glass	L	0.41
	GTRM-1	120	1030	4.3	CRM	glass	L	0.84
	GTRM-2	120	1030	4.3	CRM	basalt	L	0.93
	BTRM-1	120	1030	4.3	FRCM	basalt	n.d.	1.13
	BTRM-1	120	1030	4.3	FRCM	n.d.	n.d.	0.96
[108]	MAT-01-U	240	1200	6.4	UR	glass	n.d.	0.16
	MAT-02-D	240	1200	6.4	CRM	glass	n.d.	0.50
	MAT-03-S	240	1200	6.4	CRM	glass	n.d.	0.25
	MAT-04-D	240	1200	6.4	CRM	glass	n.d.	0.49
	MAT-05-S	240	1200	6.4	CRM	glass	n.d.	0.28
	MAT-06-S	240	1200	6.4	CRM	glass	n.d.	0.30
	MAT-07-S	240	1200	6.4	CRM	n.d.	n.d.	0.30
	PIE-01-U	240	1200	7.1	UR	glass	n.d.	0.18
	PIE-02-D	240	1200	7.1	CRM	glass	n.d.	0.45
	PIE-03-S	240	1200	7.1	CRM	glass	n.d.	0.33
	PIE-04-D	240	1200	7.1	CRM	glass	n.d.	0.51
	PIE-05-S	240	1200	7.1	CRM	n.d.	n.d.	0.34
[109]	W1	240	890	5.3	UR	n.d.	n.d.	0.28
	SW-M	240	890	5.3	Mortar	carbon	n.d.	0.44
	SW-C1	240	890	5.3	FRCM	carbon	n.d.	0.51
	SW-C2	240	890	5.3	FRCM	carbon	n.d.	0.38
	SW-C3	240	890	5.3	FRCM	n.d.	n.d.	0.43
	DW-M	240	890	5.3	Mortar	glass	n.d.	0.69
	DW-G2	240	890	5.3	FRCM	glass	n.d.	1.10

Continued on the next page

REF.	ID	Masonry			Strengthening system			DCT res.
		t	L	f_c	Conf.	Fibre type	Matrix type	τ_{max}
		mm	mm	[MPa]	-	-	-	[MPa]
[110]	DW-G3	240	890	5.3	FRCM	glass	n.d.	1.39
	DW-C1	240	890	5.3	FRCM	glass	n.d.	1.02
	DW-C2A	240	890	5.3	FRCM	n.d.	n.d.	1.42
	RL-S-N-1	180	1195	2.0	UR	n.d.	n.d.	0.21
	RL-S-N-2	180	1195	2.0	UR	n.d.	n.d.	0.21
	RL-S-N-4	180	1195	2.0	UR	n.d.	n.d.	0.19
	RL-S-N-5	180	1195	2.0	UR	n.d.	n.d.	0.19
	RL-S-N-6	180	1195	2.0	UR	PBO	n.d.	0.19
	RL-S-NF1-1	180	1195	2.0	FRCM	PBO	n.d.	0.28
	RL-S-NF1-2	180	1195	2.0	FRCM	PBO	n.d.	0.21
	RL-S-NF1-3	180	1195	2.0	FRCM	PBO	n.d.	0.24
	RL-S-NF1-4	180	1195	2.0	FRCM	PBO	n.d.	0.23
	RL-S-NF1-5	180	1195	2.0	FRCM	PBO	n.d.	0.25
	RL-S-NF1-6	180	1195	2.0	FRCM	PBO	n.d.	0.20
	RL-S-NF2-1	180	1195	2.0	FRCM	PBO	n.d.	0.34
	RL-S-NF2-2	180	1195	2.0	FRCM	PBO	n.d.	0.38
	RL-S-NF2-3	180	1195	2.0	FRCM	PBO	n.d.	0.37
	RL-S-NF2-4	180	1195	2.0	FRCM	PBO	n.d.	0.42
	RL-S-NF2-5	180	1195	2.0	FRCM	PBO	n.d.	0.37
	RL-S-NF2-6	180	1195	2.0	FRCM	n.d.	n.d.	0.42
[111]	B-M1_URM	250	1100	4.2	UR	n.d.	L	0.53
	B-M2_URM	250	1200	4.1	UR	basalt	L	0.43
	B-M1_B200-M3-A	250	1100	4.2	FRCM	basalt	L	0.78
	B-M2_B200-M4	250	1200	4.1	FRCM	basalt	L	0.65
	B-M1_B400-M3-A	250	1100	4.2	FRCM	basalt	L	0.82
	B-M2_B400-M4	250	1200	4.1	FRCM	n.d.	L	0.70
[112]	S_URM	300	1100	6.6	UR	n.d.	L	0.26
	S_I	300	1100	6.6	Mortar	n.d.	L	0.26
	S_I-MA	300	1100	6.6	Mortar	basalt	L	0.65
	S_I-MA_B200	300	1100	6.6	FRCM	basalt	L	0.57
	S_I-MA_B400	300	1100	6.6	FRCM	basalt and steel	n.d.	0.57

REF.	ID	Masonry			Strengthening system			DCT res.
		t	L	f_c	Conf.	Fibre type	Matrix type	τ_{max}
		mm	mm	[MPa]	-	-	-	[MPa]
	S_I-MA_B200-S600	300	1100	6.6	FRCM	n.d.	L	0.64
[113]	B-F_A_URM	250	1100	4.2	UR	basalt	L	0.53
	B-F_A_B1	250	1095	4.2	FRCM	basalt	L	0.91
[113]	B-F_A_B1-MA	250	1095	4.2	FRCM	basalt	n.d.	0.78
	B-F_A_B2-MA	250	1095	4.2	FRCM	n.d.	L	0.82
	B-H_A_URM	250	1155	4.2	UR	basalt	L	0.38
	B-H_A_B1	250	1160	4.2	FRCM	basalt	n.d.	0.79
	B-H_A_B1-MA	250	1160	4.2	FRCM	n.d.	L	0.72
	B-FF_A_URM	250	1095	4.2	UR	basalt	n.d.	0.57
	B-FF_A_B1-MA	250	1095	4.2	FRCM	n.d.	L	0.74
	B-F_B_URM	250	1205	4.1	UR	basalt	L	0.43
	B-F_B_B1	250	1200	4.1	FRCM	basalt	L	0.65
	B-F_B_B2	250	1200	4.1	FRCM	aramid-glass	L	0.70
	B-F_B_AG-1	250	1200	4.1	FRCM	aramid-glass	n.d.	0.62
	B-F_B_AG-2	250	1200	4.1	FRCM	n.d.	n.d.	0.67
[114]	URM-1	120	510	5.2	UR	n.d.	L	0.55
	URM-2	120	510	5.2	UR	n.d.	L	0.51
	NHL-1	120	510	5.2	Mortar	n.d.	G	0.82
	NHL-2	120	510	5.2	Mortar	n.d.	G	1.34
	GPM-1	120	510	5.2	Mortar	n.d.	L	0.74
	GPM-2	120	510	5.2	Mortar	glass	L	0.89
	FRCM-1	120	510	5.2	FRCM	glass	G	1.24
	FRCM-2	120	510	5.2	FRCM	glass	G	1.20
	FRGM-1	120	510	5.2	FRCM	glass	L	0.92
	FRGM-2	120	510	5.2	FRCM	glass	L	0.91
	CRM-1	120	510	5.2	CRM	glass	G	1.30
	CRM-2	120	510	5.2	CRM	glass	G	1.50
	CRGM-1	120	510	5.2	CRM	glass	n.d.	1.24
	CRGM-2	120	510	5.2	CRM	n.d.	n.d.	1.17

Continued on the next page

REF.	ID	Masonry			Strengthening system			DCT res.
		t	L	f_c	Conf.	Fibre type	Matrix type	τ_{max}
		mm	mm	[MPa]	-	-	-	[MPa]
[115]	D-0–0–0 1	235	750	2.6	UR	n.d.	C	0.23
	D-0–0–0 2	235	750	2.6	UR	n.d.	C	0.16
	D-0-L-0 1	235	750	2.6	Mortar	n.d.	C	0.35
	D-0-L-0 2	235	750	2.6	Mortar	basalt	C	0.25
[115]	D-B-L-0 1	235	750	2.6	FRCM	basalt	C	0.43
	D-B-L-0 2	235	750	2.6	FRCM	basalt	C	0.43
	D-B-L-A 1	235	750	2.6	FRCM	basalt	n.d.	0.44
	D-B-L-A 2	235	750	2.6	FRCM	basalt	n.d.	0.54
	D-B-T-0 1	235	750	2.6	FRCM	basalt	n.d.	0.86
	D-B-T-0 2	235	750	2.6	FRCM	basalt	n.d.	0.73
	D-B-T-A 1	235	750	2.6	FRCM	basalt	n.d.	1.04
	D-B-T-A 2	235	750	2.6	FRCM	carbon	n.d.	1.26
	D-C-T-0 1	235	750	2.6	FRCM	carbon	n.d.	0.87
	D-C-T-0 2	235	750	2.6	FRCM	n.d.	n.d.	0.71
[116]	URM	115	1200	4.9	UR	carbon	n.d.	0.13
	TRM1	115	1200	4.9	FRCM	carbon	n.d.	0.22
	TRM2	115	1200	4.9	FRCM	carbon	n.d.	0.30
	TRM3	115	1200	4.9	FRCM	n.d.	n.d.	0.30
[117]	SO-UM1	300	1200	3.0	UR	n.d.	n.d.	0.27
	SO-UM2	300	1200	3.0	UR	glass	n.d.	0.21
	SO-UMG1	300	1200	3.0	FRCM	glass	n.d.	0.65
	SO-UMG2	300	1200	3.0	FRCM	glass	n.d.	0.57
	SO-UMG3	300	1200	3.0	FRCM	n.d.	n.d.	0.74
	SO-UMM1	300	1200	3.0	Mortar	n.d.	n.d.	0.75
[118]	Un_T20_a	100	700	4.2	UR	n.d.	AA	0.24
	Un_T20_b	100	700	4.2	UR	carbon	AA	0.35
	1L_T20_a	100	700	4.2	FRCM	carbon	AA	0.94
	1l_T20_b	100	700	4.2	FRCM	carbon	AA	1.13
	2L_T20_a	100	700	4.2	FRCM	carbon	n.d.	1.12
	2l_T20_b	100	700	4.2	FRCM	n.d.	C	1.40

REF.	ID	Masonry			Strengthening system			DCT res.
		t	L	f_c	Conf.	Fibre type	Matrix type	τ_{max}
		mm	mm	[MPa]	-	-	-	[MPa]
[119]	CON	65	700	3.9	UR	Basalt	C	0.82
	CEM-B2	65	700	3.9	FRCM	glass	G	1.47
	CEM-G2	65	700	3.9	FRCM	basalt	G	1.31
	GEO-B2	65	700	3.9	FRCM	glass	G	1.49
	GEO-G2	65	700	3.9	FRCM	glass	n.d.	1.52
	GEO-G1/1	65	700	3.9	FRCM	n.d.	n.d.	1.49
[120]	N20_1	230	610	4.9	UR	n.d.	n.d.	1.20
	N20_2	230	610	4.9	UR	n.d.	n.d.	0.87
[120]	N20_3	230	610	4.9	UR	glass	n.d.	1.03
	G20_1	230	610	4.9	CRM	glass	n.d.	1.13
	G20_2	230	610	4.9	CRM	glass	n.d.	1.34
	G20_3	230	610	4.9	CRM	carbon	n.d.	1.45
	C20_1	230	610	4.9	FRCM	carbon	n.d.	1.55
	C20_2	230	610	4.9	FRCM	carbon	n.d.	1.48
	C20_3	230	610	4.9	FRCM	n.d.	n.d.	1.56
[121]	URM_1	310	1270	6.5	UR	basalt	n.d.	0.33
	URM_1_R	310	1270	6.5	FRCM	basalt	n.d.	0.49
	URM_2_R	310	1270	6.5	FRCM	basalt	n.d.	0.43
	BTRM_1	310	1270	6.5	FRCM	basalt	n.d.	0.56
	BTRM_2	310	1270	6.5	FRCM	n.d.	L	0.50
[122]	MCa	49	410	3.7	UR	PBO	L	0.15
	MCaFRCM	49	410	3.7	FRCM	n.d.	L	1.67
	MB	49	410	3.9	UR	PBO	L	0.30
	MBFRCM	49	410	3.9	FRCM	n.d.	L	1.98
	MCe	49	410	4.1	UR	PBO	n.d.	1.12
	MCeFRCM	49	410	4.1	FRCM	n.d.	n.d.	2.20
[123]	DC_REF_1	150	1020	3.5	UR	n.d.	L	0.65
	DC_REF_2	150	1020	3.5	UR	jute	L	0.60
	DC_J_1L_1	150	1020	3.5	FRCM	jute	L	0.97
	DC_J_1L_2	150	1020	3.5	FRCM	jute	L	1.02
	DC_J_2L_1	150	1020	3.5	FRCM	jute	n.d.	0.79
	DC_J_2L_1	150	1020	3.5	FRCM	n.d.	n.d.	0.95
[124]	Y-US-1	240	850	2.0	UR	n.d.	n.d.	0.27
	Y-US-2	240	850	2.0	UR	n.d.	n.d.	0.27
	Y-US-3	240	850	2.0	UR	n.d.	n.d.	0.26

Continued on the next page

REF.	ID	Masonry			Strengthening system			DCT res.
		t	L	f_c	Conf.	Fibre type	Matrix type	τ_{max}
		mm	mm	[MPa]	-	-	-	[MPa]
[124]	Y-SS-SM-1	240	850	2.0	Mortar	n.d.	n.d.	0.35
	Y-SS-SM-2	240	850	2.0	Mortar	n.d.	n.d.	0.36
	Y-SS-SM-3	240	850	2.0	Mortar	glass	n.d.	0.35
	Y-SS-SM-G120-1	240	850	2.0	CRM	glass	n.d.	0.40
	Y-SS-SM-G120-2	240	850	2.0	CRM	glass	n.d.	0.41
	Y-SS-SM-G120-3	240	850	2.0	CRM	glass	n.d.	0.41
	Y-SS-SM-G220-1	240	850	2.0	CRM	glass	n.d.	0.39
	Y-SS-SM-G220-2	240	850	2.0	CRM	glass	n.d.	0.43
	Y-SS-SM-G220-3	240	850	2.0	CRM	n.d.	n.d.	0.45
	Y-PS-AM-1	240	850	2.0	Mortar	n.d.	n.d.	0.24
	Y-PS-AM-2	240	850	2.0	Mortar	n.d.	n.d.	0.22
	Y-PS-AM-3	240	850	2.0	Mortar	glass	n.d.	0.22
	Y-PS-AM-G145-1	240	850	2.0	CRM	glass	n.d.	0.36
	Y-PS-AM-G145-2	240	850	2.0	CRM	glass	n.d.	0.39
	Y-PS-AM-G145-3	240	850	2.0	CRM	glass	n.d.	0.37
	Y-PS-AM-G165-1	240	850	2.0	CRM	glass	n.d.	0.42
	Y-PS-AM-G165-2	240	850	2.0	CRM	glass	n.d.	0.42
	Y-PS-AM-G165-3	240	850	2.0	CRM	n.d.	n.d.	0.44
[125]	Control	100	785	1.4	UR	basalt	n.d.	0.30
	BTRM-Full	100	785	1.4	CRM	carbon	n.d.	0.62
	CTRM-Full	100	785	1.4	CRM	n.d.	n.d.	0.75
[126]	M1	250	550	0.0	UR	n.d.	n.d.	0.20
	M2	250	550	0.0	UR	n.d.	L	0.33
	M3	250	550	0.0	UR	jute	L	0.24

REF.	ID	Masonry			Strengthening system			DCT res.
		t	L	f_c	Conf.	Fibre type	Matrix type	τ_{max}
		mm	mm	[MPa]	-	-	-	[MPa]
	M10	250	550	0.0	FRCM	jute	L	0.74
	M11	250	550	0.0	FRCM	jute	n.d.	0.84
	M12	250	550	0.0	FRCM	n.d.	n.d.	0.74

Research fundings

Several institutions financially contributed to the research study:

- the National Recovery and Resilience Plan (NRRP), funded by the European Union – NextGenerationEU, Mission 4 "Education and Research", Component 2 "From Research to Business", Investment 1.3 "Creation of extended partnerships between universities, research centres, businesses, and the funding of basic research projects", under the RETURN Project, Spoke 3 (VS3): Earthquakes and Volcanoes, which funded the Ph.D. scholarship;
- ReLUIS ”Progetto Esecutivo accordo DPC/ReLUIS 2024/2026, WP14- Materiali Strutturali Innovativi per la Sostenibilità delle Costruzioni”, contributed to the esperimental campaign relatet to the masonry panels;
- the National Recovery and Resilience Plan (NRRP), Mission 4, Component 2, Investment 1.1, funded by the European Union – NextGenerationEU– Project Title: sTructurAl and eneRGy rEnovation for susTainable buildingS - TARGETS – CUP B53D23027280001 Grant Assignment Decree No. 1409 adopted on 14.9.2022 by the Italian Ministry of University and Research (MUR), contributed to the experimental campaign related to masonry vaults;
- the company FIBRE NET S.p.A. provided some material used in the experimental research activity.

The author gratefully acknowledges the mentioned institutions for their financial support, essential for the fulfilment of the Thesis.

References

[1] Ambraseys, N. (2009). *Earthquakes in the Mediterranean and Middle East. Cambridge University Press.*

[2] Monaco, M., Calderoni, B., Iannuzzo, A., & Gesualdo, A. (2018). Behaviour of in-plane loaded masonry panels. *Procedia Structural Integrity*, 11, 388–393.

[3] Tomazevic, M. (1999). *Earthquake-Resistant Design of Masonry Buildings*. Series on Innovation in Structures and Construction, Vol. 1. Imperial College Press.

[4] Kaplan, H., Bilgin, H., Yilmaz, S., Binici, H., Öztas, A. (2010). Structural damages of L'Aquila (Italy) earthquake. *Natural Hazards and Earth System Sciences*, 10, 499–507.

[5] Indirli, M., Kouris, L.A. S., Formisano, A., Borg, R.P., Mazzolani, F.M. (2013) Seismic damage assessment of unreinforced masonry structures after the Abruzzo 2009 earthquake: The case study of the historical centers of L'Aquila and Castelvecchio Subequo. *International Journal of Architectural Heritage*, 7, 536–578.

[6] Calderoni, B., Prota, A., Cordasco, E. A., & Sandoli, A. (2016). Seismic vulnerability of "ancient" masonry buildings and strengthening intervention strategies. In *Proceedings of the 16th International Brick and Block Masonry Conference (IB2MAC)*, Padova, Italy.

[7] Belli, C. M., & Bruggi, M. (2015). Assessment and reduction of the seismic vulnerability of a stone masonry vault. *Periodica Polytechnica Civil Engineering*, 59(3), 287–296.

[8] Chuang S.W., & Zhuge, Y. (2005). Seismic retrofitting of unreinforced masonry buildings: A literature review. *Australian Journal of Structural Engineering*, 6, 25–36.

[9] Tumialan, J. G., Micelli, F., & Nanni, A. (2001). Strengthening of masonry structures with FRP composites. In *Structures 2001*, American Society of Civil Engineers, Reston, VA, pp. 1–8.

[10] Van Den Einde, L., Zhao, L., & Seible, F. (2003). Use of FRP composites in civil structural applications. *Construction and Building Materials*, 17, 389–403.

[11] Triantafillou, T. (2011). Innovative textile-based composites for strengthening and seismic retrofitting of concrete and masonry structures. In *Advances in FRP Composites in Civil Engineering*, Springer, Berlin, Heidelberg, pp. 3–12.

[12] Ceroni, F., Lignola, G. P., Prota, A., & Saviano, F. (2025). Experimental investigation on FRCM strengthened tuff masonry walls. *Construction and Building Materials*, 504, 144533.

[13] Vienni, C., Orlando, M., & Salvatori, L. (2024). Experimental study of CRM-reinforced brick masonry panels: Cyclic shear-compression tests and compression tests. *Engineering Structures*, 301, 117262.

[14] Facconi, L., Gandelli, E., Monaco, A., Sammartano, G., et al. (2026). Pre-damaging test of a full-scale masonry cross vault subjected to in-plane cyclic shear loading: Main results and design of the FRCM-based strengthening intervention. *Procedia Structural Integrity*, 78, 867–874.

[15] De Santis, S., Aiello, M.A., Boem, I., Calò, S., Cascardi, A., D'Antino, T., Di Leto, M., Gattesco, N., La Mendola, L., Micelli, F., Rizzi, E., & Speranzini, E. (2026). Experimental investigations and analytical models on Composite Reinforced Mortar (CRM) systems for masonry strengthening: A state-of-the-art review. *Journal of Building Engineering*, 129, 116799.

[16] Calabrese, A., D'Antino, T., Poggi, C., Colombi, P., Fava, G., & Pisani, M. (2020). Application of externally bonded inorganic-matrix composites to existing masonry structures. In *Structural rehabilitation of masonry structures*. Springer.

[17] American Concrete Institute (2020). *Guide to Design and Construction of Externally Bonded Fabric-Reinforced Cementitious Matrix and Steel-Reinforced Grout Systems for Repair and Strengthening of Concrete Structures (ACI 549.4R-20)*. American Concrete Institute.

[18] Consiglio Nazionale delle Ricerche. (2018). *Guide for the Design and Construction of Externally Bonded Fibre Reinforced Inorganic Matrix Systems for Strengthening Existing Structures (CNR-DT 215/2018)*. Rome, Italy: CNR.

[19] Ascione, L., De Felice, G., & De Santis, S. (2015). A qualification method for externally bonded Fibre Reinforced Cementitious Matrix (FRCM) strengthening systems. *Composites Part B: Engineering*, 78, 497–506.

[20] Boem, I. (2022). Masonry elements strengthened through textile-reinforced mortar: Application of detailed level modelling with a free open-source finite-element code. arXiv.

[21] Boem, I., & Gattesco, N. (2023). Composite Reinforced Mortar (CRM) and Fiber-Reinforced Cementitious Matrix (FRCM) for the seismic protection of masonry vaults. *Procedia Structural Integrity*, *44*, 1260-1267.

[22] Bertolesi, E., Carozzi, F. G., Milani, G., Poggi, C. (2017). Masonry arches retrofitted with steel reinforced grout materials: In-situ experimental tests and advanced FE simulations. In *AIP Conference Proceedings* (Vol. 1906, No. 1). AIP Publishing.

[23] Premier Premiscelati. (n.d.). *Rinforzo muratura con intonaco armato CRM su edifici storico-monumentali.* www.premierpremiscelati.it/applicazione/rinforzo-muratura-con-intonaco-armato-crm-su-edifici-storico-monumentali/

[24] Fibre Net S.p.A. (2025). *RI-STRUTTURA: Sistema CRM. Rinforzo di strutture in muratura* [Brochure]. https://fibrenet.it/wp-content/uploads/DEPLIANT-RISTRUTTURA-IT.pdf

[25] Ruregold. (n.d.). *Ruregold – Soluzioni per il rinforzo strutturale in materiali compositi*. https://ruregold.com/it/rinforzi-strutturali-sistemi-frcm-software-di-calcolo/

[26] Del Zoppo, M., Di Ludovico, M., & Prota, A. (2019). Analysis of FRCM and CRM parameters for the in-plane shear strengthening of different

URM types. *Composites Part B: Engineering*, 171, 20–33.

[27] ASTM International. (2022). *Standard Test Method for Diagonal Tension (Shear) in Masonry Assemblages (ASTM E519/E519M-22)*. ASTM International.

[28] Ferretti, F., Incerti, A., Ferracuti, B., & Mazzotti, C. (2017). FRCM strengthened masonry panels: The role of mechanical anchorages and symmetric layouts. *Key Engineering Materials*, 747, 334–341.

[29] Del Zoppo, M., Di Ludovico, M., Balsamo, A., & Prota, A. (2019). Experimental in-plane shear capacity of clay brick masonry panels strengthened with FRCM and FRM composites. *Journal of Composites for Construction*, 23(5), 04019038.

[30] Tilocca, A. R., Incerti, A., Bellini, A., & Savoia, M. (2019). Influence of matrix properties on FRCM-CRM strengthening systems. *Key Engineering Materials*, 817, 478–485.

[31] Balsamo, A., Asprone, D., Iovinella, I., Maddaloni, G., Menna, C., Prota, A., Ceroni, F., & Zinno, A. (2016). Effectiveness of inorganic matrix–grid composites for strengthening masonry walls. In *Brick and Block Masonry – Trends, Innovations and Challenges*, pp. 2013–2020. CRC Press.

[32] Mazzotti, C., Ferretti, F., Ferracuti, B., & Incerti, A. (2016). Diagonal compression tests on masonry panels strengthened by FRP and FRCM. In *Structural Analysis of Historical Constructions*, pp. 1069–1076. Taylor & Francis Group.

[33] D'Antino, T., Carozzi, F. G., & Poggi, C. (2019). Diagonal shear behavior of historic walls strengthened with Composite Reinforced Mortar (CRM). *Key Engineering Materials*, 817, 528–535.

[34] Del Zoppo, M., Di Ludovico, M., Balsamo, A., & Prota, A. (2019). In-plane shear capacity of tuff masonry walls with traditional and innovative Composite Reinforced Mortars (CRM). *Construction and Building Materials*, 210, 289–300.

[35] Ferrara, G., Caggegi, C., Martinelli, E., & Gabor, A. (2020). Shear capacity of masonry walls externally strengthened using Flax-TRM composite systems: Experimental tests and comparative assessment. *Construction and Building Materials*, 261, 120490.

[36] Menna, C., Asprone, D., Durante, M., Zinno, A., Balsamo, A., & Prota, A. (2015). Structural behaviour of masonry panels strengthened with an innovative hemp fibre composite grid. *Construction and Building Materials*, 100, 111–121.

[37] Borri, A., Casadei, P., Castori, G., Hammond, J. (2009). Strengthening of brick masonry arches with externally bonded steel reinforced composites. *Journal of composites for construction*, *13*(6), 468-475

[38] Alecci, V., Focacci, F., Rovero, L., Stipo, G., & De Stefano, M. (2017). Intrados strengthening of brick masonry arches with different FRCM composites: Experimental and analytical investigations. *Composite Structures*, *176*, 898-909.

[39] Alecci, V., Focacci, F., Rovero, L., Stipo, G., & De Stefano, M. (2016). Extrados strengthening of brick masonry arches with PBO–FRCM composites: Experimental and analytical investigations. *Composite Structures*, *149*, 184-196.

[40] Garmendia, L., San-José, J. T., García, D., & Larrinaga, P. (2011). Rehabilitation of masonry arches with compatible advanced composite material. *Construction and Building Materials*, *25*(12), 4374-4385.

[41] Gattesco, N., & Boem, I. (2017). Characterization tests of GFRM coating as a strengthening technique for masonry buildings. *Composite Structures*, *165*, 209-222.

[42] Gattesco, N., Boem, I., & Andretta, V. (2018). Experimental behaviour of non-structural masonry vaults reinforced through fibre-reinforced mortar coating and subjected to cyclic horizontal loads. *Engineering Structures*, *172*, 419-431.

[43] Boem, I., & Gattesco, N. (2021). Cyclic behavior of masonry barrel vaults strengthened through Composite Reinforced Mortar, considering the role

of the connection with the abutments. *Engineering Structures*, *228*, 111518.

[44] Longo, F., Cascardi, A., Lassandro, P., & Aiello, M. A. (2020). A new Fabric Reinforced Geopolymer Mortar (FRGM) with mechanical and energy benefits. *Fibers*, 8(8), 49.

[45] Longo, F., Cascardi, A., Lassandro, P., & Aiello, M. A. (2021). Energy and seismic drawbacks of masonry: A unified retrofitting solution. *Journal of Building Pathology and Rehabilitation*, 6(1), 31.

[46] Longo, F., Cascardi, A., Lassandro, P., & Aiello, M. A. (2021). Thermal and seismic capacity improvements for masonry building heritage: A unified retrofitting system. *Sustainability*, 13(3), 1111.

[47] ICC Evaluation Service. (2018). *AC 434-1011-R1: Acceptance Criteria for Masonry and Concrete Strengthening Using Fiber-Reinforced Cementitious Matrix (FRCM) Composite Systems*. ICC Evaluation Service.

[48] Ministero delle Infrastrutture e dei Trasporti. (2018). *Norme Tecniche per le Costruzioni (NTC 2018)*. Rome, Italy

[49] Ministero delle Infrastrutture e dei Trasporti. (2019). *Istruzioni per l'applicazione dell'«Aggiornamento delle "Norme tecniche per le costruzioni"» di cui al decreto ministeriale 17 gennaio 2018 (Circolare 21 gennaio 2019, n. 7 C.S.LL.PP).* Rome, Italy.

[50] RILEM Technical Committee 232-TDT. (2016). Recommendation of RILEM TC 232-TDT: Test methods and design of textile reinforced concrete. *Materials and Structures*, 49, 4923–4927.

[51] de Felice, G., Aiello, M. A., Caggegi, C., Ceroni, F., De Santis, S., Garbin, E., Gattesco, N., Hojdys, Ł., Krajewski, P., Kwiecień, A., Leone, M., Lignola, G. P., Mazzotti, C., Oliveira, D., Papanicolaou, C., Poggi, C., Triantafillou, T., Valluzzi, M. R., & Viskovic, A. (2018). Recommendation of RILEM Technical Committee 250-CSM: Test method for Textile Reinforced Mortar to substrate bond characterization. *Materials and Structures*, 51, 95.

[52] Consiglio Superiore dei Lavori Pubblici. (2018). *Linea Guida per la identificazione, la qualificazione ed il controllo di accettazione di compositi fibrorinforzati a matrice inorganica (FRCM) da utilizzarsi per il consolidamento strutturale di costruzioni esistenti*. Rome, Italy.

[53] Consiglio Superiore dei Lavori Pubblici. (2019). *Linea Guida per la identificazione, la qualificazione ed il controllo di accettazione dei sistemi a rete preformata in materiali compositi fibrorinforzati a matrice polimerica da utilizzarsi per il consolidamento strutturale di costruzioni esistenti con la tecnica dell'intonaco armato CRM (Composite Reinforced Mortar). Rome, Italy*.

[54] Lourenço, P. B. (2010). Recent advances in masonry modelling: micromodelling and homogenisation. *Multiscale modeling in solid mechanics: computational approaches*, 251-294.

[55] González-de-León, I., Requena García de la Cruz, M. V., Romero-Sánchez, E., & Morales-Esteban, A. (2025). Comparative study of solid and shell elements in the numerical modelling of heritage structures, pp. 264–275.

[56] Milani, G., & Tralli, A. (2012). A simple meso-macro model based on SQP for the nonlinear analysis of masonry double curvature structures. *International Journal of Solids and Structures*, *49*(5), 808-834.

[57] Li, T., & Atamturktur, S. (2014). Fidelity and robustness of detailed micromodeling, simplified micromodeling, and macromodeling techniques for a masonry dome. *Journal of Performance of Constructed Facilities*, 28(3), 480-490.

[58] Monaco, A., Minafò, G., Cucchiara, C., D'Anna, J., & La Mendola, L. (2017). Finite element analysis of the out-of-plane behavior of FRP strengthened masonry panels. *Composites Part B: Engineering*, *115*, 188-202.

[59] Ricci, E., Oliveira, D. V., Sacco, E., & Ghiassi, B. (2018). Modelling of masonry arches strengthened at extrados with FRCM. In *Proceedings of the 10th International Masonry Conference (IMC)*, Shermanbury, UK.

[60] Castellano, A., Fraddosio, A., Oliveira, D. V., Piccioni, M. D., Ricci, E., & Sacco, E. (2023). An effective numerical modelling strategy for FRCM strengthened curved masonry structures. *Engineering Structures*, *274*, 115116.

[61] Regione Siciliana. (n.d.). *Schemi di piano dei materiali lapidei di pregio.* https://www.regione.sicilia.it/la-regione-informa/aggiornamento-piani-regionali-materiali-lapidei-pregio-materiali-cava

[62] Sicilia Civil Engineering Office. (n.d.). *Characterization of Materials Constituting the Vertical Structures of Current Masonry Construction*. https://emidius.mi.ingv.it/GNDT2/Pubblicazioni/Lsu_bis/pdf/475_486

[63] Cucchiara, C. *Risposta strutturale di volte in muratura: Analisi teorico-sperimentale in regime non lineare* [Doctoral dissertation]. University of Palermo.

[64] Zimbardo, M., Nocilla, N., Evangelista, A., Ramondini, M., & Scotto di Santolo, A. (2011). Destructuration of typical Sicilian calcarenites. *Bulletin of Engineering Geology and the Environment*, 70(3), 507–515.

[65] Bellanca, A., Curcuruto, E. R., Bue, S. A. A. L., & Neri, R. (1999). Petrografia, geochimica e riferimenti all'impiego storico delle calcareniti plioceniche di Sabucina.

[66] UNI EN 1926:2007. (2007) *Metodi di prova per pietre naturali: Determinazione della resistenza a compressione uniassiale*. Ente Nazionale Italiano di Unificazione.

[67] UNI EN 12664:2002. (2002) *Prestazione termica dei materiali e dei prodotti per edilizia: Determinazione della resistenza termica con il metodo della piastra calda con anello di guardia e con il metodo del termoflussimetro – Prodotti secchi e umidi con media e bassa resistenza termica*. Ente Nazionale Italiano di Unificazione.

[68] UNI EN ISO 10456:2008. (2008). *Building Materials and Products – Hygrothermal Properties – Tabulated Design Values and Procedures for Determining Declared and Design Thermal Values*. Ente Nazionale Italiano di Unificazione.

[69] UNI EN 1015-11:2019. (2019). *Metodi di prova per malte per opere murarie – Parte 11: Determinazione della resistenza a flessione e a compressione della malta indurita*. Ente Nazionale Italiano di Unificazione

[70] UNI EN 772-1:2011. (2011). *Metodi di prova per elementi per muratura – Determinazione della resistenza a compressione*. Ente Nazionale Italiano di Unificazione.

[71] Vasanelli, E., Calò, S., Cascardi, A., & Aiello, M. A. (2024). The use of lightweight aggregates in geopolymeric mortars: The effect of liquid absorption on the physical/mechanical properties of the mortar. *Materials*, 17, 1798.

[72] Hyseni, A., Caggegi, C., Reboul, N., & Micelli, F. (2025). Diagonal shear behaviour of limestone masonry walls strengthened with jute-TRM composite systems. *Construction and Building Materials*, 470, 140572.

[73] Mantegazza, G. (2006). Retrofitting concrete and masonry building: FRCM (Fiber Reinforced Cementitious Matrix) a new emerging technology. In *Proceedings of the 3rd International Conference on Bridge Maintenance, Safety and Managemen.*

[74] Prota, A., Marcari, G., Fabbrocino, G., Manfredi, G., & Aldea, C. (2006). Experimental in-plane behavior of tuff masonry strengthened with cementitious matrix–grid composites. *Journal of Composites for Construction*, 10(3), 223–233.

[75] Faella, C., Martinelli, E., Nigro, E., & Paciello, S. (2010). Shear capacity of masonry walls externally strengthened by a cement-based composite material: An experimental campaign. *Construction and Building Materials*, 24(1), 84–93.

[76] Parisi, F., Iovinella, I., Balsamo, A., Augenti, N., & Prota, A. (2013). In-plane behaviour of tuff masonry strengthened with inorganic matrix–grid composites. *Composites Part B: Engineering*, 45(1), 1657–1666.

[77] Babaeidarabad, S., & Nanni, A. (2014). URM walls strengthened with fabric-reinforced cementitious matrix (FRCM) subjected to in-plane and out-of-plane load. In *CICE 2014 – 7th International Conference on FRP Composites in Civil Engineering*, Vancouver, Canada.

[78] Balsamo, A., Iovinella, I., & Morandini, G. (2014). FRG strengthening systems for masonry building. In *2014 NZSEE Conference*.

[79] Corradi, M., Borri, A., Sisti, R., & Buratti, C. (2014). Shear strengthening of wall panels through jacketing with cement mortar reinforced by GFRP grids. *Composites Part B: Engineering*, 64, 33–42.

[80] Ingham, J. M., & Ismail, N. (2014). Polymer textiles as a retrofit material for masonry walls. *Proceedings of the Institution of Civil Engineers – Structures and Buildings*, 167(1), 15–25.

[81] Almeida, J. A. P. P., Pereira, E. B., & Barros, J. A. O. (2015). Assessment of overlay masonry strengthening system under in-plane monotonic and cyclic loading using the diagonal tensile test. *Construction and Building Materials*, 94, 851–865.

[82] Gattesco, N., Boem, I., & Dudine, A. (2015). Diagonal compression tests on masonry walls strengthened with a GFRP mesh reinforced mortar coating. *Bulletin of Earthquake Engineering*, 13(6), 1703–1726.

[83] Gattesco, N., & Boem, I. (2015). Experimental and analytical study to evaluate the effectiveness of an in-plane reinforcement for masonry walls using GFRP meshes. *Construction and Building Materials*, 88, 94–104.

[84] Koutas, L., Triantafillou, T. C., & Bousias, S. N. (2015). Analytical modeling of masonry-infilled RC frames retrofitted with textile-reinforced mortar. *Journal of Composites for Construction*, 19(5), 04014082.

[85] Borri, A., Corradi, M., Sisti, R., Buratti, C., Belloni, E., & Moretti, E. (2016). Masonry wall panels retrofitted with thermal-insulating GFRP-reinforced jacketing. *Materials and Structures*, 49(10), 3957–3968.

[86] Marcari, G., Basili, M., & Vestroni, F. (2017). Experimental investigation of tuff masonry panels reinforced with surface bonded basalt textile-reinforced mortar. *Composites Part B: Engineering*, 108, 131–142.

[87] Micelli, F., Sciolti, M. S., Leone, M., Aiello, M. A., & Dudine, A. (2016). Shear behaviour of Fiber Reinforced Mortar strengthened masonry walls built with limestone blocks and hydraulic mortar. In *Brick and Block Masonry – Trends, Innovations and Challenges*, pp. 2137–2146. CRC Press

[88] Sagar, S. L., Singhal, V., Rai, D. C., & Gudur, P. (2017). Diagonal shear and out-of-plane flexural strength of fabric-reinforced cementitious matrix–strengthened masonry wallets. *Journal of Composites for Construction*, 21(4), 04017016.

[89] Yardim, Y., & Lalaj, O. (2016). Shear strengthening of unreinforced masonry wall with different fiber reinforced mortar jacketing. *Construction and Building Materials*, 102, 149–154.

[90] Ismail , N., El-Maaddawy, T., Najmal, A., & Khattak, N. (2017). Diagonal tension testing of as-built and fabric reinforced cementitious matrix strengthened masonry panels. In *Proceedings of the 16th World Conference of Earthquake Engineering (16WCEE)*.

[91] Mustafaraj, E., & Yardim, Y. (2018). In-plane shear strengthening of unreinforced masonry walls using GFRP jacketing. *Periodica Polytechnica Civil Engineering*, 62(2), 330–336.

[92] Ismail, N., El-Maaddawy, T., Khattak, N., & Najmal, A. (2018). In-plane shear strength improvement of hollow concrete masonry panels using a fabric-reinforced cementitious matrix. *Journal of Composites for Construction*, 22(2), 04018004.

[93] Ismail, N., El-Maaddawy, T., Najmal, A., & Khattak, N. (2018). Experimental in-plane performance of insulated concrete and brick masonry wall panels retrofitted using polymer composites. *Bulletin of the New Zealand Society for Earthquake Engineering*, 51(2), 85–91.

[94] Carozzi, F. G., et al. (2018). In-situ experimental tests on masonry panels strengthened with Textile Reinforced Mortar composites. *Procedia Structural Integrity*, 11, 355–362.

[95] Giaretton, M., Dizhur, D., Garbin, E., Ingham, J. M., & da Porto, F. (2018). In-plane strengthening of clay brick and block masonry walls using textile-reinforced mortar. *Journal of Composites for Construction*, 22(5), 04018028.

[96] Vatani Oskouei, A., Jafari, A., Bazli, M., & Ghahri, R. (2018). Effect of different retrofitting techniques on in-plane behavior of masonry wallettes. *Construction and Building Materials*, 169, 578–590.

[97] Shabdin, M., Zargaran, M., & Attari, N. K. A. (2018). Experimental diagonal tension (shear) test of Un-Reinforced Masonry (URM) walls strengthened with textile reinforced mortar (TRM). *Construction and Building Materials*, 164, 704–715.

[98] Basili, M., Vestroni, F., & Marcari, G. (2019). Brick masonry panels strengthened with textile reinforced mortar: Experimentation and numerical analysis. *Construction and Building Materials*, 227, 117061.

[99] Benedetti, A. (2019). Diagonal compression behaviour of masonry walls reinforced with FRM coatings. In R. Aguilar et al. (Eds.), *Structural Analysis of Historical Constructions* (pp. 474–483). Springer.

[100] Casacci, S., Gentilini, C., Di Tommaso, A., & Oliveira, D. V. (2019). Shear strengthening of masonry wallettes resorting to structural repointing and FRCM composites. *Construction and Building Materials*, 206, 19–34.

[101] Incerti, A., Ferretti, F., & Mazzotti, C. (2019). FRCM strengthening systems efficiency on the shear behavior of pre-damaged masonry panels: An experimental study. *Journal of Building Pathology and Rehabilitation*, 4(1), 14.

[102] Wang, X., Lam, C. C., & Iu, V. P. (2019). Comparison of different types of TRM composites for strengthening masonry panels. *Construction and Building Materials*, 219, 184–194.

[103] Angiolilli, M., Gregori, A., Pathirage, M., & Cusatis, G. (2020). Fiber Reinforced Cementitious Matrix (FRCM) for strengthening historical stone masonry structures: Experiments and computations. *Engineering Structures*, 224, 111102.

[104] Cheng, S., Yin, S., & Jing, L. (2020). Comparative experimental analysis on the in-plane shear performance of brick masonry walls strengthened with different fiber reinforced materials. *Construction and Building Materials*, 259, 120387.

[105] Del Zoppo, M., Di Ludovico, M., Balsamo, A., & Prota, A. (2020). Diagonal compression testing of masonry panels with irregular texture strengthened with inorganic composites. *Materials and Structures*, 53(5), 107.

[106] Garcia-Ramonda, L., Pelá, L., Roca, P., & Camata, G. (2020). In-plane shear behaviour by diagonal compression testing of brick masonry walls strengthened with basalt and steel textile reinforced mortars. *Construction and Building Materials*, 240, 117905.

[107] Gulinelli, P., Aprile, A., Rizzoni, R., Grunevald, Y.-H., & Lebon, F. (2020). Multiscale numerical analysis of TRM-reinforced masonry under diagonal compression tests. *Buildings*, 10(11), 196.

[108] Castori, G., Corradi, M., & Speranzini, E. (2021). Full size testing and detailed micro-modeling of the in-plane behavior of FRCM–reinforced masonry. *Construction and Building Materials*, 299, 124276.

[109] Dong, Z., Deng, M., Dai, J., & Ma, P. (2021). Diagonal compressive behavior of unreinforced masonry walls strengthened with textile reinforced mortar added with short PVA fibers. *Engineering Structures*, 246, 113034.

[110] Drobiec, Ł., Jasiński, R., Mazur, W., & Jokiel, R. (2020). The effect of the strengthening of AAC masonry walls using FRCM system. *Cement Wapno Beton*, 25(5), 376–389.

[111] Ferretti, F., Incerti, A., & Mazzotti, C. (2020). Experimental study on the shear behavior of FRCM strengthened masonry panels. In *12th International Conference on Structural Analysis of Historical Constructions (SAHC 2020)*.

[112] Ferretti, F., Incerti, A., Tilocca, A. R., & Mazzotti, C. (2021). In-plane shear behavior of stone masonry panels strengthened through grout injection and fiber reinforced cementitious matrices. *International Journal of Architectural Heritage*, 15(9), 1375–1394.

[113] Ferretti, F., & Mazzotti, C. (2021). FRCM/SRG strengthened masonry in diagonal compression: Experimental results and analytical approach proposal. *Construction and Building Materials*, 283, 122766.

[114] Longo, F., Cascardi, A., Lassandro, P., & Aiello, M. A. (2021). Energy and seismic drawbacks of masonry: A unified retrofitting solution. *Journal of Building Pathology and Rehabilitation*, 6(1), 31.

[115] Mezrea, P. E., Ispir, M., Balci, I. A., Bal, I. E., & Ilki, A. (2021). Diagonal tensile tests on historical brick masonry wallets strengthened with fabric reinforced cementitious mortar. *Structures*, 33, 935–946.

[116] Ungureanu, D., Țăranu, N., Ghiga, D. A., Isopescu, D. N., Mihai, P., & Cozmanciuc, R. (2021). Diagonal tensile test on masonry panels strengthened with textile-reinforced mortar. *Materials*, 14, 7021.

[117] Thomoglou, A. K., & Karabinis, A. I. (2022). Experimental investigation of the shear strength of hollow brick unreinforced masonry walls retrofitted with TRM system. *Earthquakes and Structures*, 22(4), 355–372.

[118] Arce, A., Kapsalis, P., Papanicolaou, C. G., & Triantafillou, T. C. (2023). Diagonal compression tests on unfired and fired masonry wallettes retrofitted with textile-reinforced alkali-activated mortar. *Journal of Composites Science*, 8, 14.

[119] Cholostiakow, S., Koutas, L. N., & Papakonstantinou, C. G. (2023). Geopolymer versus cement-based textile-reinforced mortar: Diagonal

compression tests on masonry walls representative of infills in RC frames. *Construction and Building Materials*, 373, 130836.

[120] Estevan, L., Torres, B., Varona, F. B., Baeza, F. J., & Ivorra, S. (2023). Shear strengthening of masonry walls with Textile Reinforced Mortars (TRM) under high temperature exposure. *Journal of Building Engineering*, 63, 105511.

[121] Garcia-Ramonda, L., Pelà, L., Roca, P., & Camata, G. (2023). Experimental and numerical insights on the in-plane behaviour of unreinforced and TRM/SRG retrofitted brick masonry walls by diagonal compression and shear-compression testing. *Construction and Building Materials*, 402, 132997.

[122] Alecci, V., Fagone, M., Galassi, S., Rotunno, T., Stipo, G., & De Stefano, M. (2024). Experimental shear behaviour of masonry walls reinforced with FRCM. *Engineering Structures*, 315, 118425.

[123] Hyseni, A., Caggegi, C., Reboul, N., Aiello, M. A., & Micelli, F. (2025). Diagonal compression mechanical behavior of masonry walls reinforced by Jute TRM: The contribution of 2D DIC measurements in the analysis of data. *In IB2MaC 2024* (pp. 680–693). Springer.

[124] Kałuża, M. (2024). TRM strengthening as effective prevention against premature failure of masonry walls. *Engineering Failure Analysis*, 162, 108436.

[125] Özen, A., Mercimek, Ö., Bıçakçıoğlu, K., Erbaş, Y., Yılmaz, M. C., & Anıl, Ö. (2024). Masonry walls strengthening with TRM subjected to in-plane cyclic loading. *Structures*, 70, 107723.

[126] Thatikonda, N. P., Baraldi, D., Boscato, G., & Cecchi, A. (2025). Experimental characterization and numerical validation of NFRCM for strengthening masonry. *In MuRiCo 2025* (pp. 89–99). Springer.

[127] European Committee for Standardization. (2012). *Eurocode 6: Design of masonry structures—Part 1-1: General rules for reinforced and unreinforced masonry structures* (EN 1996-1-1:2005+A1:2012). CEN.

[128] Bellini, A., Bovo, M., & Mazzotti, C. (2019). Experimental and numerical evaluation of fiber-matrix interface behaviour of different FRCM systems. *Composites Part B: Engineering*, 161, 411–426.

[129] Oddo, M. C., Cavaleri, L., Papanicolaou, C., & La Mendola, L. (2024). Experimental characterization of Fabric-Reinforced Cementitious Matrix (FRCM) systems applied on calcarenite stone: Adoption of non-standard setup for double-shear bond tests. *Journal of Composites Science*, 8, 206.

[130] Fibre Net S.p.A. (2022). *Adhesion Promoter FB-IPN01 – Technical Datasheet*. https://fibrenet.it/prodotto/resina-per-incollaggio-inghisaggio-fb-ipn01/

[131] Sutton, M. A., Orteu, J. J., and Schreier, W. H. (2009). *Image Correlation for Shape, Motion and Deformation Measurements: Basic Concepts, Theory and Applications*, Springer, New York.

[132] GOM GmbH. (2017). *GOM Correlate* (Version 2017) [Computer software]. GOM GmbH. https://www.gom.com

[133] Del Zoppo, M., Di Ludovico, M., Prota, A. (2019). Analysis of FRCM and CRM parameters for the in-plane shear strengthening of different URM types. *Composites Part B: Engineering*. 171.

[134] Chamis, C.C. (1984). *Mechanics of Composite Materials: Past, Present and Future.* NASA Lewis Research Center.

[135] Petracca, M., Candeloro, F., & Camata, G. (2017). *STKO User Manual*. ASDEA Software Technology, Pescara, Italy.

[136] McKenna , F., Fenves, G. L., & Scott, M. H. (2006). *OpenSees: Open System for Earthquake Engineering Simulation*. Pacific Earthquake Engineering Research Center, University of California, Berkeley, CA.

[137] Petracca, M., Pelà, L., Rossi, R., Zaghi, S., Camata, G., & Spacone, E. (2017). Micro-scale continuous and discrete numerical models for nonlinear analysis of masonry shear walls. *Construction and Building Materials*, 149, 296–314.

[138] Petracca, M., Camata, G., Spacone, E., & Pelà, L. (2023). Efficient Constitutive Model for Continuous Micro-Modeling of Masonry Structures. *International Journal of Architectural Heritage*, *17*(1), 134–146.

[139] Lourenco, P., & Gaetani, A. (2022). *Finite Element Analysis for Building Assessment: Advanced Use and Practical Recommendations*.

[140] Monaco, A., Minafò, G., D'Anna, J., Oddo, M. C., & La Mendola, L. (2020). Constitutive numerical model of FRCM strips under traction. *Frontiers in Built Environment*, 6, 60.

[141] Heyman, J. (1966). The stone skeleton. *International Journal of solids and structures*, *2*(2), 249-279.

[142] Di Leto, M., Campisi, F., Rusticano, G., Cucchiara, C., La Mendola, L., Di Trapani, A. (2025). Experimental and numerical study on masonry barrel vault strengthened through CRM system: Preliminary results. *Procedia Structural Integrity*.